Okinawa Institute of Science and Technology
Graduate University

Thesis submitted for the degree

Doctor of Philosophy

Design, Fabrication, and Characterization of Optical Nanofiber Cavities

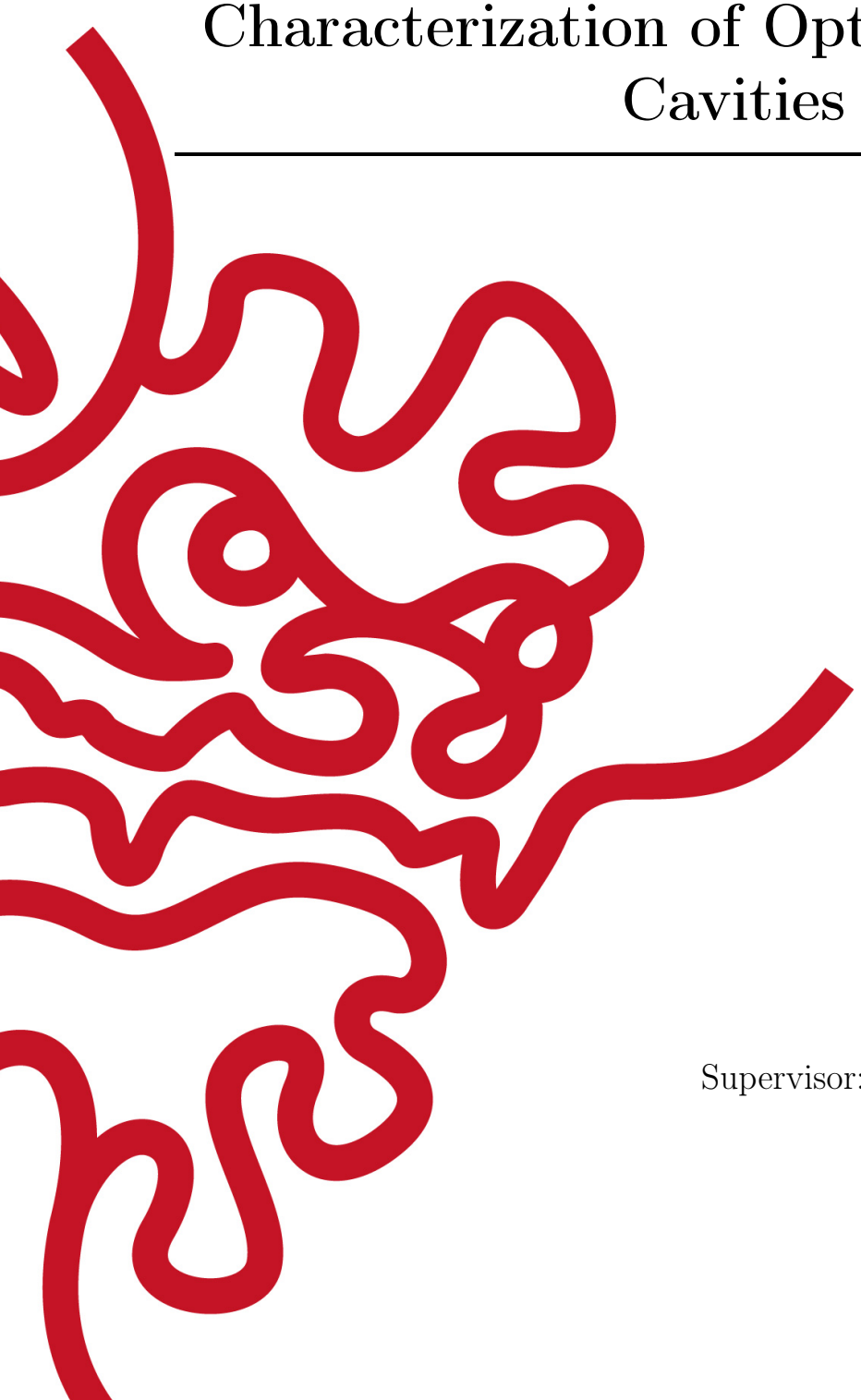

by

Maki Maeda

Supervisor: **Prof. Síle Nic Chormaic**

March 2024

Declaration of Original and Sole Authorship

I, Maki Maeda, declare that this thesis entitled *Design, Fabrication, and Characterization of Optical Nanofiber Cavities* and the data presented in it are original and my own work.

I confirm that:

- No part of this work has previously been submitted for a degree at this or any other university.
- References to the work of others have been clearly acknowledged. Quotations from the work of others have been clearly indicated, and attributed to them.
- In cases where others have contributed to part of this work, such contribution has been clearly acknowledged and distinguished from my own work.
- None of this work has been previously published elsewhere, with the exception of the following:
  - P. Romagnoli, M. Maeda, J.M. Ward, V.G. Truong, and S. Nic Chormaic, "Fabrication of optical nanofiber-based cavities using focussed ion-beam milling: a review", Appl. Phys. B **126**, 111 (2020).

    Contributions

    M.M., P.R., J.M.W. developed a new fabrication method, P.R. and M.M. operated the focused ion beam and fabricated cavities. P.R. wrote the manuscript, P.R., M.M., J.M.W., V.G.T., and S.N.C. edited the manuscript.
  - M. Maeda, J. Keloth, and S. Nic Chormaic, "Manipulation of polarization topology using a Fabry–Pérot fiber cavity with a higher-order mode optical nanofiber", Photon. Res. **11**, 1029-1037 (2023).

    Contributions

    M.M. conceived the project, M.M. designed and built the optical setup, and fabricated cavities. M.M. and J.K. wrote MATLAB code to analyze and simulate experimental results. M.M. collected, analyzed, and interpreted experimental data, and wrote the manuscript. M.M., J.K., and S.N.C. edited the manuscript.

March 2024

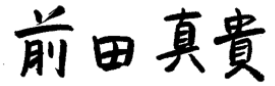

Abstract

Optical nanofibers (ONFs) pave the way for researchers to understand and control light-matter interactions at the nanoscale. Evanescent light fields at the waist of ONFs can be coupled to quantum emitters for various studies. In particular, significant experimental progress on quantum emitter coupling with an ONF-based cavity mode, for cavity quantum electrodynamics (cQED), has been achieved in the last two decades. This thesis showcases the following topics: (i) the development of novel ONF cavity fabrication methods using a focused ion beam (FIB) which provides highly reflective cavity mirrors with more stable fabrication quality than conventional fabrication methods, (ii) the optical characterization of ONF cavities fabricated using the FIB technique, (iii) the investigation of the effects of laser annealing on the cavity modes, and (iv) the realization and characterization of an ONF-based cavity supporting higher-order modes (HOMs) and controlled excitation of the desired HOMs with polarization topology. This is a significant step toward degenerate multimode cQED and potential access to evanescent field singular optics using a HOM-ONF. This PhD work advances ONF-based cavity systems, not only for cQED studies but also contributes to their fundamental understanding in quantum optics, structured light, and beyond.

Acknowledgment

First of all, I would like to thank Síle Nic Chormaic for her support in the past five and a half years. I am profoundly thankful for the opportunity I was granted to join her research unit as a PhD student, even in the absence of formal physics education. This acceptance enabled me to explore my curiosity about the natural world and delve into the role of a physicist.

I deeply thank Jameesh Keloth, with whom I worked most closely in my PhD. I learned a lot from him, not only due to his deep and wide knowledge regarding optical nanofiber cavities but also his excellent analytical skills. I really feel fortunate to have had the opportunity to work alongside him. Great thanks are further given to Jonathan Ward, from whom I learned the basic skills necessary to work in a physics lab. His remarkable proficiency in lab practices left a profound impression on me. I was inspired by his creative approach, and working with him in the lab was always enjoyable. Additional gratitude is extended to Priscila Romagnoli, with whom I shared both the bitter experience of failure and the satisfaction of success involving the nanofabrication process. Special appreciation is especially due to her kindness in teaching and encouraging me. I would like to further express my gratitude to Kristoffer Karlsson for his invaluable assistance in fabricating tapered fibers and maintaining lab equipment. I would also like to thank Metin Ozer for not only providing aid in resolving software issues and the nanofabrication process but also in his unwavering friendship and support throughout my PhD journey.

I also appreciate the discussions I had with the unit members, past and present. Many thanks to Alexey Vylegzhanin, Arina Ismail, Aswathy Raj, Angzhen Li, Christina Ripken, Cindy Esporlas, Harley Suchiang, Jean-Baptiste Ceppe, Jennifer Sanchez, Jesse Everett, Jibo Yu, Ke Tian, Liming Mao, Mohammed Zia Jalaludeen, Peter Mekhail, Shou Kasumei, Viet Giang Truong, Vishnu Kavungal, Zohreh Shahrabifarahani, and many others. I particularly enjoyed the intriguing discussion on thought experiments with Dylan Brown, Fuchuan Lei, Georgiy Tkachenko, Lewis Ruks, Ratnesh Kumar Gupta, Shilong Li, Thomas Nieddu, and Tridib Ray. Their expertise has provided me with valuable insights into their respective fields, broadening my knowledge. I also thank Domna Kostifaki, Krishnapriya Subramonian Rajasree, Theodoros Bouloumis, and Vandna Gohkroo for being not just colleagues but also friends, supporting me in various ways. I extend gratitude to Emi Nakamura, who manages all the essential administrative tasks for the unit.

Outside of the unit, I thank Fam Le Kien, whom I had great discussions with about the theoretical aspects of optical nanofiber cavity modes. Thanks also to the Nanofabrication Section, Mechanical Engineering Section, and Scientific Computing & Data Analysis Section at OIST, especially Noriko Ishizu, who taught me the basic skills of the focused ion beam. I am also thankful for staff members in the Graduate School at OIST, especially

Chiaki Chibana, who was always sympathetic and supportive of me in difficult circumstances. My gratitude extends to the amazing staff members of the Child Development Center at OIST, where my daughter had a great time, so I could focus on my work without any worry. I would also like to take this opportunity to extend my appreciation to OIST, the Japanese government, and the taxpayers of Japan for generously funding my research throughout my entire PhD journey. Moreover, thanks are given to Rita R. Colwell Impact Fund Grants, which was used to pay childminders outside of daycare hours.

Last, but definitely not least, I owe a great debt of gratitude to my family and friends who were always there for me to pursue my dream and make my life enjoyable. My deepest gratitude is given to Miyuki Maeda, Yuichi Maeda, David Chandlee, and especially Chika Maeda, who helped me in all aspects of my personal life over the last two and a half years. It was truly fortunate to have her in my life and I cannot thank her enough for her extraordinary support. I would like to thank my dearest little one, Hikari, who was extremely understanding of her mother having to work not only during daycare hours but also late at night as well as on weekends. She always made me happy and gave me the motivation to push myself forward.

Abbreviations

3D	three dimensional
A	antidiagonal
CCD	charge coupled device
cQED	cavity quantum electrodynamics
D	diagonal
EH	hybrid mode with dominant magnetic field in the longitudinal components
EME	eigenmode expansion
FBG	fiber Bragg grating
FDTD	finite-difference time-domain
FIB	focused ion beam
FM	few-mode
FSR	free spectral range
FWHM	full-width half-maximum
H	horizontal
HE	hybrid mode with dominant electric field in the longitudinal components
HOM	higher-order mode
HWP	half-wave plate
IPA	isopropyl alcohol
IPC	inline polarization contrller
ITO	indium tin oxide
L	left-handed
LG	Laguerre-Gaussian
LP	linearly polarized
NV	nitrogen-vacancy
OAM	orbital angular momentum
ONF	optical nanofiber
OMF	optical microfiber
OSA	optical spectrum analyzer
PhC	photonic crystal
QD	quantum dot
QED	quantum electrodynamics
QWP	quarter-wave plate
R	right-handed
SAM	spin angular momentum
SEM	scanning electron microscope
SiV	silicon-vacancy

SLM	spatial light modulator
SM	single-mode
SOP	state of polarization
TE	transverse electric
TM	transverse magnetic
V	vertical

Nomenclature

a	fiber radius
a_0	initial fiber radius
a_f	final fiber radius
A_eff	effective mode area
A_M	amplitude of mode M
c	Speed of light ($2.997\ 924\ 58 \times 10^8$ ms^{-1})
$\mathscr{c}$	simple closed path
$\mathcal{C}$	cooperativity
d	fiber diameter
d_0	initial fiber diameter
d_c	diameter of circular shape
d_eff	effective fiber diameter
d_f	final fiber diameter
d_i	the i^{th} intermediate fiber diameter with $i \in \mathbb{Z}^+$
$\mathbf{E}$	electric field vector
$\mathbf{E}_\mathrm{M}$	electric field vector of mode M
$\mathbf{e}$	reduced profile function of electric field vector
$\mathcal{E}$	spatial envelop function of electric field vector
e_r, r_θ, e_z	electric field components in each cylindrical coordinate
f	propagation direction
F	finesse
F_min	minimum required finesse for a strong coupling regime
g_0	emitter-photon coupling rate of free-space
g	emitter-photon coupling rate of optical nanofiber
$\mathbf{H}$	magnetic field vector
$\mathbf{h}$	reduced profile function of magnetic field vector
$\mathcal{H}$	spatial envelop function of magnetic field vector
h_r, h_θ, h_z	magnetic field components in each cylindrical coordinate
$\mathscr{H}$	hotzone
$\hbar$	reduced Planck constant ($1.054\ 572\ 66 \times 10^{-34}$ Js)
I	intensity
I_l	modified Bessel function of first kind with l^{th} order
J_l	Bessel function of first kind with l^{th} order
$\mathbf{J}_\mathrm{M}$	arbitrary birefringence Jones matrix
k	wavenumber
K_l	modified Bessel function of second kind with l^{th} order

l	azimuthal mode order
L	cavity mirror separation length
$\mathcal{L}$	intensity loss
$\mathscr{L}$	fiber pull length
L_{eff}	effective cavity length
L_{max}	maximum cavity length for a strong coupling regime
m	the radial mode order
n	refractive index
N	number of grating period
$\mathcal{N}$	number of emitter
$\mathscr{N}$	number of modes
n_1	refractive index of the core
n_2	refractive index of the cladding
n_{eff}	effective refractive index
n_{g}	group index
p	phase circulation direction
$\mathcal{P}$	Purcell factor
P_{a}	annealing laser power
Q	quality factor
R	intensity reflection
R_i	intensity reflection of the i^{th} mirror with $i \in \{1, 2\}$
(r, θ, z)	cylindrical coordinates
$(\hat{\mathbf{r}}, \hat{\boldsymbol{\theta}}, \hat{\mathbf{z}})$	unit vectors in cylindrical coordinates
S_i, S_j	Stokes parameters with with i, $j \in \{1, 2, 3\}$
s_x	width of rectangular shape in fiber transverse x direction
s_z	width of rectangular shape in fiber axial z direction
T	intensity transmission
V	V-number
V_{m}	mode volume
(x, y, z)	Cartesian coordinates
$(\hat{\mathbf{x}}, \hat{\mathbf{y}}, \hat{\mathbf{z}})$	unit vectors in Cartesian coordinates
Y_l	Bessel function of second kind with l^{th} order
z_{b}	beat length
z_{t}	local taper length
β	propagation constant
β_i	propagation constant of the i^{th} mode
γ_0	emitter decay rate of free-space
γ	emitter decay rate of optical nanofiber
γ_{g}	emitter decay rate to the optical nanofiber guided mode
γ_{r}	emitter decay rate to the radiation mode
Δn_{eff}	change of effective refractive index
$\Delta\Lambda$	change of grating period
$\Delta\lambda_{\text{B}}$	change of Bragg wavelength
$\Delta\lambda_{\text{B}}^{\text{Ga}}$	change of Bragg wavelength due to Ga desorption
$\Delta\lambda_{\text{B}}^{h}$	change of Bragg wavelength due to heating

ϵ_0	permittivity of free-space ($8.854\ 188 \times 10^{12}$ Fm^{-1})
η	channeling efficiency
η_M	relative phase retardation of mode M between the fast slow axis
θ_M	orientation of the first axis of mode M with respect to fiber transverse x-axis
θ_pol	orientation of the symmetry axis of the mode profile
κ	cavity decay rate
κ_s	cavity decay rate due to scattering loss
λ_r	resonant wavelength
λ	vacuum wavelength
Λ	grating period
λ_B	Bragg wavelength
μ_0	permeability of free-space ($4\pi \times 10^{-7}$ Hm^{-1})
ν_r	resonant frequency
σ	single emitter absorption cross-section
σ_{ij}	Stokes index with i, $j \in \{1, 2, 3\}$ in order
ϕ_{ij}	Stokes phases with i, $j \in \{1, 2, 3\}$ in order
ϕ_M	relative phase of mode M
χ	polarization ellipticity
ψ	polarization ellipse orientation
ω	angular frequency
Ω	core taper angle
Ω_i	the i^{th} local core taper angle with $i \in \mathbb{Z}^+$

To Takashi Maeda and my little quantum of light, Hikari.

Contents

List of Figures

List of Tables

Chapter 1

Introduction[1]

Light is the most familiar type of electromagnetic wave in our daily lives. The interaction of light and matter is an extremely ubiquitous physical phenomenon that enables us not only to see things but also is responsible for photosynthesis in plants, vitamin D synthesis in our bodies, and why the sky is blue. The interaction of light and matter described by the laws of quantum electrodynamics (QED) has led to essential scientific and technological achievements —lasers, light-emitting diodes (LEDs), and atomic clocks are only a few well-known examples. In recent years, nano-optics and nanophotonics have been of increasing interest for researchers to understand and control such interactions [2]. Optical nanodevices are attractive tools to investigate fundamental non-paraxial optical phenomena, such as transverse spin [3] and spin-orbit coupling [4, 5]. Such devices are also useful tools for quantum information applications, which include quantum computation and quantum cryptography [6, 7]. A single photon of light, which can be generated by a quantum emitter, can be trapped in an optical resonator. This can lead to a coherent interaction known as strong coupling, where the interaction between a quantum emitter and a cavity mode is so strong that it leads to observable and significant quantum (nonclassical) effects, and this is a key ingredient to advancing functional quantum technologies. This strong coupling in an optical cavity is part of a field of study called cavity QED (cQED) [8].

Among the various types of optical nanodevices, optical nanofibers (ONFs) —conventional optical fibers with a nanoscale diameter section —have some advantages due to easy integration into the existing fiber communication network to realize an all-fiber quantum system [4]. Light guided in the ONF contains a significant evanescent field, which can be further increased in an optical cavity at resonance for cQED [9]. There are various designs of the ONF-based cavity for cQED applications, falling into two main categories: (i) an internal mirror cavity where the mirror separation is on the micron scale and (ii) an external mirror cavity where the mirror separation is on the centimeter to meter scale [1, 8]. Each type of cavity has its own advantages and disadvantages and one of the challenges to realizing off-the-shelf all-fiber cavity quantum system is in fabricating opti-

[1]Section 1.4 in this chapter contains the following published work with permission licensed under a CC BY license: P. Romagnoli, M. Maeda, J.M. Ward, V.G. Truong, and S. Nic Chormaic, "Fabrication of optical nanofiber-based cavities using focussed ion-beam milling: a review", Appl. Phys. B 126, 111 (2020) [1]. M. Maeda contributed to the development of new fabrication methods with P. Romagnoli and J.M. Ward, the fabrication of the cavities with P. Romagnoli, and editing the paper.

mal cavity configurations according to the application purpose. Thus far, strong coupling was demonstrated using cold atom(s) and the fundamental mode of an external mirror type ONF-based cavity [10, 11]. Despite their achievement in the ONF community, such systems have a number of limitations. One of these limitations is the use of cold atom(s), which require a magneto-optical trap (MOT) and many optical components, leading to larger and more costly experimental setups. To facilitate the development of quantum technologies, it becomes crucial to reduce both the size and cost of the system. Another constraint of the existing ONF-based cavity system is that it supports exclusively the fundamental mode. Incorporating higher-order modes (HOMs) would broaden the cavity's capabilities as a tool for quantum information applications. This extension would be particularly valuable in scenarios involving cavity-based quantum information processing, where qubits associated with various cavity modes interact through a shared atom [12]. However, constructing an ONF-based cavity accommodating HOMs has not been achieved so far.

This PhD research explores ONF-based cavities, which are primarily aimed at, but not limited to, cQED experiments and applications. This chapter presents a brief history of ONFs and investigations on the light-matter interactions using ONFs and various ONF-based cavities representing the current state-of-the-art.

1.1 Introduction to ONFs

To begin with, let us first review a standard step-index silica (SiO_2) fiber. A specific path or pattern that light can take when it travels through the fiber is called a mode. The conventional fiber modes are assumed as nearly transverse fields and they are commonly referred to as linearly polarized (LP) modes [13]. Figure 1.1(a) shows a schematic of the step-index profile of a conventional single-mode (SM) fiber, which supports the fundamental LP_{01} mode, which propagates along the fiber axis in the z-direction. The optical fiber is made of two components, the core and cladding. The refractive index of such a fiber is a function of fiber radius position, r, and the refractive index in the core, n_1, has a slightly higher value compared to the refractive index in the cladding, n_2. The refractive index of the environment, n_3, is typically lower than n_2. The optical fiber is an efficient waveguide as the light is well confined and guided at the core/cladding interface by total internal reflection as shown in Figure 1.1(b). At the reflection sites, a small fraction of light penetrates into the cladding region as an evanescent field. The portion of energy in the evanescent field increases as the core diameter decreases [14]. Reducing the diameter of the optical fiber to the same order of magnitude as the wavelength of the fiber-guided light can lead to some unique properties. Not only does transverse confinement of the guided modes increase and, thereby, the field intensity, but an intense evanescent field also extends from the boundary of the fiber into its surroundings [14–18]. In fact, in some cases, the amount of energy in the evanescent field exceeds what remains inside the fiber, so that the light is essentially guided not only inside but also outside the fiber as depicted in Figure 1.1(b). In this scenario, it is more appropriate to describe the light ray as an electromagnetic field, i.e., the fundamental eigenmode, HE_{11}, rather than employing ray optics [14]. Such a subwavelength diameter optical fiber, a so-called optical microfiber (OMF) or ONF, is surrounded by the environment such as air, vacuum, or water, in which

the evanescent field extends. As a result, the guided mode is altered by the properties of the medium [19].

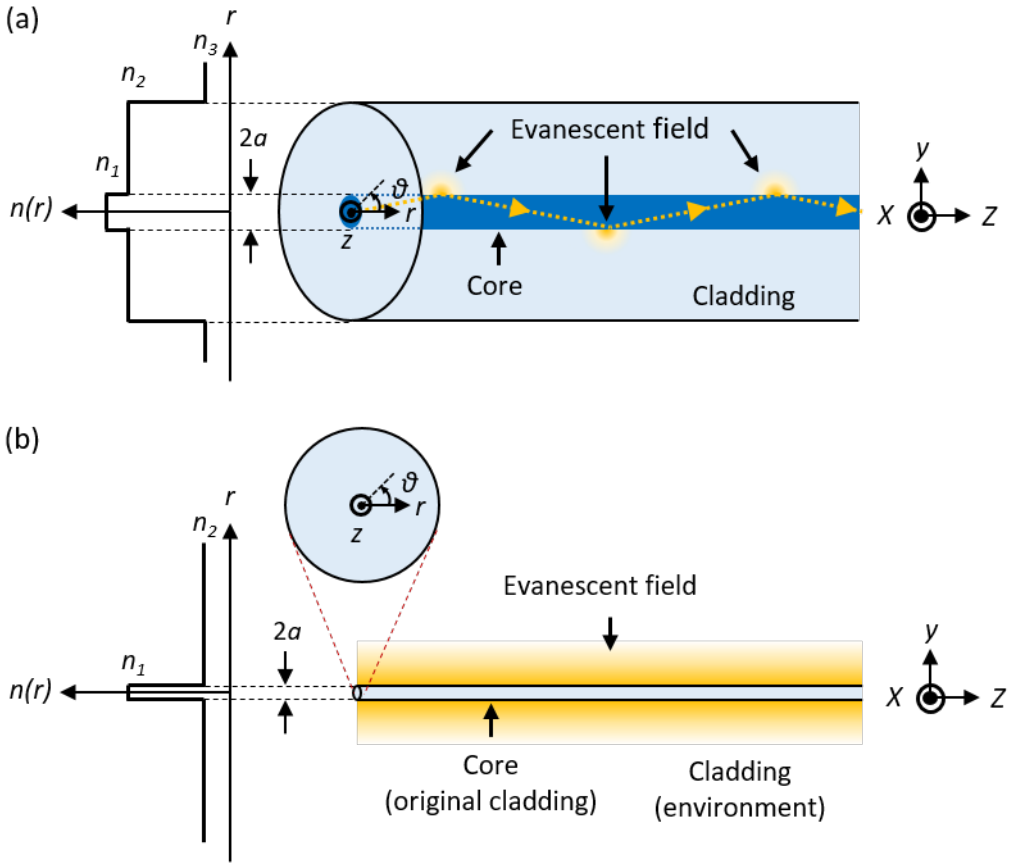

Figure 1.1: (a) Schematic of a standard step-index SM optical fiber and its refractive indices, $n(r)$: the core index, n_1, and the cladding index n_2 as well as the index of the environment, n_3, as a function of fiber radius position, r. Light propagation relies on total internal reflection, as viewed from the perspective of ray optics. (b) Schematic of an ONF and its $n(r)$, n_1, and n_2 as a function of r.

In perhaps the most extreme example, silica ONFs with diameters as small as 50 nm and lengths of tens of millimeters were reported by Tong et al. [16]. These ONFs or nanowires were fabricated using a flame-heated fiber drawing method, in which a conventional fiber was tapered to micrometer size, with a sapphire tip placed at the end of the taper. The sapphire tip was heated by a flame and used to draw out the nanowire. The authors coupled light into the nanowire via the evanescent field from a tapered optical fiber attached to the nanowire by van der Waals forces. Single-mode light guiding with low loss (below 0.1 dB mm^{-1}) at a wavelength of 633 nm was achieved for a 450 nm diameter wire and at a wavelength of 1550 nm for a 1100 nm diameter wire. This example demonstrates the capabilities of light guidance in optical fibers that are pushed to their physical limits. These unique properties have been exploited for a large number of applications, such as nonlinear optics [20, 21], cold atoms [22–24], particle manipulation, [25–29] and sensors [30–34]. Several reviews related to their fabrication and uses are available [1, 8, 14, 18, 31, 33–40].

Optical nanofibers are typically made by tapering a section of commercial optical fiber via heating and stretching [38, 41–44] in a fiber pulling rig, with either a stationary or moving (brushing) heat source. Different heat sources may be used, depending on the compound and melting point of the glass [33], such as a CO_2 laser [45], resistance heating [46] or a graphite microheater [47]. A drawing of a tapered fiber by heating and stretching is illustrated in Figure 1.2(a). After fabrication, a biconical, tapered fiber is formed, i.e., it has a down taper, transitioning from the initial diameter to a thin waist. The waist is followed by an up taper returning the fiber to its initial diameter. The thin waist region is referred to as the OMF or ONF, depending on the scale of the final diameter. As an alternative method, one can also use solvents to dissolve the fiber material to fabricate tapered fibers [48]. A scanning electron microscope (SEM) image of an ONF with a diameter of ∼690 nm is shown in Figure 1.2(b).

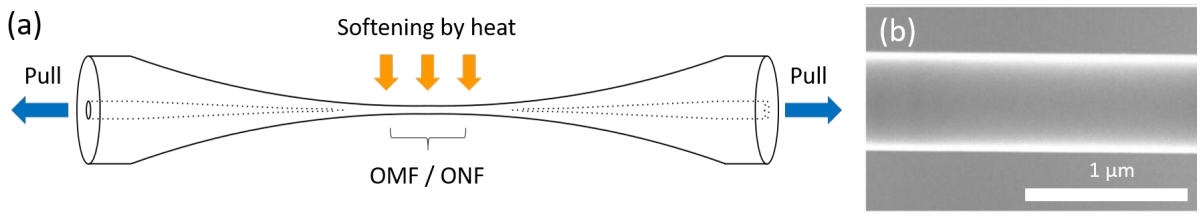

Figure 1.2: (a) Schematic of a tapered fiber drawn by heat-and-pull technique. (b) SEM image of a section of a typical ONF with a diameter of ∼690 nm.

Dedicated theoretical studies in the field of ONFs began to emerge approximately two decades ago. Le Kien et al. [49] calculated the field intensity distribution in an ONF and showed a large discontinuity of the field distribution at the core/cladding (SiO_2/vacuum) boundary due to high contrast between the refractive indices (∼0.45-0.46). The medium surrounding the ONF can interact with the guided light via the evanescent component. With this in mind, the spontaneous emission of a cesium (Cs) atom near an ONF was studied by Le Kien et al. [50]. The authors showed that confinement of the ONF-guided modes can change the decay rate of the Cs atom. Coupling between the emission from an atom on the surface of an ONF with a diameter of ∼400 nm and the guided mode was studied and a coupling efficiency of 28% was theoretically predicted.

Later experiments [23, 51] confirmed these predictions. For example, Nayak et al. [51] manipulated and probed the fluorescence of Cs atoms using ONFs. The authors used a MOT to confine and cool Cs atoms around an ONF with a diameter of 400 nm. With an effective number of atoms of 5, they showed an average coupling efficiency of spontaneous emission into the guided mode of ∼ 6%. The following year, a similar setup was used by Nayak et al. [23] to detect a single Cs atom and the coupling of the atom's spontaneous emission into the modes of the ONF. Aside from neutral atoms, similar experiments can be performed using a variety of single-photon emitters such as quantum dots (QDs) [52–55], diamond nanocrystals with a nitrogen-vacancy (NV) or silicon-vacancy (SiV) [56–58], single molecules [59] and hexagonal boron nitride [60]. Channeling efficiency of fluorescence from QDs into ONF-guided modes was demonstrated by Yalla et al. [54], see Figure 1.3. The number of photons in the guided and radiation modes was measured and a channeling efficiency up to 22.0 ± 4.8% was obtained for a 350 nm ONF and an emission wavelength of 780 nm, thus demonstrating a fiber-coupled single-photon source

with a bright output in the range of 10-100 of kilocounts/second. The ease with which OMFs or ONFs can be integrated into experimental setups means that they offer many advantages for applications in areas as diverse as optical sensing [30–34], atomic physics [22, 61–65], photonics [66–69] and quantum optics [11, 23, 40, 70, 71].

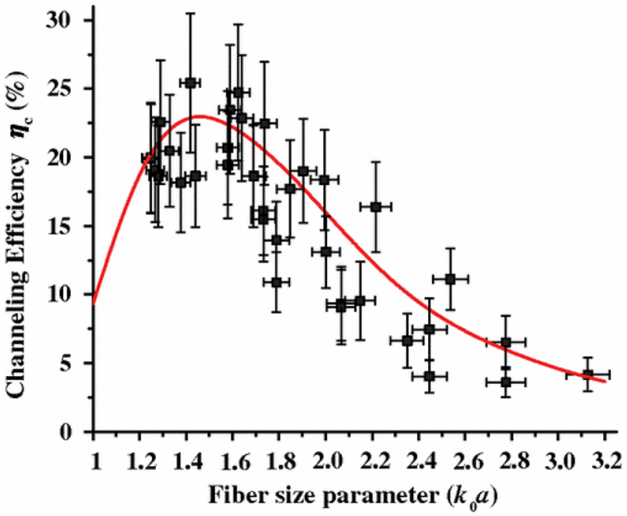

Figure 1.3: The channeling efficiency is depicted as a function of the fiber size parameter ($ka = 2\pi a\lambda$). The red solid curve represents the theoretical prediction, while the measured values are denoted by black squares with error bars. Reproduced from [54] with permission, copyright (2012) by the American Physical Society.

1.2 HOMs in ONFs

So far, we have introduced the early research focused on the light-matter interactions using ONFs with quantum emitters. Those various quantum emitters are coupled to the fundamental mode guided along an SM-ONF, supporting one mode per polarization. However, optical fiber can support multiple modes, and any modes propagating along a fiber rather than the fundamental mode are called HOMs. Figure 1.4 shows a cross-section of standard multimode fiber, where the core diameter is larger than the SM fiber (see Figure 1.1). The multimode fiber can support more than one guided mode, and multimode fibers with a small number of guided modes are termed few-mode (FM) fibers. In the multimode fiber, each mode has a distinctive propagation constant, thus rays' paths are different from each other as illustrated in Figure 1.4. HOMs can also propagate in an ONF with a waist diameter sufficiently large enough for specific wavelengths.

Most ONF research focuses on SM-ONFs. One of the most significant advantages of SM-ONFs is the absence of a cutoff diameter, allowing the fundamental mode to propagate along the fiber until the diameter is reduced to the point where the light is lost in free space [9]. This unique feature enables the propagation of the fundamental mode even in extremely small fibers, as long as the bulk material can accurately represent the response of a dielectric medium to an incident electric field [14]. Moreover, the fundamental mode in an ONF, HE_{11}, has a small mode area and simple mode structure. In the meantime,

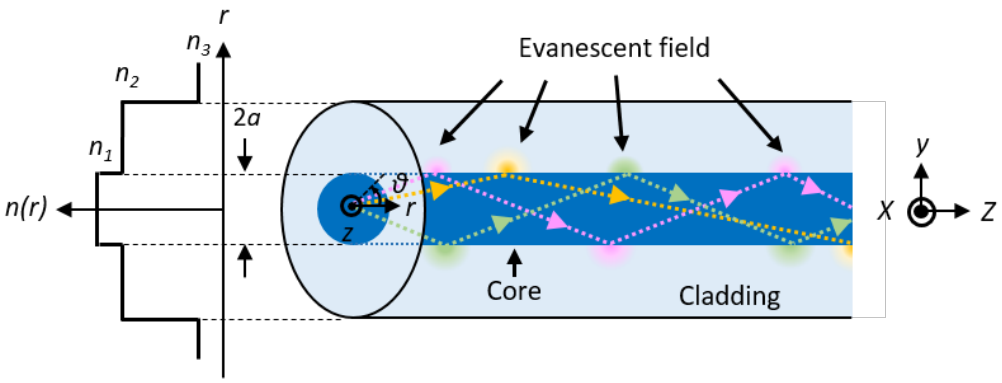

Figure 1.4: Schematic of a standard step-index FM optical fiber and its $n(r)$: n_1 and n_2 as well as n_3, as a function of r. Light propagation relies on internal total reflection, as viewed from the perspective of ray optics.

increasing attention has been paid to HOMs in ONFs for potential applications in many fields of optics and nanophotonics. The first group of HOMs in a conventional fiber is called the LP_{11} mode, which separates into the transverse electric (TE), transverse magnetic (TM), and hybrid modes, termed TE_{01}, TM_{01}, and HE_{21}. In what follows, we introduce the profiles of HOMs and their distinctive and captivating attributes not only in terms of cQED applications but also for the fundamental aspects.

1.2.1 Polarization structures of fiber modes

In recent years, there has been a significant increase in interest in the field of structured light optics [72]. Structured light involves the engineering of light in terms of its amplitude, phase, and polarization [73]. While all light inherently possesses structure, it is only in recent times that we have gained the capability to manipulate it comprehensively in terms of all its degrees of freedom and dimensions. This development has driven significant progress in both fundamental understanding and practical applications [72]. Historically, most instances of structured light fields have exclusively dealt with scalar beams, typically either neglecting the polarization component or regarding it as an independent degree of freedom during the design phase [73].

Polarization of light is the way its electric field vector oscillates [74] and the state of polarization (SOP), i.e., how the polarization is distributed in the cross-section of a given mode, can be controlled by mechanical perturbations in an optical fiber. One possibility is a bend perturbation, which induces birefringence. This occurs when the fiber bends along an in-plane path, and, as a result, linear and circular polarizations change their SOPs into elliptical fields [75]. Another important mechanical perturbation is the slow perturbation with an adiabatic redirection of light out-of-plane, namely the Pancharatnam–Berry phase, or the so-called geometrical phase [76, 77]. The phase introduced by geometric transformations differs from the more typical propagating phase linked to the phase propagation constant of a light beam [75]. Such phenomena can be observed in helically wound optical fibers, i.e., an optical fiber is placed in an out-of-plane path [78]. In this manifestation, linear polarization remains linear with a rotation of its SOP along

the azimuthal orientation, while circular polarization only acquires a phase [75].

One can classify polarized fields into three categories: scalar, vector, and ellipse fields. The scalar field has a homogeneous SOP at any point of the beam [73]. Figure 1.5(a) shows four examples of such fields. Figure 1.5(a)(i-iii) are the fiber fundamental mode, HE_{11}, with x-polarization, y-polarization, and circular-polarization, denoted as HE_{11}^{x}, HE_{11}^{x}, and HE_{11}^{circ}, respectively. The intensity pattern is Gaussian shaped and polarization is uniform at every point in each mode. Figure 1.5(a)(iv) is the circularly polarized HE_{21} mode, denoted as HE_{21}^{circ}. This mode has a donut-shaped intensity pattern so that there is a point with zero intensity at the center of the beam. Moreover, the polarization is homogeneously left-handed circular as indicated by blue circles, and is therefore classified as a scalar field. The zero intensity point in the scalar light field is called the optical phase singularity point (marked as a white dot), around which the phase changes by a multiple of 2π. Singularities in this context pertain to points or regions within a field where one or more parameters become undefined or exhibit extreme values. Such a field of study is known as singular optics, and it has been rapidly growing in the last 50 years [79, 80] since the discovery of phase singularity by Nye and Berry [81]. Singularities exhibit a natural characteristic, meaning they remain stable when subjected to perturbations and their natural behavior typicality includes generic, structurally stable, and universal [80]. Phase singularities can be generated by an optical fiber [82, 83]. In the case of the HE_{21}^{circ} mode, this phenomenon is observed in helical beams that carry orbital angular momentum (OAM). This beam displays an optical vortex where the wavefront swirls and forms a distinctive pattern.

The SOP can be inhomogeneous at each point of a beam. When the field oscillates linearly, the field can be categorized as a vector field [84]. In standard terminology, which we will adhere to in this PhD thesis, vector states of light pertain to states where the linear polarization pattern is nonuniformly spread across the spatial mode. In fact, linearly polarized fiber HOMs fall into this category, as shown in Figure 1.5(b)(i-iv). The HE_{21} mode with "*even*" and "*odd*" polarizations, denoted as HE_{21}^{e} and HE_{21}^{o}, are illustrated in Figure 1.5(b)(i, ii), respectively. These modes have polarization orthogonal at every point. Similarly, the TE_{01} and TM_{01} modes, Figure 1.5(b)(iii, iv), respectively, also have an orthogonal polarization relationship at every point of the cross-section. For orthogonal SOPs, the polarization ellipse shares the same ellipticity with the azimuths differing by $\pi/2$ and opposite handedness [74]. As clearly seen, all of these modes possess a donut-shaped intensity pattern, but these modes have nonuniform polarization as opposed to the donut mode of HE_{21}^{circ} (Figure 1.5(a)(iv)). The inhomogeneous electric field across the beam can form topological defects in the polarization, termed a polarization singularity [85]. Polarization singularities constitute a distinct branch within the field of singular optics, coexisting alongside phase singularities [79, 80]. In our examples here, there is a point with zero intensity at the center of the vector fields as indicated by pink dots in Figure 1.5(b)(i-iv). These points have undefined polarization and are termed V-points [86].

Similar to vector fields, the SOP can be inhomogeneous but not necessarily as a linear polarization at every point of the beam. Modes with an inhomogeneous polarization spread across a spatial mode with elliptical polarization are called ellipse fields [84]. Some examples are depicted in Figure 1.5(c)(i-iv). For example, an arbitrary ellipse field with a flower-like intensity shape, Figure 1.5(c)(i), shows various polarizations such as a

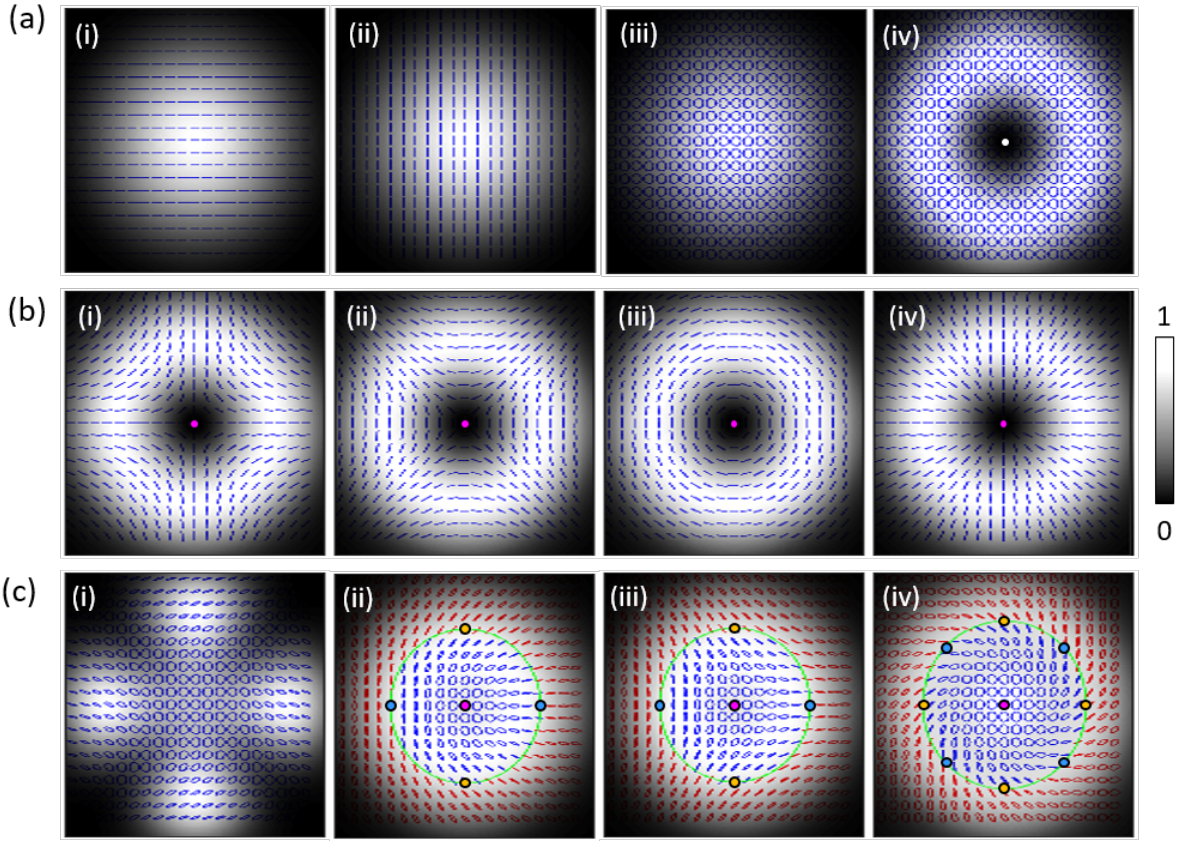

Figure 1.5: (a) The intensity profiles and polarization distribution of a scalar field: (i) the HE_{11}^{x} mode, (ii) the HE_{11}^{y} mode, (iii) the HE_{11}^{circ} mode, and (iv) the HE_{21}^{circ} mode. The phase singularity point is indicated by a white dot. (b) The intensity profiles and polarization distribution of a vector field: (i) the HE_{21}^{e} mode, (ii) the HE_{21}^{o} mode, (iii) the TE_{01} mode, and (iv) the TM_{01} mode. (c) The intensity profiles and polarization distribution of the ellipse field: (i) an arbitrary ellipse field, (ii) the lemon mode, (iii) the star mode, and (iv) the spiral mode. The red and blue SOPs indicate right-handed and left-handed ellipticities, respectively. V-points and C-points are indicated as pink dots, and Poincaré vertices are indicated as blue and orange dots. L-lines are indicated as green lines. The scale bars show the normalized intensity (from 0 to 1).

thin ellipse or a fat ellipse with various orientations. This particular mode only has left-handedness ellipses as indicated in blue and does not possess topological defects. However, ellipse fields can facilitate complex polarization textures with multiple types of singularities. Here we introduce relatively simple and well-known examples in the community of the singular optics: the lemon mode [87], star mode [87], and spiral mode [88], shown in Figure 1.5(c)(ii-iv), respectively. These modes have a point at the beam center with an unknown ellipse orientation, termed the C-point, as indicated by a pink dot. The ellipses rotate around the C-points thereby changing their ellipticities and they are linearly polarized fields at the contour marked in green. This line is called the L-line, where a line is formed by polarizations with unknown ellipticity. The ellipse orientation changes at the border of the L-line, as indicated by red ellipses being right-handed circulation. There

are also points where the polarization ellipticity is undefined and its polarization is either perfectly horizontal (H), vertical (V), diagonal (D), or antidiagonal (A). These points are termed Poincaré singularities, as indicated by blue (for H and V) and orange dots (for D and A).

In contrast to phase singularities, theoretical research on polarization singularities commenced quite early [87, 89]. These singularities are ubiquitous in our lives, such as in skylight [90]. However, experimental research on polarization singularities and their practical applications has been limited due to the constraints of manipulating the SOP in optical fields. In recent years, the study of vector and ellipse fields has led to the development of more sophisticated techniques for manipulating the SOP of optical fields [91–96]. Polarization defects can be generated and controlled via various methods [85]. For example, uniform birefringence materials can facilitate polarization singularities and their topological charge remains constant as they propagate through the medium [97–99]. Materials with non-isotropic and slowly varying birefringence can be used to control the entrance or exit of singularity points from the beam cross-section [100]. Another commonly used method to generate and manipulate polarization topology is multimode interference [86, 101–104]. Polarization singularities can be described as superpositions of OAM states within orthogonal circular polarization bases [105]. Overlapping a number of different modes produces unique polarization patterns. In this context, FM or multimode optical fibers are ideal candidates as a tool to create such beams, as they support multiple modes in a birefringence medium. In fact, FM fiber has been used to generate complex polarization topologies such as C-points [106, 107]. However, the propagation of these singularities in ONFs has never been previously observed.

1.2.2 The potential of HOM-ONFs

There are numerous interesting physical phenomena that can be investigated using a HOM-ONF. For example, theoretical studies proposed that the relationship between spin angular momentum (SAM) and OAM can be explored with a HOM-ONF [4, 5, 108, 109]. Possession of OAM in HOM-ONFs is attractive in its potential use for quantum multiplexing [110]. The rate of data transmission through optical fibers is reaching a threshold due to nonlinear optical effects. However, multiplexing offers a solution by encoding data in various modes of light, including polarization, wavelength, amplitude, and phase, enabling parallel transmission through the fibers. Moreover, OAM presents an additional degree of freedom, wherein photons are imparted with well-defined twists or helicity [111]. Storage of the fundamental mode of an ONF in cold atoms was experimentally demonstrated [112, 113]. Expanding the ONF-based quantum memory system into the multimode regime holds great appeal as it allows for the exploration of the feasibility of an HOM-ONF-based quantum memory.

The attraction of HOM-ONFs is not only around OAM but also their complex polarization topology. There are various fundamental studies revealing the behavior and dynamics of polarization singularities in three-dimensions (3D) with the presence of the longitudinal field component. These include the optical Möbius strip [114, 115], ribbon strips [116], pure transverse spin [115], and photonic skyrmion [117, 118]. It is noteworthy to emphasize that the optical fields inevitably undergo distortion from external disturbances during propagation. However, optical fields with topological characteris-

tics remain unaffected by external disturbances throughout the propagation process, due to their topological invariability [85]. Topological invariants are characterized by values associated with a topological space, remaining constant and discrete, unchanged by continuous deformations applied to the space [119]. This behavior makes them attractive in applications for information, communication, encryption, Bose–Einstein condensation, and quantum spin Hall effect as a kind of topological protection status [85]. In this context, the exploration of the evanescent fields associated with HOM-ONFs is not only intriguing from a fundamental perspective but also holds promise for future technological advancements.

Additionally, theoretical work proposed that a HOM-ONF could be used to trap, probe, and manipulate small particles including atoms [120–124]. As shown in Figure 1.5(b)(i-iv), each ONF mode has its own unique polarization structure and this is true in the evanescent field. Engineering the shape of the evanescent field by interfering multiple modes may enable us to control the position of trapped particles.

Until now, significantly more attention has been devoted to HOM-ONFs in theoretical research [4, 109, 123, 125–128] than experimental research. This discrepancy can be attributed to the numerous obstacles that need to be overcome in experimental studies. Fabrication of an ONF or OMF that supports the HOMs was achieved [38, 48, 129–131]. Nevertheless, such fabrication demands meticulous care during the fiber tapering process and achieving low-loss HOM-ONFs is not a widespread achievement. An early study to fabricate an exponential-shaped tapered fiber supporting the LP_{11} mode was demonstrated by Frawley et al. [130]. Their approach used an original fiber cladding diameter of 80 μm instead of the most commonly used cladding diameter of 125 μm. Transmission of the LP_{11} at the waist of an ONF was demonstrated as 55%. Ward et al. [38] produced low-loss HOM-ONFs, with transmission as high as 95%, using a double linear-shaped tapered fiber from the originally reduced cladding diameter of 80 μm. Harrington et al. [132] and Jung et al. [133] used the unconventional refractive index distribution in the fiber, i.e., a non-step-index profile, to produce HOM-OMFs. Ha et al. [48] employed wet-etching methods, in which the cladding with its original diameter of 125 μm was etched below 20 μm, followed by the flame brushing and pulling technique. Extra care is required even after the fabrication of low-loss HOM-ONFs, as identifying the excited modes at the ONF waist is not straightforward. Hoffman et al. [134] employed imaging techniques to identify specific HOMs at the waist of the ONF. They deduced the intermodal beat lengths by analyzing the scattering images obtained from the ONF waist. Fatemi et al. [135] also distinguished modes propagating in an ONF by measuring the intermodal beat lengths using a probe crossed-tapered fiber. However, selective mode excitation at the waist has not yet been achieved. Thus, experimental studies on the light-matter interactions using HOM-ONFs are limited to the generalized HOMs, where all TE_{01}, TM_{01}, and HE_{21} modes are excited at the ONF waist at the same time. For instance, manipulation of microbeads around an OMF was performed using this set of HOMs [136, 137]. Other experimental work showed that these HOMs interacting with cold atoms have stronger signals than when using the fundamental mode only [138].

Unlike the case for the SM-ONF-based cavities, which are already well-established systems and have been used for many applications including cQED as described in Section 1.3, the HOM-ONF-based cavity is still under development. The utilization of multiple degenerate HOMs in free-space has demonstrated strong light-matter coupling [12, 139],

emphasizing the significance of realizing a HOM-ONF-based cavity system at this juncture. Indeed, the advantages extend beyond enhanced interactions via cQED effects. The realization of a cavity also encompasses a more comprehensive understanding of the spectral and spatial mode behavior. Previously, the generation of TE_{01} and TM_{01} modes in a laser cavity was demonstrated using an OMF directional coupler-based mode converter [140]. However, earlier attempts by Jöckel to realize a passive HOM-OMF-based cavity did not result in any resonant peaks in the cavity spectrum, except for the fundamental mode [141]. This limitation can be primarily attributed to the challenges encountered while engineering the taper shape to effectively minimize losses. Indeed, there is ample room for further investigation and exploration of this topic forms the focus of this thesis work in Chapter 5.

1.3 Introduction to ONF-Based cQED

An optical cavity, also known as an optical resonator, is a structure that is designed to enhance the interaction and accumulation of light within a confined space. An ONF-based optical cavity typically consists of two highly reflective mirrors placed facing each other (i.e., Fabry-Pérot cavity configuration), creating a region between them where light can bounce back and forth. The mirrors reflect a large portion of the incident light, allowing it to build up within the cavity over multiple reflections. This accumulation of light leads to the phenomenon of resonance, where certain frequencies (wavelengths) of light are amplified while others are suppressed. The constructive interference resulting from multiple reflections between the mirrors causes certain frequencies to experience reinforcement, resulting in a more intense and coherent output.

By placing a quantum emitter in an optical cavity, the confinement of photons by the cavity is used in essentially two ways. First, photons can interact with the quantum emitter multiple times, and second, light resonant in the cavity adds constructively to create high-intensity intracavity fields. By combining an optical cavity with the small mode volumes that ONFs can offer, it is possible to further concentrate the mode field and improve light-matter interaction rates [142]. The spontaneous emission of an atom is not a fixed property but rather is the result of coupling between the atom and the vacuum field. An optical cavity can modify vacuum field fluctuations, thereby altering the properties of spontaneous emission from the atom, such as the decay rate and transition energy [143–146]. The study of this phenomenon is known as cQED.

Let us consider a SM optical cavity coupled with an atom (assumed to be initially in the excited state of a dipole transition) and that the cavity's mode is resonant with the dipole transition. The atom's spontaneous emission and the mode field of the cavity will couple and the energy in the system will oscillate at the vacuum Rabi frequency [142]. However, the Rabi oscillations are limited by the cavity's finite photon lifetime, i.e., energy loss from the system. A cavity that is typically used is the Fabry-Pérot type, where confinement of the photon is provided by two mirrors [142].

In order to quantify the efficiency of light-matter interactions, it is useful to compare the vacuum Rabi frequency, $2g$, where g is the emitter-photon coupling rate, with the cavity decay rate, κ, and the emitter spontaneous emission rate, γ, [8, 9, 147]. There are two coupling regimes that can be used to classify cQED. The first regime occurs when

$\kappa > \{2g, \gamma\}$ and is termed weak coupling [148, 149] or the Purcell regime, where the emitter-cavity interaction is slower than the dissipation [145]. The second regime is when $2g > \{\gamma, \kappa\}$ and is termed strong coupling [148, 149]. This occurs when a cavity can support, even if only briefly, Rabi oscillations notwithstanding the energy leaking out [142]. In other words, the emitter-cavity interaction is faster than the dissipation and the emitted photon remains in the cavity long enough to have a high probability of being reabsorbed by the atom [143, 145].

Optical nanofiber-based cavities can be viewed as inline optical cavities since the mirror structure can be built into a single fiber. In-line all-fiber Fabry-Pérot type cavities can be produced by two different approaches: (i) the mirrors are fabricated directly on the ONF region and are designated hereafter as internal cavities (see Figure 1.6(a)) or (ii) the mirrors are fabricated outside the ONF region, but still on or within the fiber. We refer to these as external cavities (see Figure 1.6(b)) [8]. In both approaches, the most common method to produce cavity mirrors is to fabricate fiber Bragg gratings (FBGs) by generating a strong, permanent modulation of the refractive index in the fiber.

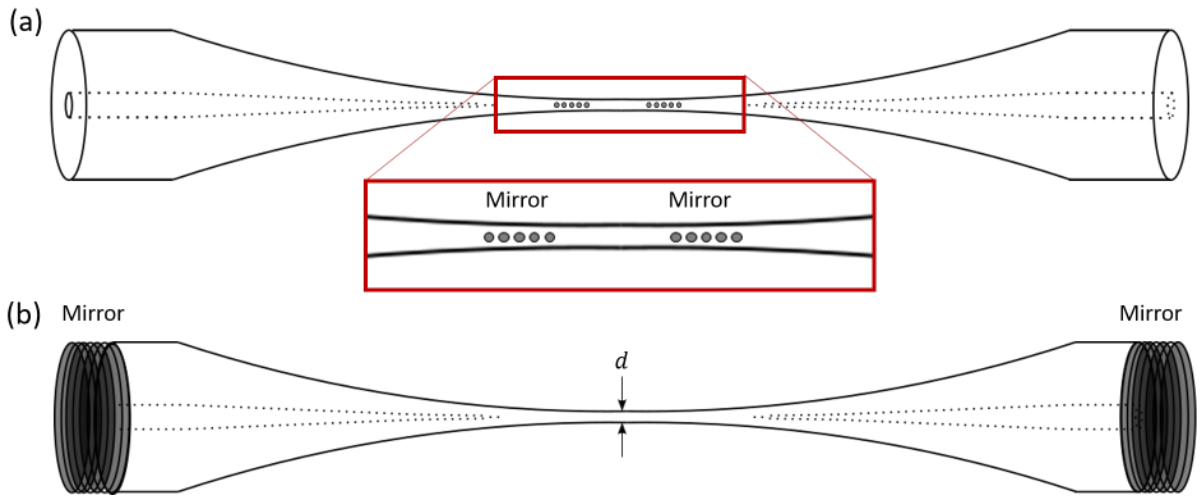

Figure 1.6: (a) Schematic view of an internal mirror ONF-based cavity. Cavity mirrors are fabricated along the ONF region. (b) Schematic view of an external mirror ONF-based cavity. Cavity mirrors are placed outside of the ONF region. The ONF waist diameter, d, is on submicron scale.

Le Kien et al. [9] developed a theoretical formalism to understand the dynamics of the interaction between an ONF-based cavity created by FBGs and the spontaneous emission of a single, nearby atom. They showed that even with a moderate finesse cavity, coupling between the atom and an ONF-guided mode could be enhanced. They found that with a 400 nm diameter ONF and a cavity finesse of about 30, up to 94% of the spontaneous emission from the atom could be coupled into the cavity. Additionally, it was shown that strong coupling could be achieved for a moderate finesse of 30 and a reasonably long cavity of 10 cm to 1 m.

Experimentally, an external FBG ONF-based cavity was fabricated by Wuttke et al. [150] in 2012. The cavity with a finesse of 86 fulfilled the requirements for the strong coupling regime with atomic Cs. In 2015, Kato et al. [10] observed strong coupling

between the external FBG ONF-based cavity and a single trapped Cs atom. The coupling regime was tuned by temperature since one of the FBGs was designed to have the edge of its reflection band at the Cs emission D_2 line transmission at 351.73 THz. The ONF had a 400 nm diameter and the cavity length and finesse were, respectively, 33 cm and less than 40. Ruddell et al. [11] also succeeded in observing strong coupling of an ONF mode and an ensemble of Cs atoms. Their cavity was a ring fiber type with a length of 1.3 m, which is longer than the theoretical maximum length [9]. However, by employing the so-called Dicke model [151, 152], using a cloud of atoms instead of a single atom, they achieved an increase in the coupling rate g by a factor of $\sqrt{\mathcal{N}}$, where $\mathcal{N}$ represents the number of atoms. An ONF-based ring fiber cavity with a length of 30 m and following the Dicke model was demonstrated by Johnson et al. [153], in the superstrong coupling regime with an ensemble of Cs atoms, achieving $g > \Delta\nu_r$, where $\Delta\nu_r$ represents the free spectral range (FSR), i.e., the distance between two consecutive cavity modes.

In 2013, Nayak et al. [154] experimentally demonstrated a fabrication technique to create internal FBG ONF cavities. The authors could produce thousands of periodic nanocraters on the ONF using a femtosecond laser ablation technique, see Figure 1.7(a). For ONFs with diameters ranging from 450-650 nm, crater diameters down to 95 nm were formed. This structure can act as a one-dimensional photonic crystal (PhC) and provides strong confinement of the electric field in both the transverse and longitudinal directions. A section of fabricated FBGs is shown in Figure 1.7(b) and one can see a nanocrater structure in the ONF cross-section in Figure 1.7(c).

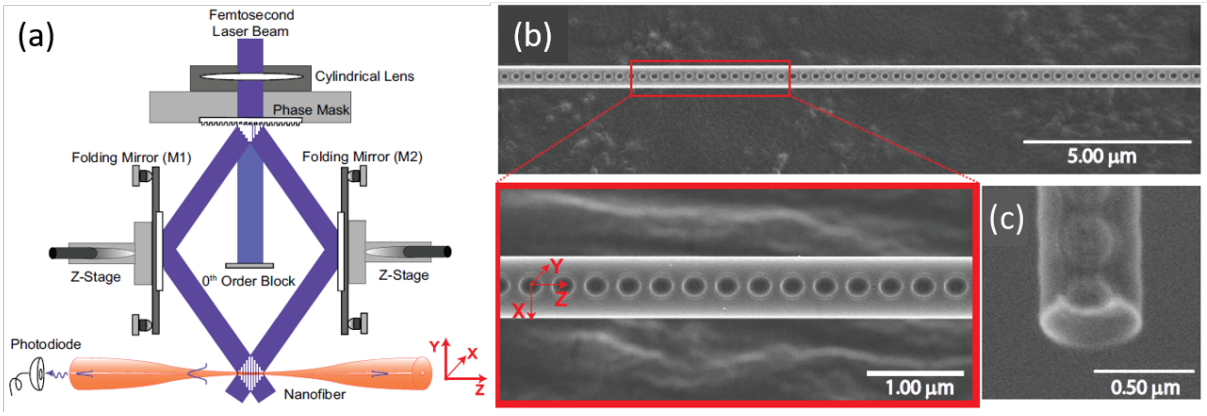

Figure 1.7: (a) Schematic view of the ONF cavity fabrication setup using femtosecond laser ablation. (b) SEM image of an ONF cavity mirror section fabricated using single-shot irradiation. (c) SEM image of a cross-section of the ONF at a nano-crater position taken by tilting the ONF at an angle of 33°. Reprinted with permission from [154] © The Optical Society.

Thereafter, the femtosecond laser ablation technique continued to produce high-quality cavities [149, 155]. Keloth et al. [149] reported on a 1.2 cm cavity produced with this technique that supported both the weak and strong coupling regimes. The ONF was $\sim$ 1.7 cm long and had a diameter of $\sim$ 500 nm. The authors could observe many modes in the cavity and it was shown that those with finesse between 200-400 were suitable to achieve strong coupling, while other modes were only suitable for the weak coupling regime.

A different approach to producing ONF cavities in the weak coupling regime was presented by Yalla et al. [156]. The authors created a composite PhC cavity, formed by placing a grating with a defect in contact with the ONF, see Figure 1.8(a, b). The grating was fabricated by electron beam lithography on a SiO_2 substrate. The structure was polarization-dependent and the cavity quality (Q) factors measured for the x- and y-polarizations were 1410 and 2590, respectively. They also observed enhancement of the spontaneous emission rate from colloidal QDs into the ONF-guided modes.

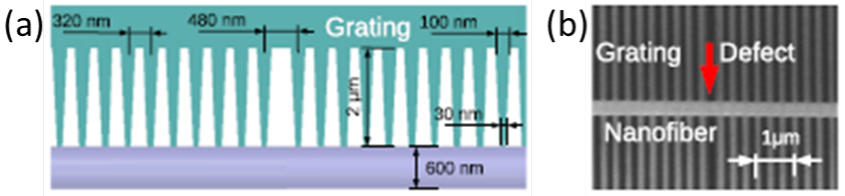

Figure 1.8: (a) Schematic view of a composite PhC ONF cavity. (b) SEM image of an experimentally demonstrated composite PhC ONF cavity. Reproduced from [156] with permission, copyright (2014) by the American Physical Society.

There is another important ONF cavity fabrication technique using focused ion beam (FIB) milling [157–160] and this is the method explored for fabricating internal mirror cavities as part of this PhD. In the following section, important aspects of the FIB milling technique are discussed and a review of ONF-based cavities made by FIB is presented.

1.4 ONF Cavities Fabricated by FIB

As introduced in Section 1.3, there are several different techniques to produce optical cavities directly in ONFs [28, 29, 149, 154–156, 159, 161]. One method that is proving particularly successful is the use of FIB milling to fabricate Bragg mirrors for ONF-based optical cavities [157–160, 162]. This technique uses a focused beam of ions to cut patterns into the fiber with very high resolution.

FIB milling is widely used in the semiconductor industry for high-quality, high-precision fabrication of devices ≤ 1 μm [163] and for transmission electron microscope sample preparation [164]. To date, several studies have demonstrated optical cavities milled directly onto OMFs or ONFs using FIB milling and some studies have already demonstrated that it is possible to mill structures in OMFs and ONFs for quantum optics applications [157, 158, 165].

The mode volume of fiber-based optical cavities can be extremely small. It depends on the fiber diameter and the distance between the mirrors, or more precisely, the effective length of the cavity. Therefore, fiber-based microcavities can produce mode volumes of only a few μm^3. Early examples demonstrated milling in fibers with diameters of a few microns. To further reduce the volume and increase transverse confinement, it is necessary to make cavities in fibers with diameters of a few hundred nanometers. The advantage of ion milling is clear here since the distance between the mirrors is only limited by the resolution of the ion beam. Hence, ONFs are the most suitable structures for creating fiber cavities with dimensions close to the physical limits of optical confinement.

Focused ion beam milling of Bragg gratings to generate cavities in ONFs has been experimentally demonstrated [157] and theoretically studied [166]. Nayak et al. [157] milled Bragg grating mirrors to form a fiber cavity, see Figure 1.9(a). The grating had 120 periods and the resonance wavelength, λ_r, was around 852 nm with the achieved F of 117.

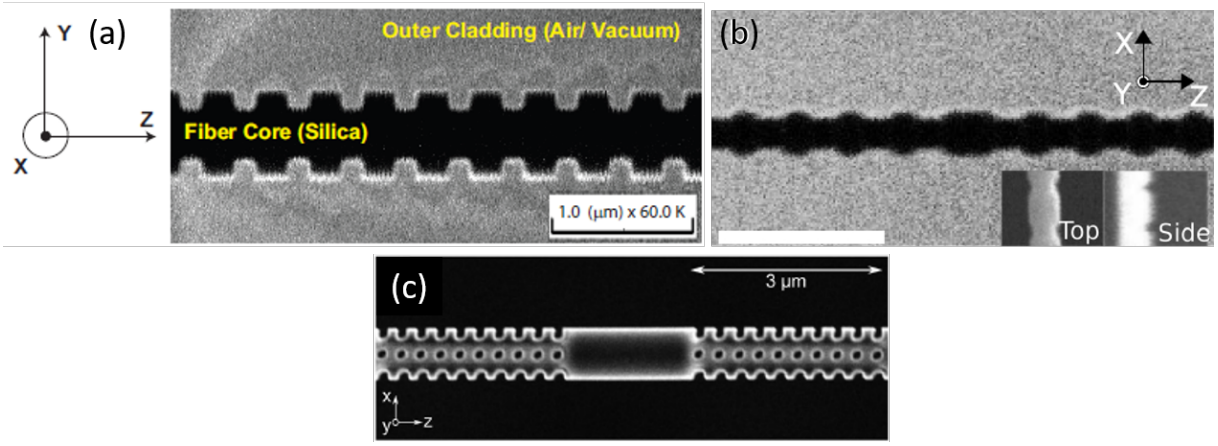

Figure 1.9: (a) Scanning ion microscope (SIM) images of ONF Bragg grating structures on ONFs fabricated using FIB with ∼ 560 nm diameter fiber and grooves of ∼ 100 nm deep and ∼ 150 nm wide. Reprinted with permission from [157] © The Optical Society. (b) SIM images of a section of an ONF cavity with Bragg grating structures fabricated by FIB. Scale bar of 1 μm, ∼ 270 nm diameter fiber and grooves of 45 nm, 300 nm pitch, and 450 nm defect length. Reproduced from [158] with permission licensed under a CC BY license. (c) SEM image of the combined structure of a PhC with a Bragg grating. SEM image. The cavity length is 2.2 μm. Reproduced from [159] with permission licensed under a CC BY license.

An ONF cavity composed of a PhC structure was demonstrated by Wuttke [167]. Interestingly, to discharge the sample, the author used a copper mirror in a custom-designed holder, placed underneath the ONF. A F of 11.1±0.2 was obtained for a λ_r ∼838 nm with 30 periods of mirror structure.

An ONF cavity with Bragg grating structures was also demonstrated by Schell et al. [158]. This device, shown in Figure 1.9(b), was formed by cutting 160 periods of small grooves in the side of the fiber. The achieved Q-factor was 250 at λ_r ∼630 nm with a corresponding mode volume of only 0.7 μm^3. A key capability of an optical cavity is the tunability of the cavity modes by applying strain to the cavity via a piezo-activated translation stage on which the tapered fiber was mounted, giving a tuning span of up to 25.8 nm.

An alternative ONF-based cavity design that combined a PhC structure with Bragg gratings was proposed by Li et al. [159]. The authors showed that the combined structure can achieve higher reflectivity with 20 periods of gratings. An SEM picture of the structure is shown in Figure 1.9(c). A Q-factor up to 784±87 was achieved at λ_r ∼780 nm with the mode volume ∼ 1.05 μm^3. The following year, the authors extended their study to include a slot inside the cavity between the mirrors in simulation [168], similar to what was shown in slotted fiber [29] and hole-tailed fiber [169]. The slot permits the deposition of

single emitters at the position of strongest field intensity, that is, within the slot, thereby enhancing emission into the cavity.

As discussed earlier, the deposition of Ga ions can be a source of loss in the fiber cavity. To overcome this limitation, ion milling using a different ion was demonstrated by Takashima et al. [160]. A helium (He) ion beam was used to mill Bragg gratings. He is a noble gas; therefore, electrical, optical, and chemical alteration of the target material is minimized [170], i.e., it can be considered contamination-free. In this work [160], the authors compared cavities produced with He and Ga ions by milling 160 periods of grooves. They showed that the Q-factor was higher in the cavity milled with He (450 versus 250 for the Ga FIB milling). The He FIB was then used to mill 640 periods of Bragg gratings and a high Q-factor of 4170 at $\lambda_r = 699.80$ nm was achieved. Tashima et al. [165] also fabricated an ONF cavity with a mirror separation length of 755 nm using He FIB with 250 periods of Bragg gratings and showed Q-factor of 807.

As a quick reference for the reader, Table 1.1 contains summaries of the important parameters of ONF cavity fabrication using FIB.

Table 1.1: Summary of ONF cavities by FIB milling. V, I, and N in the first raw indicate voltage, current, and number of grating periods, respectively.

Reference	Ion	V	I	Spot size	d	L	N	Q	F	Nanostructure	Discharge
[157]	Ga	30 kV	∼10 pA	∼14 nm	∼560 nm	100 μm	120	-	117	Bragg	-
[167]	Ga	30 kV	1-10 pA	∼10 nm	∼520 nm	2.39±0.1 mm	30	9.6×10^4	11.1±0.2	PhC	Cu substrate
[158]	Ga	30 kV	9.3 pA	13 nm	270 nm	450 nm	160	250	-	Bragg	-
[159]	Ga	30 kV	7 pA	9 nm	∼830 nm	∼2.2 μm	20	784±87	-	PhC + Bragg	ITO coating
[160]	He	-	1 pA	-	306 nm	840 nm	640	4170	-	Bragg	-
[165]	He	-	-	-	400 nm	755 nm	250	807	-	Bragg	-

Progress in FIB-fabricated ONF cavities mentioned herein shows great potential to achieve strong coupling in cQED. Nevertheless, there still are a number of limitations that should be overcome in order to further advance the ONF cavity system to be a more promising quantum technological tool. Perhaps, the biggest limiting factor of the FIB technique to fabricate ONF cavities may be associated with the fact that the ONF is extremely fragile, so FIB milling requires patience and significant technical experience not to break the ONF samples. Additionally, precise milling of periodic nanostructures directly to an ONF is challenging due to many factors. For example, FIB milling on highly curved structures with large aspect ratios, such as silica ONFs, is difficult in practice due to mechanical vibrations and the resulting misalignment due to charge accumulation on the device. In addition, contamination is not only from ion beams but also from a conductive layer which is necessary to operate the FIB. Furthermore, it is not easy to correctly adjust the ion beam focus and stigmatism on the fiber surface, where the fiber edge is the only reference for the beam adjustments. Correcting the stigmatism is especially difficult when the fiber is aligned in one direction. Exposing the ONF sample to the ion beam for such beam adjustment also results in damaging and scraping the fiber surface, and deposition and implantation of unnecessary Ga ions. To improve the repeatability and quality of the fabrication process, methods were developed to mitigate these challenges, and details are

contained in Chapter 3.

1.5 Conclusion

This PhD work revolves around the development of ONF-based cavities. In this introduction chapter, we have thus far provided summaries of the current research status on the fields of HOM-ONFs and ONF-based cavities.

In Chapter 2, a belief introduction to fundamental aspects of ONFs, including HOMs, and theoretical considerations in ONF-based cQED are depicted. These mathematical concepts are highly relevant to this PhD work and theoretical predictions based on these concepts are also presented in the following chapters.

Chapter 3 focuses on the fabrication of ONFs and ONF cavities. Here, two well-established ONF fabrication techniques, the flame brushing technique and the ceramic heater technique, are explained. We also report a novel method to fabricate ONF cavities using Ga FIB.

The optical characterization of ONF cavities is presented in Chapter 4. The cavities were fabricated for light-matter interactions, assuming a single colloidal QD at a cryogenic temperature. The optical qualities of cavities were characterized from cavity spectroscopy.

Chapter 5 describes the effects of laser annealing on the ONF cavities. Here, cavity spectroscopy was performed under a vacuum environment and the annealing laser power was sequentially increased to observe any positive or negative effects on the optical quality.

Chapter 6 presents the experimental realization of an HOM-ONF-based cavity. The fiber cavity was meticulously designed to support the first set of the HOM family, namely the TE_{01}, TM_{01}, and HE_{21} modes.

Finally, in Chapter 7, we conclude this thesis by highlighting some of the PhD work presented above as well as potential experiments and theoretical investigations that can be pursued in the future.

Chapter 2

Theory [1]

In Chapter 1, we presented a review of previous research in the areas of HOM-ONF and cavities based on ONF. The emphasis in this review was primarily on experimental investigations. However, theoretical studies on the behavior of modes guided by an ONF are well investigated [4, 49, 172–174]. Before conducting experiments involving ONFs, it is essential to take into account various theoretical predictions, such as the number of supported modes and the mode intensity distribution. One also needs to be aware that the speed of light propagating along an ONF varies with the fiber diameter due to material dispersion. Moreover, there are a number of parameters which need to be controlled in order to achieve the best fabrication outcomes. In the case of HOM-ONFs, it is important to consider the impact of interference and birefringence caused by the presence of multiple modes on the resultant mode profiles. Meanwhile, the ONF-based cavity has unique cavity characteristics where the light is tightly guided by the subwavelength diameter fiber. This distinctive feature of an ONF-based cavity leads to a considerable theoretical modification of the cQED system compared to in free-space. Consequently, there are specific parameters tailored to the ONF-based cavity that require manipulation to attain an ideal light-matter interaction regime.

This chapter introduces important fundamental concepts of ONFs that are crucial for the scope of this PhD work. We also showcase the structural dynamics of HOMs which are needed for deeper insight into the topological features of the polarizations states. Furthermore, a brief overview of the theoretical aspects of ONF-based cQED is presented.

2.1 Mode Propagation

ONFs are optical fibers that are heated and pulled so that the diameters are in the submicron scale. An ONF is composed of three regions with different physical properties:

[1] Section 2.5 in this chapter has contents of Section 2.B Simulations and 2.C Analysis from the following published work with permission from Chinese Laser Press: M. Maeda, J. Keloth, and S. Nic Chormaic, "Manipulation of polarization topology using a Fabry–Pérot fiber cavity with a higher-order mode optical nanofiber," Photon. Res. 11, 1029-1037 (2023) [171]. M. Maeda led all aspects of the work including the fabrication of the cavity, the construction of the optical setup, taking data, the development of MATLAB codes with J. Keloth, analysis of experimental results, simulation of results, and writing/editing the paper.

the pigtail, the taper, and the waist regions. One can modify the shape of the taper region according to needs. Here, we introduce two taper shapes: an exponential shape and a linear shape. Figure 2.1(a) shows a schematic illustration of the exponential-shaped ONF. Due to simple procedures and the short required time for fabrication (a few minutes), exponential-shaped ONFs are the most commonly used in SM-ONF studies. However, for some studies, such as making an extremely high transmission fiber (>99%) [38, 175, 176], a broadband transmission fiber [177], a very short tapered fiber (overall length of 2.3 cm) [175], or an ONF with a very long waist region (ONF waist length of 1.7 cm) [149], linear-shaped SM-ONFs can also be used. One can obtain high transmission SM-ONFs (99.6% [175] and 99.95% [176, 178]) with a single linear taper angle, although it results in a relatively long tapered fiber length (63 mm [175]). Adding an optimal larger number of linear angles, i.e., multilinear taper angles, the tapered fiber length can be minimized (23 mm for ∼300 varying angles [175]), and, consequently, this reduces possible mechanical vibrations of the ONF. Linear taper shapes can be employed to fabricate HOM-ONFs in order to satisfy stricter adiabatic criteria, i.e., the condition in which an ONF mode does not couple to another mode [38]. As an example, Figure 2.1(b) is a schematic view of a trilinear-shaped ONF.

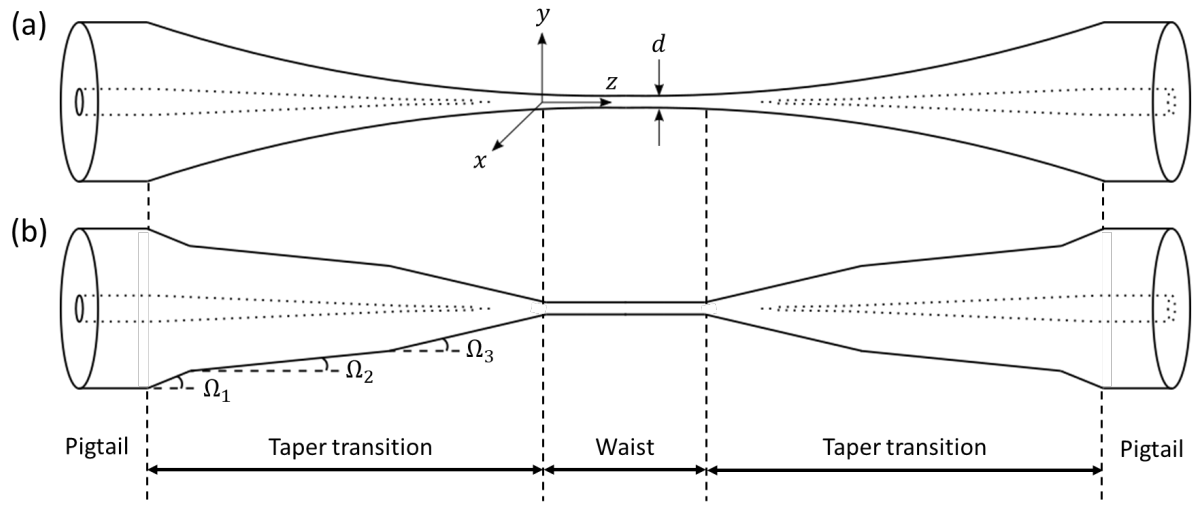

Figure 2.1: (a) Schematic of a typical exponential-shaped ONF. The waist, d, is typically subwavelength. The fiber diameter is exponentially reduced along the propagation direction, z, in the taper transition region to the waist. (b) Schematic view of a typical trilinear-shaped ONF. The fiber diameter is reduced with three different local core taper angles, Ω_i where $i \in \mathbb{Z}^+$, along the propagation direction z in the taper transition region to the waist.

Typically, conventional step-index silica fibers are used to fabricate ONFs. The theoretical properties of ideal step-index fiber are well-known [172, 173, 179–181], and we largely follow the formalism developed in [181]. The refractive index distribution of the step-index fiber, $n(r)$, as a function of the radial distance in cylindrical coordinates centered at the fiber axis, r, is defined as:

$$n(r) = \begin{cases} n_1 & 0 \leq r \leq a, \quad \text{for core} \\ n_2 & r > a, \quad \text{for cladding,} \end{cases} \tag{2.1}$$

where n_1 and n_2 are the refractive indices of the core and the cladding, and a is the core radius. Figure 1.1(a) illustrates such an index relationship together with the refractive index of the environment, n_3.

There are different types of modes that can propagate through an ONF and these can be determined by solving Maxwell's equations (see Appendix A). The exact solutions of Maxwell's equations yield four different modes, so-called exact eigenmodes. They are transverse electric (TE), which has no electric field in the direction of propagation modes, denoted as $\text{TE}_{0,m}$, transverse electric (TM) modes, which has no magnetic field in the direction of propagation, denoted as $\text{TM}_{0,m}$, and hybrid modes in which the TE component dominates, $\text{HE}_{l,m}$, and hybrid mode in which the TM component dominates, $\text{EH}_{l,m}$. Here, $l \in \mathbb{Z}^+$ is the azimuthal mode order, which defines the helical phase front and the associated phase gradient in the fiber transverse plane, $m \in \mathbb{Z}^+$ is the radial mode order, and indicates the m^{th} solution of the corresponding eigenvalue equations (Equations A.22, A.23, A.25, and A.26).

The pigtail region of an ONF is essentially the original fiber region, where the refractive indices of the core and cladding hardly differ, generally on the order of $n_1 - n_2 \sim 0.01$. When the difference between the core and cladding refractive indices is small ($n_2/n_1 \simeq 1$), we can use the weakly guiding approximation to describe light guided in this region as linearly polarized (LP) modes, denoted as $\text{LP}_{l,m}$ modes. The notations l and m are physically the same as for the exact eigenmodes. The general eigenvalue equation of the LP modes is [180]

$$\frac{J_l(ha)}{haJ_{\ell-1}(ha)} = -\frac{K_l(qa)}{K_{\ell-1}(qa)} \tag{2.2}$$

where

$$\ell = \begin{cases} 1, & \text{for } \text{TE}_{0,m} \text{ and } \text{TM}_{0,m} \\ l+1, & \text{for } \text{EH}_{l,m} \\ l-1, & \text{for } \text{HE}_{l,m}. \end{cases} \tag{2.3}$$

where the parameters $h = \sqrt{n_1^2k^2 - \beta^2}$ and $q = \sqrt{n_2^2k^2 - \beta^2}$ describe the scales of the spatial field variations inside and outside of the fiber, respectively. k and β are a free-space wavenumber and the phase propagation constant, respectively. $J_\ell(ha)$, $J_{\ell-1}(ha)$ represent the ℓ^{th} and $(\ell-1)^{th}$ order Bessel function of the first kind with respect to ha, and $K_\ell(qa)$ and $K_{\ell-1}(qa)$ represent the ℓ^{th} and $(\ell-1)^{th}$ order modified Bessel functions of the second kind with respect to qa, respectively. Detailed derivation of Equation 2.2 can be found in Appendix A or elsewhere [13, 172, 180]. Notice from Equations 2.2 and 2.3 that there is a relationship between the LP modes and the exact fiber modes, see Table 2.1.

Solving Equations 2.2 for β, we can obtain dispersion curves of the LP modes. Here, we introduce the effective refractive index of the mode, n_{eff}, a product of β and k, with the following relations

Table 2.1: Relationship of LP modes with exact eigenmodes.

LP modes ($m \geq 1$)	Exact eigenmodes ($m \geq 1$)
LP_{0m} ($l = 0$)	HE_{1m}
LP_{1m} ($l = 1$)	TE_{0m} TM_{0m} HE_{2m}
LP_{lm} ($l \geq 2$)	$EH_{l-1,m}$ $HE_{l+1,m}$

$$\beta = kn_{\text{eff}} = \frac{2\pi}{\lambda} n_{\text{eff}}. \tag{2.4}$$

where λ is the wavelength of the light in vacuum. For any lossless modes confined in the core, the range of β is restricted to

$$n_2 k \leq \beta \leq n_1 k. \tag{2.5}$$

Light propagation within a step-index fiber can be characterized by the V-parameter, also called V-number, such that

$$V = \frac{2\pi}{\lambda} a \sqrt{(n_1^2 - n_2^2)}, \tag{2.6}$$

where a is the core radius. Figure 2.2(a) shows n_{eff} as a function of the V-parameter. As a decreases, n_{eff} and the number of supported modes in the fiber also decrease, while for decreasing λ, n_{eff} and the number of guided modes increase.

The transition region is the part of the ONF where the original core starts to decrease and becomes negligibly small, and the light starts to propagate in a new core, which is the original cladding of the fiber, and a new cladding, which is the surrounding medium of the ONF. The refractive index of the surrounding medium is usually lower than the refractive index of the original cladding (n_1 ∼1.45-1.46). Typically, when the surrounding medium is air, the refractive index of the new cladding $n_2 \approx 1$. This results in the refractive index difference of the new core and cladding becoming much more significant ($n_1 - n_2$ ∼0.45-0.46), as depicted in Figure 1.1(b). This causes a very high numerical aperture and a small effective mode area [4], and the weakly guiding approximation is no longer valid and one needs to express the guided modes as exact eigenmodes. The light that is confined within this region is also referred to as strongly guided modes.

The general eigenvalue equation of exact eigenmodes is given by [4]

$$\left[\frac{J_l'(hr)}{hrJ_l(hr)} + \frac{K_l'(qr)}{qrK_l(qr)}\right]\left[\frac{n_1^2 J_l'(hr)}{hrJ_l(hr)} + \frac{n_2^2 K_l'(qr)}{qrK_l(qr)}\right] = l^2 \left(\frac{1}{h^2 r^2} + \frac{1}{q^2 r^2}\right)^2 \frac{\beta^2}{k^2}. \tag{2.7}$$

where $J_l(hr)$ and $K_l(qr)$ represent the l^{th} order Bessel function of the first kind and the modified Bessel functions of the second kind as a function of hr and qr, respectively.

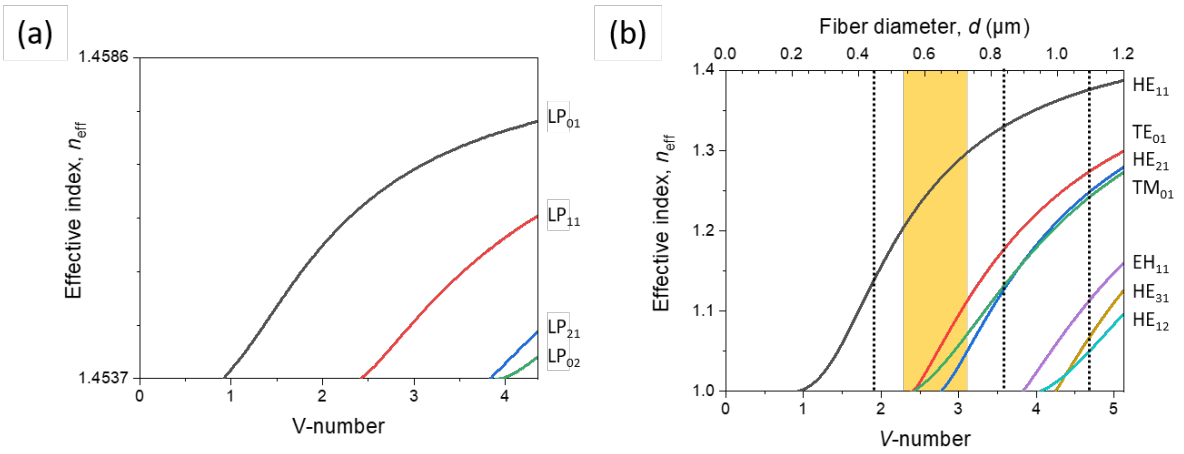

Figure 2.2: (a) Effective index, n_{eff}, of the weakly guided modes as a function of V-number for the first four LP modes. The values of n_1 and n_2 in the calculation were 1.4586 and 1.4537, respectively, at $\lambda = 776$ nm. (b) Effective index, n_{eff}, of the strongly guided modes as a function of V-number for the first seven eigenmodes. The values of n_1 and n_2 in the calculation were 1.4537 and 1, respectively, at $\lambda = 776$ nm. The orange-coloured region indicates the range of d (540 nm $< d <$ 728 nm) used in experiments in Chapter 4, where experiments were operated with parameters of $n_1 = 1.4528$ and $n_2 = 1$ at $\lambda = 780$ nm. The exact d values for these n_1, n_2, and λ only differ by 0.6%. Three black dotted lines indicate the d ($d = 450$ nm, 840 nm, and 1100 nm) used in experiments in Chapter 5, where experiments are conducted with the same values of n_1, n_2 and λ as the calculation. n_{eff} in both (a) and (b) was calculated using the eigenmode expansion (EME) method of the software FIMMPROP.

Moreover, $J_l'(ha)$ and $K_l'(qa)$ represent the derivatives of the l^{th} order modified Bessel functions of the first kind with respect to arguments ha and the modified Bessel functions of the second kind with respect to arguments qa, respectively. A rigorous derivation of this eigenvalue equation for ONF modes is documented in Appendix A.

Solving Equation 2.7 gives us the propagation constant, β, of each eigenmode. Figure 2.2(b) shows the exact eigenmodes propagating in a tapered fiber for HE_{11}, TE_{01}, TM_{01}, HE_{21}, EH_{11}, HE_{31}, and HE_{12}, which are guided as in the first four LP family modes plotted in Figure 2.2(a). Same as the case for LP modes, as the V-number decreases for a fixed wavelength, i.e., as a decreases, n_{eff} of the modes also decreases, and the number of modes that can be supported in the fiber decreases. The cutoff core radius at $\lambda = 780$ nm with $n_1 = 1.4537$ and $n_2 = 1$ for the TE_{01} and TM_{01} modes is $a \simeq 283$ nm and the cutoff core radius for the HE_{21} mode is $a \simeq 325$ nm [4]. Thus by tailoring the diameter and refractive index it is possible to control the number of modes in the fiber.

2.2 Mode Profiles

By utilizing the mode conditions presented in Equation 2.7, it becomes feasible to express the mode profiles in cylindrical coordinates. Here, we follow the mode profile functions developed by Le Kien et al. [4]. In this PhD work, we studied six distinct modes, namely

HE_{11}^{x}, HE_{11}^{y}, HE_{21}^{e}, HE_{21}^{o}, TE_{01} and TM_{01}. Mode profiles of these modes in the weakly guiding regime are presented in Figures 1.5(a)(i, ii) and (b)(i-iv). In this section, we visually present the mode profiles for the strongly guided HE_{11}^{x}, HE_{11}^{y}, HE_{21}^{e}, HE_{21}^{o}, TE_{01} and TM_{01} of an ONF with the following parameters: $n_1 = 1.4537$, $n_2 = 1$, $a = 420$ nm, and $\lambda = 780$ nm.

Let us now briefly introduce the electric and magnetic components of the eigenmodes, such that [4]

$$\begin{bmatrix} \mathbf{E} \\ \mathbf{H} \end{bmatrix} = \frac{1}{2} \begin{bmatrix} \mathcal{E} \\ \mathcal{H} \end{bmatrix} e^{-i\omega t} + c.c., \tag{2.8}$$

where $\mathbf{E}$ and $\mathbf{H}$ are the electric and magnetic field, and $\mathcal{E}$ and $\mathcal{H}$ are the complex amplitudes of the electric and magnetic field, respectively. For the eigenmodes with a propagation constant, β, and the azimuthal mode order, l, $\mathcal{E}$ and $\mathcal{H}$ can be expressed as [4]

$$\begin{bmatrix} \mathcal{E} \\ \mathcal{H} \end{bmatrix} = \begin{bmatrix} \mathbf{e} \\ \mathbf{h} \end{bmatrix} e^{-if\beta z + ilp\theta}, \tag{2.9}$$

where $\mathbf{e}$ and $\mathbf{h}$ are the reduced mode profile functions with the propagation direction, $f = +$ or -, and phase circulation direction $p = +$ or -, respectively. The reduced mode profile function can be further decomposed into three components: radial component, e_r or h_r, azimuthal component, e_θ or h_θ, and axial component e_z or h_z, for the electric field and the magnetic field, respectively. In the cylindrical coordinates, the unit vectors lie on $\hat{\mathbf{r}} = \hat{\mathbf{x}}\cos\theta + \hat{\mathbf{y}}\sin\theta$, $\hat{\theta} = -\hat{\mathbf{x}}\sin\theta + \hat{\mathbf{y}}\cos\theta$, and $\hat{\mathbf{z}}$, with $\hat{\mathbf{x}}$ and $\hat{\mathbf{y}}$ the unit vectors in the Cartesian coordinates. The fiber transverse plane is spanned by $r\hat{\mathbf{r}} + \hat{\theta} = x\hat{\mathbf{x}} + y\hat{\mathbf{y}}$, and denoted as $r\theta$ or xy (see Figure 1.1(b)). The rigorous expressions of e_r, e_θ, e_z, h_r, h_θ, and h_z for each mode are given in Appendix A. The mode intensity distribution, I, can be obtained by [4]

$$I = |\mathbf{e}|^2 = |e_r|^2 + |e_\theta|^2 + |e_z|^2. \tag{2.10}$$

2.2.1 Hybrid modes

Hybrid modes possess both the electric and magnetic field components in the longitudinal direction. The reduced mode functions of the electric and magnetic components of a hybrid mode with circular polarization in the transverse plane can be characterized by the propagation direction, $f = +$ or -, azimuthal mode order l, and phase circulation direction $p = +$ or -, as follows [4],

$$\begin{aligned} \mathbf{e}^{(flp)} &= \hat{\mathbf{r}} e_r + p\hat{\boldsymbol{\theta}} e_\theta + f\hat{\mathbf{z}} e_z, \\ \mathbf{h}^{(flp)} &= \hat{\mathbf{r}} h_r + p\hat{\boldsymbol{\theta}} h_\theta + f\hat{\mathbf{z}} h_z. \end{aligned} \tag{2.11}$$

Note that these modes contain all components, i.e., the radial, azimuthal, and axial

components of the electric and magnetic fields. The full mode functions for such hybrid modes can be written as [4]

$$\begin{aligned} \mathcal{E}_{\text{circ}}^{(flp)} &= \mathbf{e}^{(flp)} e^{if\beta z + ipl\theta}, \\ \mathcal{H}_{\text{circ}}^{(flp)} &= \mathbf{h}^{(flp)} e^{if\beta z + ipl\theta}, \end{aligned} \tag{2.12}$$

where the subscript "circ" stands for the transversely circular polarization, also called quasi-circular polarization. The term "quasi-" refers to the contribution of the field from the axial components.

On the other hand, hybrid modes with quasi-linear polarization can be seen as superpositions of the quasi-circularly polarized hybrid modes with left-handed and right-handed directions, such that [4]

$$\begin{aligned} \mathcal{E}_{\text{lin}}^{(fl\theta_{\text{pol}})} &= \frac{1}{\sqrt{2}} \mathcal{E}_{\text{circ}}^{(fl+)} e^{-i\theta_{\text{pol}}} + \mathcal{E}_{\text{circ}}^{(fl-)} e^{-i\theta_{\text{pol}}}, \\ \mathcal{H}_{\text{lin}}^{(fl\theta_{\text{pol}})} &= \frac{1}{\sqrt{2}} \mathcal{H}_{\text{circ}}^{(fl+)} e^{-i\theta_{\text{pol}}} + \mathcal{H}_{\text{circ}}^{(fl-)} e^{-i\theta_{\text{pol}}}, \end{aligned} \tag{2.13}$$

where the subscript "lin' stands for linear polarization and θ_{pol} represents the orientation of the mode profile's symmetry axes within the transverse plane of the fiber. The particular phase angle values $\theta_{\text{pol}} = 0$ and $\pi/2$ establish two perpendicular polarization profiles: one exhibits symmetry relative to the x-axis, while the other arises from rotating the former by an angle of $\pi/2L_{\text{eff}}$ within the xy-plane. Equations 2.13 can be also written as [4]

$$\begin{aligned} \mathcal{E}_{\text{lin}}^{(fl\theta_{\text{pol}})} &= \mathbf{e}^{(fl\theta_{\text{pol}})} e^{if\beta z}, \\ \mathcal{H}_{\text{lin}}^{(fl\theta_{\text{pol}})} &= \mathbf{h}^{(fl\theta_{\text{pol}})} e^{if\beta z}, \end{aligned} \tag{2.14}$$

where $\mathbf{e}^{(fl\theta_{\text{pol}})}$ and $\mathbf{h}^{(fl\theta_{\text{pol}})}$ are the reduced profile functions of quasi-linearly polarized hybrid modes, such that [4]

$$\begin{aligned} \mathbf{e}^{(fl\theta_{\text{pol}})} &= \frac{1}{\sqrt{2}} (\mathbf{e}^{(fl+)} e^{i(l\theta - \theta_{\text{pol}})} + \mathbf{e}^{(fl-)} e^{-i(l\theta - \theta_{\text{pol}})}), \\ \mathbf{h}^{(fl\theta_{\text{pol}})} &= \frac{1}{\sqrt{2}} (\mathbf{h}^{(fl+)} e^{i(l\theta - \theta_{\text{pol}})} + \mathbf{h}^{(fl-)} e^{-i(l\theta - \theta_{\text{pol}})}). \end{aligned} \tag{2.15}$$

Now, substituting Equations 2.11 into Equations 2.15, we obtain the following forms [4];

$$\begin{aligned} \mathbf{e}^{(fl\theta_{\text{pol}})} &= \sqrt{2}[\hat{\mathbf{r}} e_r \cos(l\theta - \theta_{\text{pol}}) + i\hat{\theta} e_\theta \sin(l\theta - \theta_{\text{pol}}) + f\hat{\mathbf{z}} e_z \cos(l\theta - \theta_{\text{pol}})], \\ \mathbf{h}^{(fl\theta_{\text{pol}})} &= \sqrt{2}[if\hat{\mathbf{r}} h_r \sin(l\theta - \theta_{\text{pol}}) + f\hat{\theta} h_\theta \cos(l\theta - \theta_{\text{pol}}) + i\hat{\mathbf{z}} h_z \sin(l\theta - \theta_{\text{pol}})]. \end{aligned} \tag{2.16}$$

For $\theta_{\text{pol}} = 0$, we find [4]

$$\begin{aligned}\mathbf{e}^{(fl,0)} &= \sqrt{2}[\hat{\mathbf{r}}e_r\cos(l\theta) + i\hat{\theta}e_\theta\sin(l\theta) + f\hat{\mathbf{z}}e_z\cos(i\theta)],\\ \mathbf{h}^{(fl,0)} &= \sqrt{2}[if\hat{\mathbf{r}}h_r\sin(l\theta) + f\hat{\theta}h_\theta\cos(l\theta) + i\hat{\mathbf{z}}h_z\sin(i\theta)],\end{aligned} \tag{2.17}$$

and, for $\theta_{\text{pol}} = \pi/2$, we obtain

$$\begin{aligned}\mathbf{e}^{(fl,\pi/2)} &= \sqrt{2}[\hat{\mathbf{r}}e_r\sin(l\theta) - i\hat{\theta}e_\theta\cos(l\theta) + f\hat{\mathbf{z}}e_z\sin(i\theta)],\\ \mathbf{h}^{(fl,\pi/2)} &= \sqrt{2}[-if\hat{\mathbf{r}}h_r\cos(l\theta) + f\hat{\theta}h_\theta\sin(l\theta) - i\hat{\mathbf{z}}h_z\cos(i\theta)].\end{aligned} \tag{2.18}$$

Figure 2.3(a) shows the electric field, i.e. the SOPs, and the electric field intensity of the quasi-linear x-polarized fundamental mode, HE_{11}^{x}. The SOPs across the beam are relatively uniform, i.e. the vector changes direction slightly as the field goes away from the center of the fiber. One can also note the higher intensity of the evanescent field along the x direction. The 3D view of such an intensity profile is illustrated in Figure 2.3(b). The fiber region is marked as a solid black line in Figures 2.3(a, b). The intensity profile peaks at the center inside the fiber, while there is a sudden increase in the intensity at the external boundary of the fiber. This shows the significance of the evanescent field even when the fiber diameter ($d = 840$ nm) is not subwavelength dimension ($\lambda = 780$ nm). The orthogonal polarization of a y-polarized fundamental mode, HE_{11}^{y}, has the distribution of the SOPs and the intensity exactly perpendicular to HE_{11}^{x}.

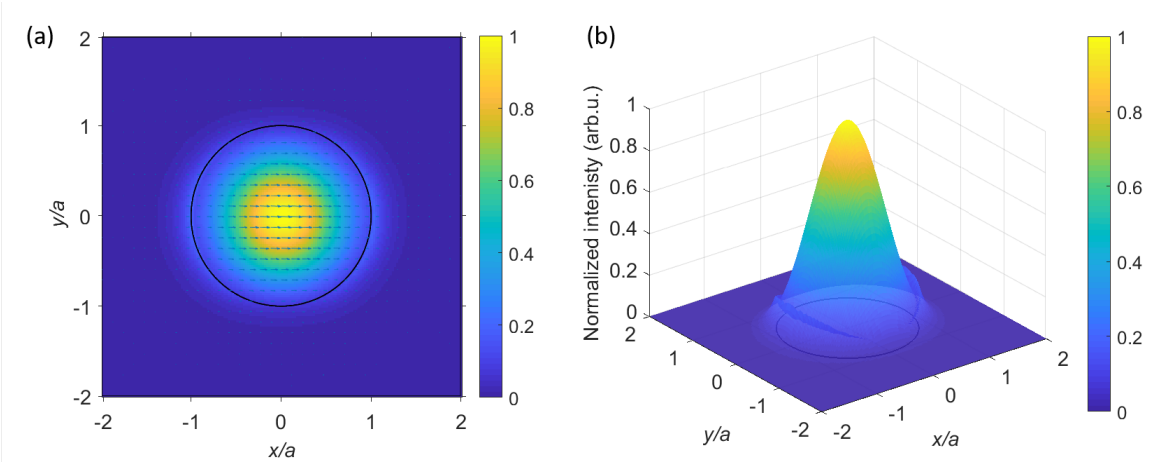

Figure 2.3: (a) Cross-sectional normalized intensity distribution of the HE_{11}^{x} mode. The blue arrows show local polarization vectors. The black circle indicates the fiber edge. (b) Three-dimensional representation of the intensity distribution in (a). The electric field was calculated using Lumerical FDTD method and plotted by MATLAB.

Figure 2.4(a) shows the cross-sectional view of the SOP and intensity profiles of the HE_{21}^{e} mode. The SOPs are not as uniform as for the fundamental mode, with alternating field vectors pointing to radial and azimuthal directions. This mode has a donut-like shaped intensity profile, i.e., null intensity at the center of the fiber. It also possesses four regions of high evanescent field intensity around the $\{x/a, y/a\} = \{0, 1\}$, $\{0, -1\}$, $\{1, 0\}$, and $\{-1, 0\}$ positions, where the SOPs are radially oriented. The 3D view of the intensity

profile is shown in Figure 2.4(b). From this point of view, it is clear that the intensity at those four regions of the evanescent field is higher than the intensity inside the fiber.

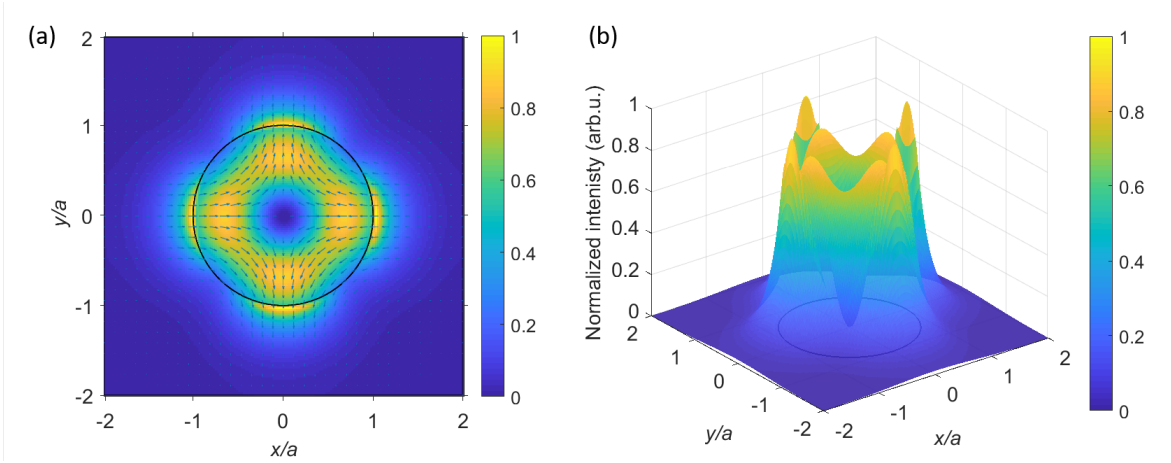

Figure 2.4: (a) Cross-sectional normalized intensity distribution of the HE^e_{21} mode. The blue arrows show local polarization vectors. The black circle indicates the fiber edge. (b) Three-dimensional representation of the intensity distribution in (a). The electric field was calculated using Lumerical FDTD method and plotted by MATLAB.

The transverse view of SOP and intensity distributions of the HE^o_{21} mode is shown in Figure 2.5(a). The mode structure of HE^o_{21} is exactly perpendicular to that of HE^e_{21}. Four intense evanescent field at $\{x/a, y/a\} = \{\sim 0.7, \sim 0.7\}$ and $\{\sim 0.7, \sim$-$0.7\}$, $\{\sim$-$0.7, \sim 0.7\}$ and $\{\sim$-$0.7, \sim$-$0.7\}$ regions, where the SOPs are radially oriented. Figure 2.5(b) presents the electric intensity from the 3D point of view, which also shows the higher intensity at those four positions outside the fiber region.

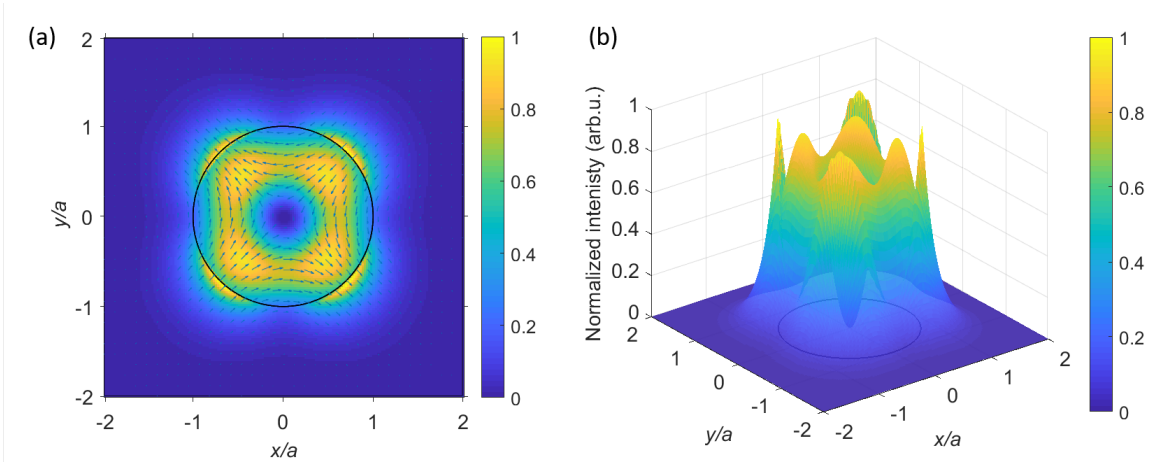

Figure 2.5: (a) Cross-sectional normalized intensity distribution of the HE^o_{21} mode. The blue arrows show local polarization vectors. The black circle indicates the fiber edge. (b) Three-dimensional representation of the intensity distribution in (a). The electric field was calculated using Lumerical FDTD method and plotted by MATLAB.

2.2.2 TE modes

The reduced mode functions of the electric and magnetic components for TE_{01} mode are given by

$$\begin{aligned} \mathbf{e}^{(f)} &= \hat{\boldsymbol{\theta}} e_\theta \\ \mathbf{h}^{(f)} &= f\hat{\mathbf{r}} h_r + f\hat{\mathbf{z}} h_z. \end{aligned} \tag{2.19}$$

Figure 2.6(a) shows the cross-section of SOP and intensity distributions of the TE_{01} mode. As is clear from Equation 2.19, the SOPs of this mode are purely transverse ($e_z = 0$), and purely azimuthal ($e_r = 0$). This results in the perfect donut pattern, i.e., a uniform intensity profile in the azimuthal direction, in contrast with hybrid modes. This intensity profile is further illustrated in a 3D perspective in Figure 2.6(b). There is no sharp increase in intensity at the core-cladding interface, indicated as a solid black line, and the mode intensity decays smoothly away from the fiber. The field is continuous because tangential field components, e_θ, and e_z, at the boundary do not generate discontinuity.

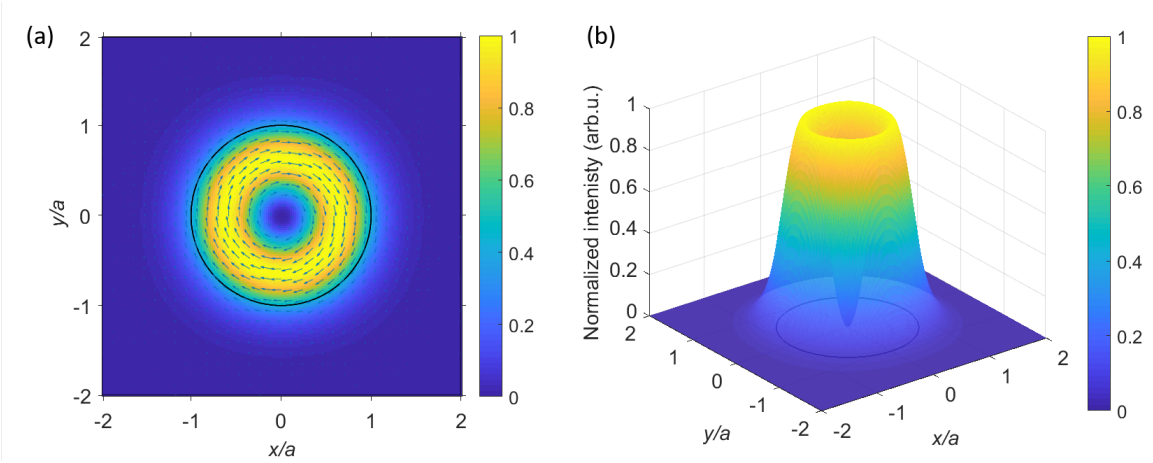

Figure 2.6: (a) Cross-sectional normalized intensity distribution of x-polarized TE_{01} mode. The blue arrows show local polarization vectors. The black circle indicates the fiber edge. (b) Three-dimensional representation of the intensity distribution in (a). The electric field was calculated using Lumerical FDTD method and plotted by MATLAB.

2.2.3 TM modes

Finally, we now introduce the reduced mode functions of the electric and magnetic components for the TM_{01} mode, which are given by

$$\begin{aligned} \mathbf{e}^{(f)} &= \hat{\mathbf{r}} e_r + f\hat{\mathbf{z}} e_z \\ \mathbf{e}^{(f)} &= f\hat{\boldsymbol{\theta}} h_\theta. \end{aligned} \tag{2.20}$$

Figure 2.7(a) presents the SOP and intensity distributions for the TM_{01} mode within the transverse plane. In this mode, the electric field distribution is solely radial ($e_\theta = 0$), evident from Equation 2.20. Analogous to the TE_{01} mode, the TM_{01} mode also exhibits azimuthal symmetry. The intensity of the evanescent field reaches its peak at the interface between the core and cladding, marked by a solid black line. Notably, at the fiber's central position $\{x/a, y/a\} = \{0, 0\}$, the intensity is not zero unlike for the other HOMs discussed here. It is worth noting that, at this location, the field vector does not possess a transverse component and the dominant contribution to the electric field comes from the axial component e_z. Indeed, the TM_{01} mode exhibits its most intense point at the center of the 840 nm diameter fiber for a wavelength of 780 nm. This characteristic is prominently evident in the 3D representation, as depicted in Figure 2.7(b). Additionally, an abrupt increase in intensity at the core-cladding interface is noticeable for this mode.

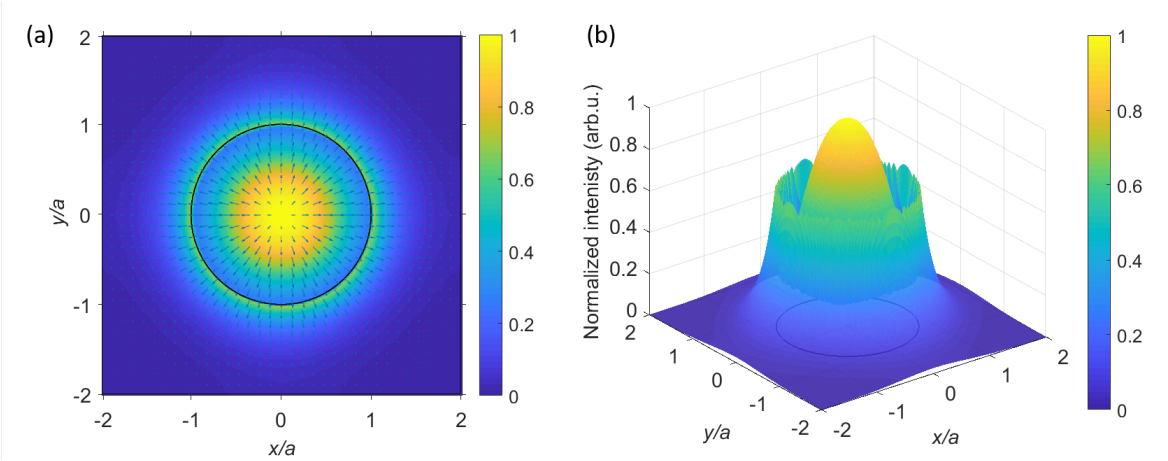

Figure 2.7: (a) Cross-sectional normalized intensity distribution of the TM_{01} mode. The blue arrows show local polarization vectors. The black circle indicates the fiber edge. (b) Three-dimensional representation of the intensity distribution in (a). The electric field was calculated using Lumerical FDTD method and plotted by MATLAB.

2.3 Adiabatic Criterion

An ONF with negligible power loss due to mode coupling is termed as being adiabatic [173]. An ONF can support the desired number of modes at high transmission not only if the fiber diameter is above the cutoff size for said modes, but also if the adiabatic tapering condition for these modes is satisfied [38, 172].

Light propagation along optical fibers varies as $e^{i(\beta z - \omega t)}$, where β is the phase propagation constant. The most critical factor for the adiabatic condition is the local coupling length between two modes, the so-called beat length $z_b = z_b(z)$, such that

$$z_b = \frac{2\pi}{\beta_1 - \beta_2} = \frac{\lambda}{n_{\text{eff},1} - n_{\text{eff},2}}, \tag{2.21}$$

where $\beta_1 = \beta_1(z)$ and $\beta_2 = \beta_2(z)$ stand for propagation constants of two distinctive modes, and $n_{\text{eff},1}$ and $n_{\text{eff},2}$ are corresponding effective refractive indices. Thus, mode coupling

creating a non-adiabatic taper is most likely to occur between two adjacent modes as they propagate along the taper transition region. Another important note is that an LP_{lm} mode only couples to other modes with the same mode order l, i.e., with similar circular symmetry [173]. In order to obtain an insight into the mode coupling, the beat length is compared with the local taper length, z_t [173]:

$$z_t = \frac{a(z)}{\tan[\Omega(z)]} \approx \frac{a(z)}{\Omega(z)}, \tag{2.22}$$

where $a(z)$ is the local core radius as a function of position z and $\Omega(z)$ is the local taper angle as a function of position z, with $\Omega(z) \ll 1$ rad. The local taper angle has to be small enough for the modes to see a fiber as straight [173]. Modes can be conserved in a taper when $z_t \gg z_b$; mode coupling occurs when $z_t \ll z_b$ [173]. Thus, the condition $z_t = z_b$ gives an indication of an approximate adiabatic-lossy boundary regime, defined by a critical local taper angle, which is equivalent to [173]

$$\Omega = \frac{a(\beta_1 - \beta_2)}{2\pi}. \tag{2.23}$$

Note that the adiabatic criterion requires that the local taper angle be lower than the critical local taper angle, but *not* its rate of change. In other words, the taper angle can be suddenly changed without significant loss as long as the changed angle also meets the adiabatic criterion [8]. This leads to the fabrication of high transmission ONFs by using multiple angles achieved by changing the heated region on the fiber during tapering [174]. The adiabatic condition for SM fiber has been known and demonstrated since the 1990s [173]; however, adiabatic tapering for HOMs was only realized in 2011 after the discovery that not only taper angle but the initial core-cladding ratio plays a critical role [129].

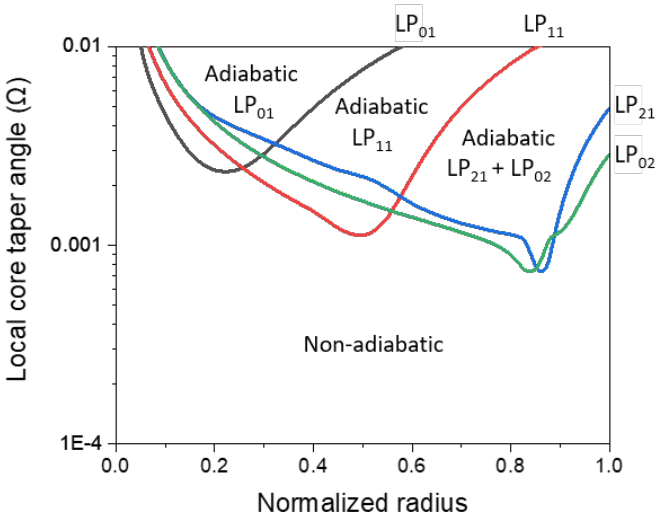

Figure 2.8: The delineation curves of LP_{01} (black), LP_{11} (red), LP_{21} (blue), and LP_{02} (green), as a function of normalized core radius. Ω_i must be smaller than the critical local core taper angle Ω for each set of LP modes to fabricate an adiabatic ONF. These plots were generated from the same parameters as Figures 2.2(a, b).

The critical core taper angles as a function of normalized fiber radius for the first four sets of LP modes, i.e., LP_{01}, LP_{11}, LP_{21}, and LP_{02}, are shown in Figure 2.8. It is evident that HOMs have lower critical taper angles compared to the fundamental mode. This poses challenges in experimental works involving HOM-ONFs, which have not been well-developed. Furthermore, the critical angles decrease as the mode order increases, adding to the difficulty in operating experiments with LP_{21} and LP_{02} modes. However, a recent breakthrough in fabrication involves the successful production of adiabatic ONFs through chemical etching of the fiber before the conventional tapering process [48].

2.4 Material Dispersion

We now consider material dispersion, which occurs when n_{eff} changes with λ and/or the fiber diameter, d. This applies to the silica ONF system with $n_{\text{eff}} = n_{\text{eff}}(V)$, where $V(\lambda, 2a = d)$ as Equation 2.6 indicates. Light in a dispersive medium propagates at the group velocity v_{g}, which is given by [172]

$$v_{\text{g}} = \frac{d\omega}{d\beta} = \frac{c}{n_{\text{g}}}, \tag{2.24}$$

where c is the speed of light in vacuum and n_{g} is the group index, which is given as [172]:

$$n_{\text{g}} = n_{\text{eff}}(d, \lambda) - \lambda \frac{\partial n_{\text{eff}}(d, \lambda)}{\partial \lambda}. \tag{2.25}$$

Figure 2.9(a) shows the change in n_{g} of the fundamental mode HE_{11} for different d ranging from 0-1500 nm for $\lambda = 780$ nm. We selected this wavelength because all ONF samples fabricated for this thesis work were designed to match a specific QD and ^{87}Rb D_2 emission wavelength at $\lambda = 780$ nm. n_{g} reaches a maximum at d $\sim$600 nm and rapidly decreases as d gets thinner. It goes down nearly as low as 1, meaning that the group velocity is almost reaching the speed of light in a vacuum.

The change of n_{g} of the HE_{11} mode as a function of λ ranging from 500-1000 nm for an ONF with $d = 720$ nm is illustrated in Figure 2.9(b). n_{g} reaches a maximum at $\lambda \sim 900$ nm and slowly decreases as λ gets shorter. One can clearly see that the effect of change in d (for typical ONF diameters from 400-800 nm) on n_g is an order of magnitude larger than the change in λ (for the wavelength range 750-810 nm) on n_{g}. We use n_{g} to calculate the effective cavity length, L_{eff}, in Chapter 4.

2.5 Polarization in the Multimode Regime

When studying the optical fiber system in the multimode regime, it is important to take into account the effect of interference between the modes. Moreover, in the case where the fiber contains loops and bends, it is necessary to consider the possible effects of birefringence on the resulting modes. Birefringence and interference in fiber can create a complex polarization topology that cannot be seen in pure fiber eigenmodes. Here, we introduce the mathematical expressions describing the effects of birefringence and interference with some examples of these complex polarizations. Furthermore, their topological defects are

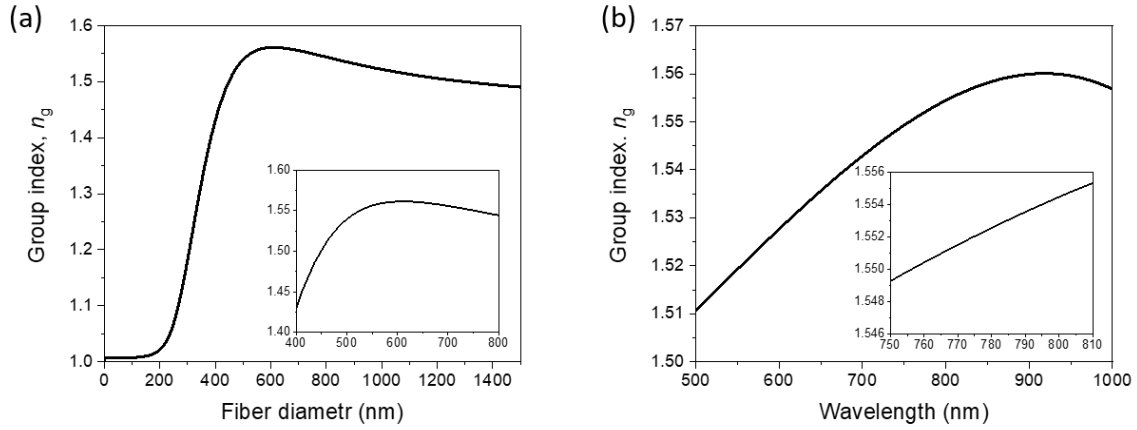

Figure 2.9: (a) Change of n_g of the HE_{11} mode as a function of d at $\lambda = 780$ nm. The insert is the typical fiber diameters of the ONFs in Chapter 4. (b) Change of n_g of the HE_{11} mode as a function of λ at $d = 720$ nm. The insert is for the typical vacuum wavelength range of the ONF-based cavities in Chapter 4. n_g was calculated using the EME method of the software FIMMPROP with $n_1 = 1.4528$ and $n_2 = 1$.

also found. This is critical for an introduction to the material contained in Chapter 5.

2.5.1 Birefringence and interference

Each mode experiences arbitrary birefringence as it propagates along the fiber. The total field in the fiber at any point is the sum of the propagating modes with a corresponding phase shift. The addition of FBG mirrors to the fiber induces an additional birefringence [166, 182], which can be incorporated in a single birefringence matrix. Note that this model does not include cavity boundary conditions since we only aim to simulate the spatial profiles of the fiber modes. We can calculate an arbitrary fiber field, $\mathbf{E}$, due to interference and birefringence by taking a summation over different fiber modes, such that

$$\mathbf{E} = \sum_{\mathrm{M}}^{\mathscr{N}} \mathbf{J}_{\mathrm{M}} A_{\mathrm{M}} \mathbf{E}_{\mathrm{M}} e^{i\phi_{\mathrm{M}}}, \tag{2.26}$$

Here, $\mathscr{N}$ is the number of eigenmodes to be interfered, $\mathbf{E}_{\mathrm{M}}$ is the electric field of a fiber eigenmode, where the mode subscript $\mathrm{M} \in \{\mathrm{TE}_{0,m}, \mathrm{TM}_{0,m}, \mathrm{HE}_{l,m}$ and $\mathrm{EH}_{l,m}\}$. A_M is the amplitude, ϕ_{M} is the phase between modes, and $\mathbf{J}_{\mathrm{M}}$ represents the arbitrary birefringence Jones matrix of each eigenmode $\mathbf{E}_{\mathrm{M}}$, such that [183]

$$\mathbf{J}_{\mathrm{M}} = e^{i\eta_{\mathrm{M}}/2} \begin{pmatrix} \cos^2\theta_{\mathrm{M}} + e^{i\eta_{\mathrm{M}}} \sin^2\theta_{\mathrm{M}} & (1 - e^{i\eta_{\mathrm{M}}}) \cos\theta_{\mathrm{M}} \sin\theta_{\mathrm{M}} \\ (1 - e^{i\eta_{\mathrm{M}}}) \cos\theta_{\mathrm{M}} \sin\theta_{\mathrm{M}} & \sin^2\theta_{\mathrm{M}} + e^{i\eta_{\mathrm{M}}} \cos^2\theta_{\mathrm{M}} \end{pmatrix}, \tag{2.27}$$

where η_{M} is the relative phase retardation induced between the fast axis and the slow axis, and θ_{M} is the orientation of the fast axis with respect to the horizontal-axis, i.e., perpendicular to mode propagation.

Let us now consider the system with the fiber supporting HE_{11}^{x}, HE_{11}^{y}, TE_{01}, TM_{01},

HE^o_{21} and HE^e_{21}, so that the number of modes that can be interfered is $\mathcal{N} \leq 6$. The cross-sectional profiles and SOPs of TE_{01} and HE^e_{21} are shown in Figure 2.10(a, b), respectively. The TM_{01} and HE^o_{21} modes are not shown here but their vector fields are orthogonal to the TE_{01} and HE^e_{21} at every point, respectively (see Figure 1.5(b)(iv, ii)). These modes have donut-shape mode profiles with linearly polarized vector fields at any point in the mode cross-section. As an example of possible fiber modes using Equation 2.26, Figure 2.10(c) illustrates in-phase interference of the TE_{01} and HE^e_{21} modes with equal amplitudes. The resulting mode has a lobe-shape intensity pattern with scalar fields. Figure 2.10(d) is an example of a mode resulting from the interference of the circularly polarized HE_{11} and an out-of-phase (a $\pi/2$ phase difference) TE_{01} and TM_{01} with equal amplitudes. The SOP, which is overlapped on the intensity profile images, are marked as red and blue ellipses, corresponding to right and left-handed orientation, respectively. This mode is the so-called lemon [107], which contains not only linear polarization but also elliptical and circular polarization components in one mode. The dots and line in Figure 2.10(d) are highlighting what are known as Stokes singularities and are discussed in detail in the next section.

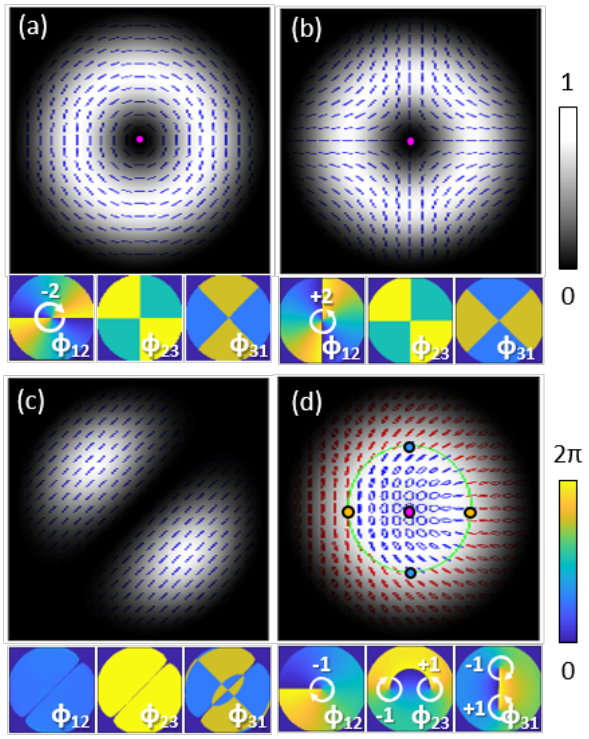

Figure 2.10: Simulations of (a) TE_{01}, (b) HE^e_{21}, (c) TE_{01} + HE^e_{21} and (d) lemon. The red and blue SOPs indicate right-handed and left-handed ellipticities, respectively. The scale bars show the normalized intensity (from 0 to 1) and the Stokes phase (from 0 to 2π). Stokes singularity points of σ_{12}, σ_{23}, and σ_{31} are indicated as pink, orange, and blue dots, respectively. An L-line is indicated in green.

2.5.2 Stokes singularities

The polarization gradient was calculated in order to identify Stokes singularities in the cross-section of the mode. The gradient map is known as the Stokes phase, ϕ_{ij}, which is given by [184, 185]

$$\phi_{ij} = Arg(S_i + iS_j), \tag{2.28}$$

where S_i and S_j are Stokes parameters with $\{i, j\} \in \{1, 2, 3\}$ in order, and $i \neq j$, such that [74, 186]

$$\begin{aligned} S_0 &= \sqrt{S_1^2 + S_2^2 + S_3^2}, \\ S_1 &= S_0 \cos(2\chi)\cos(2\psi) = I_{\mathrm{H}} - I_{\mathrm{V}} \\ S_2 &= S_0 \cos(2\chi)\sin(2\psi) = I_{\mathrm{D}} - I_{\mathrm{A}}, \\ S_3 &= S_0 \sin(2\chi) = I_{\mathrm{L}} - I_{\mathrm{R}}. \end{aligned} \tag{2.29}$$

where ψ and χ represent the orientation of the major axis and the polarization azimuth in the spherical angular coordinate, respectively. In this context, $I_{\mathrm{H}}, I_{\mathrm{V}}, I_{\mathrm{D}}, I_{\mathrm{A}}, I_{\mathrm{L}}$ and I_{R} indicate the electric field intensity with polarization with subscripts H, V, D, A, L and R implying horizontal, vertical, diagonal, antidiagonal, left-circular, and right-circular directions, respectively. We can identify the SOP at a point in the transverse plane by calculating the ellipse orientation, ψ, and ellipticity, χ, using Equations 2.29 [186]:

$$\begin{aligned} \chi &= \frac{1}{2}\sin^{-1}\left(\frac{S_3}{S_0}\right), \\ \psi &= \frac{1}{2}\tan^{-1}\left(\frac{S_2}{S_1}\right). \end{aligned} \tag{2.30}$$

The SOP can be visually represented on the Poincaré sphere, see Figure 2.11. Linear SOPs, H, L, D, and A, have $\psi = 0$ and are located on the equator of the Poincaré sphere. The northern hemisphere represents the right-handed elliptical states with positive ψ, while the southern hemisphere represents the left-handed elliptical or circular states. In particular, the north/south poles correspond to circular states of R and L, respectively.

The Stokes phase uncertainty points, i.e., Stokes singularities, can be identified by obtaining the Stokes indices, σ_{ij}, which are defined as [184, 185]

$$\sigma_{ij} = \frac{1}{2\pi}\oint_{\mathscr{c}} \nabla\phi_{ij} \cdot d\mathscr{c}, \tag{2.31}$$

where $\oint_{\mathscr{c}} \nabla\phi_{ij} \cdot d\mathscr{c} = \Delta\ \phi_{ij}$ is the counterclockwise azimuthal change of the Stokes phase around the Stokes singularity, i.e., $\Delta\ \phi_{ij} = \phi_{ij}^{\mathrm{final}} - \phi_{ij}^{\mathrm{initial}}$ is the winding angle of ϕ_{ij}, with $\phi_{ij}^{\mathrm{initial}}$ ($\phi_{ij}^{\mathrm{final}}$) being the value of ϕ_{ij} at the starting point (ending point) of any simple closed path $\mathscr{c}$ that encircles the vortex [184]. Singularities of σ_{12} are known as V-points and C-points, in vector and ellipse fields, respectively [184]. Singularities of σ_{23} and σ_{31} are known as Poincaré vortices [103, 185, 187]. L-lines are located where $\phi_{23} = \{0, \pi, 2\pi\}$. Table 2.2 is a summary of the classification of the Stokes singularity types in terms of the

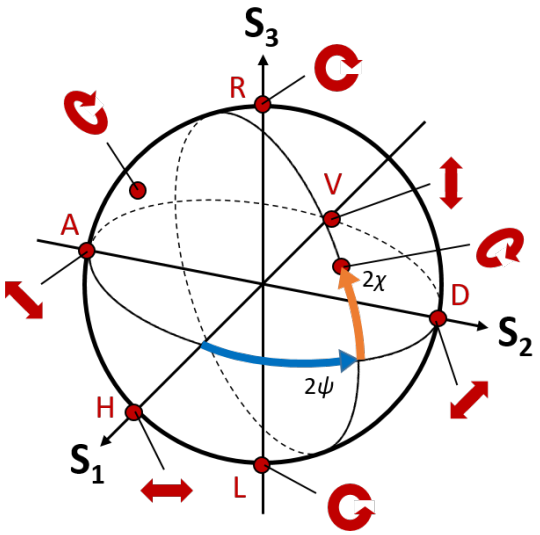

Figure 2.11: Schematic of Poincaré sphere presenting SOPs at a total of eight positions (red dots): H, V, D, A, L, and R as well as arbitrary elliptical SOPs.

Stokes phases and singularity indices with the corresponding polarizations in the vector and ellipse fields [86, 102, 103, 185].

Table 2.2: List of Stokes singularities in vector fields (v) and ellipse fields (e) by the singularity index, σ_{ij}, using the Stokes phase, ϕ_{ij}, with $\{i, j\} \in \{1, 2, 3\}$ in order.

Stokes singularity	Stokes phase	Stokes index/ Phase values	Polarization
V-point (v)	ϕ_{12}	σ_{12}	Null
C-point (e)	ϕ_{12}	σ_{12}	R/L
Poincaré vortex (e)	ϕ_{23}	σ_{23}	H/V
	ϕ_{31}	σ_{31}	D/A
L-line (e)	ϕ_{23}	$0, \pi, 2\pi$	Linear

The Stokes singularity points and L-lines are found from the Stokes phases, then superimposed and marked on the mode profiles. As examples, from Figures 2.10(a, b), the center of the mode profiles for both TE_{01} and HE^{e}_{21} contain a V-point, with $\sigma_{12} = -2$ and $+2$ (pink dot), respectively. These points are found from their Stokes phases ϕ_{12} (lower panels in Figures 2.10(a, b)). In contrast, the lemon mode in Figure 2.10(d) has a closed loop representing an L-line (green) and all three types of Stokes singularities: a C-point with $\sigma_{12} = -1$ (pink dot), Poincaré vortices with $\sigma_{23} = -1$ and $+1$ (orange dots), and $\sigma_{31} = -1$ and $+1$ (blue dots) are found from ϕ_{12}, ϕ_{23}, and ϕ_{31}, respectively. The lobe-shaped scalar mode in Figure 2.10(c) does not have a 2π gradient in any associated Stokes phases, since topological defects can only exist in non-scalar fields [85].

2.6 cQED using an ONF

The light-matter interaction is a series of processes involving a photon being absorbed, emitted, or scattered by charged particles. The strength of such an interaction can be increased when a resonant cavity is incorporated so-called Purcell enhancement [188]. This remarkable observation led to a dynamically expanding field of study, which is called cavity quantum electrodynamics, cQED [189]. Researchers have been engineering various cavity systems ever since to achieve strong light-matter interactions by controlling tunable parameters. This section briefly summarizes the important parameters to be controlled specifically in an ONF-based cQED system.

Typically, in order to observe the strong cQED effects using a Fabry-Pérot cavity, one needs to obtain a sufficient value of finesse, F, which describes how narrow the full-width half-maximum (FWHM) of resonances are in relation to their frequency separation, that is [190]

$$F = \frac{\mathrm{FSR}}{\mathrm{FWHM}}, \tag{2.32}$$

with both FSR and FWHM being either in wavelength or frequency. For a cavity with two mirrors of intensity reflectivities R_1 and R_2, and when both of which are equal, i.e., $R_1 = R_2 = R$, F is given by [191]

$$F = \frac{\pi}{2\arcsin\left(\frac{1-R}{2\sqrt{R}}\right)}. \tag{2.33}$$

The optical quality of cavities can be also measured by the Q-factors, which describe the damping of resonator modes, such that [190]

$$Q = \frac{\lambda_\mathrm{r}}{\mathrm{FWHM}} = \frac{\nu_\mathrm{r}}{\mathrm{FWHM}}, \tag{2.34}$$

where λ_r and ν_r are the wavelength and the frequency of resonance, respectively, with FWHM either in units of wavelength or frequency. The Q-factor is often used for a short Fabry-Pérot cavity where FSR cannot be measured.

The study of single atoms coupling to free-space Fabry-Pérot cavities has been extensively developed in free-space [147, 192, 193]. Strong coupling is achieved when the coherent energy exchange rate between a photon and an emitter is significantly greater than the energy dissipation rate of the system and this is evident from Rabi splitting. The light-matter interaction dynamics are primarily governed by the interplay between the coherent rate and the incoherent rate involving three key factors: the emitter-photon coupling rate (represented by $2g_0$, which corresponds to the single-photon Rabi frequency), the cavity decay rate (κ_0), and the emitter spontaneous emission rate (γ_0). These parameters for free-space cavities are given by

$$g_0 = \sqrt{\frac{\mu^2\omega_c}{2\hbar\epsilon_0 V_\mathrm{m}}}, \tag{2.35}$$

$$\kappa_0 = \frac{\omega_c}{Q} = \frac{\pi c}{F L_\mathrm{eff}}, \tag{2.36}$$

$$\gamma_0 = \frac{8\pi^2\mu^2}{2\hbar\epsilon_0\lambda^3}, \tag{2.37}$$

where μ is the dipole moment, $\omega_c = 2\pi c/\lambda$ is the emitter transition frequency at wavelength λ, $\hbar$ is the reduced Planck's constant, ϵ_0 is the free-space permittivity, L_{eff} is the optical effective cavity length, and V_{m} is the cavity mode volume. The effective cavity length of the Fabry-Pérot cavity can be calculated from the FSR value $\Delta\lambda_{\text{FSR}}$ ($\Delta\nu_{\text{FSR}}$) and the group index n_{g}, such that [194]

$$L_{\text{eff}} = \frac{\lambda^2}{2n_{\text{g}}\Delta\lambda_{\text{FSR}}}. \tag{2.38}$$

We now introduce figure-of-merit to describe the light-matter interaction, the so-called cooperativity parameter, $\mathcal{C}$, which characterizes the degree of coherence of the coupling, and is determined from the following expression [8, 189, 195]:

$$\mathcal{C} = \frac{(2g_0)^2}{\kappa_0\gamma_0}. \tag{2.39}$$

The essential condition for observing coherent interactions between light and a single quantum emitter is $\mathcal{C} \gg 1$. Even when $\mathcal{C} \gg 1$, there are typically two different regimes, namely 'the weak coupling regime' and 'strong coupling regime' in an ONF-based cQED system. The weak coupling regime is when the incoherent rate(s) exceeds the coherent rate, that is, $2g_0 < \kappa_0,\ \gamma_0$. Meanwhile, the strong coupling regime has the following condition [8, 9]:

$$2g_0 > \kappa_0, \gamma_0. \tag{2.40}$$

The light-matter interactions are improved by increasing the Q-factor (or F) or reducing the mode volume. Nevertheless, when expressing the cQED parameters in relation to the mode volume, the transverse and longitudinal dimensions become combined. Specifically, the mode volume is inversely proportional to the energy density and can be represented as the product of the effective mode area, A_{eff}, at the emitter's position and the optical effective length, L_{eff}, of the cavity. Thus, Equation 2.35 and Equation 2.39 can be expressed by considering transverse and longitudinal dimensions separately as follows [8]:

$$g = \sqrt{\left(\frac{c\gamma}{n_{\text{g}}L_{\text{eff}}}\right)\left(\frac{\sigma}{A_{\text{eff}}}\right)}, \tag{2.41}$$

$$\mathcal{C} = \frac{4}{\pi}\left(\frac{\sigma}{A_{\text{eff}}}\right)F, \tag{2.42}$$

where γ is the spontaneous emission rate of an emitter vicinity of an ONF and $\sigma = 3\lambda^2/2\pi$ is the single emitter absorption cross-section. In the case of waveguide cavities, the speed of light in the medium decreases due to material dispersion (see Section 2.4), so the cavity decay rate for the ONF cavities is expressed as

$$\kappa = \frac{\pi c}{F n_{\text{g}} L_{\text{eff}}}, \tag{2.43}$$

Importantly, for ONF-based cavities, due to the strong transverse confinement of the ONF-based cavity, a moderate value of finesse ($F \sim$ a few tens) can create a strong coupling condition. This important feature of cQED on an ONF is a major difference from the conventional free-space Fabry–Pérot cQED system, where it typically requires extremely high finesse values ($F \sim 4 \times 10^4$ - $4{\times}10^5$) [8].

As mentioned in Section 1.1, the spontaneous emission rate of an emitter placed on the surface of an ONF increases compared to the free-space scenario due to the aforementioned Purcell effect [188], and can be expressed as $\gamma = \gamma_{\mathrm{g}} + \gamma_{\mathrm{r}}$, where γ is the emission total decay rate, γ_{g} is the emitter decay rate into a fiber guided mode, and γ_{r} is the emitter decay rate to the radiation mode [9]. This means the rate of the emission into an ONF-guided mode, the so-called channeling efficiency, can be expressed as $\eta = \gamma_{\mathrm{g}}/\gamma$, and such efficiency is dependent on the fiber diameter, i.e., the transverse confinement, as shown in Figure 1.3 [9, 54]. Based on this unique characteristic of the ONF system, Equations 2.41 and 2.42 can further be rewritten as:

$$g = \sqrt{\frac{c\gamma_{\mathrm{g}}}{n_{\mathrm{g}} L_{\mathrm{eff}}}} = \sqrt{\frac{c\gamma\eta}{n_{\mathrm{g}} L_{\mathrm{eff}}}}, \tag{2.44}$$

$$\mathcal{C} = \frac{4}{\pi}(\eta\frac{\gamma}{\gamma_0})F = \frac{4}{\pi}\eta\mathcal{P}F, \tag{2.45}$$

where $\mathcal{P} = \gamma/\gamma_0$ is the Purcell factor. Note that the value of $\mathcal{C}$ primarily relies on two factors: the longitudinal confinement, which is determined by $F \propto 1/L_{\mathrm{eff}}$, and the transverse confinement of the optical mode, which is $\eta \propto 1/d_{\mathrm{eff}}$, where d_{eff} is the effective mode waist. The effective mode waist of ONFs is smaller than 1 μm, which is one order of magnitude smaller than the typical mode waist of 10–30 μm in the conventional free-space Fabry-Pérot cavities. This significant reduction in waist size results in a two-order improvement in $\mathcal{C}$ for ONF-based cavities [8]. Moreover, in the context of ONF-based cavities, there exists the advantage of independently controlling the cavity length, L_{eff}, without impacting the transverse confinement. As a result, it becomes feasible to adjust L_{eff} to attain the strong coupling regime, since the cavity decay rate decreases more rapidly than the emitter–field coupling rate with increasing L_{eff}. Furthermore, the emitter–field coupling strength can be enhanced by choosing an emitter with a high spontaneous emission rate. This offers the flexibility to select suitable values for the cavity length, fiber diameter, as well as the type of emitter within the achievable finesse range, thereby enabling both regimes of cQED as desired.

2.7 Conclusion

This chapter provides a foundational understanding of optical nanofibers (ONFs), including a concise explanation of the mathematical descriptions of guided modes within ONFs. The propagation of modes along an ONF is articulated in cylindrical coordinates, derived from Maxwell's equations, with further elaboration provided in Appendix A. Additionally, visual representations of the eigenmodes belonging to the LP_{01} and LP_{11} families, operating within the weakly guided regime, are presented.

Moreover, this chapter provides a brief overview of the theoretical expectations regard-

ing taper profiles. These profiles are crucial factors to consider when producing low-loss ONFs. Taper profiles can take the form of exponential or linear shapes, depending on the specific requirements. The key factor is ensuring that the taper angles remain adequately low for the desired mode. Typically, HOMs necessitate even lower tapering angles compared to the fundamental mode.

We also highlighted the essential attributes of cQED systems, particularly those employing ONF-based cavities. An ONF-based cQED setup holds a significant advantage in terms of finesse requirements to achieve a strong coupling regime for light-matter interaction phenomena. This advantage is realized with a moderate finesse value, often several orders of magnitude lower than what is needed for free-space cQED systems.

All these fundamental concepts play a pivotal role in this PhD research and, as such, we apply these concepts extensively in the subsequent chapters. In the next chapter, we introduce the fabrication methods of ONFs and cavities.

Chapter 3

Fabrication of ONFs and Cavities using a Ga FIB[1]

In the previous chapter, we went through key mathematical expressions to study mode propagation and profiles in ONFs, polarizations in HOM-supporting fibers, and the ONF-based cQED system. Here, we introduce the important technical details for the fabrication of ONFs and ONF cavities. Various fabrication methods of ONFs are already well established, as presented in Section 1.1. Here, we focus on two fiber-pulling systems with different heat sources: the hydrogen(H_2)/oxygen(O_2) flame and the ceramic microheater, both of which were used in this PhD work. We also introduce an ONF/OMF cavity fabrication technique. To create such cavities, we employ a FIB, which stands out as one of the most promising methods for constructing ONF-based cavities designed for applications in cQED, as discussed in Section 1.4. This chapter provides not only comprehensive explanations of newly developed FIB techniques for crafting internal mirror-type ONF cavities but also details the pre- and post-FIB processes, all aimed at achieving optimal results in cavity fabrication.

3.1 Fabrication of ONFs

There are a number of important parameters to control ONF fabrication outcomes. These parameters vary for different taper shapes of ONFs. This section briefly summarizes these key parameters for the fabrication of exponential-shaped ONFs and linear-shaped ONFs. The parameters described in this section are variables that were changed for different types of experiments and inserting these parameters in the existing MATLAB code and/or LabVIEW program communicates with a fiber-pulling rig, details of which are described in Subsection 3.1.2. Note that many different fibers and various parameters were used for different experiments in this PhD work, so this section only describes the general knowledge and methods used to fabricate ONFs used for this thesis work.

[1]This chapter contains Section 4 of the following published work: P. Romagnoli, M. Maeda, J.M. Ward, V.G. Truong, and S. Nic Chormaic, "Fabrication of optical nanofibre-based cavities using focussed ion-beam milling: a review", Appl. Phys. B 126, 111 (2020) [1]. M. Maeda contributed to the development of new fabrication methods with P. Romagnoli and J.M. Ward, the fabrication of the cavities with P. Romagnoli, and editing the paper.

3.1.1 Key parameters for ONF fabrication

The shape of the taper transition region, as indicated in Figure 2.1(a, b), is determined by the size of the heated part of the fiber, the so-called hotzone, $\mathscr{H}$. For a fixed constant hotzone, the taper profile follows an exponential shape and is suitably adiabatic for the fundamental HE_{11} mode. This is the most common and simplest way to fabricate an SM-ONF. The final fiber diameter, d_f, is a function of the initial fiber diameter d_0, the total pull length, $\mathscr{L}$, and the constant and uniform hotzone, $\mathscr{H}$, such that [15, 38, 173]

$$d_f = d_0 e^{(-\frac{\mathscr{L}}{2\mathscr{H}})}. \tag{3.1}$$

Once the diameter of the original fiber is decided, one only needs to set parameters $\mathscr{H}$ and $\mathscr{L}$. By using Equation 3.1, it is possible to estimate these parameters to obtain a desired ONF diameter. However, in reality, the hotzone may not be constant or uniform, and one may be required to use more complex models, such as linear hotzone variation [15], for more controlled and accurate outcomes. Nevertheless, the simplest model given by Equation 3.1 was sufficient for our experiments.

Linear and more complex taper shapes are also possible by varying the size of the hotzone during the fiber-pulling process. As mentioned, linear taper transitions are especially useful for achieving ultrahigh transmission in an SM-ONF and for low-loss HOM propagation in a HOM-ONF [38, 129, 178]. Linear-shaped ONFs require extra parameters to be considered. Well-described derivations of these parameters are found in [38]. For this PhD work, a trilinear taper shape of ONFs was used, as illustrated in Figure 2.1(b). Parameters required for the fabrication of a trilinear-shaped ONF are the initial fiber diameter d_0, two intermediate fiber diameters d_1 and d_2, the waist diameter d, and most importantly, three local core taper angles Ω_1, Ω_2, and Ω_3 (see, Figure 2.1(b)). These local core taper angles must be under the delineation curves for a specific mode of interest. For instance, in the case of one of the projects in Chapter 5, which requires the LP_{11} family, the local core taper angles have to be $\Omega \lesssim 1$ mrad at a normalized fiber radius $\sim$0.5, as shown in Figure 2.8.

3.1.2 ONF fabrication procedure

ONFs are typically made by tapering a section of commercial optical fiber in a fiber-pulling rig, with either a stationary or moving (brushing) heat source. Before starting the fiber-pulling process, it is extremely important to prepare and clean a section of to-be-ONF. In this PhD work, several different commercially available silica optical fibers were used for different experiments. Specific fibers are listed in the method section of each chapter. To begin with, the acrylic coating of the fiber is removed by a stripper, followed by wiping the stripped section with dry optical tissue. Next, the stripped fiber region was cleaned by another two optical tissues which contain isopropyl alcohol (IPA) and acetone, respectively, to remove residual acrylic and any dust particles.

Different heat sources may be used, depending on the compound and melting point of the glass [33], such as a CO_2 laser [45], resistance heating [46] or a graphite microheater [47]. Two systems were employed, each equipped with distinct heat sources: a H_2/O_2 flame and a ceramic heater. Despite the differing heat sources, both systems operate on the same fundamental principle. A schematic of the fiber-pulling system is illustrated in

Figure 3.1(a). Similar to the cleaning preparation of the fiber, it is also very important to clean the fiber-pulling rig using IPA before the fabrication to eliminate as much dust as possible to obtain high-transmission ONFs. The fiber is fixed on two linear motor stages (A in Figure 3.1(a)) that pull, while heating is done by a heat source coming from another linear motor stage (B in Figure 3.1(a)) and a stepper motor stage (C in Figure 3.1(a)).

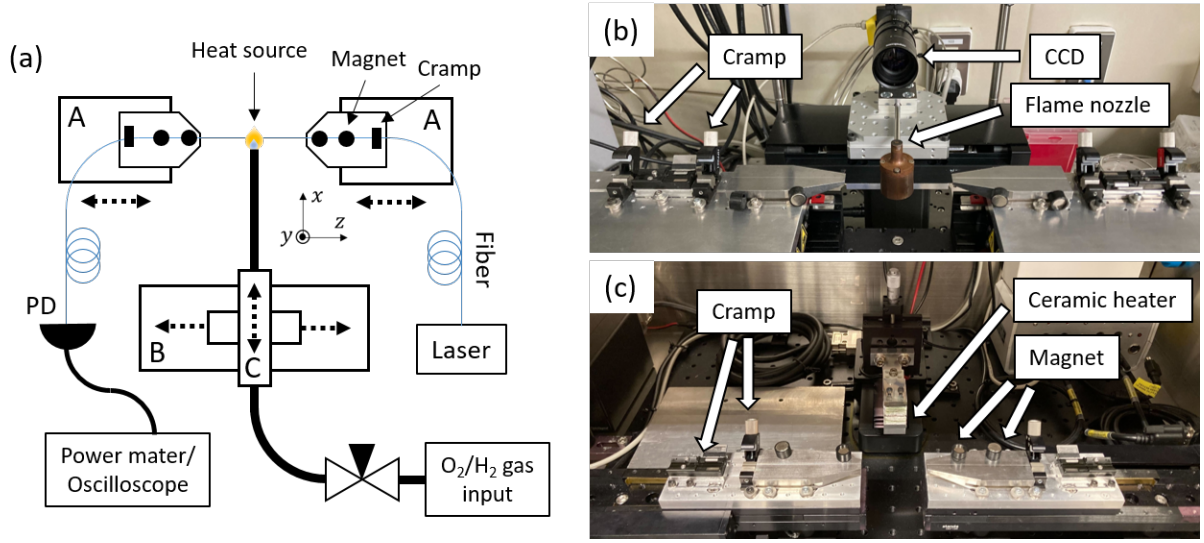

Figure 3.1: (a) Schematic of the fiber-pulling rig with stationary flame technique. A: Newport XMS linear motor stage, B: Newport ILS-LM linear motor stage, C: stepper motor stage, PD: photodiode. (b) Image of the H_2/O_2 flame system. (c) Image of the ceramic heater system. These fiber-pulling rig setups were mainly designed and constructed by Dr. Jonathan Ward and Dr. Kristoffer Karlsson.

Let us first introduce the H_2/O_2 flame system, with the stoichiometric ratio of H_2:O_2 being 2:1, see Figure 3.1(b). The flame has a temperature range of 1200-1500°C so that the fiber is plastic and can be stretched without breaking [38]. The flame nozzle faces toward the y direction with the stationary stage positions. The flame nozzle has 3×3 holes and is occasionally cleaned by IPA followed by acetone in a sonicator to remove dust. There is also a charge-coupled device (CCD) camera from the side of the hotzone area, where a section of the fiber is heated. This is to monitor if the fiber has dust particles or if the fiber is broken.

Figure 3.1(c) shows the ceramic heater system. The ceramic micro heater was purchased from NTT Advanced Corporation, and it has a fiber insertion slot with a width of 1 mm. The applied current is set so that the ceramic heater has a temperature of 1300-1400°C. Unlike the gas flame system, the ceramic heater size is fixed (22 mm), i.e., the hotzone needs to be carefully controlled by the movement of the ceramic heater. In the case of our stationary ceramic heater system, the pulling length is the only variable that can be used to control the ONF waist diameter. Therefore, the ceramic heater rig is only suitable for the fabrication of exponential taper-shaped ONFs.

Both fabrication setups are covered by acrylic seals and the setup can be closed except when the fiber is mounted on the stages. A positive air pressure is applied to the setup to minimize dust contamination of the ONF sample from the surrounding, but the filter is turned off during the fabrication process to avoid unexpected flame movement.

3.2 Characterization of ONFs

Characterization of ONFs is important as a quality check before using the samples for experiments. Some studies related to the fabrication of HOM-ONFs use transmitted imaging as a quality check [48, 130, 134]. This is ideal to confirm the adiabaticity of HOMs during the fabrication process; however, this requires extra optical components, such as a spatial light modulator (SLM) or a Q-plate, a telescope, and a camera. The fiber-pulling rig setup has limited space and it is not always possible to image the fiber output during the fabrication of ONFs. Some SM-ONF studies measure the diameter of the taper region and the length of ONFs [38, 149]. These measurements are only required when proving the critical adiabatic angle was achieved [38] or when fabricating a uniform ONF waist to create an ONF cavity with internal mirrors imprinted on the waist [149]. Typically, most ONF studies rely on the characterization of ONFs just by measurement of the transmission during the ONF fabrication and pre-measurement and calibration of the ONF waist diameter. Therefore, these two characterization methods were also performed.

To measure the transmission of an ONF, a laser beam was launched into the fiber and the transmission during the tapering process was monitored using a power meter or a photodiode, which was connected to a digital oscilloscope, see Figure 3.1(a). Varying wavelengths for different experiments were used and these specific wavelengths are noted in the method section in each chapter. The transmission after the tapering process was normalized to the original transmission before the tapering process.

Fabricating an ONF with the desired diameter is essential since it fixes the number of modes guided in the ONF. There are several methods to precisely measure the ONF diameter without damaging the ONF, such as the use of whispering gallery modes [196, 197], second harmonic generation [198], composite photonic crystal cavity [199], and a crossing microfiber [135, 200]. SEM imaging is commonly used to measure the ONF diameters. The problem with SEM measurement is that it needs conductivity to image an ONF sample. The fabricated ONFs were composed of silica, an insulating material, necessitating the application of a conductive coating. Consequently, the ONFs become unsuitable for direct use in actual experiments. To ensure the attainment of the desired ONF diameter, multiple ONF diameters were assessed via SEM before fabrication for experimental purposes.

After the fiber-pulling process, the sample was placed on a microscope glass slide, and glued on it using optical glue and a UV gun. The mounted sample was then coated with a 3 nm conductive platinum-palladium (Pt-Pd) layer by an ion-sputtering machine. The coated sample was then placed in the SEM and the waist diameter was measured. The SEM measurement has nanometer-scale errors, thus, we measured the waist diameter ten times, and the measured values were averaged and one standard deviation of the measurements was also calculated as a possible error in measurements. A typical SEM image of an ONF with a waist diameter $d = 605$ nm is shown in Figure 3.2. It is important to note that the diameter measurement procedure was not conducted for samples undergoing the FIB process, as their diameters can be directly measured using the SEM configuration integrated within the FIB machine.

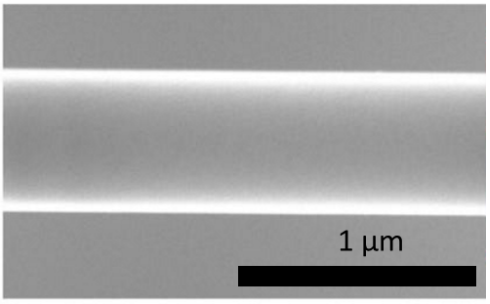

Figure 3.2: SEM image of a section of a typical ONF waist.

3.3 Cavity Fabrication using a Ga FIB

An ONF cavity with a complex mirror structure was previously fabricated by our unit, see Figure 1.9(c) [159]. To achieve high-quality devices, one must be careful about the preparation of the ONF, such as fabrication, and handling of tapered fibers, both before and after the milling process. The conventional fabrication procedure, as detailed in Li et al. [159], involves a three-step process:

1. The optical fiber was tapered and then fixed onto an aluminum (Al) substrate, using optical glue. In this case, the tapered fiber was suspended over the substrate in the air;

2. The sample/tapered fiber was coated with an ITO layer with a thickness of 20 nm to reduce surface charges;

3. the sample was milled using a Ga source FIB.

However, fabrication results using this process were not consistent, see Figure 3.3(a-d), primarily due to the low conductivity of the thin (∼20 nm) ITO layer and vibrations of the silica fiber when impacted by Ga ions. Therefore, a way to dispense with this fiber coating step was sought in order to improve repeatability and sample quality.

The versatility of ion beam milling enables the direct fabrication of nanostructures on ONFs. Low lateral scattering of ions ensures that only the intended regions are exposed to the ion beam [201]. However, this works only if charge accumulation is minimal, which can be achieved by discharging the sample. The usual practices for solving this issue, include a direct coating of the sample with a conductive material (which may be removed later) [29, 159, 202–207] or placing the sample on top of a conductive substrate [167, 208–211]. Negatively charging the sample with an electron beam from an SEM can also be used to avoid this charging effect and can partially compensate for sample charging [208], although an electron beam can damage the sample.

For OMFs or ONFs that are to be used for experiments involving quantum emitters (e.g. QDs, defect colour-centered diamond, or neutral atoms) interacting with light in the ONF's evanescent field, fiber coatings, such as the conductive ITO layer, can lead to undesirable transmission loss [212]. Also, coating the ONF before milling necessitates an additional procedure. Additional handling increases the difficulty of the process and exposes the fiber to different sources of contamination. It may be possible to remove the

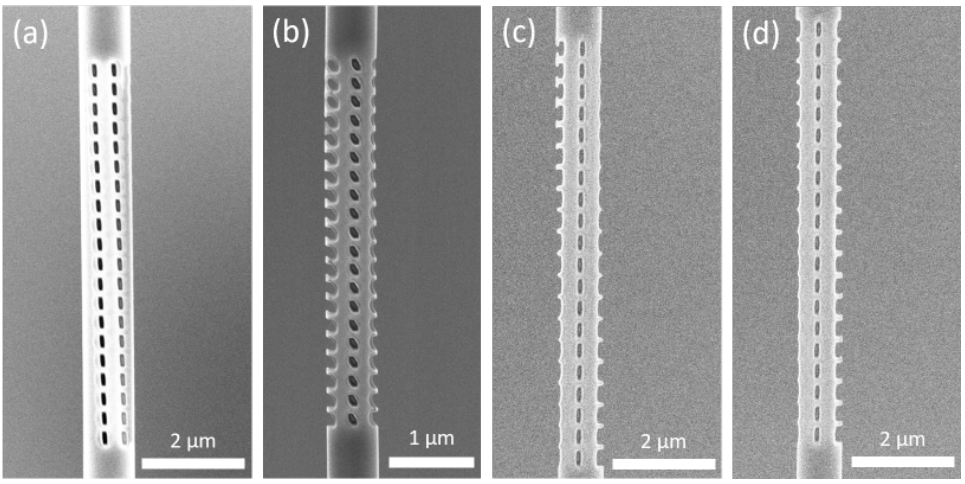

Figure 3.3: SEM images of mirror nanostructures on (a) OMF and (b-d) ONFs, aimed to fabricate periodic triple rectangular nanostructures as Figure 1.9(c), fabricated by early FIB methods. The FIB milled structures were almost always distorted from the aimed structures. Some of these samples were fabricated with Dr. Priscila Romagnoli.

coating by etching or even milling again using an FIB, but such invasive methods may damage the final structure.

If a fiber is uncoated and a conductive substrate is used, in order to avoid contamination due to the redeposition of the sputtered atoms during milling, the substrate material should be chosen so that it does not significantly absorb in the wavelength range being used in later experiments. This is important when milling holes through the fiber because the ion beam will also cut into the substrate, and sputtered atoms from the substrate can redeposit on the holes, causing optical losses in cavity transmission, as demonstrated previously for a copper substrate [167].

We developed techniques to overcome the obstacles described above by simply using a silicon wafer coated with ITO as a conductive substrate. ITO is almost transparent for visible wavelengths and Maniscalco et al. [212] showed that a 238 nm ITO layer sputtered on soda lime glass can have transmission values exceeding 75% for a wavelength range of 600-800 nm. As a result, the effect of contamination can be minimized when using an ITO-coated substrate instead of a metal substrate. This enables us to eliminate the conductive coating on the ONF, thereby reducing loss due to handling and increasing the mechanical stability of the ONF during milling due to van der Waals force between the ONF and the substrate. In what follows, the sequence for the fabrication of an ONF-based cavity is described in detail.

3.3.1 Pre-FIB fabrication

Optical nanofibers in this section are produced using the ceramic heater fiber-pulling system, see Figure 3.1(c). This section explicitly explains many key points to mount an ONF for FIB milling. Indeed, the manner in which an ONF is mounted holds equal significance to the FIB process itself. This is crucial not only for enhancing cavity quality but also for increasing the survival rate of the fiber which relates to the probability of

ONF-based cavities avoiding breakage. The ONF preparation procedure specifically for Ga FIB milling involved the following steps. The tapered fiber was placed onto an ITO-coated substrate and fixed on an Al fiber mount using optical glue to ensure the waist of the tapered fiber is in contact with the ITO-coated substrate. Optionally, two small pieces of Pt-Pd coated fibers may be placed on the taper transmission parts of the tapered fiber.

For this work, a commercial SM800(5.6/125) fiber from Fibercore, with an initial cladding diameter $d_0 = 125$ μm, was tapered down to a submicron waist with transmission of $> 90\%$ at $\lambda = 785$ nm (Thorlabs SM fiber-pigtailed laser diode, LPS-785-FC). The fiber cavity resonance wavelength was chosen to be near 780 nm, to coincide with the emission profile of a particular cadmium selenide telluride/zinc sulfide (CdSeTe/ZnS) QD or the ^{87}Rb D_2 atomic transmission.

After tapering, the fiber was glued onto an Al base plate that was specifically designed by myself, Dr. Priscilla Romagnoli, and Dr. Jonathan Ward, and fabricated by the Engineering Support Section at OIST, to hold the tapered fiber during FIB milling. Figure 3.4(a) illustrates a schematic representation of the ONF and the fiber mount which was designed for FIB milling purposes. The base plate has a rectangular slot, in which a rectangular block sits. Stuck on top of the block is an ITO-coated substrate. The block is held in place in the slot by Al slab-holding screws. The height of the substrate is relative to the tapered fiber and can be adjusted prior to tightening the screws. It is also important not to tighten the Al slab-holding screws (G in Figure 3.4(a)) for removing the Al slab later without breaking the ONF. The main idea of the Al base plate was to ensure that the ONF was physically in contact with the ITO-coated substrate. A small piece of carbon tape was stuck on the Al mount as well as the substrate to further improve the conductivity. The mount was also designed to have a screw (H in Figure 3.4(a)) so that we could shift the resonance wavelength of the milled fiber cavity. After removing the Al slab, the cavity can be easily transferred for the optical experiments, see Figure 3.4(b).

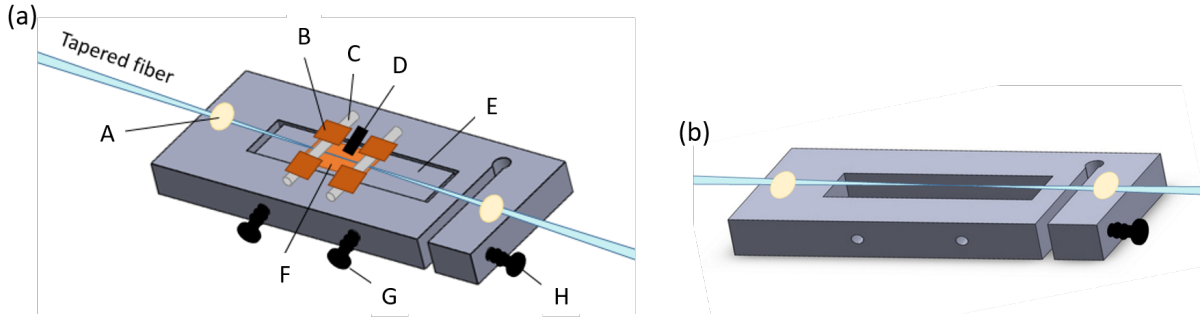

Figure 3.4: (a) Schematic of ONF Al mount for FIB fabrication process. A: UV optical glue, B: Kapton tape, C: Pt-Pd coated fiber, D: carbon tape, E: Al slab, F: ITO coated Si wafer, G: Al slab holding screw, and H: cavity length tuning screw. Use of Pt-Pd coated holding fibers and Kapton tapes is optional. (b) Schematic of ONF fiber mount after FIB fabrication process and for optical characterization.

The silicon substrate was sputtered with ITO in a sputtering deposition machine to create a uniform ITO coating. We sputtered in argon plasma, using a flow of 20 sccm, at 100°C, with 100 W of power, and rotation at 5 rpm. The exposure time of the substrate

to the ITO target was typically 480 s, yielding a layer thickness of $\sim$ 40 nm [213]. The substrate was fixed to the Al slab with carbon tape and was designed to be $\sim$ 0.5 mm higher than the base plate and approximately the length of the tapered region. The substrate must be cut into a small-enough size. If the ITO-coated substrate size was excessively large compared to the ONF waist region, as shown in Figure 3.5(a) with a stretched ONF, and Figure 3.5(b) with a slightly loose ONF, it could lead to poor SEM imaging and FIB fabrication quality due to low conductivity, because the ONF does not come in contact with the conductive ITO-coated substrate. The ITO-coated substrate length should not overly exceed the length of the fiber waist so that the to-be-milled section is in good contact with the ITO layer, as shown in Figure 3.5(c, d).

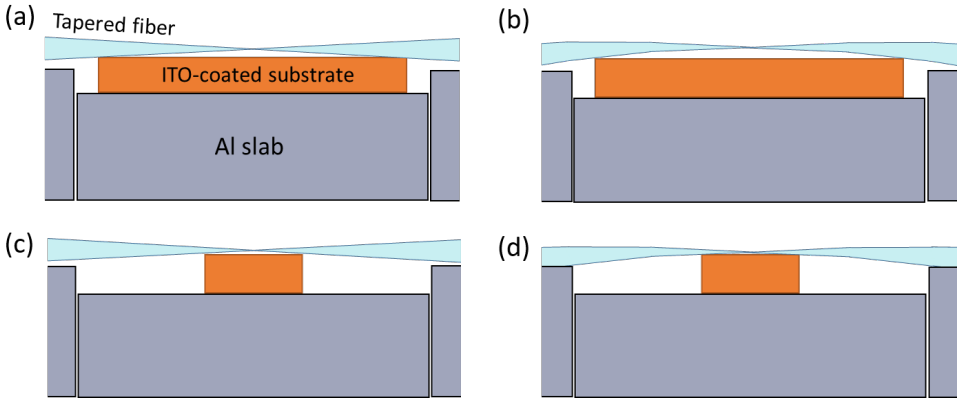

Figure 3.5: Schematic cross-sectional side view of how-to-mount an ONF. (a) A taut ONF on a large ITO-coated substrate. (b) A loose ONF on a large substrate. (c) A taut ONF on a small ITO-coated substrate. (d) A loose ONF on a small substrate is taken to be the best ONF mounting configuration for FIB milling.

It is also important to make sure that the ONF waist or the to-be-milled section of the tapered fiber is actually close to submicron size $d \sim 1$ μm. If the fiber diameter exceeds this, i.e., $d > 1$ μm, the conductivity may be too weak to resolve the fiber edge or mill the fiber, and the focus may be off for the actual FIB milling process. One should also be careful not to over-tighten the tapered fiber during and after ONF fabrication. In fact, it is best to leave the fiber slightly slack, as shown in Figure 3.5(b) and (d). There were so many incidents where Ga ions broke the samples during the FIB milling process. One of the main reasons for this was over-taut ONFs/OMFs, which do not have enough flexibility to release some of the mechanical vibrations and tension during the fabrication process.

To doubly ensure that the taper waist is in contact with the substrate, two small pieces of optical fiber, which we term "holding" fibers, could be used to push the taper downward. These small pieces of fibers were coated with 3 nm of Pt-Pd to reduce surface charges. They were attached to the substrate using Kapton tape, see Figure 3.5(a). Note that the tapered optical fiber is quite flexible and can be easily pushed into contact with the ITO-coated substrate using the holding fibers. While extra mechanical stability and conductivity can be achieved by adding these holding fibers, there are a few disadvantages to having them. For instance, it requires extra time to fabricate these conductive holding fibers. In addition, there is potential dust contamination from the holding fibers. Furthermore, removing these holding fibers can cause breakage of successfully FIB-fabricated

ONF cavities in the post-milling stage. One needs to weigh up the pros and cons of using the holding fibers and they were not used in many FIB-fabricated cavities in this thesis work.

3.3.2 FIB milling of an ONF/OMF

To demonstrate the validity of the new FIB milling mounting method, a nanostructure of complex periodic triple rectangular holes [159] was chosen as a mirror structure, see Figure 3.6(a). Such structures are composed of rectangular shapes with side lengths s_x and s_z. In this experiment, the to-be-milled section was chosen to be a region of uniform diameter of the taper transition region d_{m1} and d_{m2}, for Mirror-1 and Mirror-2, respectively. For proof-of-principal, we selected the milling positions where $d_{\mathrm{m1}} \approx d_{\mathrm{m2}} \approx 1$ μm, which is the maximum fiber diameter that could still be conductive enough from the ITO-coated substrate. The fiber diameter only had a small deviation of ± 10 nm in each milling site when the total grating length is 10 μm at this diameter. A schematic of the cross-section of such a structure is shown in Figure 3.6(b). The center and two sides of the fiber were milled, so the fiber cross-section had significant index modulation, enabling fewer periods to achieve high reflectivity (e.g. $>$ 80% transmission with 30 grating periods) [159]. The two mirrors were separated by a length L. It is important to consider the pitch, or the distance between each grating period, Λ, see Figure 3.6(a). This determines the resonant center frequency, or the so-called Bragg wavelength, λ_{B}, such that

$$\lambda_{\mathrm{B}} = 2n_{\mathrm{eff}}\Lambda. \tag{3.2}$$

Typically, a FIB machine has an SEM built into the system. The SEM is used to image a sample to locate an exact spot for FIB fabrication and to take pictures without damaging the sample by ion beams. Operating the FIB requires tilting the sample relative to the position for SEM imaging. In the case of the FIB machine that was used in this PhD work (FEI system, Helios NanoLab G3 UC), the sample was mounted at 0° with respect to the table surface for SEM imaging, as shown in Figure 3.7(a). The working distance, i.e., the distance between the sample surface and the electron source, needs to be separated by 4 mm for the best electron beam focus. To use FIB imaging and milling, the sample needs to be tilted at 52°, see Figure 3.7(b). The working distance between the sample and the ion source also has to be 4 mm for the best fabrication and imaging outcome using the FIB. The Ga ion beam was extracted using a voltage of 30 kV. The beam dwell time was 1 μs, corresponding to the time the beam spends at each pixel. These values were selected from the literature [159]. The sputtering rate is characterized as the target volume removed per charge and is defined by the material. For silica, its value is 0.24 $\mu\mathrm{m}^3$/nC at 30 kV [214]. The two lowest beam current settings (2 pA and 7 pA) did not give a significant difference in fabrication outcomes, so the second lowest beam current of 7 pA was selected to achieve high precision at a low time cost. The corresponding beam diameter of 7 pA was $\sim$ 9.8 nm. The FIB milling procedure comprised the following three steps: (i) Some nanostructures were milled by the FIB on a small section of the ITO-coated substrate; (ii) the ion beam alignment (adjustment of focus and stigmatism) was performed on the milled nanostructures on the ITO-coated substrate; (iii) the fiber was

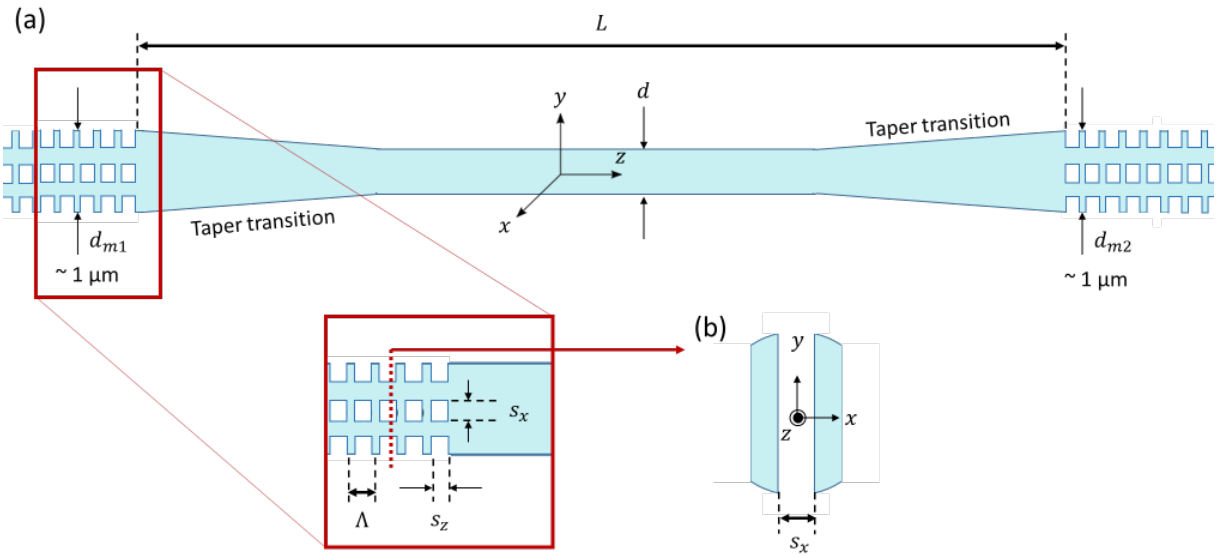

Figure 3.6: Schematic of the ONF-based cavity with a mirror nanostructure of periodic triple rectangular holes. The waist region of the tapered fiber has a diameter of d. The FIB milling positions of Mirror-1 and Mirror-2 have fiber diameters $d_{\mathrm{m1}} \approx d_{\mathrm{m2}} \approx 1$ μm. An FBG parameter Λ represents the grating period, i.e., the pitch of nanorectangular holes with a rectangular side length of s_x and s_y. Two sets of periodic mirror structures are separated by a distance L along the z-coordinate.

milled by the FIB without changing the beam alignment.

For aligning the ion beam before milling the sample, a small section ($\sim$1 μm^2) of the ITO-coated substrate $\sim$5 μm away from the sample was used to adjust the focus and stigmatism of the electrostatic lens of the FIB. Aligning the ion beam necessitates exceptionally sensitive control over the focus and stigmatism. Unlike with an electron beam, even a brief exposure to the ion beam can cause substantial damage to the sample. Therefore, at higher magnifications, we initially milled rectangular holes with identical sizes and pitch to the actual milling dimensions on the fiber, without exposing the sample to the ion beam. Premilled nanostructures were then imaged using a locally magnified FIB snapshot, with the fiber sample positioned outside the FIB imaging window. This process was reiterated until the structures were distinctly delineated. Figure 3.8(a) shows typical premilling nanorectangular shapes on an ITO-coated substrate. One can notice that the first premilling resulted in tilted nano-ellipses which indicates the ion beam astigmatism was not optimized. The beam focus and stigmatism were adjusted at these nano-ellipses which improved the second premilling. The beam focus and astigmatism were adjusted again at these second premilled nanostructures. The third premilling structure had clear edges and corners. It is important not to image the premilled structures on the substrate by SEM which can only be done by tilting the sample back to 0° from 52°, see Figure 3.7(a). This causes slight misalignment of the ion beam relative to the ONF, even after the optimization with the premilled structures.

A fiber sample, namely Cavity-1, had 90% transmission at $\lambda = 785$ nm at the tapering process. The ONF waist diameter, d, was 600 nm, the fiber diameter at Mirror-1 and Mirror-2 were $d_{\mathrm{m1}} = 1053$ nm$\pm$4 nm and $d_{\mathrm{m2}} = 1068$ nm$\pm$4 nm, respectively. The number

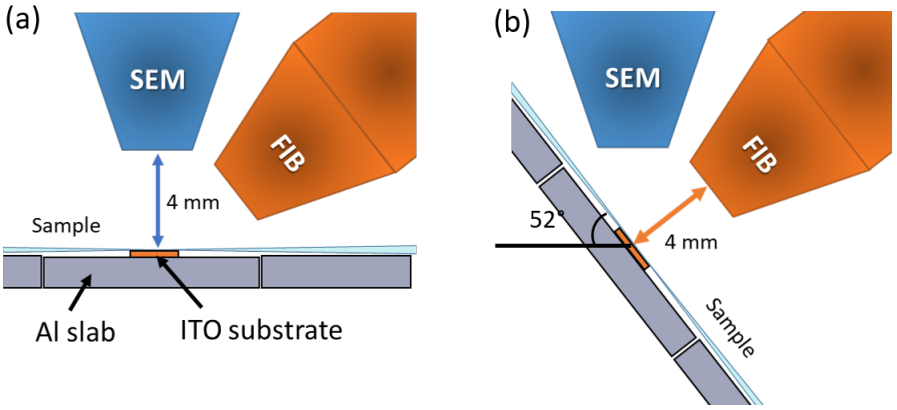

Figure 3.7: (a) Schematic of the SEM imaging setup. The sample stage position is parallel to the ground level. (b) Schematic of the FIB milling and imaging setup. The sample stage position is 52° tilted with respect to the ground level.

of mirror structures were set as $N = 30$ periods of triple rectangular holes $s_x = 150$ nm, $s_z = 120$ nm, and a pitch $\Lambda = 300$ nm. Once the beam alignment was optimized, as shown in Figure 3.8(a), the magnification was decreased until it was possible to just see a to-be-milled section of the ONF. FIB milling of the fiber was finally initiated, without changing the focus or stigmatism. Figure 3.8(b) is an SEM image of Mirror-1 and the premilled nanostructures. A close-up image of the mirror structures is shown in Figure 3.8(c). Alternatively, if a dust particle was found near the sample, the first focus and astigmatism alignment can be performed on the dust particle, as shown in Figure 3.8(d). The mirror separation length, that is the distance between the two mirrors, was $L \sim 6.450$ mm.

This method significantly improved the quality of mirror structures, compared to ones fabricated using the previous methods (Figure 3.3(a-d)). SEM measurements were performed by measuring ten points in a sample, and the mean value and one standard deviation were calculated as a possible error. The nanorectangular structural sizes were measured as $s_{x1} = 152\pm3$ nm, $s_{x2} = 154\pm5$ nm, and $s_{z1} = 122\pm3$ nm, $s_{z2} = 122\pm1$ nm, where the subscripts 1 and 2 denote Mirror-1 and Mirror-2, respectively. The measured pitches for Mirror-1 and Mirror-2 were $\Lambda_1 = 293\pm12$ nm and $\Lambda_2 = 292\pm8$ nm, respectively. These measured values agree very well with the target values of $s_x = 150$ nm, $s_z = 120$ nm, and $\Lambda = 300$ nm, considering a measurement error of $\pm$ several nm. The nanorectangular structures shown in Figure 3.8(b-d), have clear edges and corners, which were not observed in the previous samples (Figure 3.3(a-d)).

Not only is there an improvement in the nanostructure shapes, but this FIB method also improved the success rate of fabrication without breaking a sample during the milling, see Figure 3.9(a, b) and Table 3.1. We have milled a number of ONF-based cavities using the ITO-coated silica substrate and found that the overall stability and conductivity lead to improved repeatability and reduced turn-around time. It is important to note that the overall shape and pitch of the structure were repeatedly maintained and errors on the order of a few to tens of nm are reasonable for high-precision milling of complex structures.

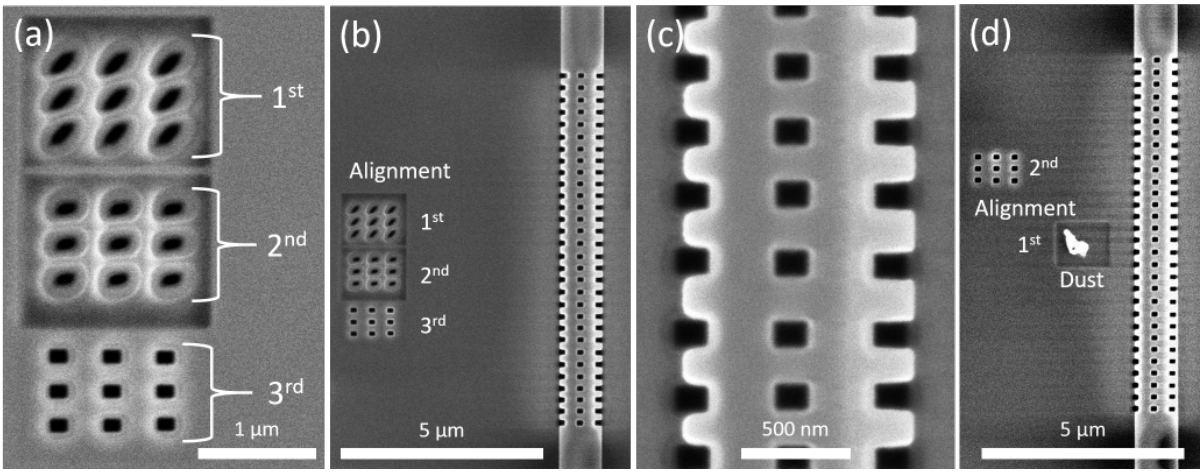

Figure 3.8: (a) SEM image of 3 × 3 rectangular nanostructures on the ITO-coated substrate of the first, the second, and the third millings. (b) SEM image of Cavity-1 Mirror-1 of an FIB-fabricated ONF-based cavity after three ion beam alignments with the 3 × 3 rectangular shapes on the ITO-coated substrate. (c) Close-up SEM image of the nano-structures milled by the FIB in a section of Mirror-1. (d) SEM image of the Cavity-1 Mirror-2, after the FIB alignment with a dust particle followed by 3 × 3 rectangular nanostructures on the ITO-coated substrate.

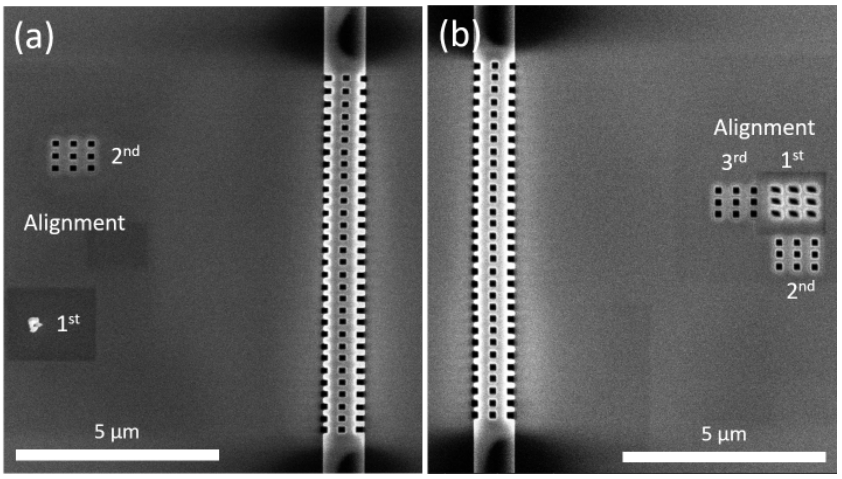

Figure 3.9: (a) SEM image of Mirror-1 of an FIB-fabricated ONF-based Cavity-2, after FIB alignment with a dust particle (white object) followed by 3 × 3 rectangular nanostructures on the ITO-coated substrate. (b) SEM image of the cavity Cavity-2 Mirror-2, the other side of the mirrors of Cavity-2, after three ion beam alignments with the 3 × 3 rectangular nanostructures on the ITO-coated substrate.

Table 3.1: Summary of nanostructural sizes in ONF-based cavity mirrors. The measured value ± error value indicates the mean and one standard deviation of 10 measurements, respectively. The following notation was used in the table, C#: Cavity-#, M#:Mirror-#.

Sample	Figure	Measured d	Measured $d_{\mathrm{m1,m2}}$	Aimed s_x	Measured s_x	Aimed s_z	Measured s_z	Aimed Λ	Measured Λ
C1 M1	3.8(b, c)	600 nm	1,050±4 nm	150 nm	152±3 nm	120 nm	122 nm±3	300 nm	293±12 nm
C1 M2	3.8(d)		1060±3 nm	150 nm	154±5 nm	120 nm	122 nm±1	300 nm	292±8 nm
C2 M1	3.9(a)	630 nm	1023±5 nm	170 nm	165±3 nm	150 nm	141±1 nm	300 nm	307±11 nm
C2 M2	3.9(b)		1016±6 nm	170 nm	164±4 nm	150 nm	156±2 nm	300 nm	290±18 nm

3.3.3 Post FIB fabrication

The cavities are susceptible to contamination by dust and humidity of the environment exposed in the between-steps, i.e., mounting the tapered fiber on the substrate, loading it in the FIB machine, and in the optical characterization setup. Thus, the cavity was kept in a clear plastic container with two fiber feed-through holes to minimize the risk of dust contamination during the optical characterization. Moreover, cavities were kept in a vacuum chamber (pressure < 0.6 MPa), and the lifetime can be more than one month, as opposed to the usual lifetime of the samples about a few weeks in ambient conditions. If the holding fibers were used, the Kapton tapes along with the holding fibers were removed, and then the Al slab with the ITO-coated substrate was removed by loosening the side bolts. The ITO-coated substrate on the Al slab was removed just before loading the sample into the optical characterization setup, as shown in Figure 3.4(b). Even though this FIB-milling method significantly improved fabrication quality as well as fiber survival rate, i.e. significantly reduced the chance of breaking the fiber during the FIB process, removing the ITO-coated substrate and the Al slab could cause a break of FIB-fabricated ONF-based cavities. This problem was mitigated by (i) slightly loose screwing of the Al slab-holding screws (see Figure 3.4(a)) before mounting an ONF, and (ii) unscrewing these screws very slowly in the positive pressured fume hood to avoid dust contamination. Optical characterization of ONF cavities is described in Chapter 4.

3.4 Conclusion

We have successfully devised a method that uses a Ga FIB to create nanostructures on an ONF, enabling the fabrication of an ONF cavity. The fabrication of an ONF-based cavity using FIB had numerous challenges, such as concerns regarding the mechanical stability of the ONF, time-consuming processes, achieving nanostructural quality, ensuring repeatability, and addressing fragility issues. The application of the presented FIB methods to create complex, periodic, triple rectangular nanostructural shapes for cavity mirrors resulted in significant improvements in fabrication.

We used an ITO-coated substrate underneath an ONF sample, thereby not requiring a conductive layer directly on the ONF. The van der Waals force between the fiber and the ITO-coated substrate stabilized the mechanical movement of the fiber during the ion milling. The fiber cavities on the ITO-coated substrate are also easier to handle than the

earlier suspended fiber design in both the pre-and post-FIB process. Additionally, this method reduced the overall fabrication time by eliminating the step of ITO sputtering directly onto the fiber sample which typically entails several extra hours per sample.

The premilling of the nanostructure can be performed on the ITO-coated substrate for the ion beam alignment. This premilling step significantly enhances the precision of nanostructure shape and size. Having good ion beam alignment is critical for obtaining high nanostructural quality as well as repeatable outcomes. This new fabrication method substantially enhanced the overall success rate of FIB milling in comparison to the conventional approach. Moreover, this also reduced unwanted damage from ion beam imaging and Ga ion contamination.

The Ga FIB technique offers distinct advantages in the fabrication of nano- and micro-length internal mirror ONF cavities when compared to alternative methods such as femtosecond laser ablation [149, 154, 155], composite PhC cavity configuration [156], or He FIB. While these methods are acknowledged for their contamination-free nature, both femtosecond laser-ablated ONF cavities and composite PhC cavities necessitate a lengthy index modulation region per mirror, thereby requiring the fabrication of a uniquely shaped ONF with an extended waist region to achieve high reflectivity. Although the He FIB process does not demanding such intricate efforts, it is not widely available, and its high resolution makes the fabrication process time-consuming. In contrast, Ga FIB is more readily accessible, allowing for the creation of substantial index modulation in a brief mirror length within a shorter time frame. Through our innovative Ga FIB fabrication methods, we have demonstrated the capability to consistently produce nanostructures with minimal deviations of only a few nm, underscoring the significant potential of Ga FIB in ONF cavity fabrication. Additionally, we will address and mitigate a potential drawback associated with this technique, that is the risk of Ga contamination during the fabrication process, as discussed in Chapter 5.

The focus on Ga FIB fabrication in this PhD work was ONF-based cavities for cQED. These all-fiber integrated devices are suitable for studying single quantum emitters in fiber-based quantum networks. These FIB-fabricated cavities are much shorter (scale of μm to mm) than external-mirror types of ONF-based cavities (scale of cm to m), meaning that they are more suited to applications where high Purcell enhancement or small loss are required. Therefore, this technique can also be applied to other applications that require FIB milling, including the fabrication of Bragg gratings and cavity structures for sensing purposes. The cavities fabricated for the work reported in this chapter had complex periodic triple rectangular shapes to demonstrate the validity of our new fabrication methods using the Ga FIB. However, despite high reflectivity, such complex periodic triple rectangular shapes induce higher scattering losses compared to simpler nanostructures, such as periodic single circular holes. In the next chapter, we discuss the fabrication and optical characterization of ONF micro-length cavities with periodic single circular holes using the same developed methods.

Chapter 4

Characterization of ONF Cavities Fabricated using Ga FIB

4.1 Introduction

A reliable method to create FBGs of periodic complex nanostructures using a FIB was described in Chapter 3. The use of an ITO-coated substrate to mitigate issues related to Ga FIB milling, such as mechanical instability, charging, and Ga contamination was successful. Such a method can be applied not only to fabricate ONF cavities, but also other ONF-based devices, such as slotted fibers for cold atom trapping or particle manipulation [27–29] as well as hole-tailored fibers for enhancing emitter coupling [169]. It is important to investigate the optical quality of such cavities to aim for repeatable and consistent optical outcomes.

One of the important optical qualities of an ONF-based cavity for cQED is the finesse, F, which can be controlled by using an ONF with high transmission and designing cavity mirrors with high reflectivity and low loss. There are two earlier works that claim to achieve strong coupling in cQED using an ONF-based cavity with $F < 40$ [10, 11]. These experiments used a single cold atom [10] or an ensemble of cold atoms [11] and relatively long external mirror type cavities (a Fabry-Pérot fiber cavity with 33 cm [10] and a fiber ring resonator of 1.3 m [11]). Moreover, a 1.2 cm long internal mirror type cavity was fabricated using femtosecond laser ablation and was proposed for strong coupling with a single cold atom [149]. Cold atoms are ideal quantum emitters in terms of their well-characterized transition states, narrow line widths, and indistinguishability. The natural linewidth (i.e., $\gamma_0/2\pi$) of cold atoms is as narrow as several MHz. Additionally, multiple atoms can be used to increase the coupling rate g_0 to $\sqrt{\mathcal{N}}g_0$ [151, 166], where $\mathcal{N}$ is the number of emitters. Such a model is only valid for indistinguishable emitters such as atoms. However, experiments involving cold atoms require an MOT, which makes the whole experimental setup bulky and rather expensive. In order to realize commercial quantum technologies, it is important to minimize the size, complexity, and cost of the system.

In this context, an ONF-based hybrid quantum system with solid-state quantum emitters, such as QDs or color center defect diamonds, has some advantages. In contrast to other emitters, QDs, i.e., nanocrystals with core/shell structures, offer a substantial ad-

vantage, which stems from their compatibility with standard semiconductor nanotechnology processes due to their material composition [215]. Unlike atoms, defect color-center diamonds, or molecules, the emission wavelength can be modified. The emission wavelength of QDs can span a broad spectral range from approximately 300 nm to over 1.55 μm, and can be achieved by selecting appropriate materials and employing strain engineering techniques [216]. Notably, this wavelength span encompasses the telecom bands, which is significant to achieve all fiber-based quantum communication [217]. Although high quantum conversion efficiency of telecom-compatible QDs is still under development [218], there is tremendous potential in a QD-based quantum communication scheme [217, 219]. In fact, cQED experiments using ONF cavities with QD(s) were already achieved [156, 158]. Nonetheless, these studies only achieved weak coupling or the so-called Purcell regime, and the realization of the strong coupling regime with a non-atomic ONF hybrid system has never been reported to the best of our knowledge. It is possible to realize such a novel system by considering the various parameters involved in ONF-based cQED requirements.

In the following section, we will describe parameters of ONF-based cavities, to determine whether it is possible to enter the strong coupling regime, assuming a single QD under cryogenic conditions as the quantum emitter. Section 4.3 presents the design and fabrication of the ONF cavity. Section 4.4 describes experimental setups and methods to measure cavity spectra. Section 4.5 showcases the optical characterization of ONF cavities and examines the validity of those cavities for cQED. Finally, this chapter concludes with Section 4.6, which discusses potential applications and the outlook for such cavities.

4.2 Device Parameterization

As mentioned in Section 2.6, to achieve strong coupling in light-matter interactions, one needs to satisfy the condition in Equation 2.40. An important experimental parameter to qualitatively assess the optical property of a cavity mode is the finesse, F, which can be calculated from the FWHM of a cavity mode linewidth, $\Delta\lambda_{\mathrm{FWHM}}$ ($\Delta\nu_{\mathrm{FWHM}} = \kappa/2\pi$, where κ is the cavity decay rate), and the FSR, $\Delta\lambda_{\mathrm{FSR}}$ ($\Delta\nu_{\mathrm{FSR}}$), as shown in Equation 2.32. As described in Section 2.6, one of the greatest advantages of an ONF-based cavity is its high potential to achieve strong coupling with a moderate finesse value (the order of a few 10s) when the cavity length is sufficiently long [9]. Now, let us introduce a new parameter, F_{min}, the minimum theoretical finesse to enter the strong coupling regime, by rearranging Equations 2.43 and 2.44 to satisfy one of the conditions $2g > \kappa$, such that

$$F_{\mathrm{min}} = \frac{\pi}{2}\sqrt{\frac{c}{\eta\gamma n_{\mathrm{g}} L_{\mathrm{eff}}}} < F. \tag{4.1}$$

From Equation 4.1, it is clear that F_{min} reduces as the cavity length increases.

However, it is also important to consider the decay rate of a quantum emitter. QDs have a disadvantage due to their broad emission linewidth, which is typically several tens of nm at room temperature. Shafi et al. [55] demonstrated an ONF-QD hybrid system at 3.7 K to reduce a single CdSe QD emission linewidth down to 0.12 nm, which is equivalent to $\gamma/2\pi$ = 59,171 MHz at λ = 780 nm (including Purcell factor $\mathcal{P} \sim 1.5$ [50]). Here, γ is the spontaneous emission rate when the emitter is in the vicinity of an ONF and, typically, $\gamma > \gamma_0$ (i.e., $\gamma = \mathcal{P}\gamma_0$) [50]. This linewidth is still four orders of magnitude

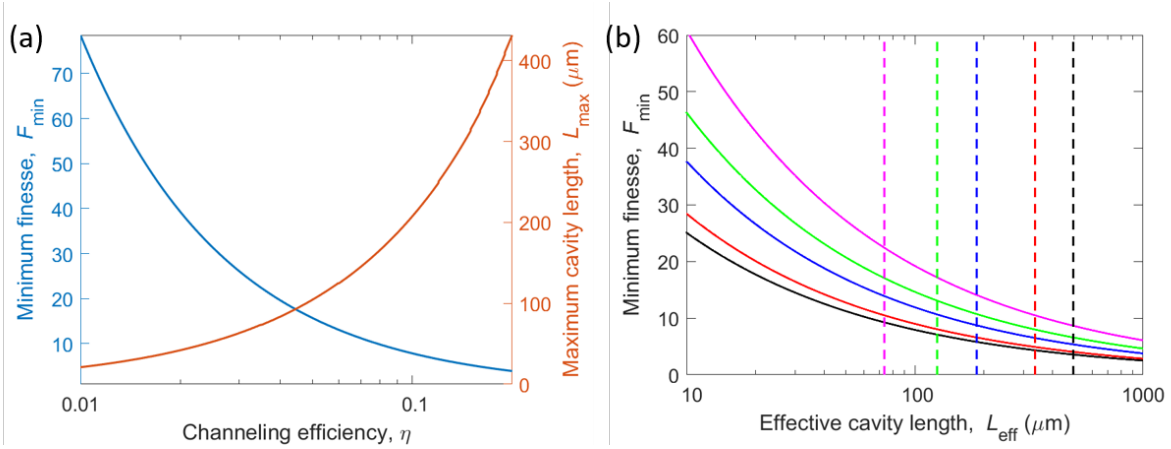

Figure 4.1: (a) Minimum finesse $F_{\text{min}}(L_{\text{eff}} = L_{\text{max}})$ (blue) and maximum cavity length, L_{max} (red), as a function of channeling efficiency, η. (a) F_{min} (solid lines) as a function of L_{eff} and corresponding maximum cavity length, L_{max} (vertical dashed lines) with different η values: 0.22 (black), 0.16 (red), 0.09 (blue), 0.06 (green), and 0.035 (pink). These η values are theoretically equivalent to a fiber diameter of 400 nm, 500 nm, 600 nm, 700 nm, and 800 nm, respectively.

broader than, for example, the linewidth of the ^{87}Rb D_2 transition of ∼6.4 MHz when the atom is 200 nm away from an ONF (a typical distance between an ONF and a trapped atom [220]) at $\lambda = 780$ nm (with $\mathcal{P} \sim 1.05$ [50]). Let us introduce a new parameter, L_{max}, the theoretical maximum cavity length in order to achieve strong coupling. It can be determined by rearranging Equation 2.44 with the condition $2g > \gamma$, such that

$$L_{\text{max}} = \frac{4\eta c}{n_{\text{g}}\gamma} > L_{\text{eff}}. \tag{4.2}$$

It is important to know the optical cavity length, i.e., the effective cavity length, L_{eff}, from the FSR (Equation 2.38). This is to ensure that the optical cavity length does not exceed L_{max} for strong coupling, i.e., $L_{\text{eff}} < L_{\text{max}}$ must be satisfied.

Typically, each ONF cavity sample has a different Bragg wavelength, λ_{B}, see Equation 3.2. However, from simulations, the change in group index, n_{g}, over 20 nm (770-790 nm) is less than 0.003, see Figure 2.9(b). Moreover, the cavity mode resonant frequency can be adjusted by controlling the mirror separation, L, by mechanically stretching the fiber cavity. The repeatable tunability of the resonant wavelength of ONF-based cavities fabricated using an FIB has been experimentally demonstrated, with an almost constant transmittance and Q-factor over 20 nm being achieved; such tuning can also be performed at cryogenic temperatures [158].

Notice that both F_{min} and L_{max} are functions of channeling efficiency, η. We plot the relationship between $F_{\text{min}}(L_{\text{eff}} = L_{\text{max}})$ and L_{max} with $\gamma = 2\pi\times59$ GHz (equivalent to a single QD emission rate at $\lambda = 780$ nm) as a function of η in Figure 4.1(a). As η increases, F_{min} decreases and L_{max} increases. It is possible to achieve strong coupling by choosing the mirror reflectivity (which can be obtained from F_{min} as Equation 2.33 indicates) and the mirror separation, L, to fabricate the ONF cavity once d, thus n_{g} and η, are known. Figure 4.1(b) shows F_{min} as a function of L_{eff} for five different η values and the equivalent

d values [54]: 0.22 (400 nm), 0.16 (500 nm), 0.09 (600 nm), 0.06 (700 nm), and 0.035 (800 nm). As d gets larger, η decreases, hence F_{min} increases, while as L_{eff} increases, F_{min} decreases. Also notice that L_{max} gets longer for high η (small d). This means that having a small d is a key to relaxing the conditions to reach strong coupling. In practice, two theoretical parameters, F_{min} and L_{max}, were calculated for each cavity sample and compared with the experimentally measured F and L_{eff} to evaluate the cavity quality.

4.3 ONF Cavity Design and Fabrication

As mentioned in Section 4.2, the ONF cavity should match the conditions $F > F_{\text{min}}$, $L_{\text{eff}} < L_{\text{max}}$, and, typically, $L < L_{\text{eff}}$ [194]. From Equations 4.1 and 4.2, both F_{min} and L_{max} are functions of the channeling efficiency, η, with $\eta \propto 1/d$ reaching a maximum of 22% when $d = 350$ nm at $\lambda = 780$ nm, see Figure 1.3 [54]. Nonetheless, performing FIB milling on a fiber with such a small diameter is not a straightforward task due to the increased fragility. Therefore, it is important to design a cavity with an optimal but also practical L and d as well as the shape of the nanostructure.

The cavities discussed in Section 3.3.2 consisted of complex nanostructures composed of periodic triple rectangular shapes (see Figure 3.6(a, b)) to show the validity of the FIB fabrication method. These were milled at $d_{\text{m1}} \approx d_{\text{m2}} \approx 1$ μm on the taper region of samples with a waist $d = 600$ nm and 630 nm. These cavities, therefore, had several mm of mirror separation, L. For strong coupling with a QD emission with $\gamma/2\pi =$ 59,171 MHz, ONF cavities with $d = 600$ nm ($\eta = 0.09$) and 630 nm ($\eta = 0.075$) have $L_{\text{max}} = 240$ μm and 290 μm, respectively. Milling periodic triple rectangular shapes at the ONF waist with $d = 600$ nm increases the fragility as there is less fiber material remaining. Moreover, despite high reflectivity, periodic triple rectangular nanostructures induce higher scattering losses compared to simpler nanostructures, such as periodic single circular holes. For this reason, we used a simpler cavity mirror shape consisting of periodic circular holes, a so-called one-dimensional (1D) PhC as often employed for nanobeams [221, 222] and ONF cavities [167], see Figure 4.2(a). See also Figure 4.2(b) for the cross-section schematic view of such an index modulation. This nanostructure only has a single hole per period, as opposed to three holes in the triple rectangular shapes, hence it has a weaker refractive index modulation per period [159]. Nonetheless, it is possible to increase reflectivity by increasing the number of grating periods per mirror [159]. With this 1D PhC-type mirror structure, ONF cavities were designed with d ranging from 600 nm ($\eta = 0.09$) to 800 nm ($\eta = 0.04$), with corresponding L_{max} of 290 μm and 130 μm, respectively.

In total, we fabricated seven ONFs, namely Cavity-3 through Cavity-9, that had transmissions ranging from 90% to 97% by pulling a section of SM800(5.6/125) fiber (Fibercore). The cavities had d ranging from 540±1 nm to 728±3 nm. These values were obtained from the mean and one standard deviation of ten sample measurements using an SEM. The circular hole diameter, d_c, was set to be 100 nm, 120 nm, or 150 nm, depending on d for each ONF sample, as shown in Table 4.1. The nanostructures were milled at the ONF waist region with a relatively uniform d. Each circular hole was separated by the grating period $\Lambda = 320$ nm. Two sets of periodic circular nanostructures were separated by a length, L, of either 100 μm or 140 μm. The number of grating periods was $N = 50$

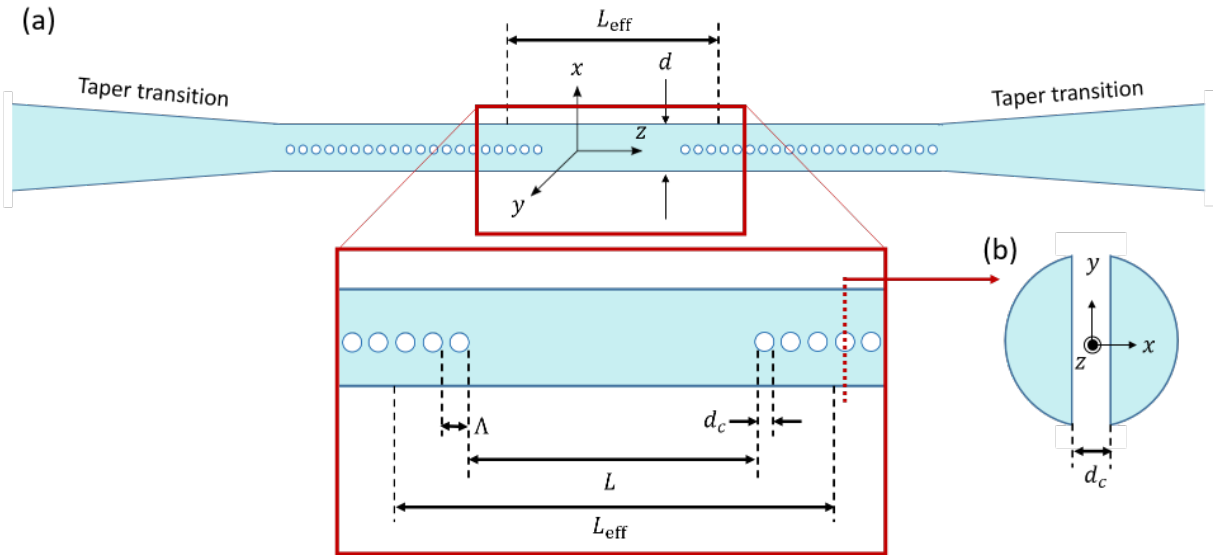

Figure 4.2: (a) Schematic of an ONF cavity with FIB-milled periodic circular holes. The uniform waist region of the ONF with a diameter d. An FBG parameter Λ represents the grating period, i.e., the pitch of the nano-circular holes with a diameter d_c, separated by the length L along the z-coordinate. Here, L_{eff} is visually represented as a physical graphic, but it is, in fact, an optical parameter with the relationship $L_{eff} > L$. (b) Schematic of the cross-section of an ONF-based cavity at FIB-milled circular hole.

for both sides of the mirror in all samples.

As an example of fabrication outcomes, Figure 4.3(a) shows Mirror-1 of Cavity-3. The PhC structures are well aligned near the center of the ONF and the hole sizes and grating period are almost constant, see Figure 4.3(b). The set circular hole diameter was $d_c = 120$ nm, while the actual measured sizes along the x-direction and z-direction were $d_{c(x)} = 122\pm10$ nm and $d_{c(z)} = 135\pm8$ nm, respectively. The grating period was measured as $\Lambda = 327\pm14$ nm. Mirror-2 of the same cavity, on the other hand, had slight misalignment along the ONF, see Figure 4.3(c). The periodic nano-circular shapes and the grating periods were also constant, see Figure 4.3(d), and the measured circular hole sizes and grating period were $d_{c(x)} = 124\pm7$ nm, $d_{c(z)} = 135\pm3$ nm, and $\Lambda = 315\pm3$ nm, respectively. These values matched well with the set dimensions with errors of several nm. Nanostructural properties of each mirror in Cavity-4, Cavity-5, Cavity-6, Cavity-7, Cavity-8, and Cavity-9 were similarly characterized (see Figures B.1-B.6). All the cavities had a good match to the set circular hole sizes as well as the grating period. The fabrication results are summarized in Table 4.1.

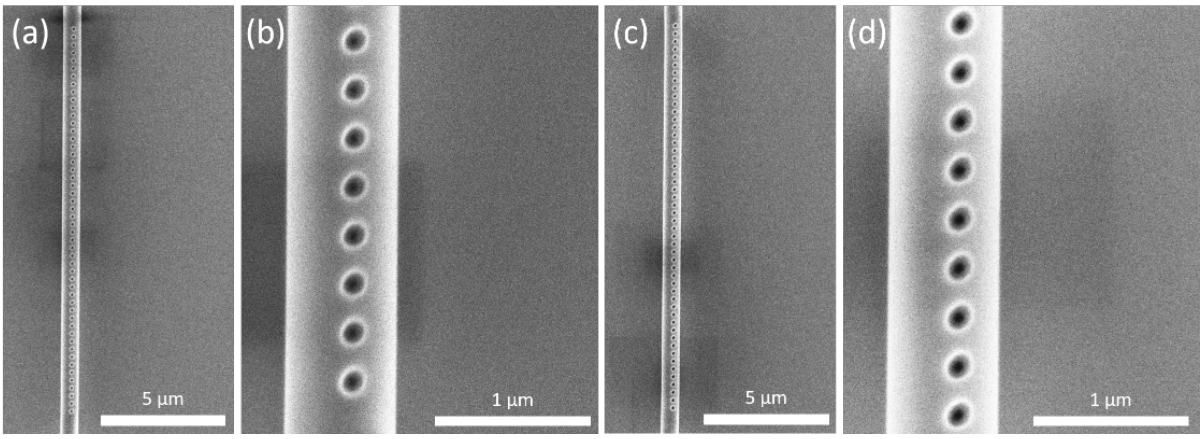

Figure 4.3: (a) SEM images of Mirror-1 in Cavity-3 in wide-field view and (b) close-up view. (c) SEM images of Mirror-2 in Cavity-3 in wide-field view and (d) close-up view.

Table 4.1: Summary of nanostructural sizes in ONF-based cavity mirrors fabricated by the FIB technique. The measured value (± error) indicates the mean and one standard deviation of 10 measurements. The following notation was used in the table, C#: Cavity-#, M#: Mirror-#.

Sample	Figure	Measured d	Set d_c	Measured $d_{c(x)}$	Measured $d_{c(z)}$	Set Λ	Measured Λ	Estimated L
C3 M1	4.3(a, b)	713±4 nm	120 nm	122±10 nm	135 nm±8 nm	320 nm	327±14 nm	100 μm
C3 M2	4.3(c, d)	715±4 nm	120 nm	124±7 nm	135 nm±3 nm	320 nm	315±3 nm	100 μm
C4 M1	B.1(a, b)	580±3 nm	100 nm	99±5 nm	108 nm±3 nm	320 nm	320±1 nm	140 μm
C4 M2	B.1(c, d)	579±2 nm	100 nm	98±5 nm	105 nm±4 nm	320 nm	316±9 nm	140 μm
C5 M1	B.2(a, b)	540±1 nm	100 nm	92±5 nm	96 nm±6 nm	320 nm	315±5 nm	140 μm
C5 M2	B.2(c, d)	545±1 nm	100 nm	86±3 nm	90 nm±4 nm	320 nm	314±5 nm	140 μm
C6 M1	B.3(a, b)	588±1 nm	120 nm	102±2 nm	102 nm±2 nm	320 nm	317±4 nm	140 μm
C6 M2	B.3(c, d)	588±1 nm	120 nm	108±3 nm	109 nm±3 nm	320 nm	317±4 nm	140 μm
C7 M1	B.4(a, b)	720±7 nm	150 nm	142±2 nm	137 nm±5 nm	320 nm	320±4 nm	140 μm
C7 M2	B.4(c, d)	727±4 nm	150 nm	135±3 nm	142 nm±4 nm	320 nm	313±3 nm	140 μm
C8 M1	B.5(a, b)	728±3 nm	150 nm	134±7 nm	140 nm±4 nm	320 nm	317±5 nm	140 μm
C8 M2	B.5(c, d)	722±4 nm	150 nm	136±3 nm	128 nm±5 nm	320 nm	313±3 nm	140 μm
C9 M1	B.6(a, b)	633±3 nm	120 nm	98±3 nm	101 nm±4 nm	320 nm	315±7 nm	140 μm
C9 M2	B.6(c, d)	628±4 nm	120 nm	90±4 nm	105 nm±4 nm	320 nm	311±7 nm	140 μm

4.4 Methods

An experimental setup, see Figure 4.4, was built to study the transmission and reflection spectra from the ONF cavities. A supercontinuum white light laser (SuperK COMPACT, NKT Photonics) beam with H polarization (i.e., electric field oscillates in x-direction, see the Cartesian coordinates in Figure 4.2), was collimated in free-space and injected into a 2×2 SM fiber coupler (805±75 nm, with a coupling ratio of 50:50). One line was spliced to one of the fiber pigtails of an ONF cavity, enclosed in a plastic container to reduce dust.

The other pigtail of the cavity was directly connected to an optical spectrum analyzer (OSA) (AQ6373B, Yokogawa) to measure the transmission. This line also contained an inline-polarization controller (IPC), to change the polarization of light into the cavity as desired. The other line was connected to an OSA and was used to measure a reference signal. Reflection was measured from the other input line, also connected to the OSA. This setup enabled us to measure transmission, reflection, and source simultaneously. Transmission and reflection were normalized to the measured input light source.

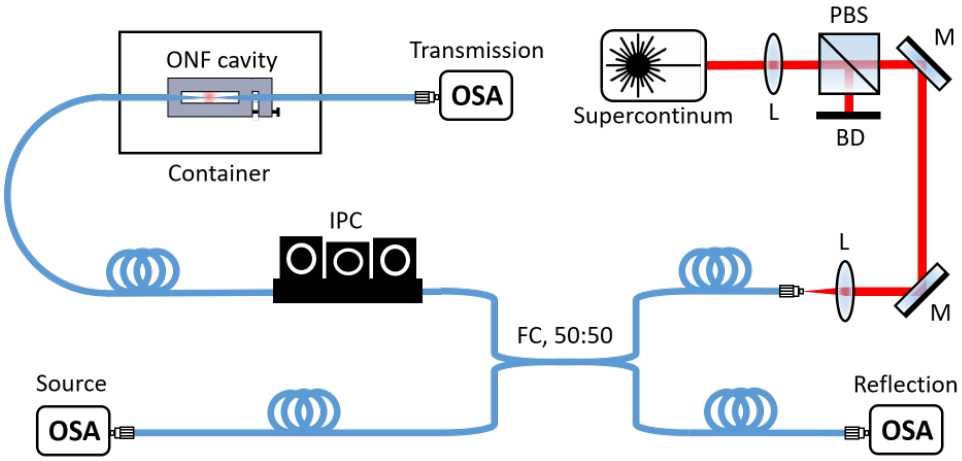

Figure 4.4: Schematic of the experimental setup to measure cavity spectra. L: lens, PBS: polarization beam splitter, BD: beam dump M: mirror, FC: fiber coupler, IPC: inline polarization controller, OSA: optical spectral analyzer.

4.5 Cavity Spectroscopy

A typical cavity spectrum of Cavity-3 is presented in Figure 4.5(a) for x-polarized input light. Both transmission and reflection spectra show a series of cavity modes. The stopband in the transmission spanned from ∼775 nm to ∼808 nm. For a mode at $\lambda_B = 792.89$ nm, $\Delta\lambda_{FWHM} = 0.0316 \pm 0.0325$ nm ($\Delta\nu_{FWHM} = \kappa/2\pi = 15.52 \pm 4.39$ GHz), and $\Delta\lambda_{FSR} = 1.96$ nm, see Figure 4.5(b). These values were determined by the average and standard error values generated from the Lorenz fitting using Origin. This leads to $F = 60 \pm 17$ and $Q = 24{,}382 \pm 6{,}898$, respectively. We did not observe resonant peaks between 780 nm and 790 nm due to high reflectivity in this wavelength range. Decreases or loss of transmission at the center of the stopband are also seen in other ONF-based cavity works [155, 157, 167].

The y-polarized cavity modes of Cavity-3 were also analyzed, see Figure 4.5(c). Both transmission and reflection spectra show multiple cavity modes at the same frequency. The stopband was observed from ∼782 nm to ∼807 nm. The minimum cavity mode linewidth was $\Delta\lambda_{FWHM} = 0.079$ nm ($\Delta\nu_{FWHM} = \kappa/2\pi = 37.20 \pm 0.59$ GHz) at $\lambda_B = 796.97$ nm with $\Delta\lambda_{FSR} = 796.97$ nm, see Figure 4.5(d). This resulted in $F = 24 \pm 0.4$ and $Q = 10,119 \pm 161$.

The stopband width of the y-polarized modes was about 8 nm shorter than that of the x-polarized modes. These outcomes reasonably match the simulated results in

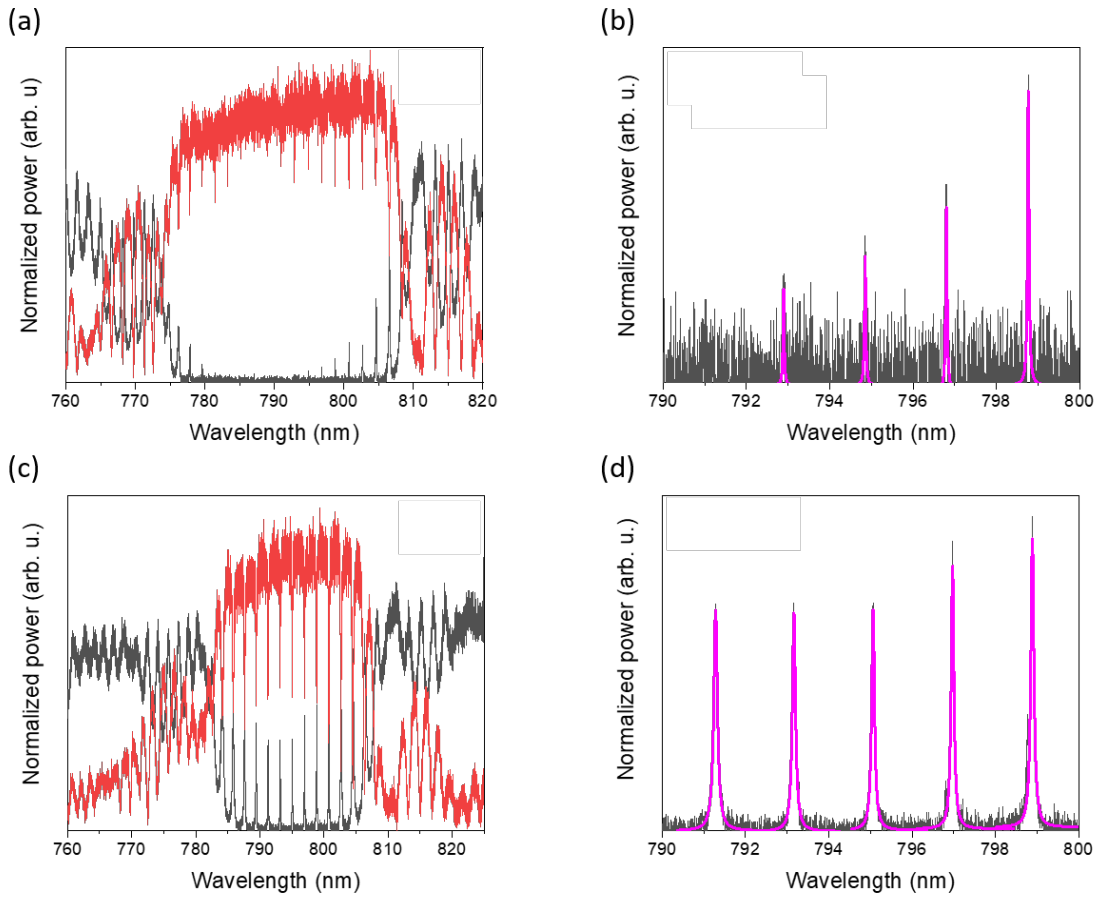

Figure 4.5: Mode spectra for Cavity-3. (a) x-polarized modes. Normalized intensities of transmission (black) and reflection (red). (b) Transmission (black) and Lorentzian fit (pink) of some x-polarized modes near $\lambda_B = 792.89$ nm. (c) y-polarized modes. Normalized intensities of transmission (black) and reflection (red). (b) Transmission (black) and Lorentzian fit (pink) of some y-polarized modes near $\lambda_B = 796.97$ nm.

Figure B.7(a, b), with the bandwidth of the y-polarized modes being about 10 nm shorter than that of the x-polarized modes. This is because x-polarized fields experience higher n_{eff} modulation in the PhC nanostructures compared to y-polarized modes (see Figure 4.2(b)); other ONF cavities fabricated using a FIB also have this polarization dependency [157, 159]. The simulated maximum reflectivity for x-polarized modes was $R = 0.973$. Assuming both sides of the mirror have the same reflectivity, i.e., $R_1 = R_2 = R$, we can estimate the theoretical maximum finesse for the x-polarized cavity by inserting R into Equation 2.32, yielding $F = 113$. This indicates that the observed F of 60 is only 53% of the theoretical maximum value.

For the y-polarized mode, on the other hand, simulation shows the maximum $R = 0.884$. This gives the theoretical maximum finesse of the y-polarized mode as $F = 24$, coinciding with the experimental value. This finding is unexpected, given that fabrication processes are not always flawless, and we initially anticipated additional scattering losses due to imperfections. There seems to be some loss that affects only the x-polarized electric field. This loss may be attributed to factors such as dust and Ga contamination, as well as scattering from the fabricated edges. An examination of Figure 4.2(b) shows that the x-polarized field oscillates across the entire FIB-milled surface, whereas the y-polarized field's oscillation is limited to a very small section near the center. Despite the higher R and, consequently, higher F in the x-polarized modes than the y-polarized modes, achieving the theoretical maximum F for the x-polarized cavity modes may prove challenging due to Ga contamination.

The FSR values were anticipated to fluctuate with changing wavelengths due to variations in the group index, n_{g}, as indicated by Equation 2.25. However, we noticed disparities in the FSR values between x- and y-polarized modes, even in a short wavelength range where the wavelength remained relatively constant, see Figure 4.6(a). The x-polarized modes (black) had slightly shorter FSR compared to the y-polarized modes (red). For three FSRs in the range of λ between 776 nm and 804 nm, the average and standard deviation of FSR values for x- and y-polarized modes are 1.96±0.01 nm and 1.90±0.02 nm, respectively. We can expect L_{eff} to be longer for the y-polarized modes, as Equation 2.38 suggests. Figure 4.6(b) shows L_{eff} of the x-polarized modes (black filled dots) and the y-polarized modes (black unfilled dots). L_{eff} was calculated from the measured FSR values and theoretically obtained n_{g} (see Figure 2.9(a, b)) using Equation 2.38. It is clear that the x-polarized modes had smaller L_{eff} than the y-polarized modes at the near-constant wavelength (see ∼792.5 nm to ∼802.5 nm). This can be explained by the difference in R values between the x- and y-polarized modes. Our experimental F values, which are a function of R (as shown in Equation 2.32), and the simulated R values indicate that cavity modes with x-polarization exhibit higher R compared to those with y-polarization. Also, notice that L_{eff} is smallest at λ_{B} for both polarizations. L_{eff} increases rapidly as the modes get closer to the stopband edges, as R is highest at λ_{B} and it decreases going toward the stopband edges. We also plot mode linewidth ($\Delta\nu_{\text{FWHM}} = \kappa/2\pi$) for the x-polarized modes (red filled dots) and the y-polarized modes (red unfilled dots), see Figure 4.6(b). Interestingly, $\kappa/2\pi$ values follow the same trend as L_{eff}. These findings indicate that as R gets higher, L_{eff} becomes smaller.

The minimum L_{eff} of the x-polarized mode and the y-polarized mode was calculated as $L_{\text{eff}} = 103.68\pm0.30$ μm and 106.91 ± 0.06 μm, respectively. Cavity mirrors were separated by a distance of $L \approx 100$ μm, so $L_{\text{eff}} > L$. This is because the actual reflector surface

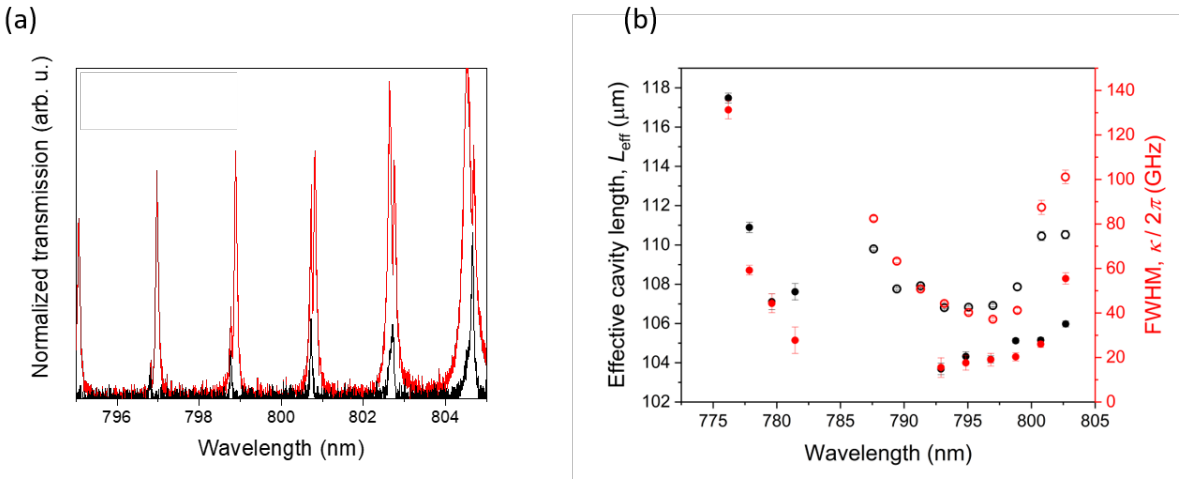

Figure 4.6: (a) Overlaid spectra of x-polarization (black) and y-polarization (red) of Cavity-3. (b) L_{eff} (black dots) and $\kappa/2\pi$ (red dots) as a function of wavelength for x-polarized modes (filled dots) and y-polarized modes (unfilled dots) of Cavity-3. The error bars indicate the standard error.

is not strictly at the start of the nanostructures milled by the FIB. There are 50 periods of circular holes separated by $\Lambda = 327\pm14$ nm and 315 ± 3 nm in Mirror-1 and Mirror-2, respectively. This means that the L_{eff} extends into about 1/8 of the mirror structure (see Figure 4.2(a)).

Next, we evaluate whether these cavity modes meet the criteria for strong coupling with a QD. Figure 4.7 shows two theoretical critical parameters F_{min} (solid black line) and L_{max} (dashed blue line) for the strong coupling regime together with the experimentally observed F and L_{eff} (red dot). It is clear that $F > F_{\text{min}}$ and $L_{\text{eff}} < L_{\text{max}}$ for both the x- and y-polarized modes. These findings suggest that Cavity-3 is very likely to enter the strong coupling regime of cQED using a single QD at cryogenic temperature, where the emitter linewidth can be as narrow as 0.12 nm [55]. Note that F calculated in this study did not actually include the deposition of a QD and any possible losses due to an emitter are ignored. In reality, some loss would be expected when depositing a QD on the surface of the ONF cavity. However, the QD deposition loss may not be as significant in ONF cavity modes. Yalla reported that the deposition of a single QD onto the ONF surface induces $< 1\%$ of loss [223]. The measured F of an x-polarized mode and a y-polarized mode of Cavity-3 was 60 and 24, even adding an extra 1% loss reduces these values to F $\sim$50 ($< 17\%$ drop) and $\sim$22 ($< 9\%$ drop), which are still over F_{min} for entering the strong coupling regime. Larger drop in F x-polarized mode compared to y-polarized mode is due to higher R in x-polarized mode, as Equation 2.33 indicates. Nevertheless, such a decrease in F value is much smaller compared to free-space cavities, where F is typically $> 40{,}000$ [8], indicating $R > 0.9999$. The addition of 1% loss to such a cavity drops F to 310 ($> 99\%$ drop). This is another advantage of ONF cavity with moderate F, as it is not significantly affected by emitter insertion loss to optical quality. The measured optical properties of Cavity-3 are tabulated in Table 4.2.

Due to the higher optical quality of the cavity for x-polarized modes, in the following, only the x-polarized cavity spectra were characterized, see Figure 4.8(a-f). All spectra

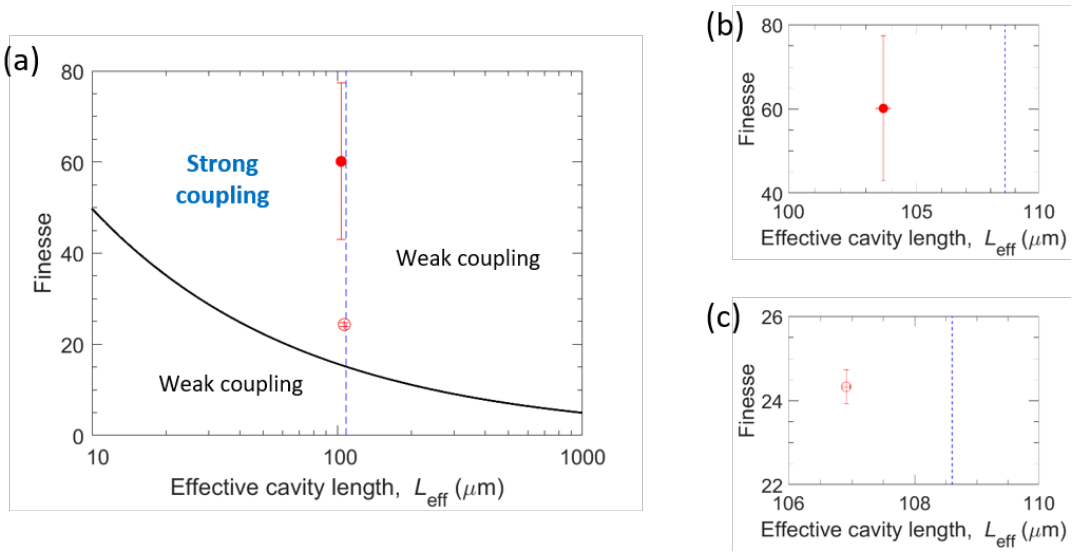

Figure 4.7: (a) Relationship between the experimentally observed finesse, F and the effective cavity length, L_{eff}. Also shown: theoretical minimum finesse, F_{min} (solid black line) and maximum cavity length, L_{max} (dashed blue line). The red filled dot and unfilled dot indicate F and L_{eff} for the x-polarized mode and the y-polarized mode, respectively. The error bar indicates the standard error. The large error for the x-polarized mode is associated with the small peak height of the high finesse modes (see Figure B.8). Zoomed in regions of (a) around (b) the x-polarized mode and (c) the y-polarized mode.

show clear stopbands and cavity modes in both transmission and reflection. The FSR varied from 1.28 nm to 1.38 nm. The mirror separation was $L = 140$ μm, but L_{eff} varied from 135 μm to 152 μm. Generally, L_{eff} is greater than L, which suggests that there may have been an error in measuring L during the FIB operation, as we have $L_{\text{eff}} = 135$ μm $< L = 140$ μm. Maximum F for these cavities were between 7 and 22. Figure 4.8(a-f) shows the experimentally obtained F and L_{eff} as well as theoretical F_{min} and L_{max} for strong coupling. The cavities in Figures 4.8(b, d, e) surpassed the F_{min}. However, despite its high F, Cavity-8 fell into the weak coupling regime since $L_{\text{eff}} > L_{\text{max}}$ (see Figure 4.8(d)). Out of seven cavities fabricated, three appear to be suitable for strong coupling with a QD (see Figure 4.7 and Figure 4.9). These estimated F values here indicate that these cavities have high losses ($T + \mathcal{L}$ ~13-34%). The introduction of an additional 1% loss, representing the maximum potential loss due to QD deposition, to the high-loss cavity results in a minor reduction in F value, with a decrease of 0.2-1.7. In fact, a study of QD coupling to an ONF cavity with a low Q mode ($Q = 250$) did not report a decreased Q after the deposition of several QDs [158]. The measured optical properties of these cavities are tabulated in Table 4.2.

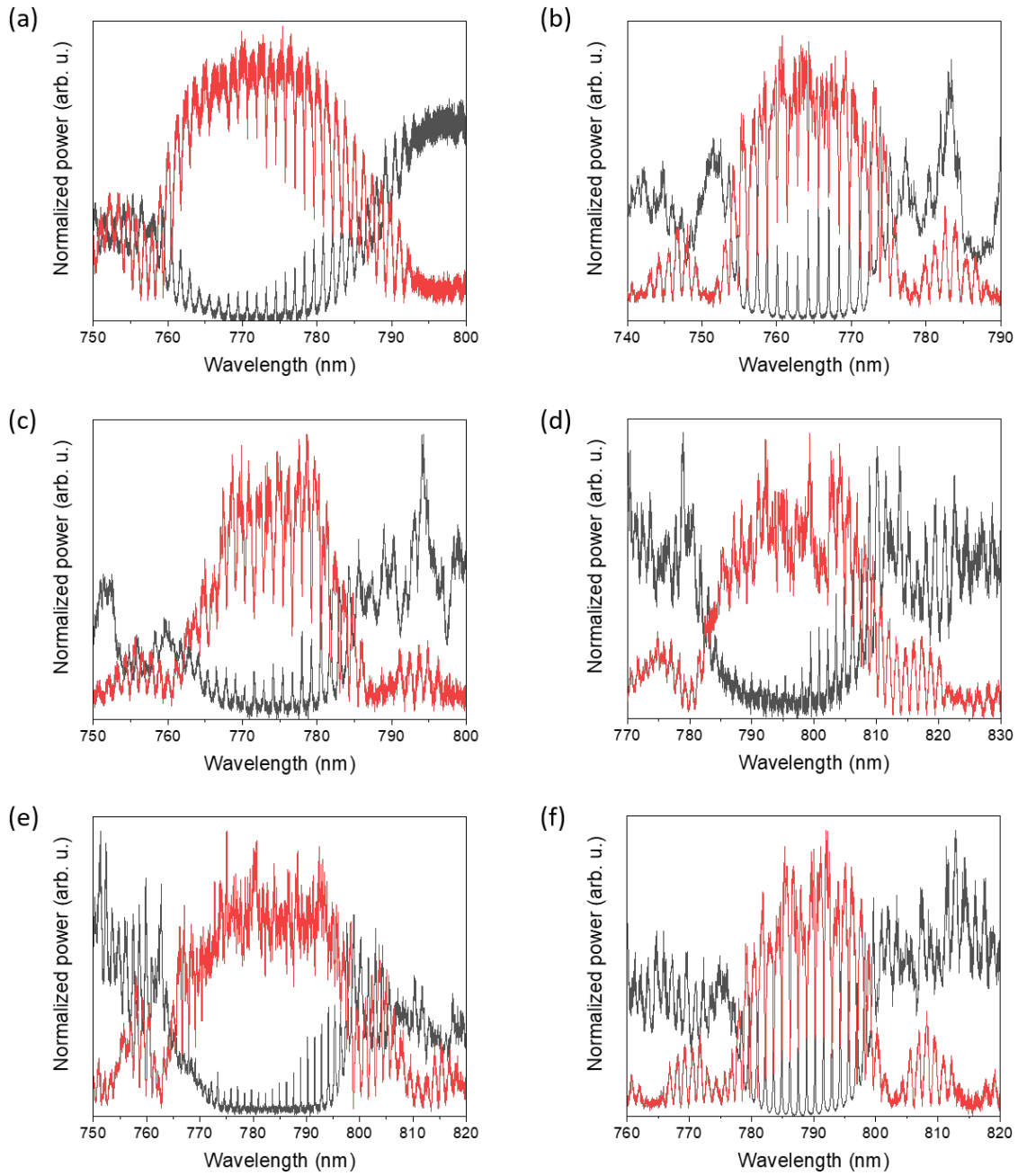

Figure 4.8: Normalized transmission (black) and reflection (red) spectra of x-polarized modes in ONF cavities: (a) Cavity-4, (b) Cavity-5, (c) Cavity-6, (d) Cavity-7, (e) Cavity-8, and (f) Cavity-9, respectively. Some of the cavity spectra were measured by Dr. Priscila Romagnoli.

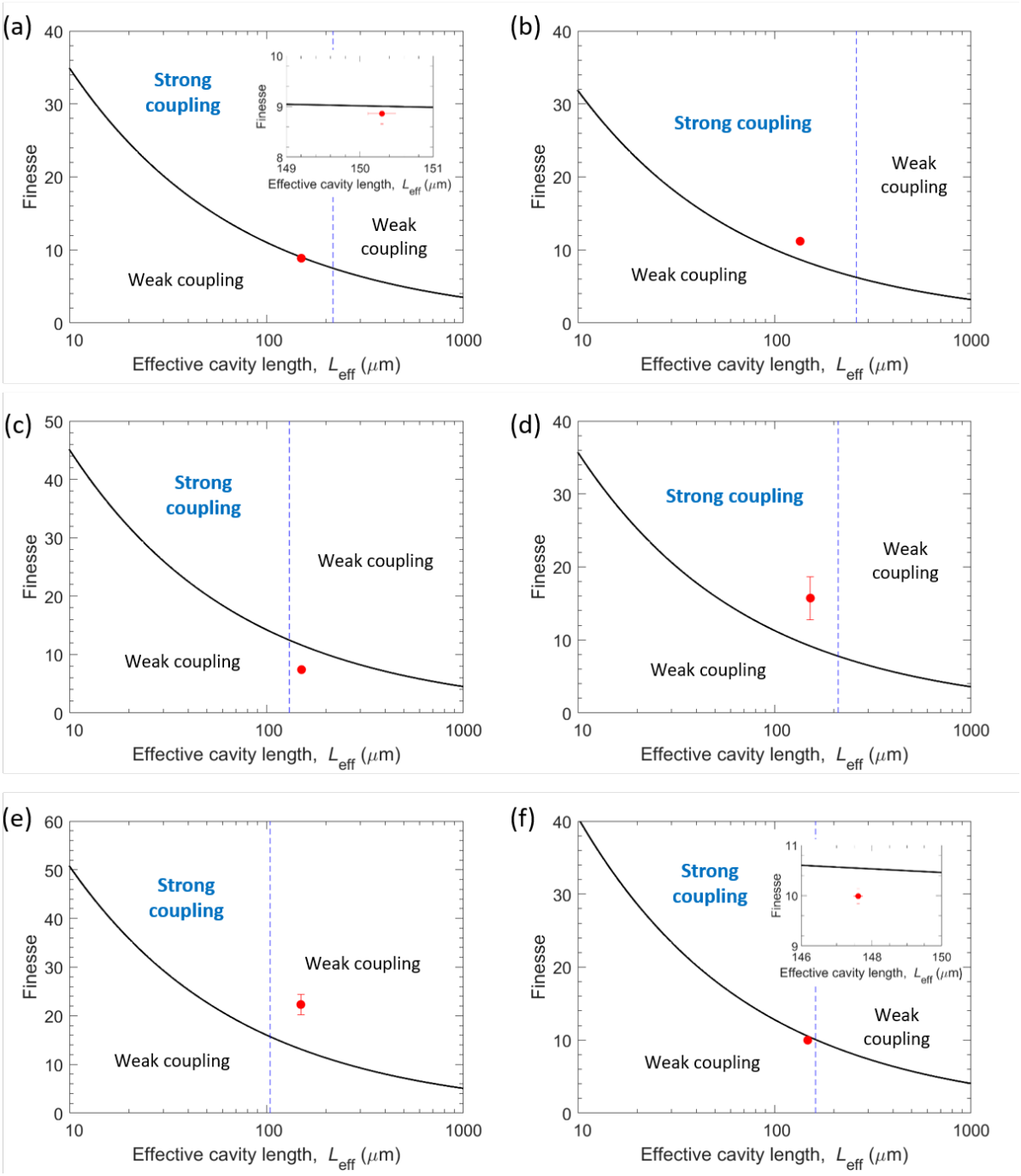

Figure 4.9: Relationship between the experimentally observed finesse, F, effective cavity length, L_{eff}, theoretically predicted minimum finesse, F_{min} (solid black line) and maximum effective cavity length, L_{max} (dashed blue line) of (a) Cavity-4, (b) Cavity-5, (c) Cavity-6. (d) Cavity-7, (e) Cavity-8, and (f) Cavity-9. The red dot indicates the experimentally determined value of F and L_{eff} with standard errors.

Table 4.2: Optical characteristics of the ONF cavities. The polarization of each cavity sample was adjusted to be x-polarized or y-polarized, as indicated in the column Sample. The error values indicate the absolute standard errors. T indicates the transmission during the ONF fabrication process. SC: strong coupling, WC: weak coupling.

Sample	Figure	T	F	Q	$\kappa/2\pi$	FSR	λ_B	L_{eff}	Regime
C3 (x)	4.5(a, b)	95%	60±17	24,382±6898	15.52±4.39 GHz	1.96 nm	792.89 nm	103.68±0.30 μm	SC
C3 (y)	4.5(c, d)	95%	24±0.4	10,119±161	37.20±0.59 GHz	1.92 nm	796.97 nm	106.91±0.06 μm	SC
C4 (x)	4.8(a)	90%	9±0.2	5,371±112	72.23±1.51 GHz	1.28 nm	774.47 nm	150.30±0.19 μm	WC
C5 (x)	4.8(b)	94%	11±0.1	6,158±6,173	63.60±0.80 GHz	1.38 nm	764.18 nm	135.06±0.10 μm	SC
C6 (x)	4.8(c)	96%	7.41±0.32	4,478±180	86.11±3.46 GHz	1.29 nm	777.95 nm	150.71±0.48 μm	WC
C7 (x)	4.8(d)	97%	15.73±2.94	9,379±1,680	40.15±7.19 GHz	1.34 nm	796.73 nm	152.28±1.15 μm	SC
C8 (x)	4.8(e)	94%	22.31±2.08	13,277±1,219	28.84±2.65 GHz	1.32 nm	783.60 nm	149.48±0.20 μm	WC
C9 (x)	4.8(f)	$>$ 90%	9.99±0.15	5,733±85	65.20±0.94 GHz	1.35 nm	788.87 nm	147.61±0.13 μm	WC

4.6 Conclusion

In this chapter, ONF cavities fabricated using a Ga FIB, as described in Chapter 3, were characterized. A set of 50 nano-circular holes was chosen as the cavity mirror in this study. Cavity spectra of seven cavities were obtained and F values for each cavity were estimated. The maximum F recorded was 60, with L_{eff} of about 104 μW. If one were to couple a single QD at cryogenic temperatures to such a cavity, it should be sufficient for strong coupling. A total of four out of seven cavities had F values that were higher than F_{min} needed to realize strong coupling. These outcomes nail down the effectiveness of the FIB milling methods detailed in Chapter 3 not only for the nanostructural property of the cavity mirrors but also the optical properties of the cavity itself.

Even for the cavities that did not reach F_{min} sufficient for strong coupling, the shortfall was minor, at about 0.6-4.2 (5-36%). The varying F values for each cavity may be attributed to dust contamination, which may be minimized by carrying a sample fiber to the FIB in a vacuum container. Optical measurements of most cavities here were conducted several weeks after the fabrication process due to COVID restrictions. This was not ideal even though the samples were kept under low vacuum. Some dust particles might have accumulated before the cavity spectroscopy [224]. Moreover, if the number of nanostructural periods were to exceed 50, it is possible that F would surpass F_{min} for all cavities.

ONF cavities fabricated via a Ga FIB have great potential to access the strong coupling regime by designing the cavities. Our approach to designing ONF cavities to meet the required parameters for strong coupling with QDs could also be extended to using emitters, such as color center nanodiamonds. Moreover, numerical analysis using FDTD methods can be used to further optimize the design of FIB nanostructures for lower scattering loss and higher Q-factor (hence F), to enhance the Purcell effect, and to obtain tunability of the cavity modes [168, 225–227]. In the next chapter, we will further investigate laser annealing of the ONF cavities to improve the optical qualities.

Chapter 5

Laser Annealing of ONF Cavities Fabricated using Ga FIB

5.1 Introuction

In the previous chapter, we performed the optical characterization of ONF cavities fabricated using a Ga FIB. We introduced two theoretical parameters, $F_{\min}$ and $L_{\max}$, to ensure the validity of the cavities to enter the strong coupling regime with a single QD under cryogenic conditions. In this chapter, we further investigate the potential to improve the optical qualities by laser annealing the cavities.

As mentioned in Section 4.1, F and L_{eff} (thus FSR) are the key experimental parameters to be investigated in ONF cavities for cQED experiments. Since F is a function of the FWHM of a cavity mode linewidth, see Equation 2.32, it is important to reduce scattering loss, κ_{s}, which is typically associated with unwanted factors such as dust contamination. In the case of ONF cavities fabricated using a Ga FIB, one needs to also consider other factors that potentially degrade the cavity's optical properties due to the FIB process. One such factor is Ga contamination; Ga ions not only deposit on the surface of a sample but also they can defuse into the silica [228, 229].

Wuttke [167] studied the effect of Ga contamination on an ONF cavity reflector (one mirror set milled directly at an ONF waist by a Ga FIB) and demonstrated an annealing procedure for reducing Ga contamination. The annealing process involved placing the ONF reflector in a vacuum chamber (at $< 10^{-5}$ mbar) and directing laser light at $\lambda = 832\pm12$ nm into the sample so that heating occurred in areas with high concentrations of Ga absorption. Ga ions were then removed by evaporation. The author showed that a heating power of 4 μW for 2 minutes was sufficient to change the refractive index of the fiber by removing Ga, changing the transmitted stopband shape and causing a blue shift of the reflected band by 50 nm from $\lambda \sim 852$ nm. The transmission increased by nearly a factor of two at shorter wavelengths in the range of ∼650-850 nm, the absorption wavelength range of Ga [230]. Not only did Ga desorption happen, but also the sharp edges of the nanostructures melted, thereby making them smoother and reducing the scattering loss. Wuttke [167] further increased the annealing power, P_{a}, to 100 μW for 2 min, thereby blue shifting the reflected band edge by an additional 40 nm. Transmission over a wide wavelength range (650-1000 nm) increased by about a factor of two and,

notably, the transmission dip at the center of the stopband, λ_B, increased by a factor of four. They assumed that the increased transmission dip at λ_B was a consequence of Ga diffusion into the silica. This study was limited to only two P_a values. It would be interesting to investigate the annealing threshold power and the feasibility of cold atom trapping using an ONF cavity fabricated using a Ga FIB, as where typically several mW of transmitted power is required [220]. Moreover, the effect of laser annealing on the ONF cavity remains unclear. Nevertheless, this technique seems promising for improving the optical characteristics of ONF cavities.

In the following section, we will describe experimental setups and methods of the laser annealing procedure. Section 5.3 shows the effect of laser annealing on the optical quality of the ONF cavity. We will then conclude this chapter with Section 5.4, which summarizes the experimental results and potential improvement of the laser annealing procedures.

5.2 Methods

The experimental setup to study the effects of laser annealing is in Figure 5.1(a). In this experiment, we studied two samples, Cavity-4 (see Figure B.1) and Cavity-8 (Figure B.5). An ONF cavity was enclosed in a vacuum chamber with a pump (HiCube 80 Eco, DN 63 CF-F, Pfeiffer Vacuum) at 1×10^{-4} mbar. Each fiber pigtail, with a diameter of 180 μm (including plastic coating around the 125 μm cladding), was inserted into a Teflon fiber feed-through with a hole of 250 μm, see Figure 5.1(b). The Teflon feed-through was placed in a Swagelok fitting on the vacuum chamber, and it was slowly tightened to seal the small gap between the fiber and feed-through until the vacuum chamber pressure dropped to $> 1{\times}10^{-4}$ mbar.

The supercontinuum white light laser beam (SuperK COMPACT, NKT Photonics) with H polarization was launched into one of the two fiber coupler input lines (805±75 nm, with a coupling ratio of 50:50). A 980 nm diode laser (CTL950, Toptica) was used as the annealing source and was connected to the other input line. The fiber coupler output was split into two lines. One of them was spliced to the input fiber pigtail of an ONF-based cavity, via IPC paddles for input polarization adjustment. The output fiber pigtail was connected to the OSA with a resolution of 0.05 nm to measure the cavity spectra. The other fiber coupler output line was directly connected to a power meter, which measured the power of the 980 nm annealing laser.

Using the IPC paddles, we selected x-polarized cavity modes before pumping the vacuum chamber. The system was then pumped down and a variable fiber attenuator (VFA) was used to slowly increase P_a. A transmission spectrum for each P_a was recorded on the OSA, see Figure 5.1(b). Spectrum measurements were made after 2 min of 980 nm laser annealing for Cavity-4 and 5 min of 980 nm laser annealing for Cavity-8. After confirming sufficiently low vacuum pressure ($< 1{\times}10^{-4}$ mbar), cavity spectra and optical images of a section of the ONF cavity were simultaneously recorded while increasing P_a until no transmission was measured. Pressure change over time for Cavity-4 and Cavity-8 are plotted in Figure C.1(a, b).

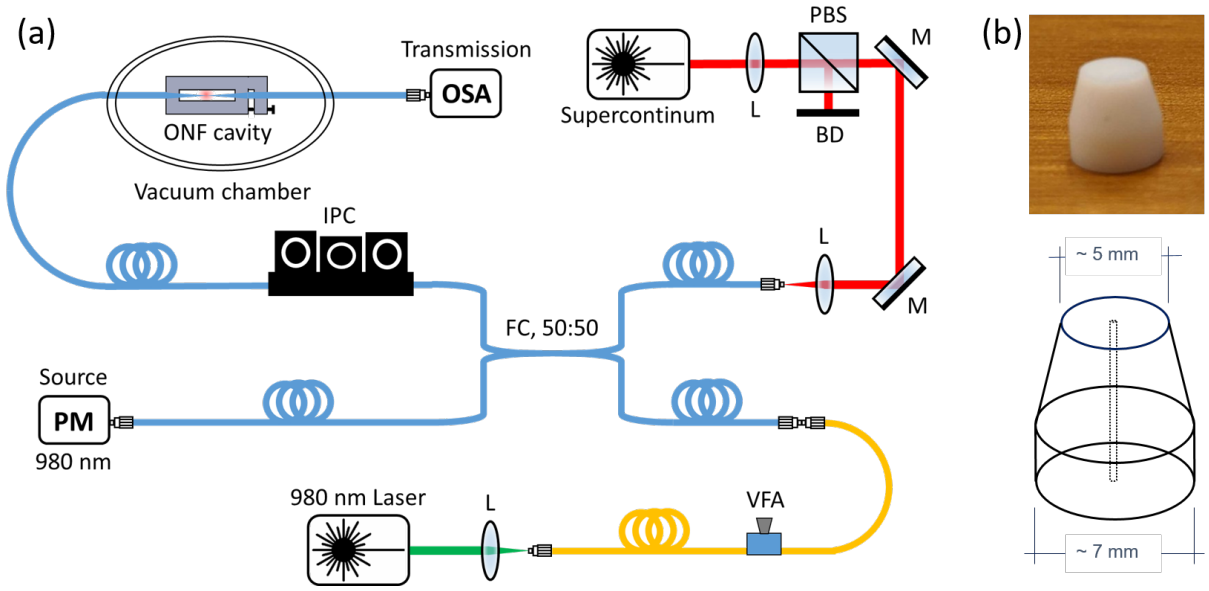

Figure 5.1: (a) Schematic of the experimental setup for annealing experiments. L: lens, PBS: polarization beam splitter, BD: beam dump, M: mirror, VFA: variable fiber attenuator, FC: fiber coupler, IPC: inline polarization controller, OSA: optical spectral analyzer, PM: power mater. (b) Teflon fiber feed-through to insert an ONF cavity into a vacuum chamber (top) and its schematic and dimensions (bottom) with a 250 μm hole (dotted line).

5.3 Effects of Laser Annealing on Optical Qualities

5.3.1 Effects on maximum transmission

The maximum cavity transmitted power of the stopband region was found from a transmission spectrum window from 740 nm to 800 nm for Cavity-4 and 750 nm to 820 nm for Cavity-8 as a function of annealing laser power, P_a. The maximum transmission at a specific P_a was normalized to the maximum transmission observed throughout the measurements, i.e., the maximum transmission in all spectra with varying P_a. Figure 5.2(a) shows the relation between the normalized maximum transmission and the annealing laser power for Cavity-4. There is a noticeable trend of increasing transmission as the annealing process progresses. The cavity transmission was about 20% before annealing and slowly increased to around 40% up to ~7 μW, then suddenly dropped back to 20% at ~10 μW. The normalized maximum transmission then rapidly increased to about 70% as P_a increased, but a significant decrease was observed just before the normalized maximum transmission reached a maximum at ~100 μW. A sudden loss of transmission was also observed just before the sample broke. On the other hand, Cavity-8 also showed a trend of increasing transmission with fluctuations in the maximum transmission over the course of the annealing process, see Figure 5.2(b). The cavity transmission was approximately 70% prior to annealing, but it dropped to around 60% at ~35 μW. Subsequently, the transmission increased to 80% at ~100 μW, although it exhibited fluctuations until it reached a peak at 400 μW. Much like the scenario observed in Cavity-4, the transmission of Cavity-8 experienced a sharp drop just before complete signal loss. The increase in the transmis-

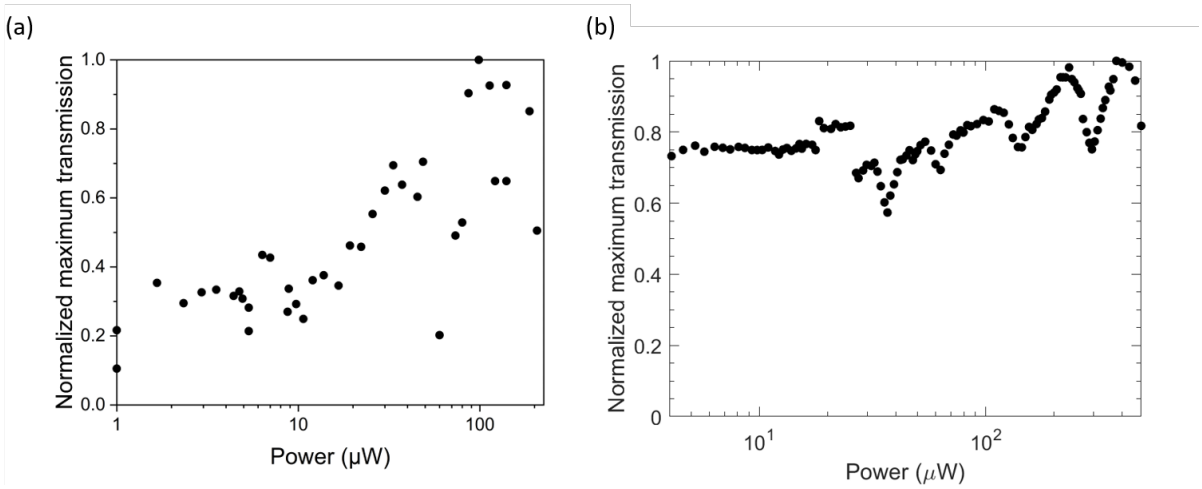

Figure 5.2: Normalized maximum transmitted power as a function of P_a for (a) Cavity-4 and (b) Cavity-8.

sion through the cavities was expected since such a phenomenon was previously reported for laser annealing of an ONF reflector fabricated using a Ga FIB [167]. However, the loss of transmission was not reported. The reduction in transmission may be attributed to either an increase in loss, which we will address in more detail in Section 5.3.4, or a potential inaccuracy in the normalization factor. Here, we examined the variation in the maximum transmission at specific P_a, normalized by the overall highest maximum transmission across all measured spectra, i.e., $T_{max}(P_a)/T_{max}(T_{max}(P_a))$. This approach was employed to comprehend the fluctuations in transmission throughout the annealing process. However, it is acknowledged that this factor may not necessarily serve as the optimal normalization parameter. In fact, a study involving laser annealing of an ONF reflector indicated decreased transmission at a specific annealing laser power [167]. This study demonstrated a decrease in transmission at 4 μW compared to the pre-annealed transmission, while the transmission increased at 100 μW. As discussed in the following sections, the profile of the cavity spectrum undergoes changes throughout the course of the annealing experiments. These alterations in spectral profile within a fixed wavelength range may pose challenges in acquiring a consistent reference transmission for normalizing the raw transmission data.

5.3.2 Effects on spectra

Figure 5.3(a) shows normalized cavity spectra for P_a for Cavity-4. The bandwidth and on resonance cavity mode transmission, T_r, changes as P_a changes. As P_a increased the stopband resonance also increased toward shorter wavelengths (the blue-detuned side). Meanwhile, the peak height of modes decreased as the annealing laser power increased. However, at = P_a = 188 μW (purple), the bandwidth reduced significantly and the peak height increased. Similar trends in the stopband were also observed for Cavity-8, see Figure 5.3(b). A large blue-shifted stopband at P_a = 26 μW (red) compared to the pre-annealing stage (black) was observed. Unlike for Cavity-4, there was no clear increase in peak height with higher P_a (516 μW (purple), and 544 μW (yellow)). We will analyze

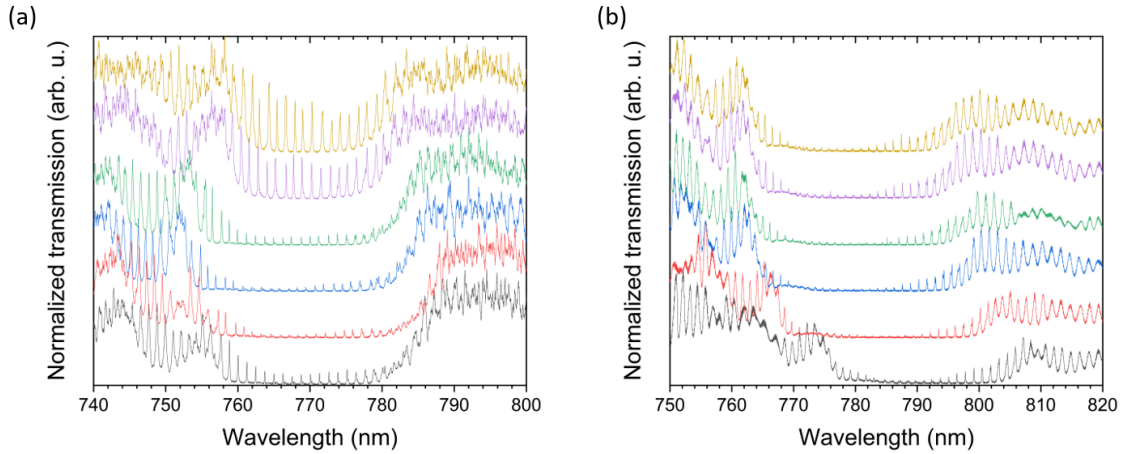

Figure 5.3: Change in cavity spectrum with varying P_a for (a) Cavity-4: 0 μW (before annealing, black), 10 μW (red), 80 μW (blue), 140 μW (green), 188 μW (purple), and 207 μW (yellow), and (b) Cavity-8: 0 μW (before annealing, black), 26 μW (red), 279 μW (blue), 377 μW (green), 516 μW (purple), and 544 μW (yellow). The raw data were recorded by Dr. Priscila Romagnoli.

the details of the stopband movement in the following section.

5.3.3 Effects on stopbands

In order to examine the cavity stopbands, we utilized approximated stopband shapes obtained by methods described in Section C.2. The blue dots (bottom curve), the black dots (middle curve), and the red dots (top curve) in Figure 5.4(a) show the blue-side, the center, and the red-side stopband wavelength as a function of annealing laser power, P_a. The stopband edges remained relatively constant until ~8 μW, but then it suddenly widened. The wavelength of the blue-side and red-side edges shifted to blue and red, respectively. Thereafter, the red-side edge slowly shifted to blue, while the blue-side edge remained approximately constant. At P_a = ~120 μW, the blue-side edge experienced a significant shift toward the red side, while the red edge underwent a notable shift toward the blue side. The center stopband wavelength (i.e., λ_B) did not undergo any dramatic change until P_a = ~40 μW, where it started to slowly decrease by ~2 nm compared to the pre-annealing condition. At P_a = ~120 μW, it shifted to the red-side.

The behavior of the stopband movement in Cavity-8 was different compared to Cavity-4. Figure 5.4(b) shows the stopband wavelengths on the blue-side (blue dots at the bottom), the center (black dots at the center), and the red-side (red dots at the top) while varying P_a. The blue, center, and red stopband wavelengths stayed constant at low P_a, but all of them suddenly shifted to the blue-side at P_a = 26 μW. The position of the blue-side stopband edge stabilized after P_a ~200 μW, while the center and red stopband wavelengths continued to decrease.

Although there were variations in the trends of stopband shifts between Cavity-4 and Cavity-8, as illustrated in Figures 5.4(a, b), both samples exhibited a consistent trend in the change of bandwidth. Figure 5.5(a) illustrates the change of bandwidth for Cavity-4

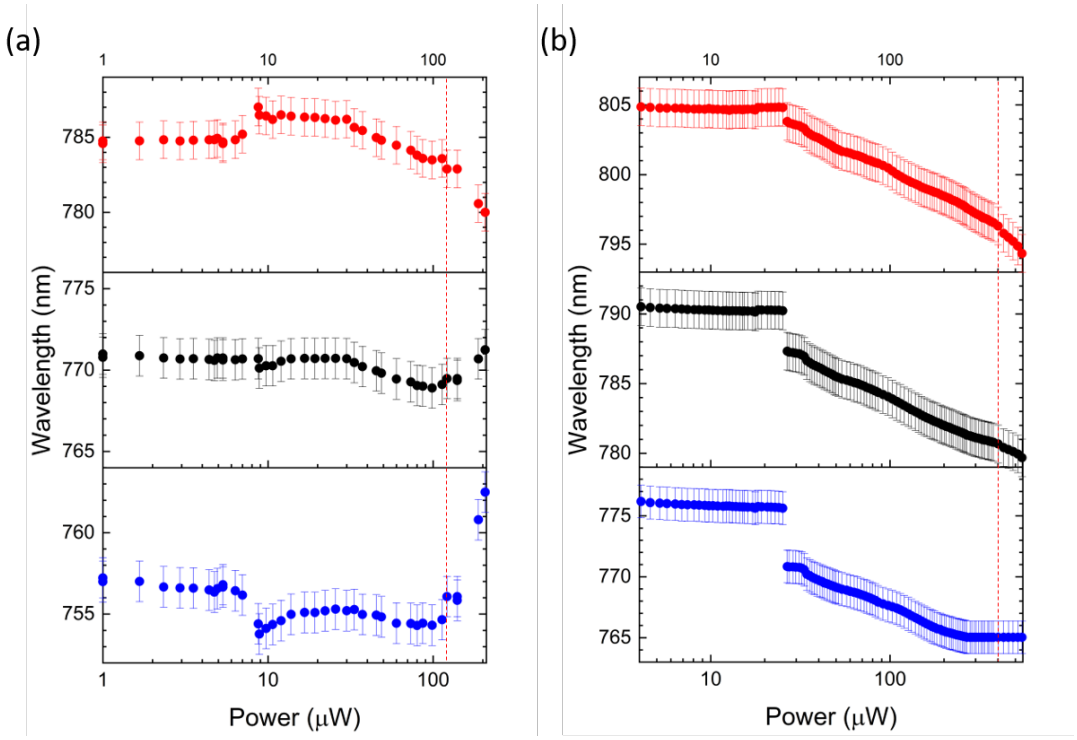

Figure 5.4: Stopband edges of shorter wavelengths (blue-side edge: blue dots in the bottom panel), longer wavelengths (red-side edge: red dots in the top panel), and λ_B (black dots in the middle panel) as a function of P_a for (a) Cavity-4 and (b) Cavity-8. The error bars indicate an approximated FSR value. The red dashed lines indicate P_a = 120 μW and 400 μW for Cavity-4 and Cavity-8, respectively.

over the course of the annealing experiments. The bandwidth remained constant at low P_a. It then suddenly increased by ~5 nm at P_a = 8 μW, and slowly decreased as P_a increased. At P_a ~120 μW, the bandwidth narrowed rapidly. Interestingly, Cavity-8 followed the same trend, see Figure 5.5(b). The bandwidth was constant before it experienced a sudden broadening of ~5 nm at P_a = 26 μW. The bandwidth stayed constant up to P_a ~200 μW, then it gradually narrowed as P_a increased. At P_a ~400 μW, a rapid decrease in the bandwidth was observed.

When P_a = ~120 μW for Cavity-4 and ~400 μW for Cavity-8 seems to be the turning point in this set of experiments. This may be the point where the ONF cavity started to excessively heat from the annealing laser. We can consider the shift as an effect of the cavity system where heating and Ga desorption occur at the same time. The shift in the Bragg wavelength, $\Delta\lambda_B$, is determined from the change in the effective refractive index, Δn_{eff}, and the grating period, $\Delta\Lambda$, as Equation 3.2 indicates. Now, let us postulate that $\Delta\lambda_B$ can be determined as follows:

$$\Delta\lambda_B(\Delta n_{eff}, \Delta\Lambda) = \Delta\lambda_B^h(\Delta n_{eff}, \Delta\Lambda) + \Delta\lambda_B^{Ga}(\Delta n_{eff}). \quad (5.1)$$

Here, $\Delta\lambda_B^h$ is the change in λ_B due to the heating effect from the laser annealing as a function of Δn_{eff} and $\Delta\Lambda$. $\Delta\lambda_B^{Ga}$ is the change in λ_B due to Ga desorption as a function of Δn_{eff}. During laser annealing, Ga deposited on the ONF may desorb, which should

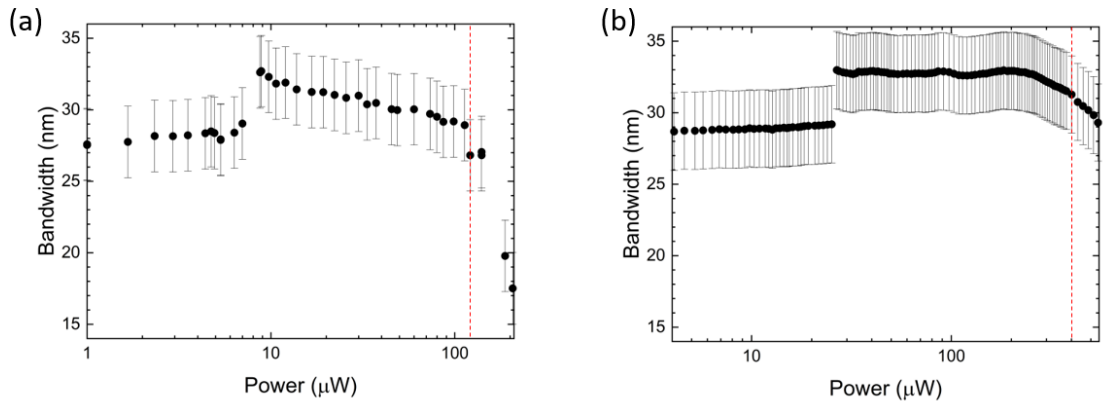

Figure 5.5: Bandwidth as a function of P_a for (a) Cavity-4 and (b) Cavity-8. The red dashed lines indicate P_a = 120 μW and 400 μW for Cavity-4 and Cavity-8, respectively. The error bars indicate a doubled approximated FSR value (estimated propagated error from stopband analysis (see details in Section C.2)).

decrease n_{eff}, henceλ_B may shift to a shorter wavelength [167]. Additionally, the higher the laser annealing power, the more the cavity will heat, thereby increasing n_{eff}. The cavity itself also experienced heating from the annealing. This may well elongate L, thus Λ, resulting in λ_B shifting to a longer wavelength. Up until ~120 μW for Cavity-4 and ~400 μW for Cavity-8, Ga desorption can be assumed to have been dominant. However, the situation may have changed at the critical P_a with heating then dominating λ_B, resulting in the red shift of the stopband and the subsequent breakage of the cavity.

We are also aware that the desorption of water could affect the change in n_{eff}, thus $\Delta\lambda_B$ [231]. However, under vacuum, the relative humidity would be ~0% [232], indicating that there may not be any water layer present, or, at most, only a single monolayer of water may be present with a thickness of 0.282 nm on the surface of silica [233]. Hence the effect of water desorption can be assumed to be negligible. Table 5.1 summarizes the potential effects of laser annealing on our ONF cavities.

Table 5.1: Summary of potential effects of heating and Ga desorption on the ONF cavity during the laser annealing process.

Phenomena	Heating	Ga desorption
Effects	Increase n_{eff} Increase L Increase Λ	Decrease n_{eff} Decrease L_{eff} Negligible change on Λ
Outcomes	Stopband shift to red side	Stopband shift to blue side

5.3.4 Effects on linewidths

Next, the FWHM of the minimum cavity mode linewidth, which is associated with the cavity decay rate, $\Delta\nu_{\text{FWHM}} = \kappa/2\pi$, was examined for each cavity spectrum while varying

P_a. Figure 5.6(a) shows $\kappa/2\pi$ as a function of P_a for Cavity-4. The black points represent experimental data with estimated standard errors, while the red solid line represents a fitted curve as a visual guide. Although the data points exhibit some scatter there is a clearly observable trend of decreasing $\kappa/2\pi$ as P_a increases. The linewidth was $\kappa/2\pi$ ~30 GHz at the beginning of the laser annealing. There was a sudden increase in $\kappa/2\pi$ by ~8 GHz at $P_a = 8$ μW and the bandwidth also suddenly increased (see Figure 5.5(a)). Then, the FWHM reduced to ~20 GHz at P_a ~120 μW. However, the linewidth suddenly increased at P_a >~120 μW and went up to ~50 GHz at 207 μW. Similar behavior was observed for Cavity-8. Figure 5.6(b) shows $\kappa/2\pi$ for Cavity-8 as a function of P_a. Here, experimental data (black) scatter more and the associated error values are larger than for Cavity-4. This is because the transmission at resonance, T_r, is small, see Figure 5.3(b). Due to the increased signal-to-noise ratio, the possible error is also increased (see Figure B.8.) The linewidth was $\kappa/2\pi$ ~30 GHz with some fluctuations of ~ $\kappa/2\pi \pm 2$ GHz at the beginning of the laser annealing. At $P_a = 26$ μW, where the bandwidth suddenly increased (see Figure 5.5(b)), there was a sudden increase in $\kappa/2\pi$ by ~5 GHz. Then, $\kappa/2\pi$ decreased until it reached the minimum at P_a ~200 μW. Fluctuations in data points and large errors make the evaluation of $\kappa/2\pi$ change over different P_a. Nevertheless, one can see a general decrease in $\kappa/2\pi$ as was also observed for Cavity-4.

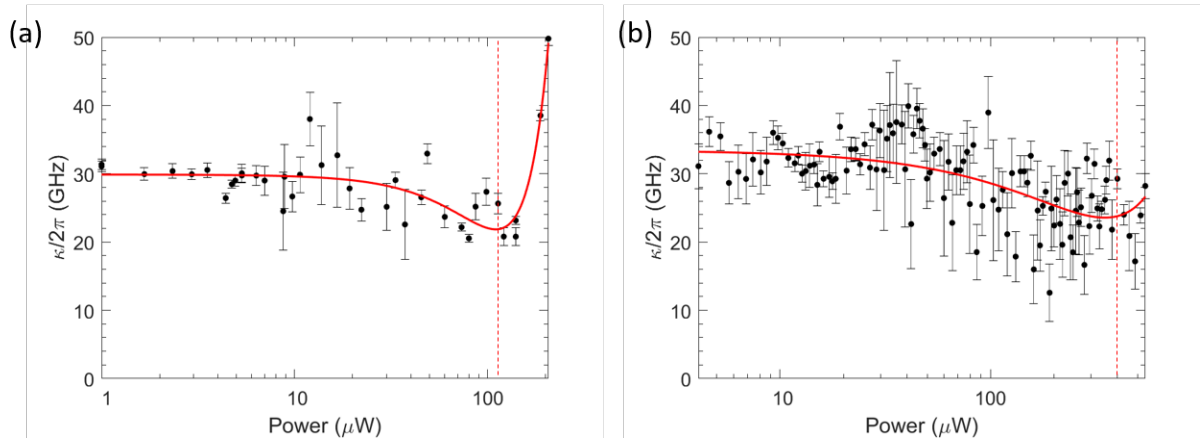

Figure 5.6: Minimum cavity mode linewidth, $\kappa/2\pi$, as a function of P_a for (a) Cavity-4 and (b) Cavity-b. The error bar indicates the standard error. The solid red line is a fitted curve to guide the eye. The dashed red line indicates $P_a = 120$ μW for Cavity-4 and 400 μW for Cavity-8.

The scattering rate, κ_s, i.e., loss, can be extracted from the linewidth and on-resonance transmission, T_r [149], such that

$$T_r = \left|1 - \frac{\kappa_s}{\kappa}\right|^2. \tag{5.2}$$

Figure 5.7(a) illustrates $\kappa_s/2\pi$ as a function of P_a for Cavity-4. Interestingly, $\kappa_s/2\pi$ dropped as $\kappa_s/2\pi$ increased, and even at higher annealing $P_a > 120$ μW. This indicates that the loss was not induced by scattering but by the cavity itself, i.e., an increase in the mirror separation length, L, so the heating effect was significant. Figure 5.7(b) shows

$\kappa_s/2\pi$ as a function of P_a for Cavity-8. Notice that the change in $\kappa_s/2\pi$ follows almost the same as the change in $\kappa/2\pi$, see Figure 5.6(b). Despite large fluctuations in the data points, as in the case of $\kappa/2\pi$, there is a tendency of a decrease in $\kappa_s/2\pi$. These findings suggest that laser annealing reduces the loss of the ONF cavities.

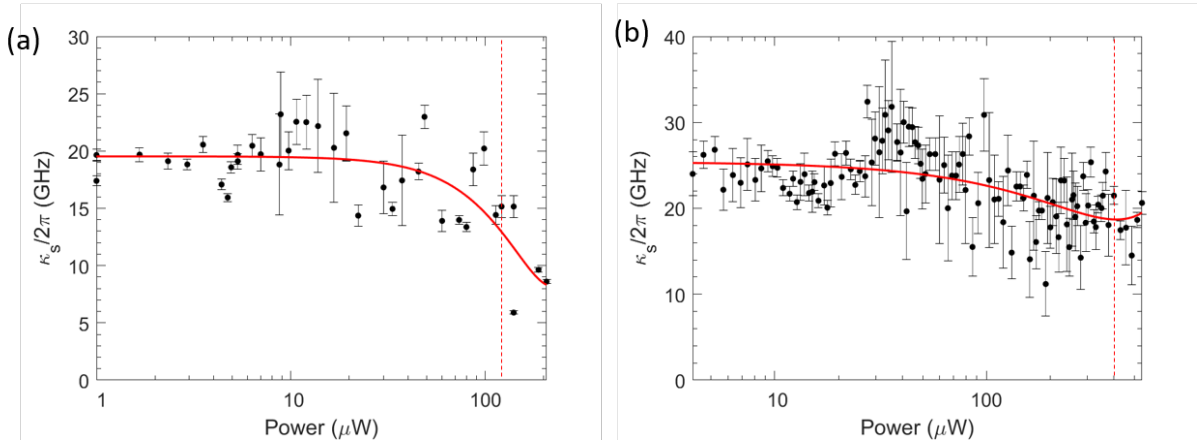

Figure 5.7: Minimum cavity mode loss, $\kappa_s/2\pi$, as a function of P_a for (a) Cavity-4 and (b) Cavity-b. The error bar indicates the standard error. The solid red line is a fitted curve to guide the eye. The dashed red line indicates $P_\mathrm{a} = 120$ μW for Cavity-4 and 400 μW for Cavity-8.

5.3.5 Effects on resonant wavelengths

We found that not only λ_B but also the resonant wavelengths of a cavity mode, λ_r, moved as P_a increased. Figure 5.8 shows the change of resonant wavelength of 14 modes of Cavity-4 as a function of P_a. The left-hand-side (LHS) panel is a section of the cavity spectrum at $P_\mathrm{a} = 1$ μW. The resonant wavelength of all of these 14 peaks shifted toward the red-detuned side, as shown in the right-hand-side (RHS) panel. λ_r did not significantly change at the low P_a, but started to shift to longer wavelengths from 5 μW. The red shift of λ_r can be explained by the Q-factor. As indicated by Equation 2.34, an increase in Q and $\kappa/2\pi$ results in an increase in λ_r. As we have established in Section 5.3.4, the general trend for $\kappa/2\pi$ is a reduction. Therefore, the movement of λ_r toward the longer wavelength is a signature of higher Q for these cavity modes.

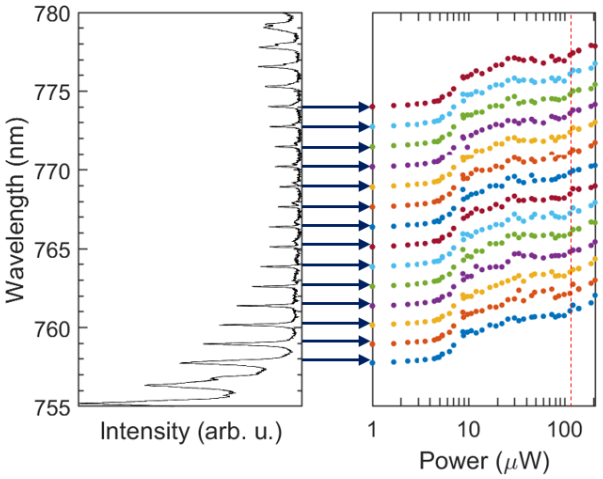

Figure 5.8: Change in λ_r as a function of P_a. The error bar indicates the standard error. The LHS shows a section of an ONF cavity spectrum of Cavity-4 taken at $P_a = 1$. Each corresponding mode was traced as P_a increased. The RHS shows λ_r shift for each mode.

5.3.6 Effects on FSR

Figure 5.10(a) shows the FSR as a function of P_a for Cavity-4. Measuring FSR values can give an insight into the cavity length over the course of the annealing experiments. Due to the dispersion effect, the FSR can vary at different wavelengths, so an FSR around 770 nm for each P_a was measured (indicated as white dots). FSR values stayed reasonably constant for the first few μW of P_a. However, after $P_a = 8$ μW, the FSR value started to fluctuate but also decreased as a general trend. The stopband edges were also dramatically shifting at $P_a = 8$ μW, see Figure 5.4(a). We also investigated the change in FSR as a function of the varying P_a by calculating the average and the standard deviation of FSR values from all the cavity mode peaks (indicated as black dots with error bars). Averaged FSR values started to exhibit larger errors at $P_a = 8$ μW, and the average FSR value very slightly lowered as P_a increased. Similar phenomena were also observed for Cavity-8. Figure 5.10(b) shows averaged FSR over a spectrum and their standard deviation as a function of P_a for Cavity-8. FSR values remained constant at the beginning of the annealing process, but they slowly decreased with larger error values at $P_a = 26$ μW, where the stopband edges rapidly shifted to the blue-side, see Figure 5.4(b). There were increases in FSR values locally around P_a ~300 μW, but sudden drops in FSR were observed after this P_a. In both cavities, the average FSR reduction of ~0.03 nm was observed at P_a = ~100 μW. From Equation 2.38, we can roughly estimate the elongation of L_{eff} to be about +6μm for P_a = ~100 μW. At $P_a = 279$ μW of Cavity-8, the FSR increased by ~0.02 nm, indicating the contraction of L_{eff} by about 4 μm.

As discussed in Section 4.5, L_{eff} increases as κ/π increases, see Figure 4.6(b). However, we found that κ/π is reduced for the annealed cavities as shown in Figures 5.6(a, b), thus, increases of the physical mirror separation length, L, seem to be significant for high P_a. Laser annealing heats up the fiber, resulting in an elongation of L. This would lead to reducing the FSR. On the other hand, Ga desorption can also happen by annealing. Removing Ga from the cavity mirror may redefine the nanostructures milled by the FIB

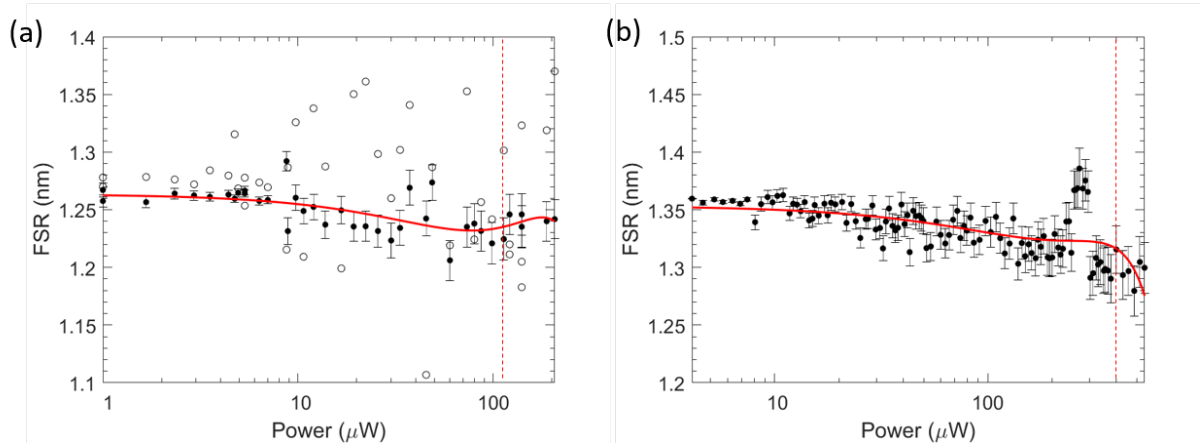

Figure 5.9: (a) FSR around 770 nm (white dots) and averaged FSR (black dots) with its standard deviation in a single spectrum as a function of P_a for Cavity-4. The error bar indicates the standard error. The dashed red line indicates P_a at 120 μW. (b) Averaged FSR (black dots) with its standard deviation in a single spectrum as a function of P_a for Cavity-8. The dashed red line indicates P_a at 4000 μW.

[167]. As a consequence, the mirror reflectivity can be increased and hence L_{eff} may be reduced, see Table 5.1. The fluctuations in the FSR values may be attributed to the effects of these two competing factors. Moreover, mode coupling may happen during the annealing process which results in a fluctuation of FSR values. This may be due to the elongation of the cavity length caused by the heating.

5.3.7 Effects on finesse

Finally, the maximum finesse, F, of the ONF cavity as a function of P_a was estimated. The averaged FSR values in Figures 5.9(a, b) were used to estimate F value for each P_a. See Figures 5.10(a) for Cavity-4. Initially, F was around 20, then it increased slowly up to around 30 till P_a = 120 μW. However, similar to many other results in this set of annealing experiments, it started to suddenly decrease after this P_a value. Figure 5.10(b) shows F as a function of P_a for Cavity-8. This cavity also initially had F ~20, but F increased slowly up to around 40 till P_a = 279μW. We can also see a decreasing trend of F after this P_a value. These outcomes may be due to collapsing nanostructural shapes, as Cavity-4 broke at P_a = 253 μW and Cavity-8 lost transmission at P_a = 544 μW.

The laser annealing increased F by a factor of about 1.6 at P_a = 80 μW for Cavity-4 and about 1.6 at P_a = 279 μW for Cavity-8 from pre-annealing under vacuum conditions. This was a reasonable improvement in F for the ONF cavity. See Figure 5.11(a) for such improvement of Cavity-4. The experimental F value was only ~0.5 lower than F_{min} before annealing. Just putting the cavity under vacuum increased F by about 120%, but laser annealing increased it even further, with the total increase to F being about 350%. There was about 6 μm increase in L_{eff} due to the heating effect, but $L_{eff} < L_{max}$, and one can clearly see $F > F_{min}$ for strong coupling. See Figure 5.11(b) for Cavity-8. This cavity was not suitable for strong coupling even before the annealing process as $L_{eff} < L_{max}$. Nevertheless, we can study how F changes for this cavity via laser annealing.

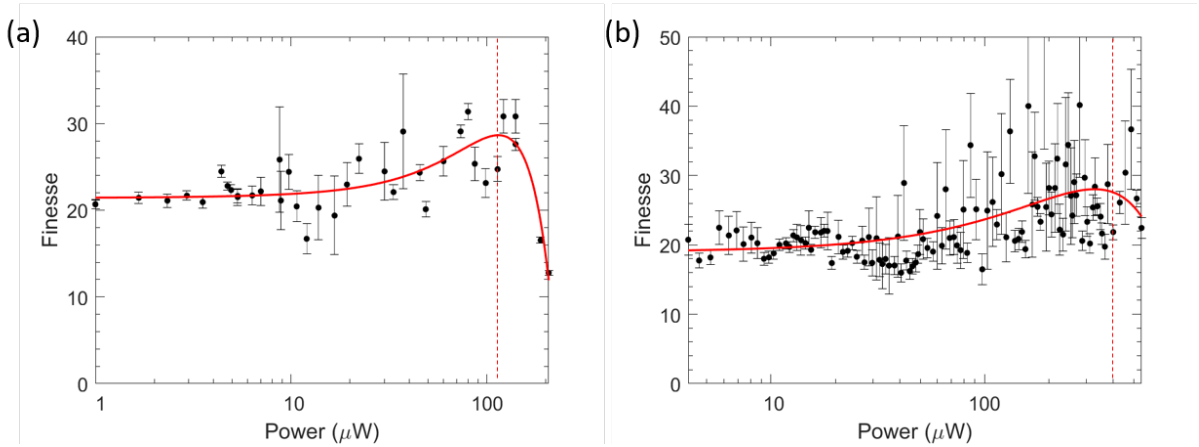

Figure 5.10: Maximum F as a function of P_a for (a) Cavity-4 and (b) Cavity-8. The error bar indicates the standard error. The dashed red line indicates P_a at 120 μW for Cavity-4 and 400 μW for cavity-8.

Putting it under vacuum did not significantly change F, but a nearly 60% increase of F was observed by the annealing, which would lead to stronger light-matter interactions, as the cooperativity, $\mathcal{C}$, increased by a factor of 1.6 as Equation 2.45 indicates.

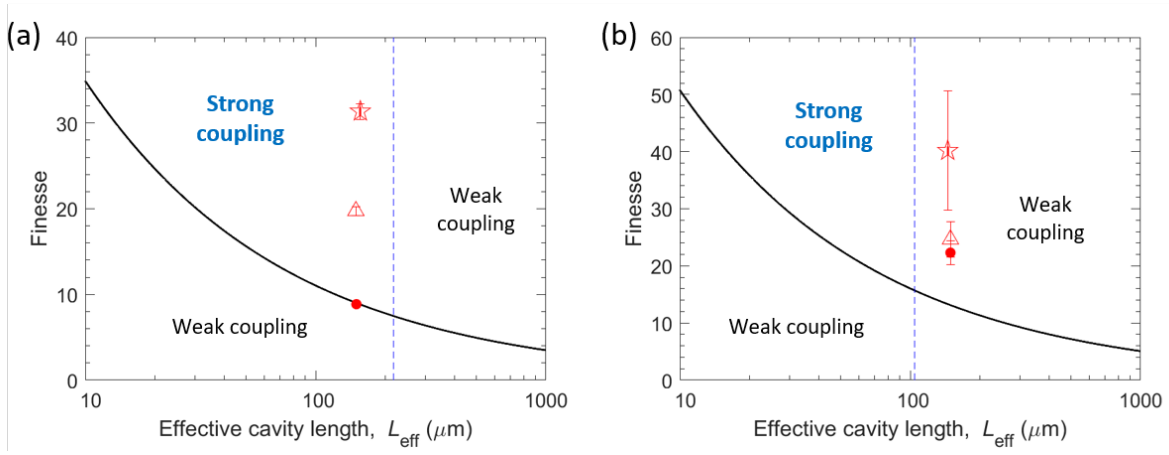

Figure 5.11: Relationship between the experimentally observed finesse, F, effective cavity length, L_{eff}, theoretically predicted minimum finesse, F_{min} (solid black line) and maximum effective cavity length, L_{max} (dashed blue line) of (a) Cavity-4 and (b) Cavity-8. The red dot indicates the experimentally determined value of F and L_{eff} with standard errors before annealing under ambient conditions. The white triangle indicates the F and L_{eff} with standard errors observed before annealing but after placing under vacuum at 1×10^{-4} mbar. The white star indicates the F and L_{eff} with standard errors observed at $P_a = 80$ μW for Cavity-4 and $P_a = 279$ μW for Cavity-8.

In this set of experiments, we observed heating effects when the critical P_a was 120 μW for Cavity-4 and 400 μW for Cavity-8. Ga ions on the surface of the ONF can be removed by annealing, but it would be quite challenging to remove Ga ions that are already implanted in the silica material of the ONF [167]. The implanted Ga may have accelerated

the heating effect. These critical P_{a} varied for different cavities. We also observed different phenomena after critical P_{a} in each cavity: Cavity-4 broke, but Cavity-8 lost its transmission before breaking. These findings imply that laser annealing needs to be stopped before the critical P_{a} is reached which is rather difficult since it is cavity-dependent. The variation in the critical P_{a} may be due to the presence/absence of dust particles and the amount of implanted Ga ions. Before performing the annealing procedure, it is advisable to estimate the necessary F for cQED experiments. Then, it is crucial to halt the annealing process once the desired F has been attained to prevent overheating and deterioration of the cavity quality.

5.4 Conclusion

Laser annealing of ONF cavities showed decreases in cavity mode linewidth, expanding the cavity stop bandwidth, and shifting λ_{B} to the blue-detuned side, up to a critical P_{a}. These findings are very likely to be a consequence of Ga desorption. However, the cavity mode resonance peak, λ_{r}, was shifted to the red-detuned side during the annealing process, which indicates increases in Q. FSR values showed a general trend of reduction over the course of annealing experiments, indicating that there were increases in L_{eff}. Mode coupling due to the laser annealing would have affected the FSR measurements. F increased as P_{a} increased up to the critical P_{a} and just before the critical P_{a} it surpassed F_{min} that would be needed to perform cQED with a single QD at a low-temperature, where the QD emission rate is low. These results indicate a significant opportunity to enhance the optical quality of ONF cavities through laser annealing prior to cQED experiments, noting the quality may degrade after the critical P_{a}. This can be avoidable by terminating the annealing process after obtaining the aimed F value at a relatively low P_{a}.

Moreover, there is potential for reducing the risk of cavity breakage while enhancing the optical qualities of cavities through alternative laser annealing approaches. For instance, using lower P_{a} for a longer duration or using a longer annealing laser wavelength may mitigate the risk of cavity breakage. Another strategy may involve applying the annealing laser not through the fiber but rather from free-space in a perpendicular orientation to the cavities. Such an approach has the potential to diminish the likelihood of cavity breakage attributed to dust particles on the sample, primarily addressing the efficient removal of deposited Ga solely from the ONF surface. Optimizing the specific techniques within the laser annealing process holds promise for further improving the optical qualities of Ga FIB-fabricated ONF cavities.

Furthermore, laser annealing may be useful for improving the optical quality of not only ONF cavities but also structured ONFs, such as slotted fibers [27–29], as well as hole-tailored fibers for enhancing emitter coupling [169]. The maximum P_{a} used in our experiments is an order of magnitude lower than the typical laser power required for cold atom trapping. This suggests that structured ONFs fabricated with the Ga FIB have limitations when used in experiments with laser-cooled atoms. In such cases, the He FIB may offer a more suitable option for constructing structured ONFs. However, it is important to note that the Ga FIB remains the most accessible tool for researchers. To mitigate heating effects resulting from implanted Ga, gas-assisted etching during FIB milling, combined with laser annealing, has the potential to reduce overall Ga contami-

nation. This reduction in the contamination may not only enable the use of the required laser power for cold atom trapping but also enhance the optical quality in the fabricated devices, benefiting applications such as cQED and beyond. Up to now in this thesis, we focused on the fundamental ONF cavity modes. In the next chapter, we will introduce HOMs in an ONF-based cavity.

Chapter 6

Higher-order mode Fabry-Pérot fiber cavity[1]

6.1 Introduction

Novel phenomena that can be revealed in non-paraxial light, such as transverse spin and spin-orbit coupling, have led to increasing interest in the tightly confined light observed in nano-optical devices [3]. Optical nanofibers, as discussed in detail in earlier chapters, are useful in this context because they provide very tight radial confinement of the electric field and facilitate diffraction-free propagation over several centimeters [40]. Most ONF research focuses on SM-ONFs that only support the fundamental mode, HE_{11}. In contrast, HOM-ONFs, fabricated from FM optical fiber, can guide HOMs (see more details in Section 1.2), such as TE_{01}, TM_{01}, HE^{e}_{21}, and HE^{o}_{21} [130]. In the weakly guided regime, which is generally used to describe light propagation in standard optical fiber, this group of modes can be viewed to form the LP_{11} mode. To date, there has been a lot more attention paid to HOM-ONFs in theoretical work [4, 109, 123, 125–128] than experimental work due to the difficulty in precisely controlling the fiber waist size and obtaining selective mode excitation at the waist [130, 134, 135].

In principle, there are many interesting phenomena that can be explored with a HOM-ONF. For example, it has been proposed that the relationship between SAM and OAM can be studied [4, 5, 108, 109]. Additionally, it was proposed that a HOM-ONF could be used to trap and manipulate cold atoms [121, 123, 124]. Fabrication of an ONF that supports the HOMs was achieved [38, 129, 130] and subsequently shown to more efficiently manipulate dielectric microbeads in the evanescent field than SM-ONFs [137, 234]. Other experimental work has shown that when cold atoms also interact with HOMs, detected signals are stronger than when one uses a SM-ONF only [138].

Introducing a cavity system to the ONF could further increase light-matter interactions due to cQED effects [1, 8, 9]. To date, numerous types of SM-ONF-based cavities have

[1]Sections 6.1-6.6, 6.9 in this chapter contain the following published work with permission from Chinese Laser Press: M. Maeda, J. Keloth, and S. Nic Chormaic, "Manipulation of polarization topology using a Fabry–Pérot fiber cavity with a higher-order mode optical nanofiber", Photon. Res. 11, 1029-1037 (2023) [171]. M. Maeda led all aspects of the work including the fabrication of the cavity, the construction of the optical setup, taking data, the development of MATLAB codes with J. Keloth, analysis of experimental results, simulation of results, and writing/editing the paper.

been proposed [149, 159, 168, 225, 235, 236] and the interactions of their resonance modes with various quantum emitters have been studied [156, 165, 237]. Strong light-atom coupling using SM-ONF-based Fabry-Pérot and ring resonators has already been achieved [10, 11]. Superstrong coupling of cold atoms and multiple longitudinal modes of a long fiber-ring resonator consisting of a SM-ONF section was demonstrated [153]. Utilizing multiple degenerate higher-order transverse modes in free-space has been shown to exhibit strong coupling [12, 139], further illustrating the importance of realizing a HOM-ONF-based cavity system at this point. The advantages are not only for enhanced interactions via cQED effects but also for a better overall understanding of the behavior of the modes in such a cavity.

Studying the behavior of the HOM-ONF cavity spectrum and the cavity mode profiles gives additional insight into the nature of the HOMs themselves, as well as how they interfere with each other and interact with the external environment. The generation of TE_{01} and TM_{01} modes in a laser cavity consisting of a microfiber directional coupler-based mode converter was demonstrated previously [140]. However, earlier attempts to realize a passive HOM optical microfiber cavity did not yield any resonant peaks in the cavity spectrum apart from the fundamental modes [141]; in other words, the typical donut- or lobe-shaped intensity profiles associated with HOMs were not observed, primarily due to challenges when engineering the taper profile to minimize losses at the taper transitions.

As discussed in Section 1.2.1, the inhomogeneous polarization structure of HOMs needs to be taken into account when studying a fiber cavity system with a HOM-ONF. In recent years, complex polarization distributions and the generation of polarization singularities have been investigated using various methods, giving rise to the relatively new field of singular optics [85]. Polarization singularities are a subset of Stokes singularities, i.e., phase singularity points in Stokes phases [103, 184]. In fact, higher-order fiber eigenmodes are vector optical fields with a polarization singularity called a V-point, where the SOP is undefined [85]. Other types of Stokes singularities can be formed in elliptical optical fields, such as the polarization singularity of C-points, where the polarization orientation is undefined [85, 184], and Poincaré vortices, where the polarization handedness is undefined [103, 185, 187]. Moreover, points of linear polarization can form continuous lines, which are classified as L-lines [85].

The generation of all Stokes singularities within a single beam has been demonstrated using a free-space interferometer [102, 103]. Modal interference in a birefringent crystal can facilitate the creation of polarization singularities [97, 98]. As a result, the SOP can significantly vary along the propagation length, with C-points and L-lines propagating as C-lines, i.e., continuous lines of circular polarization, and L-surfaces, i.e., surfaces of linear polarization, respectively [97–99]. Moreover, polarization singularities can appear, move or disappear from a given cross-sectional region with a smooth and continuous change of birefringence [100]. Birefringent media were used to create laser cavity modes containing a polarization singularity [238, 239]. These experiments were limited to the generation of low-order V-points due to a lack of control in the amplitude, phase, and SOP, all of which would be required to create other types of polarization singularities [85]. A FM optical fiber cavity has the potential to generate complex laser modes by its highly variable degree of birefringence.

Interference and birefringence are generally inseparable properties in fibers. The modal interference pattern in a fiber changes continually with a periodicity of 2π when the rela-

tive phase between modes is changed between 0 to 2π as the eigenmodes propagate along the fiber [240]. This effect was used in a FM optical fiber to generate ellipse fields containing a C-point [106, 107]. Due to the increasing complexities of modal interference in FM fibers, filtering for the desired set of HOMs, and selectively exciting them to generate and manipulate polarization singularities, are necessary. Realizing a fiber cavity containing an ONF should enable both spatial and frequency filtering for selective excitation of HOMs, as well as enhancement of the resonant mode coupling effect [166, 182].

In this chapter, we experimentally demonstrate a HOM-ONF-based Fabry-Pérot fiber cavity. The transverse polarization topology of any given resonant mode is determined by selecting modes from the cavity spectra and analyzing the images of the transmitted mode profile. We also demonstrate *in situ* intracavity manipulation of the modal birefringence to change the amplitude, frequency position, and the SOP of the modes. Moreover, the effects of the incident beam angle and polarization on the cavity modes were also examined. This work is a significant step toward gaining full control of the evanescent field at the HOM-ONF waist and extends the range of applications for which such nanodevices could be used.

6.2 Fabrication of Fabry-Pérot Fiber Cavity

For the HOMs described in Section 6.1 to propagate throughout the cavity, the tapered fiber must be low loss for the entire LP_{11} set of modes. Tapered fibers were drawn from SM1250 (9/80) fiber (Fibercore) using an O_2/H_2 flame pulling rig (see Figure 3.1(c)). The untapered fiber supports the LP_{01}, LP_{11}, LP_{21}, and LP_{02} modes at a wavelength, $\lambda = 776$ nm. The modes supported by the tapered fiber depend on the tapering profile and the waist diameter. The shape of the tapered fiber was chosen to be trilinear, see Figure 2.1(b), with angles of $\Omega_1 = 2$ mrad, $\Omega_2 = 0.5$ mrad and $\Omega_3 = 1$ mrad in order to be adiabatic for the LP_{01} and LP_{11} modes. As mentioned in Section 2.3, these tapering angles are the critical parameters for fabricating adiabatic ONFs. The ONF waist diameter was the only parameter studied here. Measured fiber diameters as a function of the set fiber diameter of trilinear-shaped ONFs are shown in Figure 6.1. The actual fiber diameters were significantly smaller than the set diameters. For set values of 800 nm, 1000 nm, 1200 nm, 1250 nm, 1300 nm, 1500 nm, and 1700 nm, the measured mean and standard deviation diameters from eight or nine samples were 503 nm±37 nm, 573 nm±94 nm, 708 nm±73 nm, 772 nm±67 nm, 839 nm±30 nm, 936 nm±112 nm, and 1185 nm±21 nm, respectively. Large errors were observed. This calibration plot provided a good guideline for getting the desired fiber diameter. The critical point in fabricating ONFs is that the ONF waist diameter does not go below the cutoff diameter size of the desired modes.

We fabricated three different tapered fibers with waist diameters of (i) ∼450 nm for SM behavior (HE_{11}^x and HE_{11}^y), (ii) ∼840 nm for the HOM-ONF, which supports HE_{11}^x, HE_{11}^y, TE_{01}, TM_{01}, HE_{21}^o, and HE_{21}^e (see Figure 2.3(a, b) to 2.7(a, b) for their mode profiles), and (iii) ∼1100 nm for the HOM-OMF, which supports all 12 modes in the LP_{01}, LP_{11}, LP_{21}, and LP_{02} families. Fiber transmission following the tapering process was >95% for the fundamental mode.

Four types of Fabry-Pérot fiber cavities were prepared: (i) a cavity with an SM-ONF, (ii) a cavity with a HOM-ONF, (iii) a cavity with a HOM-OMF, and (iv) a cavity without

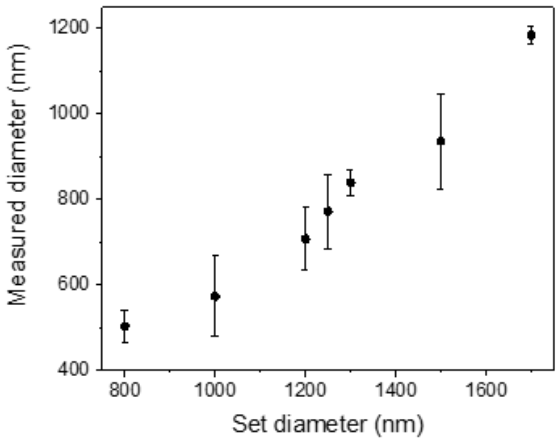

Figure 6.1: Measured diameters versus set fiber diameters for a trilinear-shaped ONF fabricated in the flame fiber-pulling rig (see Figure 3.1(a-b)), using an original fiber diameter $d_i = 80$ μm. Error bars indicate the standard deviation for eight or nine samples per set diameter.

tapered fiber. The cavities with an ONF or OMF were fabricated by splicing each pigtail of the tapered fiber to a commercial FBG mirror (Omega Optical). The two FBG mirrors consisted of stacked dielectric mirrors coated on the end faces of fiber patchcords (SM1250 (9/80), Fibercore) and had a reflectivity of 97% at $\lambda = 776$ nm. Both mirrors had almost the same reflectivity over all input polarization angles ($< 1\%$ variation, see Figure D.2(b)), details of which are described in Appendix D. A typical cavity length with an ONF was $\sim$2 m, which was physically measured and estimated from the cavity free-spectral range (FSR). The fiber cavity without an ONF had a length of $\sim$1 m.

6.3 Methods

6.3.1 Experiments with an ONF

A sketch of the experimental setup for a cavity with an ONF is given in Figure 6.2(a). The cavity contained an in-line polarization controller (IPC), (see Figure6.2(a)) to manipulate the birefringence inside the cavity. Moving the angles of the IPC induced stress and strain in the fiber, thereby changing the effective cavity length. A linearly polarized Gaussian beam from a laser at $\lambda = 776$ nm (Toptica DL100 pro) was launched into the fiber cavity. The laser frequency was either scanned or locked to a mode of interest using a Pound-Drever-Hall locking module (Toptica Digilock110). The cavity output beam was split into three paths: one for the laser feedback controller to observe the cavity spectra and to lock to specific modes, one for imaging the spatial profile of the modes with a CCD camera, and one for analyzing the transverse SOP of each mode using a removable quarter wave plate (QWP), a rotating linear polarizer, and a CCD camera, see Figure 6.2(b). Six intensity profile images were taken in total for each mode. Four images were taken without the QWP and with the linear polarizer angle set to 0° (I_{H}), 45° (I_{D}), 90° (I_{V}), and 135°

(I_A), and two images were taken by inserting the QWP set to 90° while the polarizer was set to 45° (I_R) and 135° (I_L). The SOPs were determined by analyzing the six profile images using Stokes polarimetry. Furthermore, the Stokes phase and Stokes index were determined [85], see Section 2.5.2.

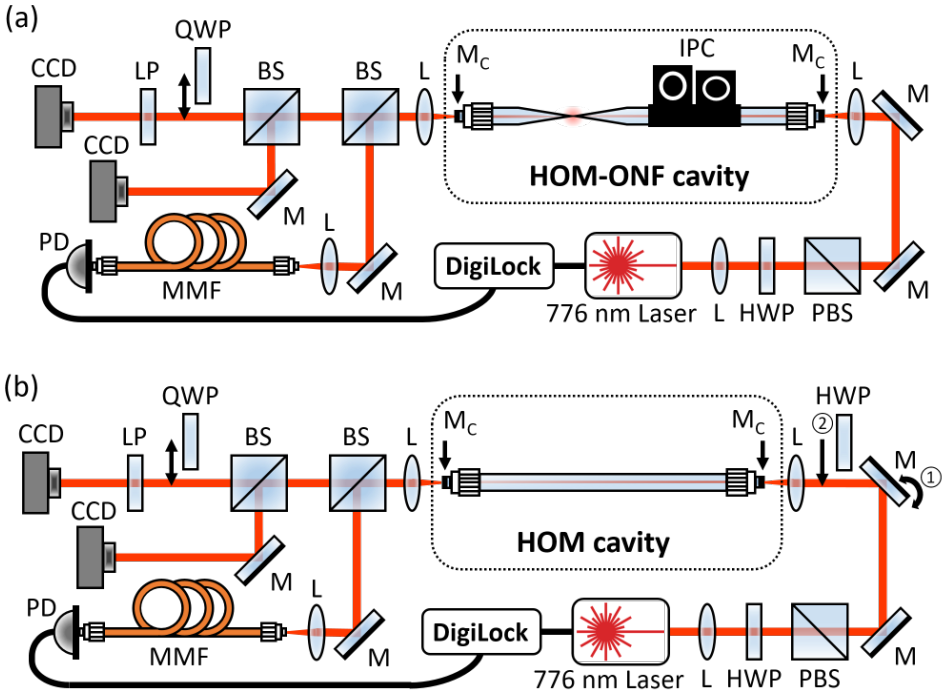

Figure 6.2: (a) Schematic of experimental setup with a tapered fiber. L: lens, HWP: half-wave plate, PBS: polarizing beam splitter, M: mirror, M_C: cavity mirror, IPC: in-line polarization controller, BS: beam splitter, QWP: quarter-wave plate, which was inserted to calculate S_3, LP: linear polarizer, CCD: camera, MMF: multimode fiber, PD: photodiode. (b) Schematic of experimental setup without tapered fiber with two experimental conditions: ① varying incident beam angle by changing mirror angles, and ② varying indecent beam polarization by changing HWP angle.

6.3.2 Experiments without an ONF

The experimental setup for the cavity without a tapered fiber is shown in Figure 6.2(b). The IPC was not used in these experiments, and the fiber was straightened and fixed on a metal plate with Kapton tape to minimize movement. Note that this cavity is composed of standard FM fiber, which supports LP_{01}, LP_{11}, LP_{21}, and LP_{02} modes (see Figure 2.2(a)) in the weakly guiding approximation as described in Section 2.1. LP mode representations are commonly used to describe a standard fiber system due to the near degenerate effective indices of exact eigenmodes within the LP family. Exact eigenmodes in this fiber are HE_{11}, TE_{01}, TM_{01}, HE_{21}, EH_{11}, HE_{31}, and HE_{12} as shown in Figure 2.2(b), and each hybrid mode has two orthogonal polarizations, resulting in the total number of supported modes to be 12. In general, the cavity modes are generated depending on a complex mixture of variables such as cavity length, birefringence, and mode coupling; hence, it is extremely

difficult or perhaps impossible to generate cavity modes with a specific polarization of a specific mode. Nevertheless, minimizing potential perturbation by straightening the fiber cavity can reduce the supported number of modes, and the resonance cavity peaks are only discernible when the cavity finesse is sufficiently high [241].

In the experiments without ONF, the cavity input beam was a linearly polarized Gaussian beam and the cavity was studied by: (i) changing the incident beam angle to the fiber cavity and (ii) changing the incident beam polarization.

First, we set the cavity input polarization horizontal direction and varied the fiber launching angle by changing the angles of the nearest mirror, numbered as ① in Figure 6.2(b). Changing the incident beam angles changed the coupling efficiency to the fiber cavity, hence the transmitted intensity of cavity modes. The fiber launching angle was adjusted to obtain maximum coupling (MAX), high coupling (HIGH), low coupling (LOW), and minimum coupling (MIN). We recorded cavity spectra for each fiber launching angle as the laser frequency was scanned. Each cavity mode was locked and a total of six intensity profile images were taken: I_{H}, I_{D}, I_{V}, I_{A}, I_{R}, and I_{L}, as we did in Section 6.3.1. The intensity profile and SOPs of each cavity mode were analyzed as described in Section 2.5.

Second, we set the angle of the mirror just before the cavity input to be constant, and the polarization of the cavity input free-space beam was modified by inserting an HWP just before the fiber launching, denoted as ② in Figure 6.2(b). The HWP angles were changed by 22.5°, which induces 45° rotations of linear polarization, up to 90°. Four different spectra were taken as the laser frequency was scanned for a polarization of H, D, V, and A. Each excited cavity mode was locked and the intensity profiles of I_{H}, I_{D}, I_{V}, I_{A}, I_{R}, and I_{L} were taken. These images were processed using Stokes polarimetry methods, see Section 2.5, to determine the SOPs and Stokes singularities.

6.4 Cavity with a SM-ONF

As an initial experimental test, the spectrum for a HOM cavity consisting an ONF of waist diameter ∼450 nm was obtained, see Figure 6.3(a). This ONF can only support the fundamental modes for $\lambda = 776$ nm, see Figure 2.2(b). The IPC paddle angles were set so that two distinct, well-separated modes, Mode 1 and Mode 2, with minimal spectral overlap were observed. The finesses of Modes 1 and 2 in Figure 6.3(a) were calculated to be 12 and 15, respectively, using Equation 2.32. The laser was locked to each of these two cavity modes consecutively and the mode profiles were observed at the output end face of the fiber cavity. The corresponding mode intensity profiles, SOPs, and Stokes phases are shown in Figures 6.3(b)(i, ii). The intensity profiles for both Modes 1 and 2 were slightly skewed Gaussian shapes. The HE_{11} eigenmode intensity shape is Gaussian, so the slight deviation from the expected shape may be attributed to aberrations in the optical beam path. In terms of polarization distribution, the Stokes phases of Modes 1 and 2 were uniform; in other words, their SOPs were scalar fields, regardless of the IPC paddle angles chosen, as expected for the HE_{11} mode.

Although the pretapered FM fiber supported the full set of eigenmodes in LP_{11}, LP_{02}, and LP_{21}, when the ONF with a diameter ∼450 nm was inserted between the two sets of mirrors, only one or two modes with quasi-Gaussian profiles were observed, no matter

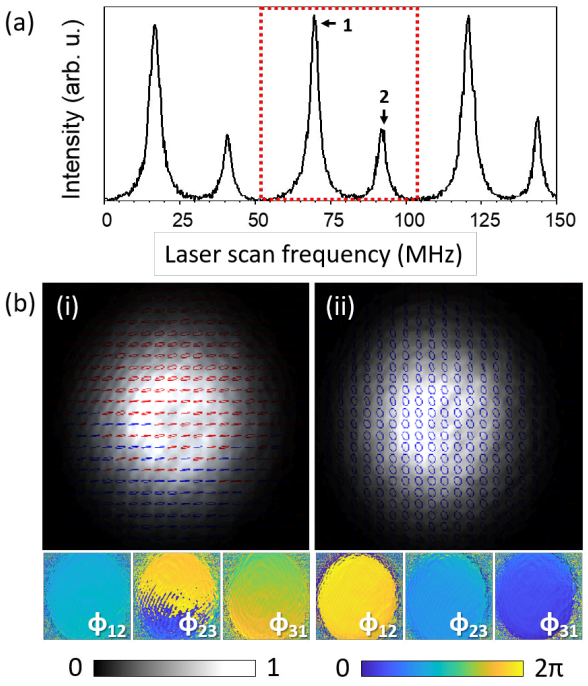

Figure 6.3: (a) A typical spectrum for a HOM cavity with a SM-ONF as the laser is scanned over 150 MHz. The spectrum over a single FSR is indicated by the red box. (b) Mode intensity profiles showing the SOPs (top) and corresponding Stokes phases (bottom) for (i) Mode 1 and (ii) Mode 2. The red and blue SOPs indicate right-handed and left-handed ellipticities, respectively. The scale bars show the normalized intensity (from 0 to 1) and the Stokes phase (from 0 to 2π).

which IPC paddle angles were chosen. The HOMs were filtered out due to the tapered fiber waist being SM, analogous to an intracavity pinhole spatial filter. Mode filtering as a function of the ONF waist diameter was observed experimentally [129]. However, here, we could additionally observe the mode filtering effect on the cavity spectrum and SOP of each mode.

In an ideal SM-ONF cavity with no birefringence, there are two degenerate orthogonal modes. However, due to random birefringence of the fiber and the cavity mirrors, the two modes become non-degenerate, i.e., separated in frequency [242]. Mode coupling of orthogonal modes can occur in a birefringent medium and this effect can increase in a cavity configuration [243]. Mode coupling in an ONF cavity due to asymmetrical mirrors has been discussed previously [166] and experimental evidence of mode coupling due to intrinsic birefringence in a SM-ONF cavity has already been reported [182]. In our experiments, non-orthogonal combinations of SOPs were observed, as seen in Figures 6.3(b)(i, ii). Mode 1 was horizontally polarized (red/blue lines in Figure 6.3(b)(i)), while Mode 2 was left elliptically polarized (blue ellipse in Figure 6.3(b)(ii)). By adjusting the IPC angles, it was possible to change the phase relationship and coupling between the HE_{11}^{o} and HE_{11}^{e} modes, and shift between orthogonal and non-orthogonal combinations of SOPs.

6.5 Cavity with a HOM-ONF

Next, the spectrum for a HOM cavity containing an ONF of waist diameter ∼840 nm was obtained, see Figure 6.4(a). This ONF can support the HE_{11}, TE_{01}, TM_{01}, HE^{o}_{21}, and HE^{e}_{21} modes at $\lambda = 776$ nm. The IPC paddle angles were set to obtain the maximum number of well-resolved modes in a single FSR, see Figure 6.4(a). One can clearly see five distinct peaks indicating that the HOM-ONF does not degrade the modes in the cavity and the finesses of the cavity modes are high enough to resolve them. The finesses of Modes 1 to 5 were 12, 16, 13, 22, and 13, respectively. The mode finesse values of the cavity with a HOM-ONF were in the same range as those for the cavity with a SM-ONF (Figure 6.3(a)), implying that the HOM-ONF was adiabatic for the LP_{11} group of modes. The laser was locked to each of the cavity modes consecutively and the mode profiles were observed at the output of the fiber cavity. The corresponding mode intensity profiles, SOPs, and Stokes phases are shown in Figures 6.4(b)(i-iv). In the spectrum shown in Figure 6.4(a), there were five distinctive modes, but locking to Mode 3 was not possible because of its close proximity to the dominant Mode 4.

Two flat-top intensity profiles were observed in Modes 1 and 4, Figures 6.4(b)(i, iii) respectively. The SOPs of these modes are markedly different to those for the Gaussian-type modes in Figures 6.3(b)(i, ii), which have simple scalar SOPs. Modes 1 and 4 were inhomogeneously polarized ellipse fields, showing regions of left and right circular polarizations divided by an L-line (Figures 6.4(b)(i, iii)). The center of these two modes exhibited diagonal and anti-diagonal polarizations, respectively, i.e., the SOPs at the center of the modes were orthogonal to each other. Going toward the edges of the modes, the polarization changes from linear to circular, with opposite handedness either side of the L-lines. Notice also in Figure 6.4(a) that Modes 1 and 4 are not well frequency separated from neighboring modes. This suggests that the mode profiles and SOPs of these modes were not only affected by birefringence and degenerate modal interference (might not be exactly degenerate, but not enough finesse to separate the resonance), but also some non-degenerate modal interference with neighboring cavity modes [243]. Additionally, for Mode 4, we identified two C-points ($\sigma_{12} = -1$), indicated by the pink dots in Figure 6.4(b)(iii), where the value of ϕ_{12} changed by 2π (see Table 2.2). Interference of HE_{11} with modes from the LP_{11} group can generate C-points in a FM fiber [107], see Figure 2.10(d).

We performed basic simulations to determine if combinations of HE_{11} and some mode(s) in the LP_{11} family could generate similar mode profiles and SOP structures as those in Figures 6.4(b)(i, iii). The simulated results are shown in Figures 6.4(c)(i, iii). The HE_{11} and TM_{01} modes were selected as possible contributors and their amplitudes, phase, and birefringence fitting parameters were tuned to match the experimental results. Modes 1 and 4, see Figures 6.4(b)(i, iii), could have been formed from different mode combinations rather than our assumed HE_{11} and TM_{01}; however, these modes were very likely formed by interference between HE_{11} and some mode(s) of the LP_{11} group, resulting in their inhomogeneous SOPs and flat-top shapes.

We also observed two distorted lobe-shaped modes, Modes 2 and 5, see Figures 6.4(b)(ii, iv). The lobe-shaped pattern also arises from modal interference between modes in the LP_{11} family [as an example, see Figure 2.10(c)). With reference to Table 2.2, Mode 2, Figure 6.4(b)(ii), showed all three types of Stokes singularities, indicated by pink dots

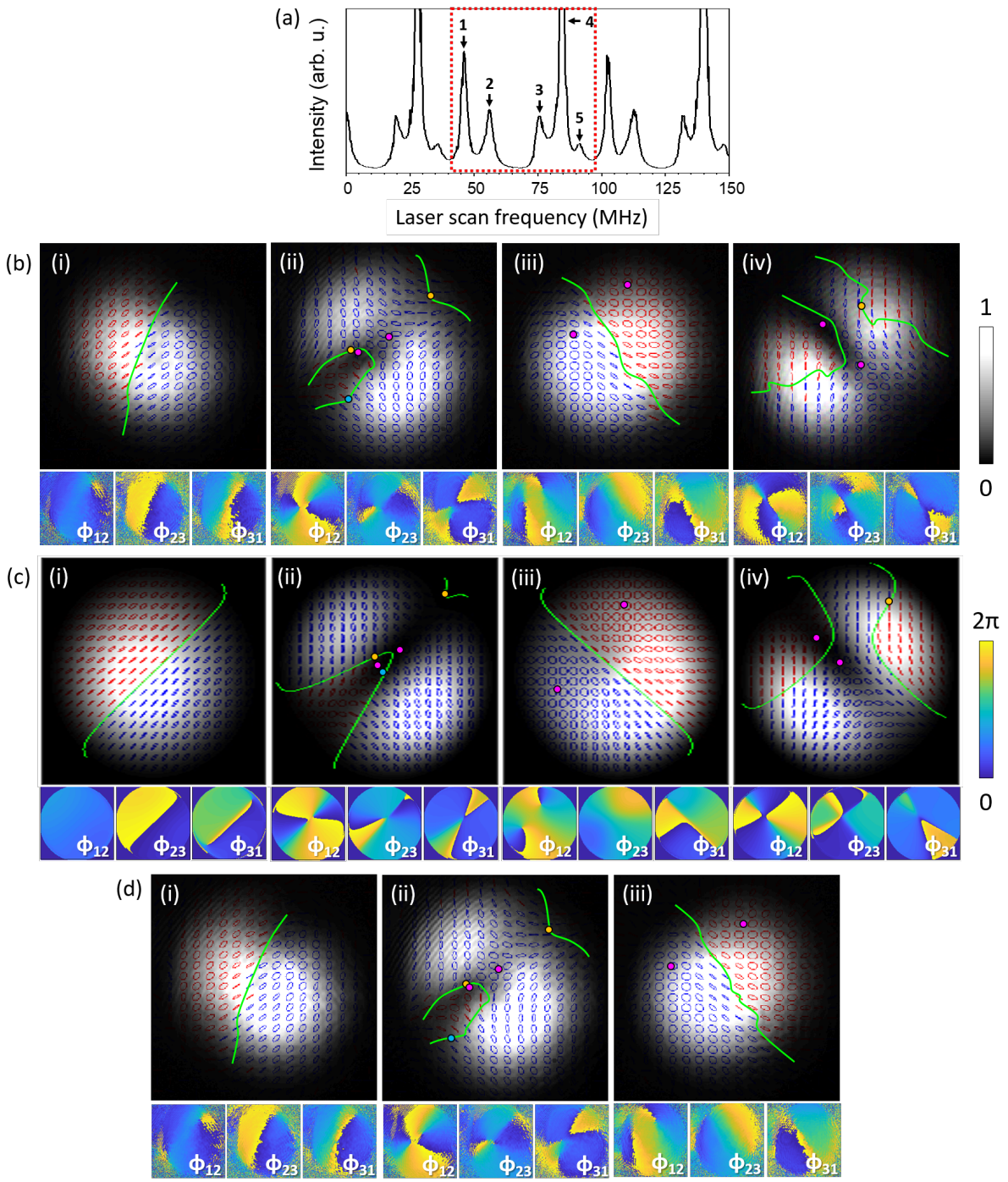

Figure 6.4: (a) A typical spectrum for a cavity with a HOM-ONF as the laser is scanned over 150 MHz. The spectrum over a single FSR is indicated by the red box. (b) Mode intensity profiles showing the SOP (top) and the corresponding Stokes phases (bottom) for (i) Mode 1, (ii) Mode 2, (iii) Mode 4, and (iv) Mode 5. The red and blue SOPs indicate right-handed and left-handed ellipticities, respectively. The scale bars show the normalized intensity (from 0 to 1) and the Stokes phase (from 0 to 2π). Stokes singularity points of σ_{12}, σ_{23}, and σ_{31} are indicated as pink, orange, and blue dots, respectively. L-lines are indicated in green. (c) Corresponding simulated results. (d) Spatial field profiles 54 min after the measurements of (b) for (i) Mode 1, (ii) Mode 2, and (iii) Mode 4.

for C-points ($\sigma_{12} = +1$) and orange/blue dots for Poincaré vortices ($\sigma_{23} = -1$ /$\sigma_{31} = +1$), as presented in ϕ_{12}, ϕ_{23}, and ϕ_{31}, respectively. A single mode containing all Stokes singularities has been demonstrated using free-space interferometers [102, 103]; here, we generated them within a single mode using a fiber cavity system. Mode 5, Figure 6.4(b)(iv), also had two C-points ($\sigma_{12} = +1$) and a Poincaré vortex ($\sigma_{23} = +1$), as seen in ϕ_{12}, and ϕ_{23}, respectively. Figure 6.4(a) shows that Modes 2 and 5 are not well frequency separated from Modes 1 and 4, respectively. Therefore, there is a likely contribution from the HE_{11} mode resulting in distortion of the lobe shape.

To simulate Mode 2 in Figure 6.4(b)(ii), we combined TE_{01}, HE^{e}_{21}, and HE_{11}, and to simulate Mode 5 in Figure 6.4(b)(iv), we used TM_{01}, HE^{e}_{21}, and HE_{11}. The amplitude of each mode, phase shift, and birefringence parameters were adjusted to achieve a close fit. The simulated results are shown in Figures 6.4(c)(ii, iv). These plots are not exact replications of the experimental results since the parameter space is large and the exact initial conditions are not known; nevertheless, the match is reasonably close.

Interestingly, many of the cavity modes obtained in different sets of spectra, which were generated using different IPC angles, exhibited Stokes singularities. Polarization singularities are known to propagate through a birefringent medium as C-lines and L-surfaces and their evolution is affected by the homogeneity of the birefringence along the propagation path [97–99]. This phenomenon is due to the conservation of the topological charge [86, 99, 101], and the Stokes index value, σ_{ij}, remains constant [86]. However, our cavity is an inhomogeneous birefringent medium as it contains a number of different birefringent elements such as the FBG mirrors and the IPC, as such, the degree of birefringence varies along the propagation direction. Therefore, the presence of Stokes singularities in the imaged field at the cavity output does not necessarily guarantee the existence of such topological defects in the ONF region. Nonetheless, singularity points can enter, move, and exit with a smooth and continuous variation of birefringence [100]. Therefore, the SOP is expected to evolve along the length of the cavity, with singularity points shifting and making numerous entries and exits in the cross-section profile of the modes. However, since the ONF waist is relatively straight and uniform, the birefringence variation at the waist should be minimal [244] and topological features appearing at the start of the waist should be preserved every 2π along the waist. It is also important to note that the strong confinement at the waist induces a large longitudinal electric field component that should perturb the local polarization and intensity patterns [4]. As a result, the spatial mode profiles that were observed in the experiments may not be identical to the spatial mode profiles at the waist. Indeed, this has already been experimentally demonstrated for tightly focused free-space C-points as Möbius [114, 115] and ribbon strips [116], as well as pure transverse spin [115]. To date, none of these unique non-paraxial phenomena have been observed in the evanescent fields of ONFs. Our cavity has great potential to experimentally uncover such phenomena in this regime.

Theoretically, the HOM-ONF can support a total of six eigenmodes as mentioned earlier. Therefore, one might expect that the spectrum should show six distinct modes. However, we typically observed three to five distinct peaks in a single FSR depending on the IPC paddle angles. This could be explained by the lack of sufficient finesse to resolve all modes, some of which are closely overlapped [243]. It may be feasible to increase the mode finesses by increasing the mirror reflectivity and using an ONF with lower transmission loss than the one used (the estimated loss of Mode 4, the highest finesse in

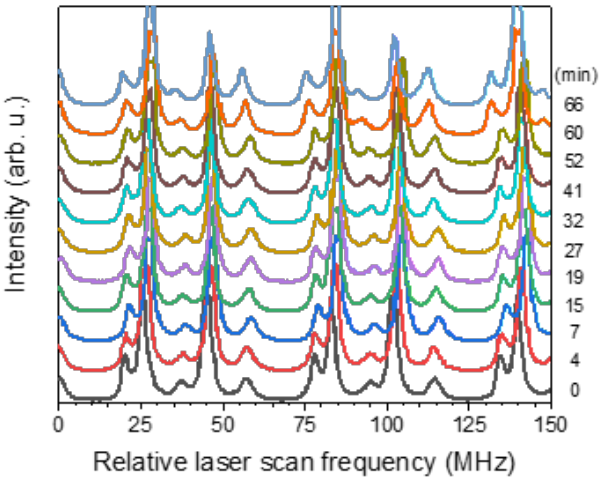

Figure 6.5: Spectra of the normalized transmitted intensity of an HOM-ONF-based cavity at different times. The first cavity spectrum was taken at 0 min, then spectra were recorded at 4 min (red), 7 min (blue), 15 min (green), 19 min (purple), 27 min (beige), 32 min (cyan), 41 min (brown), 52 min (khaki), 60 min (orange), and 66 min (light blue). The baseline of intensity was equally shifted upwards for each spectrum to better observe the mode shapes.

Figure 6.4(a), was ∼20%). Nonetheless, the finesse values of our ∼2 m long cavity with a HOM-ONF should be sufficient for cQED experiments with narrow line-width emitters such as cold atoms.

It is also important to investigate the mode stability over time for performing cQED experiments or other potential applications using the HOM-ONF cavity modes. We monitored cavity spectra over 66 min with an interval of 3-11 min. Figure 6.5 shows a total of 11 spectra over the 150 MHz laser scan frequency range. Slight changes in the frequency positions and peak heights of cavity modes were observed at different times. However, these changes in the frequency and the intensity are very likely due to the thermal effect. The heating effect constantly shifted the absolute frequency in both directions (blue side and red side). Such thermal effects could affect the cavity length change, which may result in a change of FRS, thereby a change of mode frequency. The change in FSR due to the thermal effect can also affect mode coupling, which may lead to a change in mode intensity.

Interestingly, the mode shapes remained almost constant over 66 min of measurements and, importantly, the polarization topology of these modes hardly changed. Figures 6.4(d)(i-iii) illustrate mode profiles and polarization as well as Stokes phases of Mode 1, Mode 2, and Mode 4 54 min after the measurements of Figures 6.4(b)(i-iii). Mode 5 was not locked at this time due to the thermal cavity mode drift, relatively small intensity, and close proximity to the next adjacent mode. As one can clearly see, intensity profiles, polarizations, and positions of Stokes singularity points/lines hardly differ from the original measurements. These results imply that the mode coupling due to the thermal effect is negligible. This indicates that the HOM cavity with an FM fiber is stable enough

for about one hour to perform experiments. One hour may be sufficient for experiments such as cQED involving cold atoms.

6.6 *In Situ* Cavity Mode Tuning

A key feature of this setup is the ability to tune the spectrum and SOP to create the desired mode in the cavity. We aimed to observe modes with donut-shaped intensity patterns and SOPs similar to the fiber eigenmodes TE_{01} (Figure 2.10(a)), TM_{01}, HE^{o}_{21}, and HE^{e}_{21} (Figure 2.10(b)). To achieve this, the laser was locked to a well-resolved lobe-shaped mode. The paddle angles of the IPC were then adjusted, and the mode shape was monitored with a CCD camera until a donut mode profile was observed. Unlocking and scanning the laser revealed a new spectrum with each mode containing a new profile. The IPC was adjusted again to maximize another mode and the laser was locked to this new mode. The IPC paddle angles were tuned to once more convert the mode profile to a donut shape. This procedure was repeated for four different modes, see Figures 6.6(a)(i-iv), and these modes look similar to the true fiber eigenmodes of HE^{e}_{11} (Figure 2.10(b)), HE^{o}_{11}, TE_{01} (Figure 2.10(a)), and TM_{01}, respectively. There was a slight deformation from a perfect donut shape and their SOPs were not vector fields, but rather ellipse fields with alternating regions of opposite handiness. While the donut eigenmodes possessed a V-point at the center as indicated by pink dots in Figures 2.10(a, b), the observed quasi-donut modes in Figures 6.6(a)(i-iv) had some nominal intensity at the center. These modes had two C-points of $\sigma_{12} = -1$ or $+1$ near the center (see pink dots in Figures 6.6 (a)(i-iv)), as opposed to a single point of $\sigma_{12} = -2$ or $+2$ in the true eigenmodes (Figures 2.10(a, b)). Indeed, perturbation of vector field polarization singularities can occur when scalar linearly polarized beams are interfered [104].

These donut-shaped cavity modes were also simulated, as shown in Figures 6.6(b)(i-iv). To obtain a good fit for the experimentally observed intensities, SOPs, and Stokes phases in Figures 6.6(a)(i-iv), the simulated modes included a slight deformation of the donut shape by adding some components of the HE_{11} mode to modes in the LP_{11} group. Moreover, the simulated results show that the Stokes phases are very similar to those obtained experimentally. The number of possible combinations of modal interference with varying birefringence is large and this leads to discrepancies between the experiment and simulation. However, these findings indicate that the experimentally observed quasi-donut modes are likely the result of residual interference between the HE_{11} mode and modes in the LP_{11} group. Degeneracy of multiple modes may be avoided by increasing the cavity mode finesses so that each mode can be well separated. The system demonstrated here shows that, even in a complex system, the HOMs and their SOPs can be controlled to create exotic topological states.

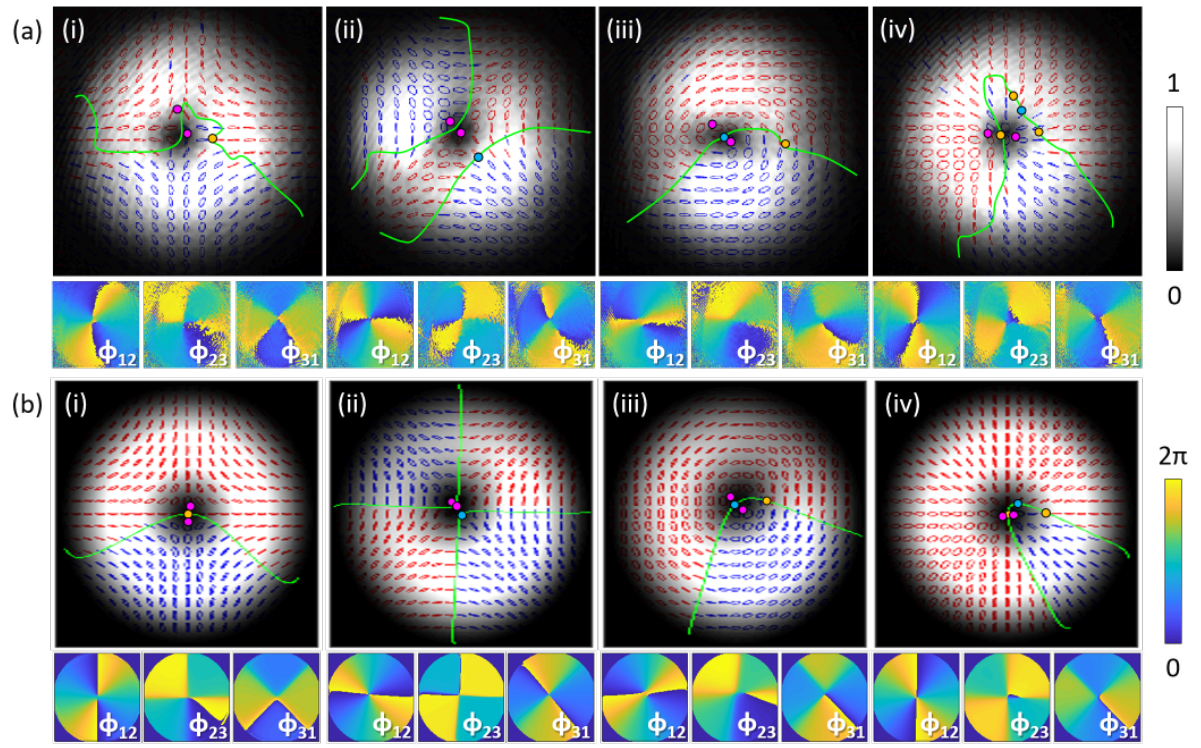

Figure 6.6: (a) Mode intensity profiles for quasi-donut-shaped cavity modes from the cavity containing a HOM-ONF with their SOPs (top) and Stokes phases (bottom) similar to the fiber eigenmodes of (i) HE^{e}_{21}, (ii) HE^{o}_{21}, (iii) TE_{01}, and (iv) TM_{01}. The red and blue SOPs indicate right-handed and left-handed ellipticities, respectively. Scale bars show intensity (from 0 to 1) and Stokes phase (from 0 to 2π). Stokes singularities of σ_{12}, σ_{23}, and σ_{31} are indicated as pink, orange, and blue dots, respectively. L-lines are illustrated as green lines. (b) Corresponding simulated results.

6.7 Cavity with a HOM-OMF

We also investigated a cavity with a HOM-OMF, where the waist diameter was ∼1100 nm. A typical cavity spectrum is presented in Figure 6.7(a). The IPC paddle was adjusted to observe the maximum number of transverse cavity modes. Depending on the IPC paddle angles, there were four to six modes in a single FSR region of a spectrum. The waist diameter of ∼1100 nm indicates the total number of supported guided modes to be 12: HE^{x}_{11}, HE^{y}_{11}, TE_{01}, TM_{01}, HE^{o}_{21}, HE^{e}_{21}, EH^{o}_{11}, EH^{e}_{11}, HE^{o}_{31}, HE^{e}_{31}, HE^{o}_{12}, and HE^{e}_{12}. However, modes in the LP_{21} and LP_{02} families (EH^{o}_{11}, EH^{e}_{11}, HE^{o}_{31}, HE^{e}_{31}, HE^{o}_{12}, and HE^{e}_{12}) were lossy due to the tapering angles, which were chosen to be adiabatic only for modes in the LP_{01} and LP_{11} families (HE^{x}_{11}, HE^{y}_{11}, TE_{01}, TM_{01}, HE^{o}_{21}, HE^{e}_{21}). The tapered angles were more acute than the critical angles for these modes (see Figure D.4). Nevertheless, we observe a maximum of six peaks, as shown in Figure 6.7(a), and this is more than the maximum number of peaks observed in the spectra of the HOM-ONF-based cavity. Note that Mode 4 is not well resolved due to the close frequency to the adjacent Mode 5. The finesse values of Mode 1, Mode 2, Mode 3, Mode 5, and Mode 6 were 15, 17, 18, 20, and 14, respectively. These values are similar to the finesse values of the cavities with a

SM-ONF and a HOM-ONF. However, unlike these ONF-based cavities, the spectra of this OMF-based cavity showed non-zero intensity at the dips of peaks. These findings indicate that some mode(s) with low finesse may overlap with the other well-resolved peaks. Non-adiabatic eigenmodes may still exist as a lossy cavity resonance mode, therefore, modes in the LP_{21} and LP_{02} families might have existed as modes with a broad linewidth.

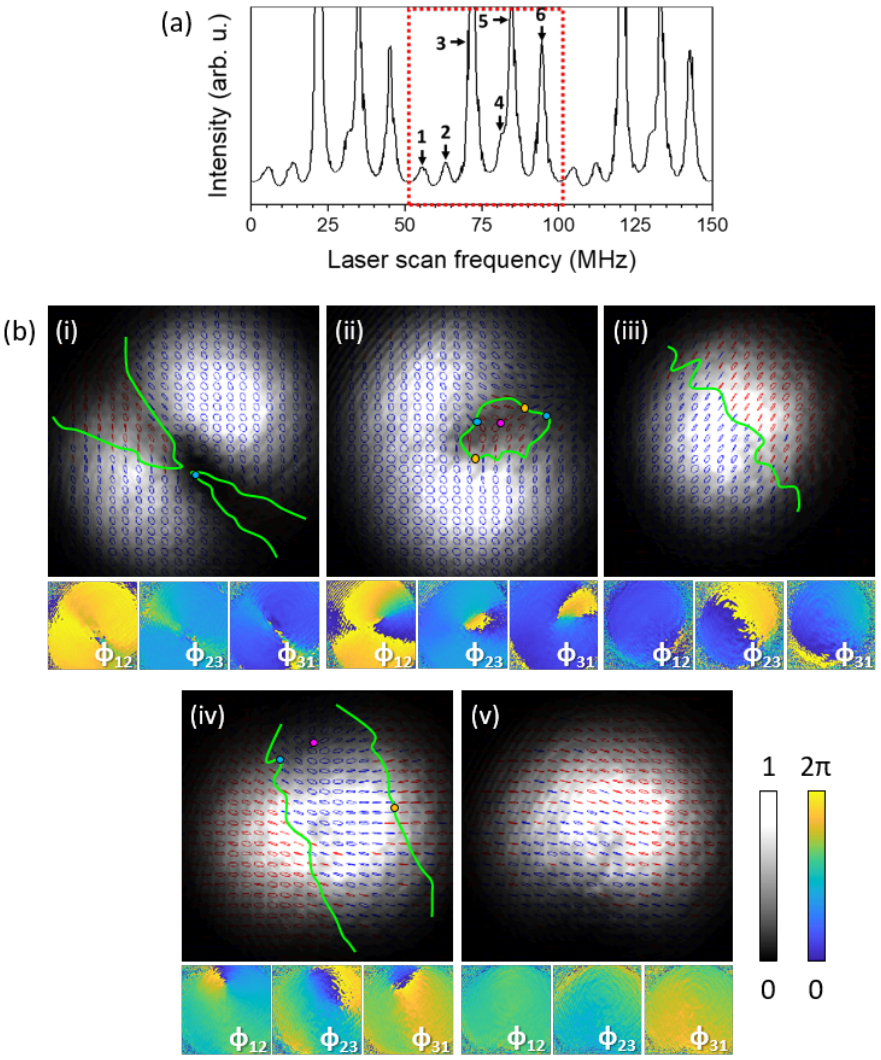

Figure 6.7: (a) A typical spectrum for a cavity with an HOM-OMF as the laser is scanned over 150 MHz. The spectrum over a single FSR is indicated by the red box. (b) Mode intensity profiles showing the SOP (top) and the corresponding Stokes phases (bottom) for (i) Mode 1, (ii) Mode 2, (iii) Mode 3, (iv) Mode 5, and (v) Mode 6. The red and blue SOPs indicate right-handed and left-handed ellipticities, respectively. The scale bars show the normalized intensity (from 0 to 1) and the Stokes phase (from 0 to 2π). Stokes singularity points of σ_{12}, σ_{23}, and σ_{31} are indicated as pink, orange, and blue dots, respectively. L-lines are indicated in green.

Spatial field structures of the cavity output modes were ellipse fields with Stokes singularities. Figure 6.7(b)(i-v) illustrates mode profiles, SOPs, and Stokes phases of

Mode 1, Mode 2, Mode 3, Mode 5, and Mode, respectively. As shown in Figure 6.7(a), the baseline of the spectrum is a non-zero intensity, indicating that these modes all experienced some interference effects. Mode 1 (Figure 6.7(b)(i)) had an intensity shape of a quasi-lobe pattern with left-handed ellipse fields. There was a single Poincaré vortex ($\sigma_{31} = +1$) and two L-lines. Mode 2 (Figure 6.7(b)(ii)) also had an intensity shape of a quasi-lobe pattern. The SOPs of this mode were dominated by left-handed ellipse fields. We observed a star-type C-point ($\sigma_{12} = +1$) around the center of the closed L-line loop, which contained three Poincaré vortices ($\sigma_{23} = -1$, $+1$ and $\sigma_{31} = +1$). Mode 3 was a Gaussian-like shape with an L-line (Figure 6.7(b)(iii)). This mode may have a significant contribution from a HE_{11} mode and slight contribution from some HOM(s), resulting in such an intensity profile but also a nonscalar field. Mode 5 and Mode 6 also had a flat-top beam shape but rather oval-shaped, see Figure 6.7(b)(iv, v). They both had horizontal polarization overall in a beam, but Mode 5 excited more complex SOPs. Note that the spatial field profile of Mode 5 would have been influenced by Mode 4, which was not locked in this experiment due to its close frequency position, see Figure 6.7(a). There were one C-point ($\sigma_{12} = -1$), two Poincaré vortices ($\sigma_{23} = +1/\sigma_{31} = +1$), and two L-lines in Mode 5, while Mode 6 did not have a value change in its Stokes phases ϕ_{12}, ϕ_{23}, and ϕ_{31}. However, even for Mode 6, where the SOPs are relatively uniform across the entire beam cross-section, this mode would have been generated by multiple guided modes as its mode shape and the baseline of the spectrum imply.

6.8 Effects of the Incident Beam on Cavity Modes

For the sake of completeness, we also investigated the roles of incident beam angle and polarization on the cavity modes. As shown in Section 6.6, birefringence is an important physical phenomenon to control and excite desired cavity modes of the Fabry-Pérot fiber cavity with an HOM-ONF. However, guided modes of a FM fiber and HOM-ONF can be manipulated by changing the incident beam angle [107] or changing modes of the incident beam [130, 134]. We originally tried to efficiently couple the light into the HOM cavity to excite a variety of modes by injecting a Laguerre-Gaussian LG_{11} beam generated via a spatial light modulator, and vector beams via a Q-plate. It was expected to observe efficient coupling to cavity HOMs from those incident beams; however, there was no significant difference in the number of excited HOMs or the intensity of HOMs between these donut-shaped beams and Gaussian-shaped fundamental modes. To better understand the roles of the incident beam as a cavity mode generator or manipulator, two sets of experiments using a straight fiber cavity without an ONF were performed: (i) changing the incident beam angle and (ii) changing the incident beam polarization. The Gaussian-shaped fundamental mode was selected in this set of experiments to simplify the system just to observe the effects of incident beams.

6.8.1 Changing incident beam angle

For the first test, we changed the coupling angle into the fiber cavity. Figure 6.8(a) shows four spectra with varying incident beam angles to the HOM fiber cavity over a laser scanning range of 400 MHz. Within the range of frequencies, each spectrum has

approximately four FSRs. Four different incident coupling angles with a varying coupling efficiency of MAX (black), HIGH (red), LOW (blue), to MIN (green) shared most modes at the same or similar frequencies, and modes are numbered from Mode 1 to Mode 6 for each coupling condition. Figure 6.8(b) shows a close-up of Figure 6.8(a), only showing one FSR over ∼100 MHz. The MAX and MIN coupling conditions has a total of five resolvable peaks, namely Mode 1, Mode 2, Mode 3, Mode 5, and Mode 6, while the incident coupling LOW had a total of five distinct peaks of Mode 1, Mode 2, Mode 4, Mode 5, and Mode 6. The HIGH incident beam coupling condition possesses four peaks: Mode 1, Mode 2, Mode 5, and Mode 6. As the cavity input beam angle changes, the cavity spectrum shape changes only in terms of the intensity of each mode, but surprisingly hardly any change in frequency.

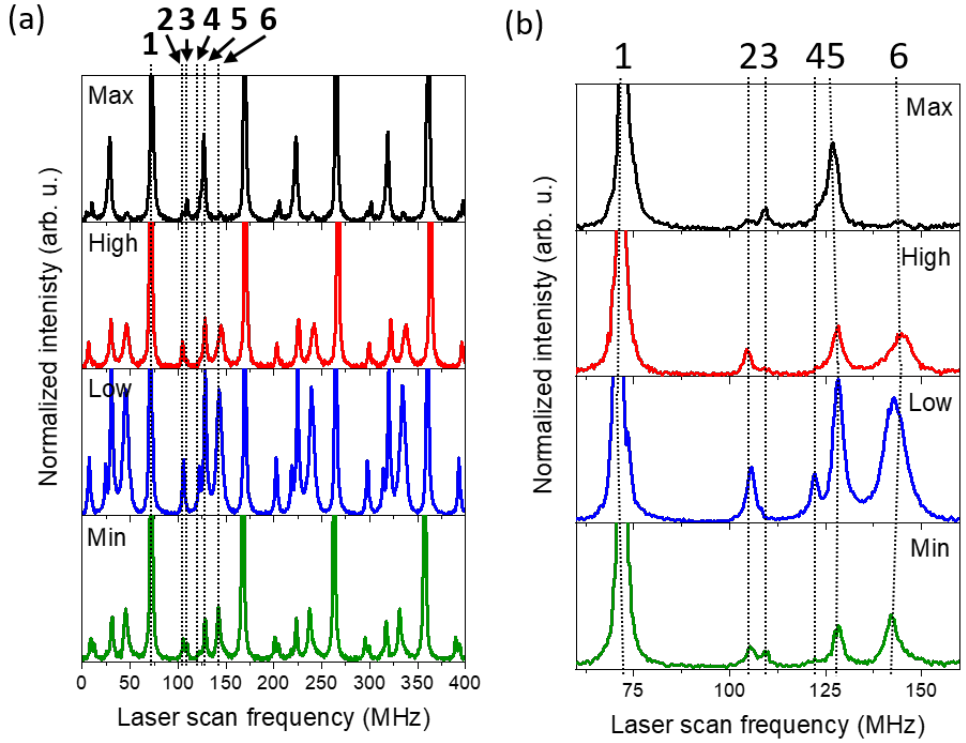

Figure 6.8: (a) Normalized transmitted intensity of a HOM fiber cavity without an ONF with different laser beam coupling by changing the incident beam angle into the fiber cavity. The coupling strength is MAX (black) > HIGH (red) > LOW (blue) > MIN (green). Frequency positions of modes 1 through 6 are indicated as black dotted lines. (b) Close-up spectra of (a).

Now, see the intensity profiles and SOPs of Mode 1 for different couplings in Figure 6.9(a)(i-iv). Clearly, Mode 1 is always Gaussian-like shapes. These modes also have horizontal polarization across the beams, and all Stokes phases, ϕ_{12}, ϕ_{23}, and ϕ_{31} are relatively uniform, as observed in one of the cavity outputs from the cavity with an SM-ONF (see Figure 6.3(a)). These modes are very likely to be generated by the H polarized Gaussian incident beam and have no effect or very little effect of interference with HOMs.

Figures 6.9(b)(i-iii) show the intensity profiles and SOPs of Mode 2 of the incident beam coupling conditions for HIGH, LOW, and MIN, respectively. These three modes

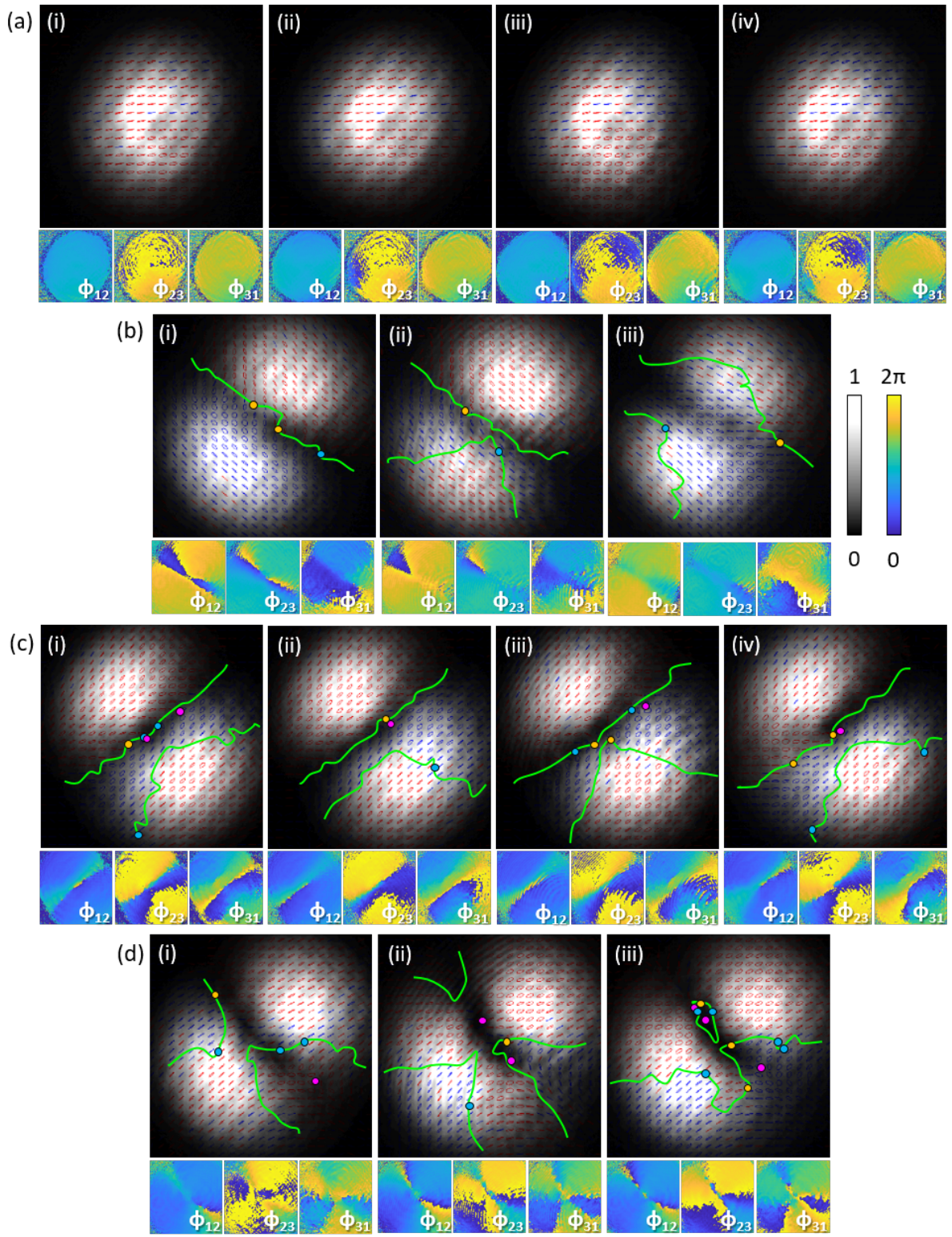

Figure 6.9: Mode intensity profiles with their SOPs (top) and Stokes phases (bottom) for (a) Mode 1 generated from coupling conditions (i) MAX, (ii) HIGH, (iii) LOW, and (iv) MIN, (b) Mode 2 generated from (i) HIGH, (ii) LOW, and (iii) MIN, (c) Mode 5 generated from (i) MAX, (ii) HIGH, (iii) LOW, and (iv) MIN, and (d) Mode 6 generated from (i) HIGH, (iii) LOW, and (iv) MIN. The red and blue SOPs indicate right-handed and left-handed ellipticities, respectively. Scale bars show intensity (from 0 to 1) and Stokes phase (from 0 to 2π).

have a lobe-like intensity shape and the intensity profiles are very similar to each other. The lobe is split in the A direction in all these modes. In terms of SOPs, they also share some of the features. For example, their major polarization direction is A polarized. The ellipticity of these modes is also very similar, and SOPs at most cross-sectional positions are close to linear but the SOPs show some elliptical polarization toward the center of the beam. In addition, these three modes have only Poincaré vortices and L-line(s), but C-point. One can also see similar Stokes phase patterns in ϕ_{12}, ϕ_{23}, and ϕ_{31}, and they only slightly change as the coupling conditions go from HIGH to LOW, and LOW to MIN. The change of SOPs is smaller between HIGH and LOW, as seen in their Stokes phases. The slight change in the SOPs among these modes may be associated with mode coupling with Mode 3, which is very close in frequency as shown in Figure 6.8(b). The spectrum from the MIN condition shows a very small peak at the relative frequency position of Mode 3. Thus, the spatial mode profile of Mode 2 for MIN coupling might have some interference effect from this adjacent mode.

For Mode 3 and Mode 4, it is only possible to analyze the coupling conditions MAX and LOW, respectively (see Figure D.5(a, b)), so it is not possible to compare more structures between different coupling conditions (details described in Section D.3).

Figures 6.9(c)(i-iv) are Mode 5 for the coupling conditions of MAX, HIGH, LOW, and MIN, respectively. Interestingly, these modes have some similar features to Mode 4, see Figure D.5(b). Mode 5 has a lobe intensity pattern with the intensity splitting line across the D orientation. This is also the same in Mode 4. Moreover, these Stokes phases ϕ_{12}, ϕ_{23}, and ϕ_{31} look also similar to the Stokes phases of Mode 4. However, the SOPs of Mode 5 have a dominant D polarization, as opposed to the dominant polarization of the ellipse field found in Mode 4. Mode 5 shows all Stokes singularity types, σ_{12}, σ_{23}, and σ_{31}. All these modes exhibit two L-lines each. Even though there are some differences in the number of singularity points, Mode 5 with different input beam angles shows very similar spatial field structures. This means changing the incident coupling, which usually changes excited guided modes of an FM fiber, does not have a strong impact on the cavity modes.

Mode 6 was only analyzed for the HIGH, LOW, and MIN coupling, see Figures 6.9(d)(i-iii). Similar to other modes, these three observed modes at the same detuning frequency also share many characteristics of their spatial mode structures. Mode intensity profiles of these modes are again lobe shape and the lobes have the splitting line at the A direction. The main SOPs of these modes were linearly polarized D, with slight right-handed ellipticity. There are many Stokes singularities of all types, σ_{12}, σ_{23}, σ_{31} as well as L-lines, in each mode. Even though the positions and the number of these singularity points differ for each mode, their Stokes phases, ϕ_{12}, ϕ_{23}, and ϕ_{31}, are very close to each other. These outcomes also suggest the incident beam angle does not significantly alter guided modes in the cavity, thereby there is no significant change in the mode spatial field.

In the meantime, these cavity outputs only had Gaussian and lobe intensity patterns. The Gaussian intensity shape is a signature of the fundamental mode (see Figure 1.5(a)(i-iii)) while the lobe intensity shape is a signature of the LP_{11} mode (see Figure 2.10(c)). However, the cavity should have guided not only these modes but also the LP_{21} and LP_{02} modes. In fact, we observed a flower-shaped intensity pattern, which is a signature of the LP_{21} mode (see Figure 1.5(c)(i)), in the images taken with a linear polarizer. Figure 6.10(a-c) are images taken for Stokes polarimetry of Mode 6 at the incident coupling

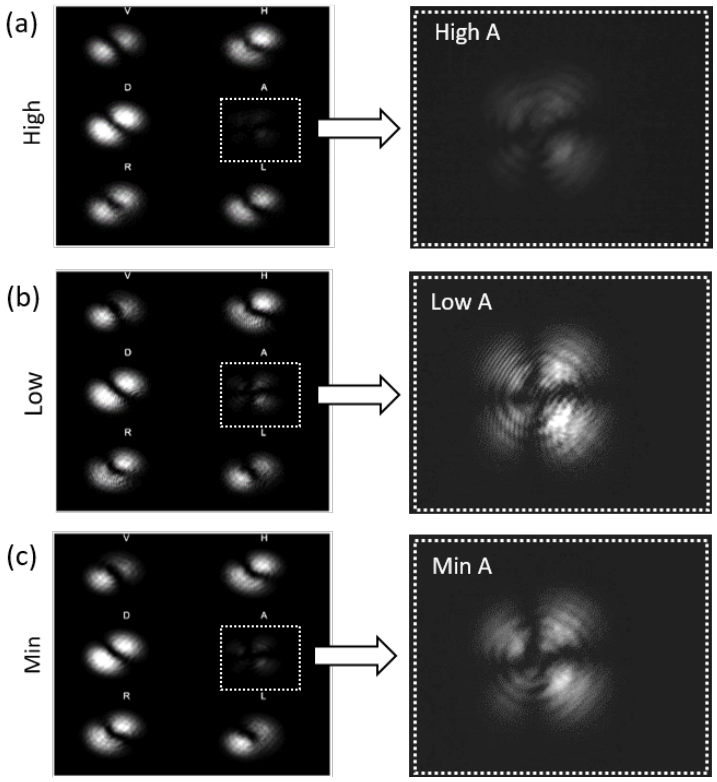

Figure 6.10: Images taken for Stokes polarimetry for Mode 6 for the incident coupling conditions of (a) HIGH, (b) LOW, and (c) MIN with close-up images of flower-like intensity pattern at the linear polarizer oriented at A.

HIGH, Low, and MIN, respectively. For the polarizer oriented in the A direction, there was a small intensity of flower shape measured. This indicates that the HOM cavity possessed the LP_{21} mode. However, the flower patterns were not observed as a cavity output mode; this is very likely due to the effect of mode interference. Theoretically, a total of 12 modes can be present in the HOM cavity without tapered fiber. Nonetheless, we only saw a maximum of six modes for any incident beam condition. Moreover, typical intensity patterns of the LP_{02} mode were not observed. This may be because of low guidance of the LP_{21} and LP_{02} modes for the fiber with V-number = 4.35, where the effective indices of these modes, particularly for the LP_{02} mode, are close to the cladding index (see Figure 2.2(a)). In addition, the lack of finesse to distinguish the near degenerate modes within the same LP family may have also been affected. The existence of many Stokes singularities in those modes indicates both constructive and destructive interference occurred in the cavity thereby reducing the number of cavity peaks and preventing direct observation of the LP_{02} mode alone. Nonetheless, it is important to highlight that this distinctive flower-shaped intensity pattern was not observed in the cavity with an SM-ONF or an HOM-ONF. This observation suggests that the ONFs continue to serve as an effective mode filter in the system.

6.8.2 Changing incident beam polarizations

Next, we studied how incident beam polarization affects the spectra. Figure 6.11(a) illustrates four spectra with different cavity incident beam polarizations to the HOM fiber cavity over a laser scanning range of 400 MHz. All spectra show approximately four FSRs in this frequency range. Four different polarization states, H, D, V, and A at a constant incident beam angle showed three or four modes each at almost the same frequency positions. These modes are numbered from Mode 1 to Mode 4 for each polarization. Figure 6.8(b) shows a close-up figure of Figure 6.8(a), only showing one FSR over ∼100 MHz. The incident beam polarization H has three resolvable peaks, namely Mode 1, Mode 3, and Mode 4, while the incident polarization of V also has three distinct peaks of Mode 1, Mode 2, and Mode 4. Both D and A beam polarizations possess four peaks: Mode 1, Mode 2, Mode 3, and Mode 4. As the cavity input beam polarization changes, the cavity spectrum shape only changes in intensity, but hardly any change in mode frequency position (< 1 MHz).

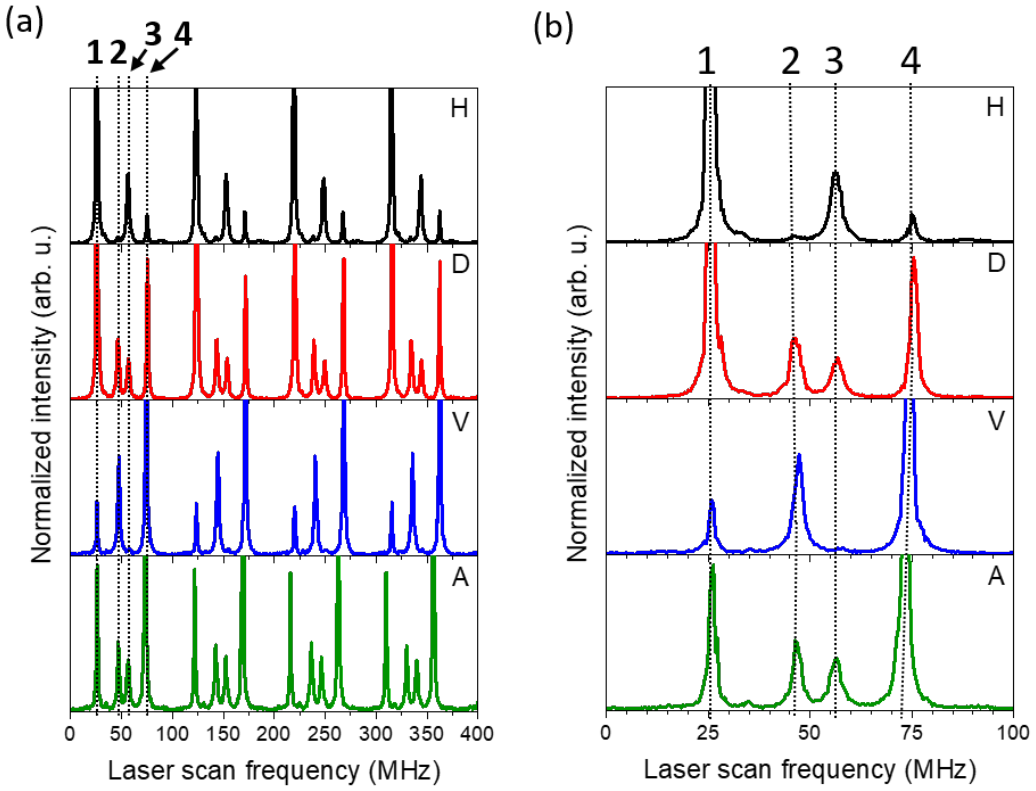

Figure 6.11: (a) Normalized transmitted intensity of HOM fiber cavity without ONF with various incident beam polarization, H: horizontal, D: diagonal, V: vertical, A: antidiagonal polarizations. Frequency positions of modes 1 through 4 are indicated as black dotted lines. (b) Close-up spectra of (a).

Mode 1 for the incident beam polarizations H, D, V, and A are shown in Figure 6.12(a)(i-iv). These modes have a Gaussian-like shape with horizontal SOPs and Stokes phases ϕ_{12}, ϕ_{23}, and ϕ_{31}, and are similar to Mode 1 of a straight HOM cavity without an ONF (Figure 6.9(a)(i-iv)) and Mode 1 of a HOM cavity of an SM-ONF (Figure 6.3(b)(i)), all

of which had a constant incident polarization H. On the other hand, it is interesting to observe that D, V, and A give a similar type of spatial mode profiles as for the H-polarized Gaussian. These results imply that the incident polarization does not affect the spatial mode structures.

Figure 6.12(b)(i-iii) show Mode 2 for the incident beam polarizations D, V, and A, respectively. These modes also look similar in many ways. The mode intensity is a lobe pattern and the intensity splitting line is located along the D orientation. The SOPs are also very similar to each other as their cross-sectional beam mainly possessed elliptical polarization, and half of the lobe is right-handed ellipses, while the other half of the lobe is dominated by left-handed ellipses. Mode 2 generated by D polarized beam has C-points and Poincaré vortices, whereas Mode 2 generated by V and A polarized light showed only Poincaré vortices. These modes all have L-lines at similar positions. Despite some differences in the number of Stokes singularity points, the SOPs, and all Stokes phases, ϕ_{12}, ϕ_{23}, and ϕ_{31}, are very close to each other. These findings also indicate that the generation of cavity modes is independent of incident beam polarization.

Figure 6.12(c)(i-iii) are Mode 3 of the cavity input polarizations for D, V, and A, respectively. One can clearly see that these modes are also similar despite the difference in polarization at the cavity input. As for many other modes, these modes also have a lobe-shaped intensity. The lobe intensity splitting line was found along D. The SOPs are mainly oriented in a D direction, but some ellipticity arises in the case of Mode 3 generated from the V polarized beam. They all have Poincaré vortices but none of these modes had C-points. All these three modes had three L-lines. We also notice that all three Stokes phases, ϕ_{12}, ϕ_{23}, and ϕ_{31}, are almost identical. Thus, Mode 3 was also not affected by different input polarizations.

Lastly, Mode 4 for the incident beam polarizations of H, D, V, and A are presented in Figure 6.12(d)(i-iv), respectively. As with all other sets of modes, Mode 4 also has common spatial features despite the different polarizations at the input to the fiber cavity. The shape of the intensity is Gaussian-like. In terms of SOPs, they all have left-handed ellipses with A ellipse orientation. Stokes phases are relatively uniform everywhere apart from beam ϕ_{23} of Mode 1 generated by a H-polarized input, which has an L-line (Figure 6.12(i)). This indicates that Mode 4 of the incident beam with polarizations D, V, and A are highly likely to be solely the HE_{11} mode or have a strong dominance of the HE_{11} mode. However, Mode 4 of the incident beam with polarization H may have originated not only from the HE_{11} mode but also from some HOMs. As depicted in Figure 6.11(b), the intensity of Mode 4 in the incident beam with polarization H is considerably lower compared to the other incidences of Mode 4. While there might have been some HOM components present in this Mode 4, it appears that the HE_{11} mode was the predominant mode in the incident beam with polarizations D, V, and A. From these findings, we can clearly see that there is hardly any effect of polarization of the cavity input beam on the generation of new cavity modes.

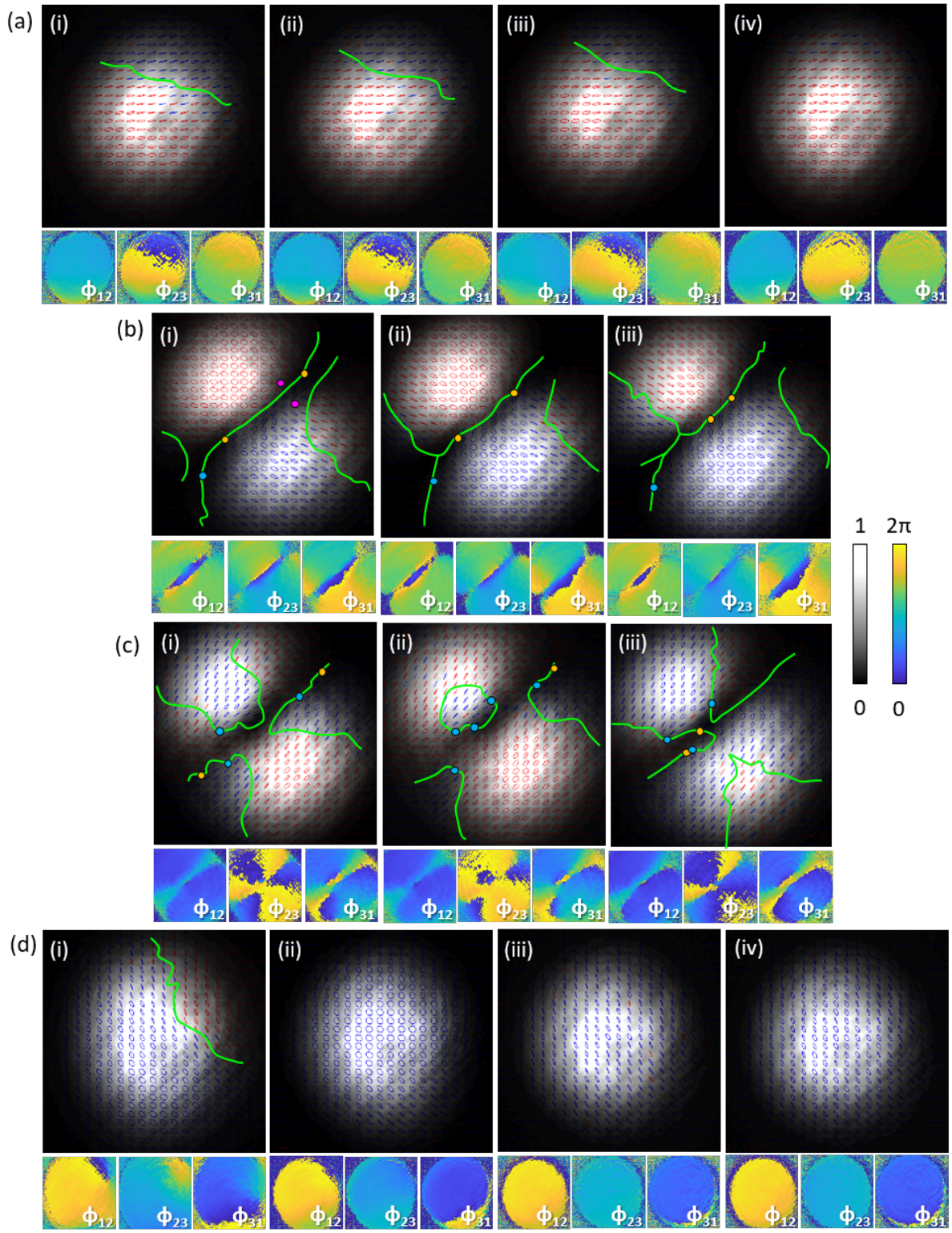

Figure 6.12: Mode intensity profiles with their SOPs (top) and Stokes phases (bottom) for (a) Mode 1 generated from different incident polarization (i) H, (ii) D, (iii) V, and (iv) A, (b) Mode 2 generated from (i) D, (ii) V, and (iii) A, (c) Mode 3 generated from (i) H, (ii) D, and (iii) A, and (d) Mode 4 generated from (i) H, (ii) D, (iii) V, and (iv) A. The red and blue SOPs indicate right-handed and left-handed ellipticities, respectively. Scale bars show intensity (from 0 to 1) and Stokes phase (from 0 to 2π).

6.9 Conclusion

We have experimentally demonstrated a Fabry-Pérot fiber cavity with a HOM-ONF and performed cavity spectroscopy. The cavity mode profiles and transverse polarization topology were also determined by imaging and analyzing the individual cavity modes at the output. These modes had inhomogeneous polarization distributions with a number of Stokes singularities. We also simulated the fiber modes which closely matched those observed at the output of the cavity. Moreover, *in situ* intracavity manipulation of the modal birefringence and interference to select a specific mode of interest was demonstrated.

The effects of the incident beam, both in angle and polarization, did not produce new cavity modes in this study. Such results were not consistent with non-cavity FM fiber, where guided modes are often generated by the incident beam. This means that the effect of intra-cavity birefringence is much more significant than the incident beam condition in the case of our cavity. This may be because of the cavity effect, where light is reflected between two mirrors so that modes experience birefringence in each path for many round trips. In this study, we also found that the incident beam angle and polarization at the input changed the relative intensity of the modes. This effect can be used to manipulate the mode intensity after obtaining desired modes by controlling the IPC paddle angles.

Our HON-ONF-based cavity primarily differs from other reported ONF-based cavities for its larger number of supported fiber modes as well as cavity modes observed in a single FSR. In this study, we aimed to fabricate a cavity which supported the LP_{01} and LP_{11} family modes. However, there exists significant potential to engineer a HON-ONF-based cavity with a greater number of HOMs. A multimode cavity can be used for multimode sensing, based on the distinct responsiveness of various resonant modes within the cavity spectrum to different parameters [245]. Alternatively, it may be even possible to fabricate a HOM-ONF-based cavity with the exclusion of the fundamental mode and/or certain lower-order modes by strategically controlling the taper shape. Our cavity stands apart from other existing ONF-based cavities not only because of its capability to sustain HOMs but also owing to its intracavity tunability for exciting cavity modes. Traditionally, birefringence in fibers has been perceived as an undesirable property, and the IPC paddles were primarily employed to eliminate undesired cavity modes [246]. In contrast, we embraced birefringence as a favorable characteristic of the fibers, successfully harnessing it to produce the desired cavity output mode structures.

In this study, we only focused on the spatial characteristics of cavity output modes. In order to utilize the evanescent field of an HOM-ONF-based cavity, it is essential to obtain modal structures at the ONF region. Such experimental investigation is challenging, as one needs to measure the electric field in 3D. Nevertheless, 3D polarization singularity in free-space has been studied [114–116], and research into the interference of HOMs at the waist of an ONF is an exciting opportunity to uncover the nature of light-matter interactions in tightly confining geometries with topological singularities. Additionally, the realization of a (de)multiplexing system using degenerate HOMs in an ONF-based cavity may be possible by improving the tunability of the modal birefringence and interference. Such a system is attractive for future quantum information platforms as efficient and secure storage.

The interference of higher-order cavity modes with fixed ratios in the evanescent field of an ONF may also be used to trap and manipulate cold atoms. Adjusting the overlap

and SOP of the HOMs should result in the movement of the trapping sites relative to each other, enabling some trap dynamics to be studied [121, 123, 124]. This cavity could be also used with quantum emitters to study multimode cQED effects using degenerate HOMs. The HOM cavity studied here had moderate finesse to enter the strong coupling of cQED regime with a cloud of cold atoms. In free-space optics, strong coupling of multiple transverse HOMs with atoms has been achieved [12], whereas this has not been achieved using an ONF-type cavity. Our work is a step toward this realization.

Moreover, the ability of our cavity to generate all three types of Stokes singularities may be useful to realize not only a C-point laser but also an all-Stokes singularity laser using a FM fiber. The combinations of fiber modes that we used in the simulations were found via manual trial-and-error estimates to obtain a visual match with the experimentally observed modes. More accurate control could be achieved by using machine learning techniques to fully cover the parameter space of permitted modes in the cavity. This may enable us to determine the correct combination of modes that lead to the observed cavity outputs and facilitate feedback to optimize the input to the system to generate desired modes in the cavity.

Chapter 7

Conclusion

The PhD work presented herein was dedicated to advancing ONF-based cavity systems for exploring novel studies, particularly in ONF-based HOM complex polarization states as well as cQED. This thesis highlights the following topics: (i) the development of innovative methods for ONF cavity fabrication using an FIB, resulting in highly reflective cavity mirrors with greater fabrication stability compared to earlier FIB work, (ii) the demonstration of ONF cavities with sufficiently high finesses to be considered for cQED experiments in the strong coupling regime, (iii) the further improvement of the optical quality by laser annealing, and (iv) the realization and characterization of an HOM-ONF-based cavity while enabling controlled excitation of the desired HOMs with polarization topology.

Firstly, we devoted considerable effort to realizing novel Ga FIB methods for fabricating an ONF-cavity, specifically tailored for cQED applications. This project required a significant amount of time, endurance, and patience, with countless failures, to match our expectations to the fabrication outcomes. Nevertheless, this work had an impact on research communities in ONF cavity [247], and nanofabrication [248, 249]. We believe that the techniques developed during this PhD will be of practical importance for those in the ONF community who wish to use FIB for nanofabrication on ONFs. Earlier FIB processes for ONF cavity fabrication faced limitations attributed to the unique characteristics of ONFs, including their fragility, curved surface, and minimal conductivity. Such a process was used to mill FGB mirrors on an ONF and relied heavily on a trial-and-error approach, leading to a distorted nanostructure of FBG mirrors due to defocused or destigmatized beam alignment and an increased risk of breakage.

Instead of directly coating a conductive ITO layer onto an ONF sample, we implemented an ITO substrate in contact with the ONF sample. This approach prevented potential contamination loss during the ITO sputtering process and significantly saved time by eliminating the need for sputtering. Additionally, the Ga ion beam alignment was successfully executed on the ITO substrate in contact with the ONF, effectively reducing unwanted damage caused by the ion beam on the ONF. The nanostructures milled on the ONF exhibited clear edges with dimension errors as small as a few to ten nanometers, which is notably close to the FIB spot size. This level of precision was consistently achieved in each fabrication process, demonstrating the high repeatability of our novel technique.

Furthermore, the application of precise and meticulous care at each fabrication step

played a crucial role in enhancing the survival rate of the ONF cavity. We emphasize that the full effectiveness and validity of our FIB technique hinge on these steps. These include the initial fabrication of the ONF, the preparation of a specialized fiber mount for the FIB, the careful placement of the ONF onto the designated fiber mount, and the delicate removal of the ITO substrate from the fabricated ONF cavity sample. It is imperative to meticulously follow the details of each step to achieve the optimal fabrication outcome and avoid any potential damage to the ONF cavity before conducting the optical characterization. These small but essential steps ensure the success and reliability of the entire fabrication process.

Secondly, we conducted optical characterization of internal ONF cavities fabricated by FIB. In this set of studies, we successfully demonstrated the finesse and effective cavity length of numerous samples that may be useful to enter the strong coupling regime of ONF-based cQED with a single QD at cryogenic temperatures. These cavities featured a 1D PhC nanostructure mirror shape, designed for ease of fabrication within a short time frame. The highest finesse observed was 60 in a cavity with an effective length of about 104 μm. This value was almost three times higher than the theoretical minimum finesse required to achieve strong coupling. So far, ONF-based cavity strong light-matter interactions have only been observed with cold atoms [10, 11]. Our proposed system, a microscale cavity, in conjunction with a solid state emitter (such as a QD) presents a potentially attractive option for miniaturizing the quantum system to a cost-effective and fiber network-ready device.

We further achieved significant advancements in improving cavity mode finesse and reducing scattering loss through laser annealing. This improvement is likely related to the evaporation of Ga from the ONF surface during the annealing process. Interestingly, we also observed shifts in the Bragg wavelength and cavity mode resonant wavelength during this process. These phenomena are likely the result of a competition between Ga desorption and the heating effect induced by the laser. It is worth noting that the heating effect occurs solely due to the laser, but the Ga implantation can cause an additional heating effect. As a consequence of these heating processes, the ONF sample began to display signs of degradation, which is probably linked to overheating. It is of utmost importance to halt the annealing process once the ideal finesse value is achieved to prevent further degradation and avoid breaking the ONF cavity. Careful control of the annealing process is critical to preserving the quality of the fabricated ONF cavities. Moreover, it may be possible to reduce Ga contamination by employing gas-assisted etching during the FIB milling. Combining this technique and laser annealing may further enhance the optical quality of the structured devices.

Despite our successful fabrication of ONF cavities with optical qualities that allowed us to approach the strong coupling regime, this PhD project was unable to advance into cQED experiments. We faced numerous challenges in the development of ONF cavity fabrication methods using a FIB. The additional work to proceed to cQED experiments required building a confocal microscope, single photon counting setup, and a QD deposition system. In this list of tasks preceding cQED experiments, the deterministic deposition of a single QD may be challenging, primarily because colloidal QDs tend to aggregate in solution. Previously, deterministic deposition of a single QD on an ONF was achieved using a subpicoliter needle dispenser (Applied Micro Systems, ND-2000), which was not accessible in this PhD work. There are a number of other techniques to precisely deposit

a single QD on photonic devices [250]. However, due to the fragility of ONF cavities, many techniques, such as a wafer bonding method involving spin coating, are not reliable. Perhaps, the most promising approach may be a pick-and-place method using an atomic force microscope [251] or a tungsten tip and motorized stage [158, 165]. Such a method seems to have a high yield of a single particle for a single NV nanodiamond [251], but it is still challenging for a single QD due to its photobleaching characteristics. Nevertheless, deterministic deposition of few QDs was realized [158] using this method, and there is a possibility of achieving a single QD deposition. In future research endeavors, the adoption of such deposition methods may play a pivotal role in facilitating the study of cQED.

Lastly, we successfully presented the first experimental demonstration of an HOM-ONF-based Fabry-Pérot fiber cavity. In this demonstration, multiple distinctive cavity modes were observed in a single spectrum, and the spatial field structure of each mode was thoroughly analyzed using Stokes polarimetry. Many of these cavity modes exhibited lobe-shaped intensity patterns, which are characteristic intensity shapes indicating HOMs in the LP_{11} family. The SOPs for these modes exhibited complex and non-uniform ellipse fields with Stokes singularities. These complex polarization topologies emerged due to interference and birefringence effects.

It is indeed fascinating that adjusting the intra-cavity birefringence allows us to generate desired modes. In our study, we successfully demonstrated the generation of cavity output fields that resemble higher-order fiber-guided modes from the LP_{11} family. This observation represents a step toward achieving full control over the modes in the Fabry-Pérot fiber cavity. The role of birefringence in generating desired cavity modes was further validated by investigating the effect of incident beam angle and polarization. Notably, we found that changing the incident beam condition did not cause significant alterations to the cavity spectra, mode intensity profiles, or SOPs. However, the incident beam did play a role in manipulating the peak height of the cavity mode. This opens up exciting possibilities for better controlling the cavity modes by strategically combining the cavity's input beam condition and the intra-cavity birefringence. This comprehensive understanding of mode control has significant implications for enhancing the versatility and performance of Fabry-Pérot fiber cavities, offering potential benefits for various applications in quantum technologies and beyond. The effect of birefringence on the mode coupling needs further investigation. Birefringence increases mode coupling [243] and it may be used as a tool to control the degree of coupling. Precise control of mode coupling may be useful to increase polarization-sensitive Purcell enhancement.

The stability demonstrated during the cavity mode stability test, where the cavity spectrum, mode intensity profile, and SOPs remained consistent for nearly one hour, highlights the effectiveness and potential of these cavity modes for a wide range of applications. These applications include not only cQED but also cold atom trapping and multimode sensing. The achievements presented in this work are a significant milestone in the field of HOM-ONF-based Fabry-Pérot fiber cavities. Cold atom trapping using HOMs in an ONF has already been theoretically suggested [121, 123, 124], but none of these studies considered the effect of birefringence in the HOM-ONF system. It is interesting to see if the trapping potential can be lowered and more trapping sites can be created by adding birefringence parameters. Moreover, as demonstrated in the free-space HOM cavity system [12, 139], it may be possible to access the strong coupling regime of cQED using a degenerate multiple transverse cavity mode and cold atoms. This is an

untouched research area in the ONF-based cQED community.

The results obtained in this project left many questions to be answered. What does the cavity mode at the ONF region look like? Is there a unique polarization topology for the evanescent fields, such as Möbius strips, pure transverse spins, and optical skyrmions? Are such topological defects useful for applications such as manipulating small particles and optical communication? Experimentally answering these questions may not be straightforward. Nonetheless, it may be feasible to break down the excited modes by analyzing the output mode of the cavity. Studying four-dimensional (4D) polarization topology for a long distance (a few mm to cm) is not possible in free-space, so the HOM-ONF is a great candidate for investigating the dynamics of complex 4D fields. Additionally, the utilization of emitters like cold atoms could offer valuable insights into the characteristics of the mode excited in the HOM-ONF region. In fact, vector and ellipse fields are more stable than scalar fields in nonlinear propagation of Rb atoms [252]. Investigating the effects of cold atoms around a HOM-ONF on the SOP is intriguing to understand topologically protected fields, which may be useful for applications that require high mode stability.

Furthermore, exploring phase singularities within HOM-ONF systems, a facet not addressed in this PhD research, offers an intriguing avenue. Engineering phase singularities has been demonstrated in free-space beam [253]. Phase singularities serve as generators of superoscillations, i.e., subwavelength spatial variations of the intensity and phase of light [254]. It is a well-known fact that optical fiber supports phase singularities in the center (i.e., inside an ONF) of some beams, such as HE_{21}^{circ}, but our curiosity extends to investigate such singular points in the evanescent field of a HOM-ONF. In fact, there is a theoretical study reporting the generation of phase singularities within evanescent fields [255]. Such singularities are not only interesting in the fundamental aspects but also have numerous applications such as subwavelength microscopy [256], as there is no diffraction limit for dark light [80]. Structured light in a HOM-ONF is still unexplored territory.

In conclusion, these ONF-based cavities presented here open new questions and many research possibilities, ranging from cQED to singular optics. Exploring the future work listed above may lead us to a deeper, yet unimagined understanding of light. ONF-based cavities may unlock new avenues for not only scientific exploration but also technological innovation in the fields of quantum optics, structured light, and beyond.

Bibliography

[1] P. Romagnoli, M. Maeda, J. M. Ward, V. G. Truong, and S. Nic Chormaic, *Fabrication of optical nanofibre-based cavities using focussed ion-beam milling: a review*, Appl. Phys. B **126**, 111 (2020).

[2] V. Sandoghdar, *Nano-Optics in 2020 ± 20*, Nano Lett. **20**, 4721–4723 (2020).

[3] K. Y. Bliokh and F. Nori, *Transverse and longitudinal angular momenta of light*, Phys. Rep. **592**, 1–38 (2015).

[4] F. Le Kien, T. Busch, V. G. Truong, and S. Nic Chormaic, *Higher-order modes of vacuum-clad ultrathin optical fibers*, Phys. Rev. A. **96**, 023835 (2017).

[5] M. F. Picardi, K. Y. Bliokh, F. J. Rodríguez-Fortuño, F. Alpeggiani, and F. Nori, *Angular momenta, helicity, and other properties of dielectric-fiber and metallic-wire modes*, Optica **5**, 1016 (2018).

[6] S. Takeuchi. *Nanodevices for Quantum Computing Using Photons*. In T. Nakamura, T. Matsumoto, H. Tada, and K. I. Sugiura, editors, *Chemistry of Nanomolecular Systems Towards the Realization of Nanomolecular Devices*, Springer Series in Chemical Physics, pages 183–193. Springer, Berlin, Heidelberg, (2003).

[7] A. Laucht, F. Hohls, N. Ubbelohde, M. F. Gonzalez-Zalba, D. J. Reilly, S. Stobbe, T. Schröder, P. Scarlino, J. V. Koski, A. Dzurak, C.-H. Yang, J. Yoneda, F. Kuemmeth, H. Bluhm, J. Pla, C. Hill, J. Salfi, A. Oiwa, J. T. Muhonen, E. Verhagen, M. D. LaHaye, H. H. Kim, A. W. Tsen, D. Culcer, A. Geresdi, J. A. Mol, V. Mohan, P. K. Jain, and J. Baugh, *Roadmap on quantum nanotechnologies*, Nanotechnology **32**, 162003 (2021).

[8] K. P. Nayak, M. Sadgrove, R. Yalla, and F. Le Kien, *Nano fiber quantum photonics*, J. Opt. **20**, 073001 (2018).

[9] F. Le Kien and K. Hakuta, *Cavity-enhanced channeling of emission from an atom into a nanofiber*, Phys. Rev. A. **80**, 053826 (2009).

[10] S. Kato and T. Aoki, *Strong coupling between a trapped single atom and an all-fiber cavity*, Phys. Rev. Lett. **115**, 093603 (2015).

[11] S. K. Ruddell, K. E. Webb, I. Herrera, A. S. Parkins, and M. D. Hoogerland, *Collective strong coupling of cold atoms to an all-fiber ring cavity*, Optica **4**, 576 (2017).

[12] A. Wickenbrock, M. Hemmerling, G. R. M. Robb, C. Emary, and F. Renzoni, *Collective strong coupling in multimode cavity QED*, Phys. Rev. A. **87**, 043817 (2013).

[13] A. Ghatak and K. Thyagarahan, *Introduction to Fiber Optics*, Cambridge University Press, New Delhi (1999).

[14] L. Tong and M. Sumetsky, *Subwavelength and Nanometer Diameter Optical Fibers*, Springer, Heidelberg, Dordrecht, London, New York (2010).

[15] T. A. Birks and Y. W. Li, *The shape of fiber tapers*, J. Lightwave Technol. **10**, 432–438 (1992).

[16] L. Tong, R. R. Gattassand, J. B. Ashcom, S. He, J. Lou, M. Shen, I. Maxwell, and E. Mazur, *Subwavelength-diameter silica wires for low-loss optical wave guiding*, Nature **426**, 816–819 (2003).

[17] L. Tong, J. Lou, and E. Mazur, *Single-mode guiding properties of subwavelength-diameter silica and silicon wire waveguides*, Opt. Express **12**, 1025–1035 (2004).

[18] G. Brambilla, F. Xu, P. Horak, Y. Jung, F. Koizumi, N. P. Sessions, E. Koukharenko, X. Feng, G. S. Murugan, J. S. Wilkinson, and D. J. Richardson, *Optical fiber nanowires and microwires: fabrication and applications*, Adv. Opt. Photon. **1**, 107–161 (2009).

[19] A. K. Patnaik, J. Q. Liang, and K. Hakuta, *Slow light propagation in a thin optical fiber via electromagnetically induced transparency*, Phys. Rev. A **66**, 063808 (2002).

[20] S. G. Leon-Saval, T. A. Birks, W. J. Wadsworth, P. S. J. Russell, and M. W. Mason, *Supercontinuum generation in submicron fibre waveguides*, Opt. Express **12**, 2864–2869 (2004).

[21] R. Kumar, V. Gokhroo, and S. Nic Chormaic, *Multi-level cascaded electromagnetically induced transparency in cold atoms using an optical nanofibre interface*, New J. Phys. **17**, 123012 (2015).

[22] G. Sagué, E. Vetsch, W. Alt, D. Meschede, and A. Rauschenbeutel, *Cold-atom physics using ultrathin optical fibers: light-induced dipole forces and surface interactions*, Phys. Rev. Lett. **99**, 163602 (2007).

[23] K. P. Nayak and K. Hakuta, *Single atoms on an optical nanofibre*, New J. Phys. **10**, 053003 (2008).

[24] M. J. Morrissey, K. Deasy, Y. Wu, S. Chakrabarti, and S. Nic Chormaic, *Tapered optical fibers as tools for probing magneto-optical trap characteristics*, Rev. Sci. Instrum. **80**, 053102 (2009).

[25] G. Brambilla, G. S. Murugan, J. S. Wilkinson, and D. J. Richardson, *Optical manipulation of microspheres along a subwavelength optical wire*, Opt. Lett. **32**, 3041–3043 (2007).

[26] S. Skelton, M. Sergides, R. Patel, E. Karczewska, O. Maragó, and P. Jones, *Evanescent wave optical trapping and transport of micro- and nanoparticles on tapered optical fibers*, J. Quant. Spectrosc. Ra. **113**, 2512–2520 (2012).

[27] M. Daly, V. G. Truong, C. F. Phelan, K. Deasy, and S. Nic Chormaic, *Nanostructured optical nanofibres for atom trapping*, New J. Phys. **16**, 053052 (2014).

[28] M. Daly, V. G. Truong, and S. Nic Chormaic. *Submicron particle manipulation using slotted tapered optical fibers.* In K. Dholakia and G. C. Spalding, editors, *Optical Trapping and Optical Micromanipulation XII*, volume 9548, pages 202–205. International Society for Optics and Photonics, SPIE, (2015).

[29] M. Daly, V. G. Truong, and S. Nic Chormaic, *Evanescent field trapping of nanoparticles using nanostructured ultrathin optical fibers*, Opt. Express **24**, 14470–14482 (2016).

[30] J. Villatoro and D. Monzón-Hernández, *Fast detection of hydrogen with nano fiber tapers coated with ultra thin palladium layers*, Opt. Express **13**, 5087–5092 (2005).

[31] J. Lou, Y. Wang, and L. Tong, *Microfiber optical sensors: a review*, Sensors **14**, 5823–5844 (2014).

[32] J. C. Beugnot, S. Lebrun, G. Pauliat, H. Maillotte, V. Laude, and T. Sylvestre, *Brillouin light scattering from surface acoustic waves in a subwavelength-diameter optical fibre*, Nat. Commun. **5**, 5242 (2014).

[33] G. Brambilla, *Optical fibre nanotaper sensors*, Opt. Fiber Technol. **16**, 331 – 342 (2010).

[34] L. Tong, *Micro/nanofibre optical sensors:challenges and prospects*, Sensors **18**, 903 (2018).

[35] G. Brambilla, *Optical fibre nanowires and microwires: a review*, J. Opt. **12**, 043001 (2010).

[36] L. Tong, F. Zi, X. Guo, and J. Lou, *Optical microfibers and nanofibers: A tutorial*, Opt. Commun. **285**, 4641–4647 (2012).

[37] M. J. Morrissey, K. Deasy, M. Frawley, R. Kumar, E. Prel, L. Russell, V. G. Truong, and S. Nic Chormaic, *Spectroscopy, manipulation and trapping of neutral atoms, molecules, and other particles using optical nanofibers: a review*, Sensors **13**, 10449–10481 (2013).

[38] J. M. Ward, A. Maimaiti, V. H. Le, and S. Nic Chormaic, *Contributed review: Optical micro- and nanofiber pulling rig*, Rev. Sci. Instrum. **85**, 111501 (2014).

[39] T. Nieddu, V. Gokhroo, and S. Nic Chormaic, *Optical nanofibres and neutral atoms*, J. Opt. **18**, 053001 (2016).

[40] P. Solano, J. A. Grover, J. E. Hoffman, S. Ravets, F. K. Fatemi, L. A. Orozco, and S. L. Rolston. *Chapter Seven - Optical Nanofibers: A New Platform for Quantum Optics*. In E. Arimondo, C. C. Lin, and S. F. Yelin, editors, *Advances In Atomic, Molecular, and Optical Physics*, pages 439–505. Academic Press, San Diego, London, (2017).

[41] G. Brambilla, V. Finazzi, and D. J. Richardson, *Ultra-low-loss optical fiber nanotapers*, Opt. Express **12**, 2258–2263 (2004).

[42] A. M. Clohessy, N. Healy, D. F. Murphy, and C. D. Hussey, *Short low-loss nanowire tapers on singlemode fibres*, Electron. Lett. **41**, 954–955 (2005).

[43] J. M. Ward, D. G. O'Shea, B. J. Shortt, M. J. Morrissey, K. Deasy, and S. Nic Chormaic, *Heat-and-pull rig for fiber taper fabrication*, Rev. Sci. Instrum. **77**, 083105 (2006).

[44] D. Lee, K. J. Lee, J. H. Kim, K. Park, D. Lee, Y. H. Kim, and H. Shin, *Fabrication method for ultra-long optical micro/nano-fibers*, Curr. Appl. Phys. **19**, 1334–1337 (2019).

[45] M. Sumetsky, Y. Dulashko, and A. Hale, *Fabrication and study of bent and coiled free silica nanowires: Self-coupling microloop optical interferometer*, Opt. Express **12**, 3521–3531 (2004).

[46] E. C. Mägi, L. B. Fu, H. C. Nguyen, M. R. E. Lamont, D. I. Yeom, and B. J. Eggleton, *Enhanced Kerr nonlinearity in sub-wavelength diameter As_2Se_3 chalcogenide fiber tapers*, Opt. Express **15**, 10324–10329 (2007).

[47] G. Brambilla, F. Koizumi, X. Feng, and D. J. Richardson, *Compound-glass optical nanowires*, Electron. Lett. **41**, 400–402 (2005).

[48] C. K. Ha, K. H. Nam, and M. S. Kang, *Efficient harmonic generation in an adiabatic multimode submicron tapered optical fiber*, Commun. Phys. **4**, 173 (2021).

[49] F. Le Kien, J. Liang, K. Hakuta, and V. Balykin, *Field intensity distributions and polarization orientations in a vacuum-clad subwavelength-diameter optical fiber*, Opt. Commun. **242**, 445–455 (2004).

[50] F. Le Kien, S. D. Gupta, V. I. Balykin, and K. Hakuta, *Spontaneous emission of a cesium atom near a nanofiber: efficient coupling of light to guided modes*, Phys. Rev. A. **72**, 1–7 (2005).

[51] K. P. Nayak, P. N. Melentiev, M. Morinaga, F. Le Kien, V. I. Balykin, and K. Hakuta, *Optical nanofiber as an efficient tool for manipulating and probing atomic fluorescence*, Opt. Express **15**, 5431–5438 (2007).

[52] K. Srinivasan, O. Painter, A. Stintz, and S. Krishna, *Single quantum dot spectroscopy using a fiber taper waveguide near-field optic*, Appl. Phys. Lett. **91**, 091102 (2007).

[53] M. Fujiwara, K. Toubaru, T. Noda, H. Q. Zhao, and S. Takeuchi, *Highly Efficient Coupling of Photons from Nanoemitters into Single-Mode Optical Fibers*, Nano Lett. **11**, 4362–4365 (2011).

[54] R. Yalla, F. Le Kien, M. Morinaga, and K. Hakuta, *Efficient channeling of fluorescence photons from single quantum dots into guided modes of optical nanofiber*, Phys. Rev. Lett. **109**, 063602 (2012).

[55] K. M. Shafi, W. Luo, R. Yalla, K. Iida, E. Tsutsumi, A. Miyanaga, and K. Hakuta, *Hybrid system of an optical nanofibre and a single quantum dot operated at cryogenic temperatures*, Sci. Rep. **8**, 13494 (2018).

[56] T. Schröder, M. Fujiwara, T. Noda, H. Q. Zhao, O. Benson, and S. Takeuchi, *A nanodiamond-tapered fiber system with high single-mode coupling efficiency*, Opt. Express **20**, 10490–10497 (2012).

[57] L. Liebermeister, F. Petersen, A. v. Münchow, D. Burchardt, J. Hermelbracht, T. Tashima, A. W. Schell, O. Benson, T. Meinhardt, A. Krueger, A. Stiebeiner, A. Rauschenbeutel, H. Weinfurter, and M. Weber, *Tapered fiber coupling of single photons emitted by a deterministically positioned single nitrogen vacancy center*, Appl. Phys. Lett. **104**, 031101 (2014).

[58] R. Yalla, Y. Kojima, Y. Fukumoto, H. Suzuki, O. Ariyada, K. M. Shafi, K. P. Nayak, and K. Hakuta, *Integration of silicon-vacancy centers in nanodiamonds with an optical nanofiber*, Appl. Phys. Lett. **120**, 241102 (2022).

[59] S. M. Skoff, D. Papencordt, H. Schauffert, B. C. Bayer, and A. Rauschenbeutel, *Optical-nanofiber-based interface for single molecules*, Phys. Rev. A **97**, 043839 (2018).

[60] A. W. Schell, H. Takashima, T. T. Tran, I. Aharonovich, and S. Takeuchi, *Coupling quantum emitters in 2D materials with tapered fibers*, ACS Photonics **4**, 761–767 (2017).

[61] E. Vetsch, D. Reitz, G. Sagué, R. Schmidt, S. T. Dawkins, and A. Rauschenbeutel, *Optical interface created by laser-cooled atoms trapped in the evanescent field surrounding an optical nanofiber*, Phys. Rev. Lett. **104**, 203603 (2010).

[62] S. M. Hendrickson, M. M. Lai, T. B. Pittman, and J. D. Franson, *Observation of two-photon absorption at low power levels using tapered optical fibers in rubidium vapor*, Phys. Rev. Lett. **105**, 173602 (2010).

[63] D. E. Jones, J. D. Franson, and T. B. Pittman, *Saturation of atomic transitions using subwavelength diameter tapered optical fibers in rubidium vapor*, J. Opt. Soc. Am. B **31**, 1997–2001 (2014).

[64] F. Le Kien and A. Rauschenbeutel, *Nanofiber-mediated chiral radiative coupling between two atoms*, Phys. Rev. A **95**, 023838 (2017).

[65] F. Le Kien, T. Ray, T. Nieddu, T. Busch, and S. Nic Chormaic, *Enhancement of the quadrupole interaction of an atom with the guided light of an ultrathin optical fiber*, Phys. Rev. A **97**, 013821 (2018).

[66] T. Aoki, B. Dayan, E. Wilcut, W. P. Bowen, A. S. Parkins, T. J. Kippenberg, K. J. Vahala, and H. J. Kimble, *Observation of strong coupling between one atom and a monolithic microresonator*, Nature **443**, 671–674 (2006).

[67] S. I. Shopova, H. Zhou, X. Fan, and P. Zhang, *Optofluidic ring resonator based dye laser*, Appl. Phys. Lett. **90**, 221101 (2007).

[68] J. Ward and O. Benson, *WGM microresonators: sensing, lasing and fundamental optics with microspheres*, Laser Photonics Rev. **5**, 553–570 (2011).

[69] F. Lei, Y. Yang, J. M. Ward, and S. Nic Chormaic, *Pump induced lasing suppression in Yb:Er-doped microlasers*, Opt. Express **25**, 24679–24689 (2017).

[70] S. Kato, N. Német, K. Senga, S. Mizukami, X. Huang, S. Parkins, and T. Aoki, *Observation of dressed states of distant atoms with delocalized photons in coupled-cavities quantum electrodynamics*, Nat. Commun. **10**, 1160 (2019).

[71] G. Araneda, S. Walser, Y. Colombe, D. B. Higginbottom, J. Volz, R. Blatt, and A. Rauschenbeutel, *Wavelength-scale errors in optical localization due to spin-orbit coupling of light*, Nat. Phys. **15**, 17–21 (2019).

[72] A. Forbes, M. de Oliveira, and M. R. Dennis, *Structured light*, Nat. Photonics **15**, 253–262 (2021).

[73] C. Rosales-Guzmán, B. Ndagano, and A. Forbes, *A review of complex vector light fields and their applications*, J. Opt. **20**, 123001 (2018).

[74] M. Chekhova and P. Banzer, *Polarization of Light*, De Gruyter, Berlin, 1st edition (2021).

[75] Z. Ma and S. Ramachandran, *Propagation stability in optical fibers: role of path memory and angular momentum*, Nanophotonics **10**, 209–224 (2021).

[76] S. Pancharatnam, *Generalized theory of interference, and its applications*, Proc. Indian Acad. Sci. (Math. Sci.) **44**, 247–262 (1956).

[77] M. V. Berry, *Quantal phase factors accompanying adiabatic changes*, Proc. R. Soc. Lond. A **392**, 45–57 (1984).

[78] A. Tomita and R. Y. Chiao, *Observation of Berry's Topological Phase by Use of an Optical Fiber*, Phys. Rev. Lett. **57**, 937–940 (1986).

[79] M. Soskin, S. V. Boriskina, Y. Chong, M. R. Dennis, and A. Desyatnikov, *Singular optics and topological photonics*, J. Opt. **19**, 010401 (2016).

[80] M. V. Berry, *The singularities of light: intensity, phase, polarisation*, LSA **12**, 238 (2023).

[81] F. N. John and V. B. Michael, *Dislocations in wave trains*, Proceedings of the Royal Society of London. A. Math. Phys. Sci. **336**, 165–190 (1974).

[82] S. Ramachandran and P. Kristensen, *Optical vortices in fiber*, Nanophotonics **2**, 455–474 (2013).

[83] Z. Xu, R. Zhao, S. Li, L. Shen, C. Du, and J. Wang, *Generation of optical vortices using asymmetrically spliced fibers*, J. Opt. **21**, 025802 (2019).

[84] Ruchi and P. Senthilkumaran, *Polarization singularities and intensity degeneracies*, Front. Phys. **8**, 140 (2020).

[85] Q. Wang, C.-H. Tu, Y.-N. Li, and H.-T. Wang, *Polarization singularities: Progress, fundamental physics, and prospects*, APL Photonics **6**, 040901 (2021).

[86] E. Otte, C. Alpmann, and C. Denz, *Polarization singularity explosions in tailored light fields*, Laser Photonics Rev. **12**, 1700200 (2018).

[87] M. V. Berry and J. H. Hannay, *Umbilic points on Gaussian random surfaces*, J. Phys. A: Math. Gen. **10**, 1809–1821 (1977).

[88] F. Cardano, E. Karimi, L. Marrucci, C. de Lisio, and E. Santamato, *Generation and dynamics of optical beams with polarization singularities*, Opt. Express **21**, 8815–8820 (2013).

[89] J. F. Nye, *Lines of circular polarization in electromagnetic wave fields*, Proceedings of the Royal Society of London. A. Math. Phys. Sci. **389**, 279–290 (1983).

[90] M. V. Berry, M. R. Dennis, and R. L. Lee, *Polarization singularities in the clear sky*, New J. Phys. **6**, 162–162 (2004).

[91] X.-L. Wang, J. Ding, W.-J. Ni, C.-S. Guo, and H.-T. Wang, *Generation of arbitrary vector beams with a spatial light modulator and a common path interferometric arrangement*, Opt. Lett. **32**, 3549 (2007).

[92] F. Flossmann, K. O'Holleran, M. R. Dennis, and M. J. Padgett, *Polarization singularities in 2D and 3D speckle fields*, Phys. Rev. Lett. **100**, 203902 (2008).

[93] W. Shu, X. Ling, X. Fu, Y. Liu, Y. Ke, and H. Luo, *Polarization evolution of vector beams generated by q-plates*, Photon. Res. **5**, 64 (2017).

[94] Y. He, Y. Li, J. Liu, X. Zhang, Y. Cai, Y. Chen, S. Chen, and D. Fan, *Switchable phase and polarization singular beams generation using dielectric metasurfaces*, Sci. Rep. **7**, 6814 (2017).

[95] S. Liu, S. Qi, Y. Zhang, P. Li, D. Wu, L. Han, and J. Zhao, *Highly efficient generation of arbitrary vector beams with tunable polarization, phase, and amplitude*, Photon. Res. **6**, 228 (2018).

[96] Y. Zhang, X. Yang, and J. Gao, *Generation of polarization singularities with geometric metasurfaces*, Sci. Rep. **9**, 19656 (2019).

[97] F. Flossmann, U. T. Schwarz, M. Maier, and M. R. Dennis, *Polarization singularities from unfolding an optical vortex through a birefringent crystal*, Phys. Rev. Lett. **95**, 253901 (2005).

[98] F. Flossmann, U. T. Schwarz, M. Maier, and M. R. Dennis, *Stokes parameters in the unfolding of an optical vortex through a birefringent crystal*, Opt. Express **14**, 11402–11411 (2006).

[99] K. Y. Bliokh, A. Niv, V. Kleiner, and E. Hasman, *Singular polarimetry: Evolution of polarization singularities in electromagnetic waves propagating in weakly anisotropic medium*, Opt. Express **16**, 695–709 (2008).

[100] S. K. Pal, Ruchi, and P. Senthilkumaran, *Polarization singularity index sign inversion by a half-wave plate*, Appl. Opt. **56**, 6181 (2017).

[101] S. Vyas, Y. Kozawa, and S. Sato, *Polarization singularities in superposition of vector beams*, Opt. Express **21**, 8972 (2013).

[102] G. Arora, Ruchi, and P. Senthilkumaran, *Full Poincaré beam with all the Stokes vortices*, Opt. Lett. **44**, 5638 (2019).

[103] G. Arora and P. Senthilkumaran, *Generation of Stokes singularities using polarization lateral shear interferometer*, Opt. Express **30**, 27583 (2022).

[104] G. Arora, S. Joshi, H. Singh, V. Haridas, and P. Senthilkumaran, *Perturbation of V-point polarization singular vector beams*, Opt. Laser Technol. **158**, 108842 (2023).

[105] Ruchi, P. Senthilkumaran, and S. K. Pal, *Phase singularities to polarization singularities*, International J. Opt. **2020**, 1–33 (2020).

[106] Y. V. Jayasurya, V. V. G. K. Inavalli, and N. K. Viswanathan, *Polarization singularities in the two-mode optical fiber output*, Appl. Opt. **50**, E131 (2011).

[107] C. H. Krishna and S. Roy, *Polarization singular patterns in modal fields of few-mode optical fiber*, J. Opt. Soc. Am. B. **37**, 2688 (2020).

[108] F. Le Kien and T. Busch, *Torque of guided light on an atom near an optical nanofiber*, Opt. Express **27**, 15046 (2019).

[109] F. Le Kien, S. Nic Chormaic, and T. Busch, *Transfer of angular momentum of guided light to an atom with an electric quadrupole transition near an optical nanofiber*, Phys. Rev. A. **106**, 013712 (2022).

[110] C. Simon, M. Afzelius, J. Appel, A. B. de la Giroday, S. J. Dewhurst, N. Gisin, C. Y. Hu, F. Jelezko, S. Kröll, J. H. Müller, J. Nunn, E. S. Polzik, J. G. Rarity, H. D. Riedmatten, W. Rosenfeld, A. J. Shields, N. Sköld, R. M. Stevenson, R. Thew, I. A. Walmsley, M. C. Weber, H. Weinfurter, J. Wrachtrup, and R. J. Young, *Quantum memories*, Eur. Phys. J. D. **58**, 1–22 (2010).

[111] N. Bozinovic, Y. Yue, Y. Ren, M. Tur, P. Kristensen, H. Huang, A. E. Willner, and S. Ramachandran, *Terabit-scale orbital angular momentum mode division multiplexing in fibers*, Science **340**, 1545–1548 (2013).

[112] C. Sayrin, C. Clausen, B. Albrecht, P. Schneeweiss, and A. Rauschenbeutel, *Storage of fiber-guided light in a nanofiber-trapped ensemble of cold atoms*, Optica **2**, 353–356 (2015).

[113] B. Gouraud, D. Maxein, A. Nicolas, O. Morin, and J. Laurat, *Demonstration of a memory for tightly guided light in an optical nanofiber*, Phys. Rev. Lett. **114**, 180503 (2015).

[114] T. Bauer, P. Banzer, E. Karimi, S. Orlov, A. Rubano, L. Marrucci, E. Santamato, R. W. Boyd, and G. Leuchs, *Observation of optical polarization Möbius strips*, Science **347**, 964–966 (2015).

[115] T. Bauer, M. Neugebauer, G. Leuchs, and P. Banzer, *Optical polarization Möbius strips and points of purely transverse spin density*, Phys. Rev. Lett. **117**, 013601 (2016).

[116] T. Bauer, P. Banzer, F. Bouchard, S. Orlov, L. Marrucci, E. Santamato, R. W. Boyd, E. Karimi, and G. Leuchs, *Multi-twist polarization ribbon topologies in highly-confined optical fields*, New J. Phys. **21**, 053020 (2019).

[117] S. Tsesses, E. Ostrovsky, K. Cohen, B. Gjonaj, N. H. Lindner, and G. Bartal, *Optical skyrmion lattice in evanescent electromagnetic fields*, Science **361**, 993–996 (2018).

[118] L. Du, A. Yang, A. V. Zayats, and X. Yuan, *Deep-subwavelength features of photonic skyrmions in a confined electromagnetic field with orbital angular momentum*, Nat. Phys. **15**, 650–654 (2019).

[119] D. S. Simon. *Topological invariants*. In *Tying Light in Knots*, 2053-2571, pages 5–1 to 5–11. Morgan & Claypool Publishers, (2018).

[120] J. Fu, X. Yin, and L. Tong, *Two-colour atom guide and 1D optical lattice using evanescent fields of high-order transverse modes*, J. Phys. B: At. Mol. Opt. Phys. **40**, 4195–4210 (2007).

[121] G. Sagué, A. Baade, and A. Rauschenbeutel, *Blue-detuned evanescent field surface traps for neutral atoms based on mode interference in ultrathin optical fibres*, New J. Phys. **10**, 113008 (2008).

[122] A. V. Masalov and V. G. Minogin, *Pumping of higher-order modes of an optical nanofiber by laser excited atoms*, Laser Phys. Lett. **10**, 075203 (2013).

[123] C. Phelan, T. Hennessy, and T. Busch, *Shaping the evanescent field of optical nanofibers for cold atom trapping*, Opt. Express **21**, 27093 (2013).

[124] M. Sadgrove, S. Wimberger, and S. Nic Chormaic, *Quantum coherent tractor beam effect for atoms trapped near a nanowaveguide*, Sci. Rep. **6**, 28905 (2016).

[125] F. Le Kien, S. S. S. Hejazi, T. Busch, V. G. Truong, and S. Nic Chormaic, *Channeling of spontaneous emission from an atom into the fundamental and higher-order modes of a vacuum-clad ultrathin optical fiber*, Phys. Rev. A. **96**, 043859 (2017).

[126] F. Le Kien, S. S. S. Hejazi, V. G. Truong, S. Nic Chormaic, and T. Busch, *Chiral force of guided light on an atom*, Phys. Rev. A. **97**, 063849 (2018).

[127] F. Le Kien, D. F. Kornovan, S. S. S. Hejazi, V. G. Truong, M. I. Petrov, S. Nic Chormaic, and T. Busch, *Force of light on a two-level atom near an ultrathin optical fiber*, New J. Phys. **20**, 093031 (2018).

[128] E. Stourm, M. Lepers, J. Robert, S. Nic Chormaic, K. Mølmer, and E. Brion, *Spontaneous emission and energy shifts of a Rydberg rubidium atom close to an optical nanofiber*, Phys. Rev. A. **101**, 052508 (2020).

[129] A. Petcu-Colan, M. Frawley, and S. Nic Chormaic, *Tapered few-mode fibers: Mode evolution during fabrication and adiabaticity*, J. Nonlinear Opt. Phys. Mater **20**, 293–307 (2011).

[130] M. C. Frawley, A. Petcu-Colan, V. G. Truong, and S. Nic Chormaic, *Higher order mode propagation in an optical nanofiber*, Opt. Commun. **285**, 4648–4654 (2012).

[131] S. Ravets, J. E. Hoffman, L. A. Orozco, S. L. Rolston, G. Beadie, and F. K. Fatemi, *A low-loss photonic silica nanofiber for higher-order modes*, Opt. Express **21**, 18325 (2013).

[132] K. Harrington, S. Yerolatsitis, D. V. Ras, D. M. Haynes, and T. A. Birks, *Endlessly adiabatic fiber with a logarithmic refractive index distribution*, Optica **4**, 1526 (2017).

[133] Y. Jung, K. Harrington, S. Yerolatsitis, D. J. Richardson, and T. A. Birks, *Adiabatic higher-order mode microfibers based on a logarithmic index profile*, Opt. Express **28**, 19126 (2020).

[134] J. E. Hoffman, F. K. Fatemi, G. Beadie, S. L. Rolston, and L. A. Orozco, *Rayleigh scattering in an optical nanofiber as a probe of higher-order mode propagation*, Optica **2**, 416 (2015).

[135] F. K. Fatemi, J. E. Hoffman, P. Solano, E. F. Fenton, G. Beadie, S. L. Rolston, and L. A. Orozco, *Modal interference in optical nanofibers for sub-Angstrom radius sensitivity*, Optica **4**, 157 (2017).

[136] A. Maimaiti, V. G. Truong, M. Sergides, I. Gusachenko, and S. Nic Chormaic, *Higher order microfibre modes for dielectric particle trapping and propulsion*, Sci. Rep. **5**, 9077 (2015).

[137] A. Maimaiti, D. Holzmann, V. G. Truong, H. Ritsch, and S. Nic Chormaic, *Nonlinear force dependence on optically bound micro-particle arrays in the evanescent fields of fundamental and higher order microfibre modes*, Sci. Rep. **6**, 30131 (2016).

[138] R. Kumar, V. Gokhroo, K. Deasy, A. Maimaiti, M. C. Frawley, C. Phelan, and S. Nic Chormaic, *Interaction of laser-cooled ^{87}Rb atoms with higher order modes of an optical nanofibre*, New J. Phys. **17**, 013026 (2015).

[139] T. Salzburger, P. Domokos, and H. Ritsch, *Enhanced atom capturing in a high-Q cavity by help of several transverse modes*, Opt. Express **10**, 1204 (2002).

[140] D. Mao, Z. He, H. Lu, M. Li, W. Zhang, X. Cui, B. Jiang, and J. Zhao, *All-fiber radially/azimuthally polarized lasers based on mode coupling of tapered fibers*, Opt. Lett. **43**, 1590–1593 (2018).

[141] A. Jöckel. *Glasfaser-Basierte Fabry-Pérot-Resonatoren mit Integrierten Ultradünnen Passagen*. M.S. thesis, Institut für Physik der Johannes Gutenberg-Universität Mainz (2009).

[142] K. J. Vahala, *Optical microcavities*, Nature **424**, 839–846 (2003).

[143] S. Haroche and D. Kleppner, *Cavity Quantum Electrodynamics*, Phys. Today **42**, 24 (1989).

[144] C. J. Hood, M. S. Chapman, T. W. Lynn, and H. J. Kimble, *Real-Time Cavity QED with Single Atoms*, Phys. Rev. Lett. **80**, 4157–4160 (1998).

[145] Y. Yamamoto, S. Inoue, G. Björk, H. Heitmann, and F. Matinaga. *Chapter 5 - Quantum Optics Effects in Semiconductor Lasers*. In E. Kapon, editor, *Semiconductor Lasers I*, Optics and Photonics, pages 361–441. Academic Press, San Diego, (1999).

[146] C. Gerry and P. Knight, *Introductory Quantum Optics*, Cambridge University Press, Cambridge, New York, Cambridge (2005).

[147] H. J. Kimble, *Strong interactions of single atoms and photons in cavity QED*, Phys. Scr. **T76**, 127–137 (1998).

[148] M. Fox, *Quantum Optics: An Introduction*, Oxford University Press, Oxford (2006).

[149] J. Keloth, K. P. Nayak, and K. Hakuta, *Fabrication of a centimeter-long cavity on a nanofiber for cavity QED*, Opt. Lett. **42**, 1003–1006 (2017).

[150] C. Wuttke, M. Becker, S. Brückner, M. Rothhardt, and A. Rauschenbeutel, *Nanofiber Fabry-Perot microresonator for nonlinear optics and cavity quantum electrodynamics*, Opt. Lett. **37**, 1949–1951 (2012).

[151] R. H. Dicke, *Coherence in spontaneous radiation processes*, Phys. Rev. **93**, 99–110 (1954).

[152] F. L. Kien and K. Hakuta, *Cooperative enhancement of channeling of emission from atoms into a nanofiber*, Phys. Rev. A **77**, 013801 (2008).

[153] A. Johnson, M. Blaha, A. E. Ulanov, A. Rauschenbeutel, P. Schneeweiss, and J. Volz, *Observation of collective superstrong coupling of cold atoms to a 30-m long optical resonator*, Phys. Rev. Lett. **123**, 243602 (2019).

[154] K. P. Nayak and K. Hakuta, *Photonic crystal formation on optical nanofibers using femtosecond laser ablation technique*, Opt. Express **21**, 2480–2490 (2013).

[155] K. P. Nayak, P. Zhang, and K. Hakuta, *Optical nanofiber-based photonic crystal cavity*, Opt. Lett. **39**, 232–235 (2014).

[156] R. Yalla, M. Sadgrove, K. P. Nayak, and K. Hakuta, *Cavity quantum electrodynamics on a nanofiber using a composite photonic crystal cavity*, Phys. Rev. Lett. **113**, 143601 (2014).

[157] K. P. Nayak, F. Le Kien, Y. Kawai, K. Hakuta, K. Nakajima, H. T. Miyazaki, and Y. Sugimoto, *Cavity formation on an optical nanofiber using focused ion beam milling technique Abstract :*, J. Mod. Opt. **19**, 200–203 (2011).

[158] A. W. Schell, H. Takashima, S. Kamioka, Y. Oe, M. Fujiwara, O. Benson, and S. Takeuchi, *Highly efficient coupling of nanolight emitters to a ultra-wide tunable nanofibre cavity*, Sci. Rep. **5**, 1–5 (2015).

[159] W. Li, J. Du, V. G. Truong, and S. Nic Chormaic, *Optical nanofiber-based cavity induced by periodic air-nanohole arrays*, Appl. Phys. Lett. **110**, 253102 (2017).

[160] H. Takashima, A. Fukuda, H. Maruya, T. Tashima, A. W. Schell, and S. Takeuchi, *Fabrication of a nanofiber Bragg cavity with high quality factor using a focused helium ion beam*, Opt. Express **27**, 6792–6800 (2019).

[161] M. Daly. *Light-Induced Interactions using Optical Near-Field Devices*. PhD thesis, Okinawa Institute of Science and Technology Graduate University (2017).

[162] K. Hakuta and K. P. Nayak, *Manipulating single atoms and photons using optical nanofibers*, Adv. Nat. Sci.: Nanosci. Nanotechnol. **3**, 015005 (2012).

[163] A. A. Tseng, *Recent developments in micromilling using focused ion beam technology*, J. Micromech. Microeng. **14**, R15–R34 (2004).

[164] S. Reyntjens and R. Puers, *A review of focused ion beam applications in microsystem technology*, J. Micromech. Microeng. **11**, 287–300 (2001).

[165] T. Tashima, H. Takashima, A. W. Schell, T. T. Tran, I. Aharonovich, and S. Takeuchi, *Hybrid device of hexagonal boron nitride nanoflakes with defect centres and a nano-fibre Bragg cavity*, Sci. Rep. **12**, 96 (2022).

[166] F. Le Kien, K. Nayak, and K. Hakuta, *Nanofibers with Bragg gratings from equidistant holes*, J. Mod. Opt. **59**, 274–286 (2012).

[167] C. Wuttke. *Thermal Excitations of Optical Nanofibers Measured with a Fiber-Integrated Fabry-Pérot Cavity*. PhD thesis, Faculty of Physics at the Johannes Gutenberg Unversität Mainz (2014).

[168] W. Li, J. Du, and S. Nic Chormaic, *Tailoring a nanofiber for enhanced photon emission and coupling efficiency from single quantum emitters*, Opt. Lett. **43**, 1674–1677 (2018).

[169] X. Wang, P. Zhang, G. Li, and T. Zhang, *High-efficiency coupling of single quantum emitters into hole-tailored nanofibers*, Opt. Express **29**, 11158 (2021).

[170] B. W. Ward, J. A. Notte, and N. P. Economou, *Helium ion microscope: A new tool for nanoscale microscopy and metrology*, Journal of Vac. Sci. Technol. B **24**, 2871–2874 (2006).

[171] M. Maeda, J. Keloth, and S. Nic Chormaic, *Manipulation of polarization topology using a Fabry–Pérot fiber cavity with a higher-order mode optical nanofiber*, Photon. Res. **11**, 1029 (2023).

[172] A. W. Snyder and J. D. Love, *Optical Waveguide Theory*, Chapman and Hall, London, New York (1983).

[173] J. D. Love, W. M. Henry, W. J. Stewart, R. J. Black, S. Lacroix, and F. Gonthier, *Tapered single-mode fibres and devices. Part 1: Adiabaticity criteria*, IEE Proc. J. Optoelectron. **138**, 355 (1991).

[174] T. Birks and Y. Li, *The shape of fiber tapers*, J. Lightwave Technol. **10**, 432–438 (1992).

[175] R. Nagai and T. Aoki, *Ultra-low-loss tapered optical fibers with minimal lengths*, Optic Express **22**, 28427–28436 (2014).

[176] J. E. Hoffman, S. Ravets, J. A. Grover, P. Solano, P. R. Kordell, J. D. Wong-Campos, L. A. Orozco, S. L., and Rolston, *Ultrahigh transmission optical nanofibers*, AIP Advances **4**, 67124 (2014).

[177] A. Stiebeiner, R. Garcia-Fernandez, and A. Rauschenbeutel, *Design and optimization of broadband tapered optical fibers with a nanofiber waist*, Opt. Express **18**, 22677 (2010).

[178] S. Ravets, J. E. Hoffman, P. R. Kordell, J. D. Wong-Campos, S. L. Rolston, and L. A. Orozco, *Intermodal Energy Transfer in a Tapered Optical Fiber: Optimizing Transmission*, J. Opt. Soc. Am. A. **30**, 20–22 (2013).

[179] A. Yariv, *Optical Electronics*, Saunders College Publishing, 4th edition (1991).

[180] K. Okamoto, *Fundamentals of Optical Waveguides*, Elsevier, Burlington, San Diego, London, 2nd edition (2006).

[181] F. Le Kien, *Selected Topics of Nanofiber Optics*, Lecture Notes for Okinawa School in Physics 2016: Coherent Quantum Dynamics, Okinawa Institute of Science and Technology Graduate University (2016).

[182] J. Keloth, K. P. Nayak, J. Wang, M. Morinaga, and K. Hakuta, *Coherent interaction of orthogonal polarization modes in a photonic crystal nanofiber cavity*, Opt. Express **27**, 1453 (2019).

[183] P. S. Theocaris and E. E. Gdoutos, *Matrix Theory of Photoelasticity*, Springer, Berlin, Heidelberg, 1st edition (1979).

[184] I. Freund, *Polarization singularity indices in Gaussian laser beams*, Opt. Commun. **201**, 251–270 (2002).

[185] I. Freund, A. I. Mokhun, M. S. Soskin, O. V. Angelsky, and I. I. Mokhun, *Stokes singularity relations*, Opt. Lett. **27**, 545 (2002).

[186] M. Martinelli and P. Martelli, *Polarization, mirrors, and reciprocity: birefringence and its compensation in optical retracing circuits*, Adv. Opt. Photonics **9**, 129 (2017).

[187] I. Freund, *Poincaré vortices*, Opt. Lett. **26**, 1996 (2001).

[188] E. M. Purcell, *Spontaneous emission probabilities at radio frequencies*, Phys. Rev. **69**, 681 (1946).

[189] A. F. Kockum, A. Miranowicz, S. D. Liberato, S. Savasta, and F. Nori, *Ultrastrong coupling between light and matter*, Nat. Rev. Phys. **1**, 19–40 (2019).

[190] W. T. Silfvast, *Laser Fundamentals*, Cambridge University Press, New York, 2nd edition (2008).

[191] C. Bond, D. Brown, A. Freise, and K. A. Strain, *Interferometer techniques for gravitational-wave detection*, Living Rev. Relativ. **19**, 3 (2016).

[192] J. McKeever, A. Boca, A. D. Boozer, J. R. Buck, and H. J. Kimble, *Experimental realization of a one-atom laser in the regime of strong coupling*, Nature **425**, 268–271 (2003).

[193] A. Reiserer and G. Rempe, *Cavity-based quantum networks with single atoms and optical photons*, Rev. Mod. Phys. **87**, 1379–1418 (2015).

[194] Y. O. Barmenkov, D. Zalvidea, S. Torres-Peiró, J. L. Cruz, and M. V. Andrés, *Effective length of short Fabry-Perot cavity formed by uniform fiber Bragg gratings*, Opt. Express **14**, 6394 (2006).

[195] P. Forn-Díaz, L. Lamata, E. Rico, J. Kono, and E. Solano, *Ultrastrong coupling regimes of light-matter interaction*, Rev. Mod. Phys. **91**, 025005 (2019).

[196] T. Birks, J. Knight, and T. Dimmick, *High-resolution measurement of the fiber diameter variations using whispering gallery modes and no optical alignment*, IEEE Photon. Technol. Lett. **12**, 182–183 (2000).

[197] M. Sumetsky and Y. Dulashko, *Radius variation of optical fibers with angstrom accuracy*, Opt. Lett. **35**, 4006 (2010).

[198] U. Wiedemann, K. Karapetyan, C. Dan, D. Pritzkau, W. Alt, S. Irsen, and D. Meschede, *Measurement of submicrometre diameters of tapered optical fibres using harmonic generation*, Opt. Express **18**, 7693 (2010).

[199] J. Keloth, M. Sadgrove, R. Yalla, and K. Hakuta, *Diameter measurement of optical nanofibers using a composite photonic crystal cavity*, Opt. Lett. **40**, 4122 (2015).

[200] M. Sumetsky, Y. Dulashko, J. M. Fini, A. Hale, and J. W. Nicholson, *Probing optical microfiber nonuniformities at nanoscale*, Opt. Lett. **31**, 2393 (2006).

[201] A. A. Tseng, *Recent developments in nanofabrication using focused ion beams*, Small **1**, 924–939 (2005).

[202] V. Hodzic, J. Orloff, and C. Davis, *Focused ion beam created periodic structures on tapered optical fibers*, J. Vac. Sci. Technol. B **21**, 2711–2714 (2003).

[203] V. Hodzic, J. Orloff, and C. C. Davis, *Periodic structures on biconically tapered optical fibers using ion beam milling and boron implantation*, J. Lightwave Technol. **22**, 1610 (2004).

[204] J. L. Kou, J. Feng, L. Ye, F. Xu, and Y. Q. Lu, *Miniaturized fiber taper reflective interferometer for high temperature measurement*, Opt. Express **18**, 14245–14250 (2010).

[205] M. Ding, P. Wang, T. Lee, and G. Brambilla, *A microfiber cavity with minimal-volume confinement*, Appl. Phys. Lett. **99**, 051105 (2011).

[206] R. M. André, S. Pevec, M. Becker, J. Dellith, M. Rothhardt, M. B. Marques, D. Donlagic, H. Bartelt, and O. Frazão, *Focused ion beam post-processing of optical fiber Fabry-Perot cavities for sensing applications*, Opt. Express **22**, 13102–13108 (2014).

[207] S. C. Warren-Smith, R. M. André, C. Perrella, J. Dellith, and H. Bartelt, *Direct core structuring of microstructured optical fibers using focused ion beam milling*, Opt. Express **24**, 378–387 (2016).

[208] C. Martelli, P. Olivero, J. Canning, N. Groothoff, B. Gibson, and S. Huntington, *Micromachining structured optical fibers using focused ion beam milling*, Opt. Lett. **32**, 1575–1577 (2007).

[209] W. Yuan, F. Wang, A. Savenko, D. H. Petersen, and O. Bang, *Note: Optical fiber milled by focused ion beam and its application for Fabry-Pérot refractive index sensor*, Rev. Sci. Instrum. **82**, 076103 (2011).

[210] Y. Liu, C. Meng, A. P. Zhang, Y. Xiao, H. Yu, and L. Tong, *Compact microfiber Bragg gratings with high-index contrast*, Opt. Lett. **36**, 3115–3117 (2011).

[211] Y. Z. Sun, Y. Yu, H. L. Liu, Z. Y. Li, and W. Ding, *Optical microfiber-based photonic crystal cavity*, J. Phys. Conf. Ser. **680**, 012029 (2016).

[212] B. Maniscalco, P. M. Kaminski, and J. M. Walls, *Thin film thickness measurements using Scanning White Light Interferometry*, Thin Solid Films **550**, 10–16 (2014).

[213] Nanofabrication, *Thickness of ITO vs. deposition time*, Engineering Section, Okinawa Institute of Science and Technology Graduate University (2016).

[214] FEI Company, 5350 NE Dawson Creek Drive, Hillsboro, OR 97124. *Helios NanoLab G3UC/G3CX/660 - User Operation Manual*, (2014).

[215] T. Heindel, J.-H. Kim, N. Gregersen, A. Rastelli, and S. Reitzenstein, *Quantum dots for photonic quantum information technology*, Adv. Opt. Photon. **15**, 613–738 (2023).

[216] Y. Arakawa and M. J. Holmes, *Progress in quantum-dot single photon sources for quantum information technologies: A broad spectrum overview*, Appl. Phys. Rev. **7**, 021309 (2020).

[217] D. A. Vajner, L. Rickert, T. Gao, K. Kaymazlar, and T. Heindel, *Quantum Communication Using Semiconductor Quantum Dots*, Adv. Quantum Technol. **5**, 2100116 (2022).

[218] C. L. Morrison, M. Rambach, Z. X. Koong, F. Graffitti, F. Thorburn, A. K. Kar, Y. Ma, S.-I. Park, J. D. Song, N. G. Stoltz, D. Bouwmeester, A. Fedrizzi, and B. D. Gerardot, *A bright source of telecom single photons based on quantum frequency conversion*, Appl. Phys. Lett. **118**, 174003 (2021).

[219] G. Khitrova, H. M. Gibbs, M. Kira, S. W. Koch, and A. Scherer, *Vacuum Rabi splitting in semiconductors*, Nat. Phys. **2**, 81–90 (2006).

[220] R. K. Gupta, J. L. Everett, A. D. Tranter, R. Henke, V. Gokhroo, P. K. Lam, and S. Nic Chormaic, *Machine learner optimization of optical nanofiber-based dipole traps*, AVS Quantum Sci. **4**, 026801 (2022).

[221] P. B. Deotare, M. W. McCutcheon, I. W. Frank, M. Khan, and M. Lončar, *High quality factor photonic crystal nanobeam cavities*, Appl. Phys. Lett. **94** (2009).

[222] P. B. Deotare and M. Loncar. *Photonic Crystal Nanobeam Cavities*. In B. Bhushan, editor, *Encyclopedia of Nanotechnology*, pages 2060–2069. Springer Netherlands, Dordrecht, (2012).

[223] R. Yalla. *Single Photon Generation and Spectroscopy Using Quantum Dots on Optical Nanofibers*. PhD thesis, The University of Electro-Communications (2012).

[224] M. Fujiwara, K. Toubaru, and S. Takeuchi, *Optical transmittance degradation in tapered fibers*, Opt. Express **19**, 8596 (2011).

[225] T. Tashima, H. Takashima, and S. Takeuchi, *Direct optical excitation of an NV center via a nanofiber Bragg-cavity: a theoretical simulation*, Opt. Express **27**, 27009 (2019).

[226] H. Takashima, A. W. Schell, and S. Takeuchi, *Numerical analysis of the ultra-wide tunability of nanofiber Bragg cavities*, Opt. Express **31**, 13566 (2023).

[227] S. Sahu, K. P. Nayak, K. R. Mangipudi, and R. Jha, *Slot waveguide enhanced asymmetric photonic crystal nanofiber cavity for fiber-coupled single photons*, Appl. Phys. Lett. **124** (2024).

[228] H. Karge and R. Mühle, *High dose ion implantation effects in glasses*, Nucl. Instrum. Methods Phys. Res. B. **65**, 380–383 (1992).

[229] D. Hole, P. Townsend, J. Barton, L. Nistor, and J. Van Landuyt, *Gallium colloid formation during ion implantation of glass*, J. Non-Cryst. Solids. **180**, 266–274 (1995).

[230] Y. Fu and N. K. A. Bryan, *Investigation of physical properties of quartz after focused ion beam bombardment*, Appl. Phys. B **80**, 581–585 (2005).

[231] Y. Yin, J. Wang, X. Wang, S. Li, M. R. Jorgensen, J. Ren, S. Meng, L. Ma, and O. G. Schmidt, *Water nanostructure formation on oxide probed in situ by optical resonances*, Sci. Adv. **5**, eaax6973 (2019).

[232] A. D. Smith, K. Elgammal, F. Niklaus, A. Delin, A. C. Fischer, S. Vaziri, F. Forsberg, M. Råsander, H. Hugosson, L. Bergqvist, S. Schröder, S. Kataria, M. Östling, and M. C. Lemme, *Resistive graphene humidity sensors with rapid and direct electrical readout*, Nanoscale **7**, 19099–19109 (2015).

[233] D. B. Asay and S. H. Kim, *Evolution of the adsorbed water layer structure on silicon oxide at room temperature*, J. Phys. Chem. B. **109**, 16760–16763 (2005).

[234] A. Maimaiti, V. G. Truong, M. Sergides, I. Gusachenko, and S. Nic Chormaic, *Higher order microfibre modes for dielectric particle trapping and propulsion*, Sci. Rep. **5**, 9077 (2015).

[235] S. K. Ruddell, K. E. Webb, M. Takahata, S. Kato, and T. Aoki, *Ultra-low-loss nanofiber Fabry–Perot cavities optimized for cavity quantum electrodynamics*, Opt. Lett. **45**, 4875–4878 (2020).

[236] Z. Li, X. Li, and X. Zhong, *Strong photon blockade in an all-fiber emitter-cavity quantum electrodynamics system*, Phys. Rev. A **103**, 043724 (2021).

[237] D. H. White, S. Kato, N. Német, S. Parkins, and T. Aoki, *Cavity dark mode of distant coupled atom-cavity systems*, Phys. Rev. Lett. **122**, 253603 (2019).

[238] D. Pohl, *Operation of a ruby laser in the purely transverse electric mode TE_{01}*, Appl. Phys. Lett. **20**, 266–267 (1971).

[239] K. Yonezawa, Y. Kozawa, and S. Sato, *Generation of a radially polarized laser beam by use of the birefringence of a c-cut Nd:YVO_4 crystal*, Opt. Lett. **31**, 2151 (2006).

[240] Y. Jiang, G. Ren, Y. Shen, Y. Xu, W. Jin, Y. Wu, W. Jian, and S. Jian, *Two-dimensional tunable orbital angular momentum generation using a vortex fiber*, Opt. Lett. **42**, 5014 (2017).

[241] M. Vaziri and C.-L. Chen, *Intermodal beat length measurement with Fabry–Perot optical fiber cavities*, Appl. Opt. **36**, 3439–3443 (1997).

[242] J. P. Gordon and H. Kogelnik, *PMD fundamentals: Polarization mode dispersion in optical fibers*, PNAS **97**, 4541–4550 (2000).

[243] K. Kolluru, S. Saha, and S. D. Gupta, *Cavity enhanced interference of orthogonal modes in a birefringent medium*, Opt. Commun. **410**, 836–840 (2018).

[244] F. Lei, G. Tkachenko, J. M. Ward, and S. Nic Chormaic, *Complete polarization control for a nanofiber waveguide using directional coupling*, Phys. Rev. Appl. **11**, 064041 (2019).

[245] Y. Wu, B. Duan, C. Li, and D. Yang, *Multimode sensing based on optical microcavities*, Frontiers of Optoelectronics **16**, 29 (2023).

[246] P. Schneeweiss, S. Zeiger, T. Hoinkes, A. Rauschenbeutel, and J. Volz, *Fiber ring resonator with a nanofiber section for chiral cavity quantum electrodynamics and multimode strong coupling*, Opt. Lett. **42**, 85 (2017).

[247] S. Sahu, K. P. Nayak, and R. Jha, *Optimization of nanofiber gratings for efficient single-photon collection*, J. Opt. **24**, 115401 (2022).

[248] B. Kamaliya and R. G. Mote. *Nanofabrication Using Focused Ion Beam*. In *Advanced Machining Science*, pages 229–248. CRC Press, (2022).

[249] L. Zhao, Y. Cui, J. Li, Y. Xie, W. Li, and J. Zhang, *The 3D Controllable Fabrication of Nanomaterials with FIB-SEM Synchronization Technology*, Nanomaterials **13** (2023).

[250] M. Sartison, O. C. Ibarra, I. Caltzidis, D. Reuter, and K. D. Jöns, *Scalable integration of quantum emitters into photonic integrated circuits*, Mater. Quantum Technol. **2**, 023002 (2022).

[251] A. W. Schell, G. Kewes, T. Schröder, J. Wolters, T. Aichele, and O. Benson, *A scanning probe-based pick-and-place procedure for assembly of integrated quantum optical hybrid devices*, Rev. Sci. Instrum. **82**, 073709 (2011).

[252] F. Bouchard, H. Larocque, A. M. Yao, C. Travis, I. D. Leon, A. Rubano, E. Karimi, G. L. Oppo, and R. W. Boyd, *Polarization Shaping for Control of Nonlinear Propagation*, Phys. Rev. Lett. **117**, 233903 (2016).

[253] S. W. D. Lim, J.-S. Park, M. L. Meretska, A. H. Dorrah, and F. Capasso, *Engineering phase and polarization singularity sheets*, Nat. Commun. **12**, 4190 (2021).

[254] N. I. Zheludev and G. Yuan, *Optical superoscillation technologies beyond the diffraction limit*, Nat. Rev. Phys. **4**, 16–32 (2021).

[255] P. A. Brandão and C. S. J. Julião, *Symmetry breaking of optical vortices: birth and annihilation of singularities in the evanescent field*, Opt. Lett. **36**, 1563 (2011).

[256] E. T. F. Rogers, J. Lindberg, T. Roy, S. Savo, J. E. Chad, M. R. Dennis, and N. I. Zheludev, *A super-oscillatory lens optical microscope for subwavelength imaging*, Nat. Mater. **11**, 432–435 (2012).

[257] A. Maimaiti. *Particle Manipulation using Ultrathin Optical Fibres*. PhD thesis, University Collage of Cork (2016).

[258] T. Nieddu. *Optical Nanofibers for Multiphoton Processes and Selective Mode Interactions with Rubidium*. PhD thesis, Okinawa Institute of Science and Technologies Graduate University (2019).

Appendix A

Fiber-Guided Modes

A.1 Exact Eigenmodes

The wave guiding behavior of ONFs is of utmost importance in the context of optical and photonic applications. These properties have been subject to extensive investigation, both in theoretical and experimental studies, and understanding the mode behavior plays a critical role in this PhD work. This section introduces a complete mathematical description of ONF modes.

A.1.1 Eigenvalue equations

Here, we derive step-index fiber eigenvalue equations from Maxwell's equations by heavily following lecture notes by Le Kien [181].

Maxwell's equations in a homogeneous and lossless dielectric medium are formulated in terms of the electric field, $\mathbf{E}$, and the magnetic field, $\mathbf{H}$, such that

$$\nabla \times \mathbf{E} = -\mu \frac{\partial \mathbf{H}}{\partial t}, \tag{A.1a}$$

$$\nabla \times \mathbf{H} = -\epsilon \frac{\partial \mathbf{E}}{\partial t}, \tag{A.1b}$$

$$\nabla \cdot (\epsilon \mathbf{E}) = 0, \tag{A.1c}$$

$$\nabla \cdot \mathbf{H} = 0, \tag{A.1d}$$

where ϵ and μ stand for the permittivity and permeability of the medium, respectively. These parameters are interconnected with their respective values in a vacuum, denoted as ϵ_0 and μ_0, through the relationship $\epsilon = \epsilon_0 n^2$ and $\mu \approx \mu_0$ for silica, where n is the refractive index. When we analyze an electromagnetic wave with an angular frequency ω propagating along the fiber axis (z-direction) characterized by a propagation constant, β, with time t, $\mathbf{E}$ and $\mathbf{H}$ can be represented using the following expressions:

$$\begin{bmatrix} \mathbf{E}(r,\theta,z,t) \\ \mathbf{H}(r,\theta,z,t) \end{bmatrix} = \frac{1}{2} \begin{bmatrix} \mathcal{E}(r,\theta) \\ \mathcal{H}(r,\theta) \end{bmatrix} e^{-i(\omega t - \beta z)} + c.c., \tag{A.2}$$

In cylindrical coordinates, the curl operator for an arbitrary differentiable vector, $\mathbf{A}$, has the following forms:

$$\begin{aligned}(\nabla \times \mathbf{A})_r &= \frac{1}{r}\frac{\partial A_z}{\partial \theta} - \frac{\partial A_\theta}{\partial z},\\ (\nabla \times \mathbf{A})_\theta &= \frac{\partial A_r}{\partial z} - \frac{\partial A_z}{\partial r},\\ (\nabla \times \mathbf{A})_z &= \frac{1}{r}\left[\frac{\partial (r A_\theta)}{\partial r} - \frac{\partial A_r}{\partial \theta}\right].\end{aligned} \tag{A.3}$$

where $\mathcal{E}$ and $\mathcal{H}$ are the complex amplitudes of the electric and magnetic components, respectively. Substituting Equations A.3 into Equations A.1a and A.1b, the following equations can be obtained in the cylindrical coordinates:

$$\frac{1}{r}\frac{\partial \mathcal{E}_z}{\partial \theta} + i\beta \mathcal{E}_\theta = -i\omega\mu_0 H_r \tag{A.4a}$$

$$-i\beta \mathcal{E}_r - \frac{\partial \mathcal{E}_z}{\partial r} = -i\omega\mu_0 H_\theta \tag{A.4b}$$

$$\frac{1}{r}\frac{\partial (r\mathcal{E}_\theta)}{\partial r} - \frac{1}{r}\frac{\partial \mathcal{E}_r}{\partial \theta} = -i\omega\mu_0 H_z \tag{A.4c}$$

$$\frac{1}{r}\frac{\partial H_z}{\partial \theta} + i\beta H_\theta = i\omega\epsilon \mathcal{E}_r \tag{A.4d}$$

$$-i\beta H_r - \frac{\partial H_z}{\partial r} = i\omega\epsilon \mathcal{E}_\theta \tag{A.4e}$$

$$\frac{1}{r}\frac{\partial (rH_\theta)}{\partial r} - \frac{1}{r}\frac{\partial H_r}{\partial \theta} = i\omega\epsilon \mathcal{E}_z. \tag{A.4f}$$

We can solve the pair of Equations A.4a and A.4e for $\mathcal{E}_\theta$ and H_r, and the pair of Equations A.4d and A.4b for $\mathcal{E}_r$ and H_θ, for example,

$$
\begin{aligned}
i\omega\epsilon\mathcal{E}_r &= \frac{1}{r}\frac{\partial H_z}{\partial\theta} + i\beta H_\theta \\
&= \frac{1}{r}\frac{\partial H_z}{\partial\theta} + i\beta\frac{1}{-i\omega\mu}(-i\beta\mathcal{E}_r - \frac{\partial\mathcal{E}_z}{\partial r}) \\
&= \frac{1}{r}\frac{\partial H_z}{\partial\theta} - \frac{\beta}{\omega\mu}\left(-i\beta\mathcal{E}_r - \frac{\partial\mathcal{E}_z}{\partial r}\right) \\
&= \frac{1}{r}\frac{\partial H_z}{\partial\theta} + \frac{\beta}{\omega\mu}\frac{\partial\mathcal{E}_z}{\partial r} + \frac{i\beta^2\mathcal{E}_r}{\omega\mu} \\
i\omega\epsilon\mathcal{E}_r - \frac{i\beta^2\mathcal{E}_r}{\omega\mu_0} &= \frac{1}{r}\frac{\partial H_z}{\partial\theta} + \frac{\beta}{\omega\mu}\frac{\partial\mathcal{E}_z}{\partial r} \\
\mathcal{E}_r &= \frac{-i}{\epsilon\omega - \frac{\beta^2}{\omega\mu_0}}\left(\frac{1}{r}\frac{\partial H_z}{\partial\theta} + \frac{\beta}{\omega\mu_0}\frac{\partial\mathcal{E}_z}{\partial r}\right) \\
&= \frac{-i}{\epsilon\omega^2\mu_0 - \beta^2}\left(-\frac{\mu\omega}{r}\frac{\partial H_z}{\partial\theta} + \beta\frac{\partial\mathcal{E}_z}{\partial r}\right),
\end{aligned}
$$

and by taking $k = \omega\sqrt{\epsilon_0\mu_0}$, we obtain transverse electromagnetic fields, such that

$$
\begin{aligned}
\mathcal{E}_r &= \frac{-i}{k^2n^2 - \beta^2}\left(\beta\frac{\partial\mathcal{E}_z}{\partial r} - \frac{\mu_0\omega}{r}\frac{\partial H_z}{\partial\theta}\right), \\
\mathcal{E}_\theta &= \frac{-i}{k^2n^2 - \beta^2}\left(\frac{\beta}{r}\frac{\partial\mathcal{E}_z}{\partial\theta} - \frac{\mu_0\omega}{r}\frac{\partial H_z}{\partial r}\right), \\
H_r &= \frac{-i}{k^2n^2 - \beta^2}\left(\beta\frac{\partial H_z}{\partial r} - \frac{\epsilon_0\omega n^2}{r}\frac{\partial\mathcal{E}_z}{\partial\theta}\right), \\
H_\theta &= \frac{-i}{k^2n^2 - \beta^2}\left(\frac{\beta}{r}\frac{\partial H_z}{\partial\theta} - \frac{\epsilon_0\omega n^2}{r}\frac{\partial\mathcal{E}_z}{\partial r}\right).
\end{aligned}
\tag{A.5}
$$

Solving the complete modal equations is simplified to determining the fields in the longitudinal direction, such that

$$
\left(\frac{\partial^2}{\partial r^2} + \frac{1}{r}\frac{\partial}{\partial r} + \frac{1}{r^2}\frac{\partial^2}{\partial\theta^2} + (k^2n^2 - \beta^2)\right)\begin{bmatrix}\mathcal{E}(r,\theta)\\ \mathcal{H}(r,\theta)\end{bmatrix} = 0. \tag{A.6}
$$

The longitudinal components in Equation A.6 can be factorized as

$$
\begin{bmatrix}\mathcal{E}_z(r,\theta)\\ \mathcal{H}_z(r,\theta)\end{bmatrix} = \begin{bmatrix}e_z(r,\theta)\\ h_z(r,\theta)\end{bmatrix} e^{il\theta}. \tag{A.7}
$$

The radial part, $e_z(r)$ and $h_z(r)$, can be determined by inserting Equation A.7 into Equation A.6, which gives the Bessel differential equation, such that

$$\left(\frac{\partial^2}{\partial r^2}+\frac{1}{r}\frac{\partial}{\partial r}+(k^2n^2-\beta^2)-\frac{l^2}{r^2}\right)\begin{bmatrix}e_z(r)\\h_z(r)\end{bmatrix}=0. \tag{A.8}$$

The wavenumber in the core is $k_1 = n_1 k$ and in the cladding is $k_2 = n_2 k$. For modes confined to the core, the axial propagation constant, β, must be

$$n_2 k \leq \beta \leq n_1 k, \tag{A.9}$$

where n_1 and n_2 are the refractive index of the core and the cladding, respectively. The general solution to Equation A.8 is dependent on the sign of $k^2n^2 - \beta^2$, with the following forms:

$$\begin{bmatrix}e_z(r)\\h_z(r)\end{bmatrix}=\begin{cases}c_1J_l(hr)+c_2Y_l(hr), & \text{if } k^2n_1^2-\beta^2>0,\\ c_3I_l(qr)+c_4K_l(qr), & \text{if } k^2n_2^2-\beta^2<0,\end{cases} \tag{A.10}$$

with

$$\begin{aligned} h&=\sqrt{k^2n_1^2-\beta^2},\\ q&=\sqrt{\beta^2-k^2n_2^2}.\end{aligned} \tag{A.11}$$

Here, J_l is the Bessel function of the first kind, Y_l is the Bessel function of the second kind, I_l is the modified Bessel function of the first kind, and K_l is the modified Bessel function of the second kind. The coefficients c_1, c_2, c_3, and c_4 are constants. Since $\lim_{hr\to 0} Y_l(hr) = \lim_{hr\to\infty} I(qr) = \infty$, we set $c_2 = c_3 = 0$ to make the solution physically reasonable. As a result, Equations A.10 can be reduced to

$$\begin{bmatrix}e_z(r)\\h_z(r)\end{bmatrix}=\begin{cases}c_1J_l(hr), & \text{if } k^2n^2-\beta^2>0,\\ c_4K_l(qr), & \text{if } k^2n^2-\beta^2<0,\end{cases} \tag{A.12}$$

Now, let us change the notation, such that

$$\begin{bmatrix}\mathcal{E}\\\mathcal{H}\end{bmatrix}=\begin{bmatrix}\mathbf{e}\\\mathbf{h}\end{bmatrix}e^{il\theta}. \tag{A.13}$$

where $\mathbf{e}$ and $\mathbf{h}$ are the mode profile functions of the electric and magnetic fields, respectively. From Equations A.12, we obtain the axial component of the electric field and magnetic field components of the mode profile functions e_z and h_z, and apply them to Equations A.5, we also have the transverse field components, e_r, e_θ, h_r and h_θ.

For $r < a$, we have

$$
\begin{aligned}
e_r &= \frac{\beta}{h}\left[iAJ_l'(hr) - \frac{\omega\mu_0 l}{\beta}B\frac{J_l(hr)}{hr}\right], \\
e_\theta &= -\frac{\beta}{h}\left[AJ_l(hr) + \frac{i\omega\mu_0}{\beta}B\frac{J_l'(hr)}{hr}\right], \\
e_z &= AJ_l(hr), \\
h_r &= \frac{\beta}{h}\left[iBJ_l'(hr) + \frac{\omega\mu_0 l}{\beta}A\frac{J_l(hr)}{hr}\right], \\
h_\theta &= -\frac{\beta}{h}\left[BJ_l(hr) - \frac{i\omega\mu_0}{\beta}A\frac{J_l'(hr)}{hr}\right], \\
h_z &= BJ_l(hr),
\end{aligned}
\tag{A.14}
$$

where A and B are normalized constants, and $J_l'(hr)$ and $J_l'(qr)$ represents the derivatives of $J_l(hr)$ and $J_l(qr)$, respectively.

For $r > a$, we have

$$
\begin{aligned}
e_r &= -\frac{\beta}{q}\left[iCK_l'(qr) - \frac{\omega\mu_0 l}{\beta}D\frac{K_l(qr)}{qr}\right], \\
e_\theta &= \frac{\beta}{q}\left[CK_l(qr) + \frac{i\omega\mu_0}{\beta}D\frac{K_l'(qr)}{qr}\right], \\
e_z &= CK_l(qr), \\
h_r &= -\frac{\beta}{q}\left[iDK_l'(qr) + \frac{\omega\mu_0 l}{\beta}C\frac{K_l(qr)}{qr}\right], \\
h_\theta &= -\frac{\beta}{q}\left[DK_l(qr) - \frac{i\omega\mu_0}{\beta}C\frac{K_l'(qr)}{qr}\right], \\
h_z &= DK_l(qr),
\end{aligned}
\tag{A.15}
$$

where C and D are normalization constants, and $K_l'(hr)$ and $K_l'(qr)$ represents the derivatives of $K_l(hr)$ and $K_l(qr)$, respectively.

The tangential components of the fields, e_θ, e_z, h_θ, and h_z, must be continuous at the core-cladding interface, where $r = a$, where a is the fiber radius, and the constants A, B, C, and D can be obtained by equating each component, i.e.,

$$
\begin{aligned}
e_\theta, z(r=a)|_{core} &= e_\theta, z(r=a)|_{cladding}, \\
h_\theta, z(r=a)|_{core} &= h_\theta, z(r=a)|_{cladding}.
\end{aligned}
\tag{A.16}
$$

Applying the boundary conditions, Equations A.16, to Equations A.14 and A.15 for $e_\theta(r=a)$, $e_z(r=a)$, $h_\theta(r=a)$, and $h_z(r=a)$ yield

$$e_\theta(a) = -\frac{\beta}{q}\left[CK_l(qa) + \frac{i\omega\mu_0}{\beta}D\frac{K_l'(qr)}{qa}\right] = \frac{\beta}{q}\left[CK_l(qa) + \frac{i\omega\mu_0}{\beta}D\frac{K_l'(qa)}{qa}\right] \tag{A.17a}$$

$$e_z(a) = AJ_l(ha) = CK_l(qa) \tag{A.17b}$$

$$h_\theta(a) = \frac{\beta}{h}\left[iBJ_l'(ha) + \frac{\omega\mu_0 l}{\beta}A\frac{J_l(ha)}{ha}\right] = \frac{\beta}{q}\left[DK_l(qa) - \frac{i\omega\mu_0}{\beta}C\frac{K_l'(qa)}{qa}\right] \tag{A.17c}$$

$$h_z(a) = BJ_l(ha) = DK_l(qa). \tag{A.17d}$$

Equations A.17b and A.17d can be rearranged to

$$\begin{aligned} C &= \frac{J_l(ha)}{K_l(qa)}A, \\ D &= \frac{J_l(ha)}{K_l(qa)}B, \end{aligned} \tag{A.18}$$

and inserting Equations A.18 into Equations A.17a and A.17c, we find

$$lA\left(\frac{1}{h^2a^2} + \frac{1}{q^2a^2}\right) = -\frac{i\omega\mu_0}{B}\left[\frac{J_l'(ha)}{haJ_l(ha)} + \frac{K_l'(qa)}{qaK_l(qa)}\right] \tag{A.19a}$$

$$lB\left(\frac{1}{h^2a^2} + \frac{1}{q^2a^2}\right) = \frac{i\omega\mu_0}{A}\left[\frac{n_1^2J_l'(ha)}{haJ_l(ha)} + \frac{n_2^2K_l'(qa)}{qaK_l(qa)}\right]. \tag{A.19b}$$

Further solving Equations A.19a and A.19b, we arrive at the fiber eigenmode equation, such that

$$\left[\frac{J_l'(ha)}{haJ_l(ha)} + \frac{K_l'(qa)}{qrK_l(qa)}\right]\left[\frac{n_1^2J_l'(ha)}{haJ_l(ha)} + \frac{n_2^2K_l'(qa)}{qaK_l(qa)}\right] = l^2\left(\frac{1}{h^2a^2} + \frac{1}{q^2a^2}\right)^2\frac{\beta^2}{k^2}. \tag{A.20}$$

Now, we introduce the following general Bessel function relation:

$$\begin{aligned} J_l'(u) &= -J_{l+1}(u) + \frac{l}{u}J_l(u) \\ &= J_{l-1}(u) - \frac{l}{u}J_l(u) \end{aligned} \tag{A.21}$$

where u is an arbitrary argument of J_l' and J_l. Solving Equation A.20 in a quadratic form for $J_l'(ha)/haJ_l(ha)$ using Equation A.21 leads to two eigenvalue equations for hybrid modes. One is for the HE modes ($l \neq 0$) and the TE modes ($l = 0$), given by

$$\frac{J_{l-1}(ha)}{haJ_l(ha)} = -\frac{n_1^2 + n_2^2}{2n_1^2}\frac{K_l'(qa)}{qaK_l(qa)} + \frac{l}{h^2a^2} - \mathcal{R} \tag{A.22}$$

and the other is for the EH modes ($l \neq 0$) and the TM modes ($l = 0$), given by

$$\frac{J_{l-1}(ha)}{haJ_l(ha)} = -\frac{n_1^2+n_2^2}{2n_1^2}\frac{K_l'(qa)}{qaK_l(qa)} + \frac{l}{h^2a^2} + \mathcal{R}, \tag{A.23}$$

where $\mathcal{R}$ is defined as

$$\mathcal{R} = \left[\left(\frac{n_1^2-n_2^2}{2n_1^2}\right)^2\left(\frac{K_l'(qa)}{qaK_l(qa)}\right)^2 + \left(\frac{l\beta}{n_1k}\right)\left(\frac{1}{q^2a^2}+\frac{1}{h^2a^2}\right)^2\right]^{1/2}. \tag{A.24}$$

In the case of $l = 0$ in Equation A.22, we obtain the eigenvalue equation for the TE modes as

$$\frac{J_1(ha)}{haJ_0(ha)} = -\frac{K_1(qa)}{qaK_0(qa)} \tag{A.25}$$

and for $l = 0$, Equation A.23 yields the eigenvalue equation for the TM modes as

$$\frac{J_1(ha)}{haJ_0(ha)} = -\frac{n_2^2}{n_1^2}\frac{K_1(qa)}{qaK_0(qa)}. \tag{A.26}$$

A.1.2 Mode profile functions

Here, each component of the mode profile functions is discussed. We follow the formalizm outlined in Le Kien et al. [4] and the derivation methods described in Okamoto [180].

Hybrid modes

The electric and magnetic field of each component in mode profile functions for hybrid modes can be determined by inserting rearranged Equation A.19a into Equations A.14 and A.15. For convention, we now introduce the parameters

$$s = l\left(\frac{1}{h^2a^2}+\frac{1}{q^2a^2}\right)\left[\frac{J_l'(ha)}{haJ_l(ha)} + \frac{K_l'(qa)}{qaK_l(qa)}\right]^{-1}, \tag{A.27}$$

$$s_1 = \frac{\beta^2}{k^2n_1^2}s, \tag{A.28}$$

$$s_1 = \frac{\beta^2}{k^2n_2^2}s. \tag{A.29}$$

Then, for $r < a$, we have

$$
\begin{aligned}
e_r &= iA\frac{\beta}{2h}\left[(1-s)J_{l-1}(hr) - (1+s)J_{l+1}(hr)\right], \\
e_\theta &= -A\frac{\beta}{2h}\left[(1-s)J_{l-1}(hr) - (1+s)J_{l+1}(hr)\right] \\
e_z &= AJ_l(hr), \\
h_r &= A\frac{\omega\epsilon_0 n_1^2}{2h}\left[(1-s_1)J_{l-1}(hr) + (1+s_1)J_{l+1}(hr)\right], \\
h_\theta &= iA\frac{\omega\epsilon_0 n_1^2}{2h}\left[(1-s_1)J_{l-1}(hr) - (1+s_1)J_{l+1}(hr)\right], \\
h_z &= iA\frac{\beta s}{\omega\mu_0}J_l(hr),
\end{aligned}
\tag{A.30}
$$

and for $r > a$, we have

$$
\begin{aligned}
e_r &= iA\frac{\beta}{2q}\frac{J_l(ha)}{K_l(qa)}\left[(1-s)J_{K-1}(qr) + (1+s)K_{l+1}(qr)\right], \\
e_\theta &= -A\frac{\beta}{2q}\frac{J_l(ha)}{K_l(qa)}\left[(1-s)J_{K-1}(qr) - (1+s)K_{l+1}(qr)\right], \\
e_z &= A\frac{J_l(ha)}{K_l(qa)}K_l qhr), \\
h_r &= A\frac{\omega\epsilon_0 n_1^2}{2q}\frac{J_l(ha)}{K_l(qa)}\left[(1-s_2)J_{l-1}(hr) + (1+s_2)J_{l+1}(hr)\right], \\
h_\theta &= iA\frac{\omega\epsilon_0 n_1^2}{2q}\frac{J_l(ha)}{K_l(qa)}\left[(1-s_2)J_{l-1}(hr) - (1+s_2)J_{l+1}(hr)\right], \\
h_z &= iA\frac{\beta s}{\omega\mu_0}\frac{J_l(ha)}{K_l(qa)}K_l(qr).
\end{aligned}
\tag{A.31}
$$

The constant A can be determined from the propagating power of the field.

TE modes

As a definition, we have $e_z = 0$ for TE modes. Let us introduce another Bessel function formula [180]:

$$
J_0'(u) = -J_1(u). \tag{A.32}
$$

Inserting $e_z = 0$ into Equations A.14 and using Equation A.32, for $r < a$, we have

$$
\begin{aligned}
e_r &= 0, \\
e_\theta &= \frac{i\omega\mu_0}{h} B J_1(hr), \\
e_z &= 0, \\
h_r &= -i\frac{\beta}{h} B J_1(hr), \\
h_\theta &= 0, \\
h_z &= B J_0(hr),
\end{aligned}
\tag{A.33}
$$

and for $r > a$, Equations A.15 are reduced as

$$
\begin{aligned}
e_r &= 0, \\
e_\theta &= -\frac{i\omega\mu_0}{q} \frac{J_0(ha)}{K_0(qa)} B K_1(qr), \\
e_z &= 0, \\
h_r &= -i\frac{\beta}{q} \frac{J_0(ha)}{K_0(qa)} B K_1(qr), \\
h_\theta &= 0, \\
h_z &= \frac{J_0(ha)}{K_0(qa)} B K_0(qr),
\end{aligned}
\tag{A.34}
$$

where the constant B can be determined from the power carried by the mode.

TM modes

For TM modes, we have $h_z = 0$ as its definition. Similar to the case of TE modes, we insert $h_z = 0$ into Equations A.14 and A.15, and then apply Equation A.32. We obtain the following forms for $r < a$,

$$
\begin{aligned}
e_r &= \frac{i\beta}{h} A J_1(hr), \\
e_\theta &= 0, \\
e_z &= A J_0(hr), \\
h_r &= 0, \\
h_\theta &= -i\frac{\omega\epsilon_0 n_1^2}{h} A J_1(hr), \\
h_z &= 0,
\end{aligned}
\tag{A.35}
$$

and for $r > a$, we have

$$
\begin{aligned}
e_r &= \frac{i\beta}{q}\frac{J_0(ha)}{K_0(qa)}AK_1(qr),\\
e_\theta &= 0,\\
e_z &= \frac{J_0(ha)}{K_0(qa)}AK_0(qr),\\
h_r &= 0,\\
h_\theta &= i\frac{\omega\epsilon_0 n_2^2}{q}\frac{J_0(ha)}{K_0(qa)}AK_1(qr),\\
h_z &= 0.
\end{aligned}
\tag{A.36}
$$

A.2 LP Modes

Now we derive LP modes using the strict eigenvalue equations found in the previous section by following Okamoto [180]. We directly adopt the solution for TE modes, Equation A.25, and also for the weakly-guided regime. For TM modes, we can apply the definition of the weakly guiding approximation, $n_1/n_2 \simeq 1$ into Equation A.26 and obtain

$$
\frac{J_1(ha)}{haJ_0(ha)} = -\frac{K_1(qa)}{K_0(qa)},
\tag{A.37}
$$

which is the same as the eigenvalue equation for TE modes, Equation A.25. For the hybrid modes, we also apply this approximation to the strict solution for the hybrid modes. Let us first introduce the following relation, which was obtained by multiplying a with Equations A.11:

$$
\frac{\beta^2}{k^2}\left(\frac{1}{h^2a^2}+\frac{1}{q^2a^2}\right) = \frac{n_1^2}{h^2a^2}+\frac{n_2^2}{q^2a^2}
\tag{A.38}
$$

By substituting Equation A.38 into Equation A.20, we can rewrite the eigenvalue equation in the form

$$
\begin{aligned}
&\left[\frac{J_l'(ha)}{haJ_l(ha)}+\frac{K_l'(qa)}{qrK_l(qa)}\right]\left[\frac{J_l'(ha)}{haJ_l(ha)}+\left(\frac{n_2}{n_1}\right)^2\frac{K_l'(qa)}{qaK_l(qa)}\right]\\
&\qquad = l^2\left(\frac{1}{h^2a^2}+\frac{1}{q^2a^2}\right)^2\left[\frac{1}{h^2a^2}+\left(\frac{n_2}{n_1}\right)^2\frac{1}{q^2a^2}\right].
\end{aligned}
\tag{A.39}
$$

We now insert the weakly guiding approximation, $n_1/n_2 \simeq 1$ into Equation A.39 and obtain a pair of equations:

$$
\frac{J_l'(ha)}{haJ_l(ha)}+\frac{K_l'(qa)}{K_l(qa)} = \pm l\left(\frac{1}{ha}+\frac{1}{qr}\right),
\tag{A.40}
$$

where $l \geq 1$. Let us now introduce the recurrence relations for Bessel functions, such that

$$J_l'(u) = \frac{1}{2}[J_{l-1)}(u) - J_{l+1}(u)], \tag{A.41a}$$

$$\frac{l}{u}J_l(u) = \frac{1}{2}[J_{l-1)}(u) + J_{l+1}(u)], \tag{A.41b}$$

$$K_l'(u) = -\frac{1}{2}[K_{l-1)}(u) + K_{l+1}(u)], \tag{A.41c}$$

$$\frac{l}{u}K_l(u) = -\frac{1}{2}[K_{l-1)}(u) - K_{l+1}(u)]. \tag{A.41d}$$

By using Equations A.41b and A.41c, Equations A.40 can be rewritten as two forms, one is for EH modes, such that

$$\frac{J_{l+1}'(ha)}{haJ_l'(ha)} = -\frac{K_{l+1}(qa)}{K_l(qa)}, \tag{A.42}$$

and the other one is for HE modes, such that

$$\frac{J_{l-1}'(ha)}{haJ_l'(ha)} = \frac{K_{l-1}(qa)}{K_l(qa)}. \tag{A.43}$$

Now, notice that the approximation of $n_1 \simeq n_2$ means that Equations A.28 and A.29 can be expressed as $s_1 \simeq s$ and $s_2 \simeq s$. From Equations A.27 and A.40, we know that $s \simeq 1$, which also results in $s_1 \simeq s_2 \simeq 1$. Therefore, one can elucidate the electromagnetic field of the EH modes by inserting $s \simeq s_1 \simeq s_2 \simeq 1$ into Equations A.30 and A.31. Similarly, $s \simeq -1$ for the HE modes using Equations A.27 and A.40, which gives us $s_1 \simeq s_2 \simeq 1$. Then the electromagnetic field of the HE modes can be obtained by substituting $s \simeq s_1 \simeq s_2 \simeq 1$ into Equations A.30 and A.31.

The eigenvalue equation for HE modes with $l \geq 2$ can be expressed as follows: reverse Equation A.43 and apply Equations A.41b and A.41d to $J_l(hr)$ and $K_l(qr)$, which yield

$$\frac{J_{l-1}'(ha)}{haJ_{l-2}'(ha)} = -\frac{K_{l-1}(qa)}{K_{l-2}(qa)}. \tag{A.44}$$

Let us now summarize the eigenvalue equations for LP modes in the unified form, such that

$$\frac{J_\ell(ha)}{haJ_{\ell-1}(ha)} = -\frac{K_\ell(qa)}{K_{\ell-1}(qa)} \tag{A.45}$$

where

$$\ell = \begin{cases} 1, & \text{for TE and TM modes,} \\ l+1, & \text{for EH modes,} \\ l-1, & \text{for HE modes.} \end{cases} \tag{A.46}$$

Here, $J_\ell(ha)$, $J_{\ell-1}(ha)$ represent the ℓ^{th} and $\ell - 1^{th}$ order Bessel function of the first kind with respect to ha, and $K_\ell(qa)$ and $K_{\ell-1}(qa)$ represent the ℓ^{th} and $\ell - 1^{th}$ order modified Bessel functions of the second kind with respect to qa, respectively.

Appendix B

Supplementary Material: Characterization of ONF Cavities

B.1 ONF Cavity Fabrication Results

Here, the SEM images of cavities, namely Cavity-4 to Cavity-9 are illustrated in Figures B.1, B.2, B.3, B.4, B.5 and B.6, respectively. Dimensions of these cavities are tabulated in Table 4.1 and their spectra are shown in Figures 4.8(a-f), respectively. On some occasions when the conductivity is not high enough due to some small gap between the fiber and the ITO substrate, FIB milling can occur on the ITO surface, instead of the fiber as shown in Figure B.4(a). One can also see a signature of the poor conductivity in Figure B.4(b) where the fiber has some shadows on its right-hand side. These spots of shadow occur when the conductivity on the sample is low and appear in the SEM scanning direction (x-axis).

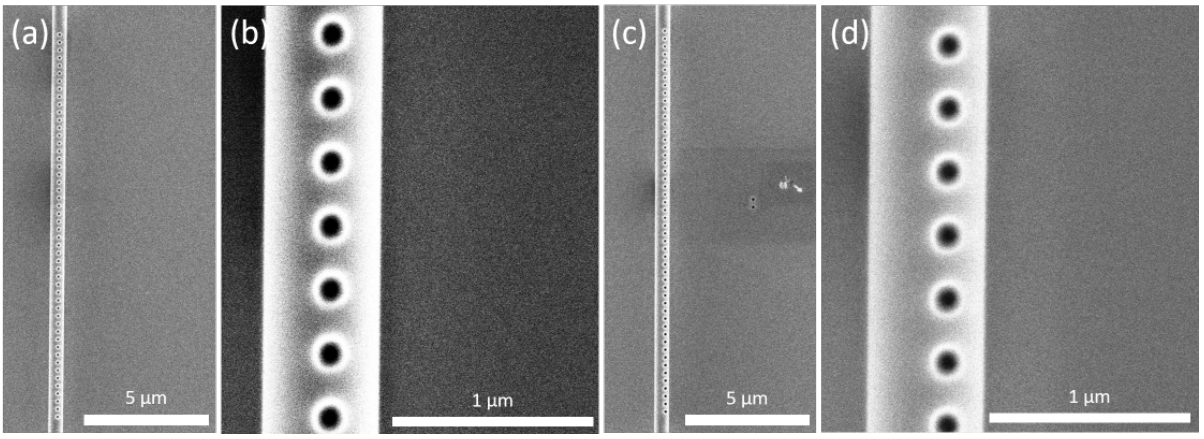

Figure B.1: SEM images of Mirror-1 in Cavity-4 in (a) wide-field view and (b) close up, as well as Mirror-2 in Cavity-4 in (c) wide-field view and (d) close up.

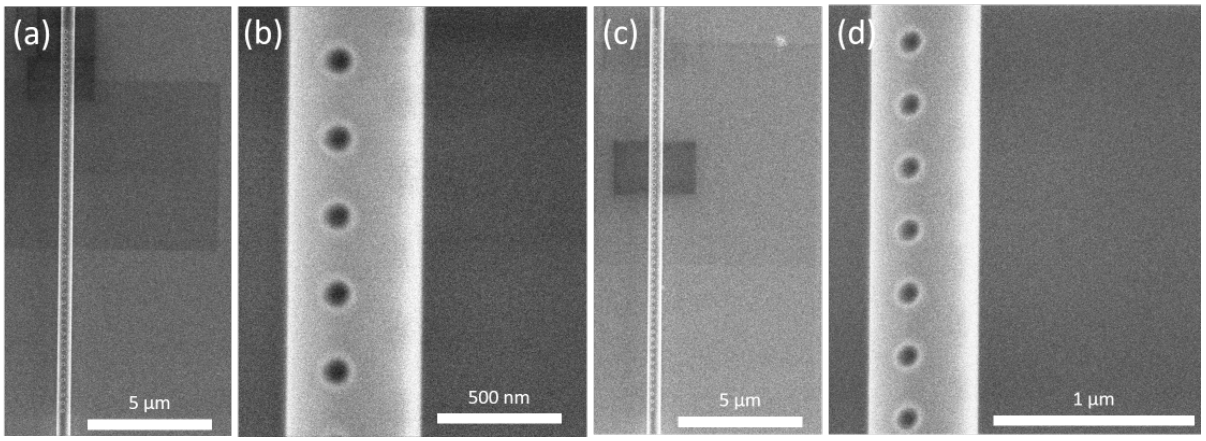

Figure B.2: SEM images of Mirror-1 in Cavity-5 in (a) wide-field view and (b) close up, as well as Mirror-2 in Cavity-5 in (c) wide-field view and (d) close up. The tapered fiber was fabricated by Dr. Kristoffer Karlsson and mirror fabrication using FIB was performed by Dr. Priscila Romagnoli.

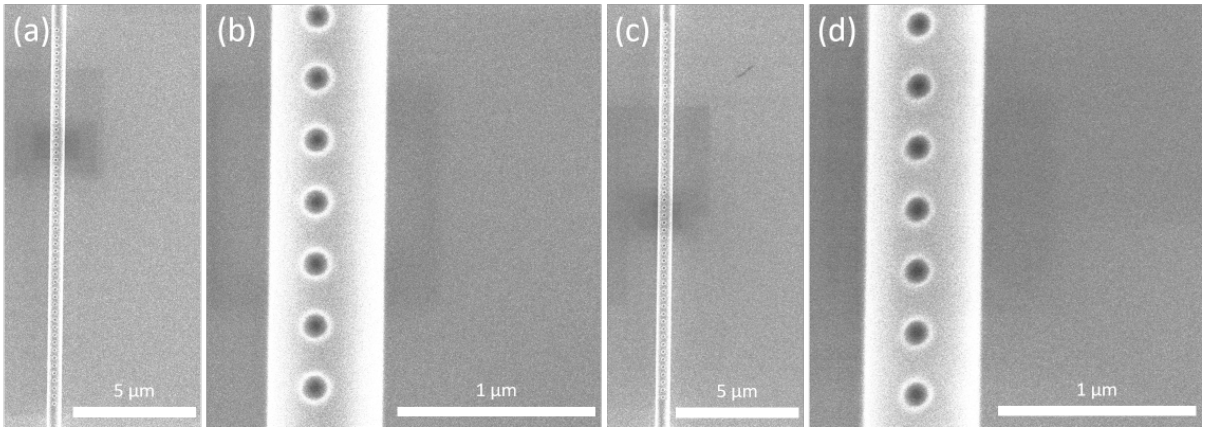

Figure B.3: SEM images of Mirror-1 in Cavity-6 ONF in (a) wide-field view and (b) close up, as well as Mirror-2 in Cavity-6 ONF in (c) wide-field view and (d) close up. The tapered fiber was fabricated by Dr. Kristoffer Karlsson and mirror fabrication using FIB was performed by Mr. Metin Ozer.

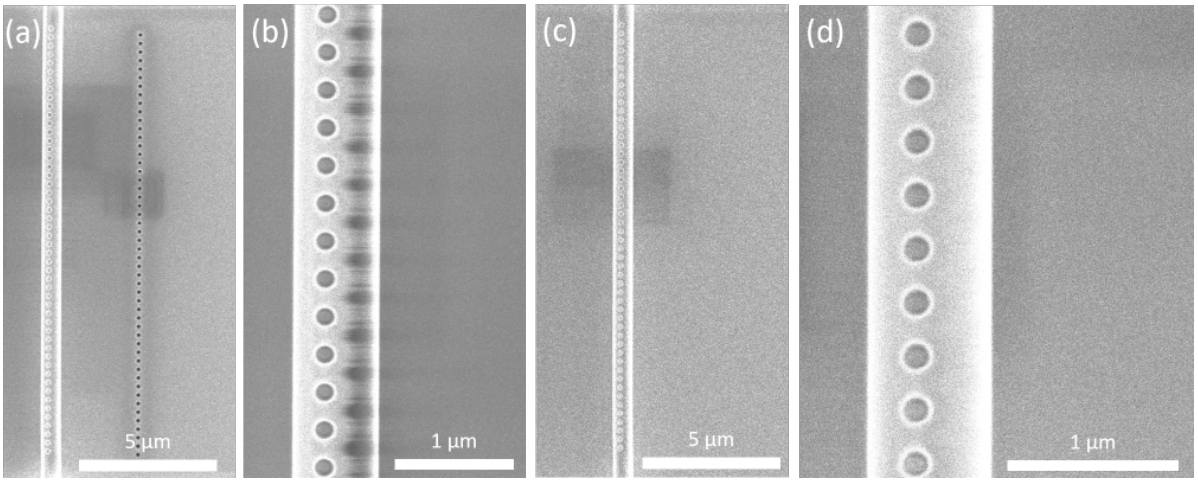

Figure B.4: SEM images of Mirror-1 in Cavity-7 in (a) wide-field view and (b) close up, as well as Mirror-2 in Cavity-7 in (c) wide-field view and (d) close up. The tapered fiber was fabricated by Dr. Kristoffer Karlsson and mirror fabrication using FIB was performed by Mr. Metin Ozer.

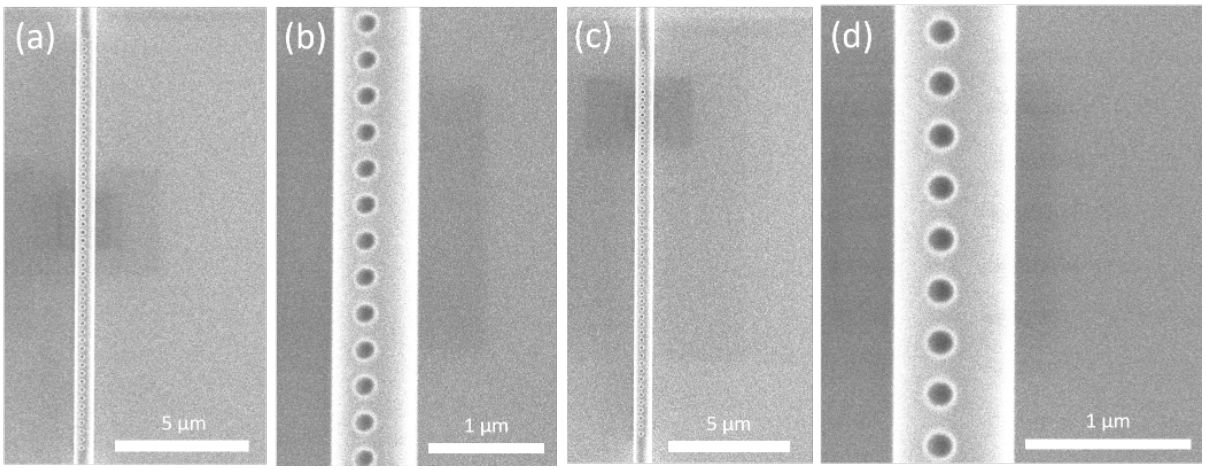

Figure B.5: SEM images of Mirror-1 in Cavity-8 in (a) wide-field view and (b) close up, as well as Mirror-2 in Cavity-8 in (c) wide-field view and (d) close up. The tapered fiber was fabricated by Dr. Kristoffer Karlsson and mirror fabrication using FIB was performed by Mr. Metin Ozer.

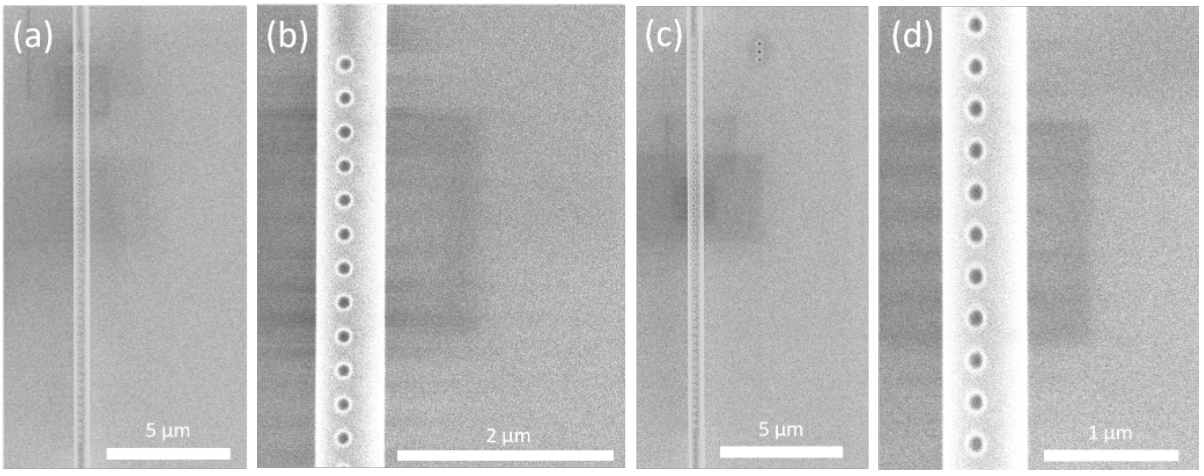

Figure B.6: SEM images of Mirror-1 in Cavity-9 in (a) wide-field view and (b) close up, as well as Mirror-2 in Cavity-9 in (c) wide-field view and (d) close up. The tapered fiber was fabricated by Dr. Kristoffer Karlsson and mirror fabrication using FIB was performed by Mr. Metin Ozer.

B.2 Simulation of ONF Reflector

In order to better understand the supported modes and their behavior in FIB-fabricated cavities, simulation by Lumerical FDTD method was performed. Due to the extremely large calculation cost (both time and memory) to simulate the whole cavity, a reflector, i.e., only a single mirror set, was simulated using transverse symmetry conditions.

The fiber material was chosen to be SiO_2 glass in the material base of Lumerical FDTD program, the fiber diameter and the grating period were set as 710 nm and 320 nm, respectively. The reflector contained 50 periods of a nano-circular hole with a diameter $d_c = 120$ nm. See Figure 4.2(a) for reference.

Simulation time was 20,000 fs. Mesh accuracy was set as 2, and the number of perfectly matched layers (PMLs) was chosen to be 8. Mesh size was 8 nm only at the section of the nanostructural grating area. The simulation area of x, y, and z spans was 1.71 μm $\times$ 1.71 μm $\times$ 25.32 μm. The polarization of the light source was either oriented along the x or y direction (transverse to the fiber axis z), and the source position was 2.825 μm away from the edge of the nanostructure. The transmission and reflection monitors were placed 3.125 μm away from the edge of the nanostructure.

Figures B.7(a, b) are the simulated results of intensity transmission (black) and reflection (red) spectra, as well as the loss (blue) spectrum for linearly polarized x or y, respectively. The intensity loss, $\mathcal{L}$, was simply calculated by

$$\mathcal{L} = 1 - (T + R). \tag{B.1}$$

where T and R are the intensity transmission and intensity reflection, respectively.

It is clear that x-polarized light reflects more than y-polarized light. The stopband is wider and the transmission dip for an x-polarized input is more prominent compared to a y-polarized input. This change comes from the nanoholes breaking the circular symmetry of the fiber cross-section, resulting in the polarization-dependent n_{eff} at the PhC nanoholes. The FIB-milled circular hole modifies the local n_{eff}. As shown in Figure 4.2(b), SiO_2-air modulation occurs along the x-direction at constant y and z positions. However, the modulation of SiO_2-air does not take place in the y-direction at constant x and z positions. As a consequence, there is a stronger perturbation in n_{eff} for the x-polarized field compared to the y-polarized field. Consequently, R increases for the x-polarized modes, leading to an expanded bandwidth for these modes.

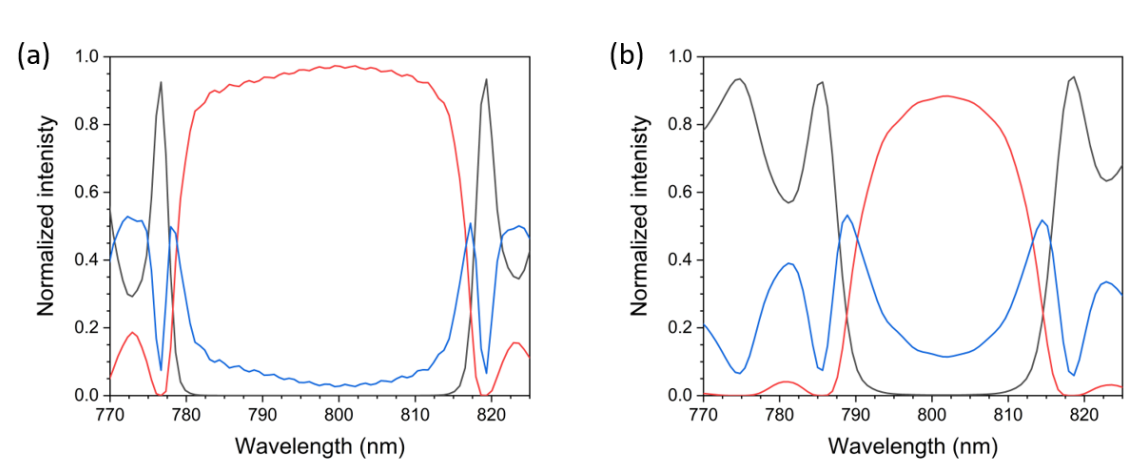

Figure B.7: FDTD simulation of transmission (black), reflection (red) and loss (blue) of a single mirror of Cavity-3 with (a) x-polarized and (b) y-polarized input beam.

B.3 Error of Cavity Linewidths

Figure B.8 shows the percentage standard error of FWHM measured in the x- and y-polarized modes of Cavity-1. There is a clear tendency to increase the error as the cavity mode peak decreases. This is caused by the reduction of the signal-to-noise ratio.

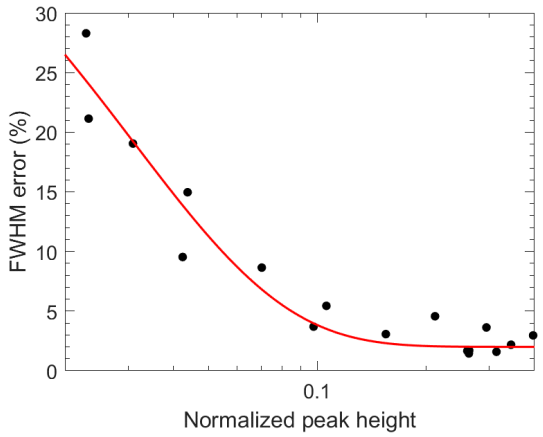

Figure B.8: Relationship between the percentage error of FWHM and normalized cavity mode peak height. The black dots are error values obtained from the standard error in Lorentzian fitting of cavity mode linewidths from experimental data, while the red line indicates the exponential fitting with $R^2 = 0.94$.

Appendix C

Supplementary Material: Laser Annealing of ONF Cavities

C.1 Vacuum Pressure and Annealing Laser Power

See Figure C.1(a, b) for the relationship between vacuum chamber pressure and the annealing laser power. The measurements were stopped overnight ($\sim$ 13-18 h) and the vacuum chamber was continued to pump down. We confirmed the spectrum did not significantly change during the night. Optical measurements and the annealing were again conducted up to $P_{\mathrm{a}} = \sim$207 μW for Cavity-4 and 544 μW for Cavity-8, respectively. Cavity-4 broke at $P_{\mathrm{a}} = 253$ μW, and Cavity-8 lost transmission at $P_{\mathrm{a}} = 544$ μW, so the experiments were terminated.

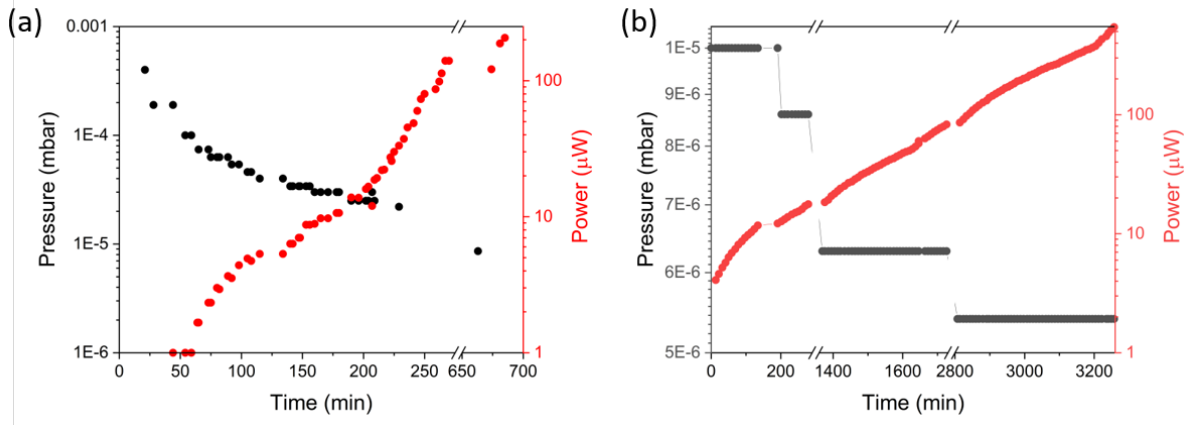

Figure C.1: Vacuum chamber pressure (black dots) and P_{a} (red dots) over time for (a) Cavity-4 and (b) Cavity-8. Annealing was initiated after the vacuum chamber reached 10^{-4} mbar. Breaks in the time axis (top and bottom) indicate the overnight pumping without measurements. The data were recorded by Dr. Priscila Romagnoli.

C.2 Stopband Analysis Methods

The approximated cavity stopbands were extracted using a MATLAB code, which returned an array of local λ mean values over a sliding window of 5 nm, see red lines in Figures C.2(a, b) for Cavity-4 and Cavity-8, respectively. We set the blue stopband edge for Cavity-4 at its normalized transmitted intensity of 0.2 for all P_a, while the red stopband edge was extracted at the normalized transmission of 0.5. In the case of Cavity-8, we set both the blue and red stopband edges at a normalized transmission of 0.3 for all P_a. These transmission values were selected by approximated averaged transmission values from the first spectrum (at $P_a = 0$ μW) and the last spectrum (at a maximum P_a). We estimated the error as an approximated averaged FSR ($\pm$1.25 nm for Cavity-4 and $\pm$1.3 nm for Cavity-8).

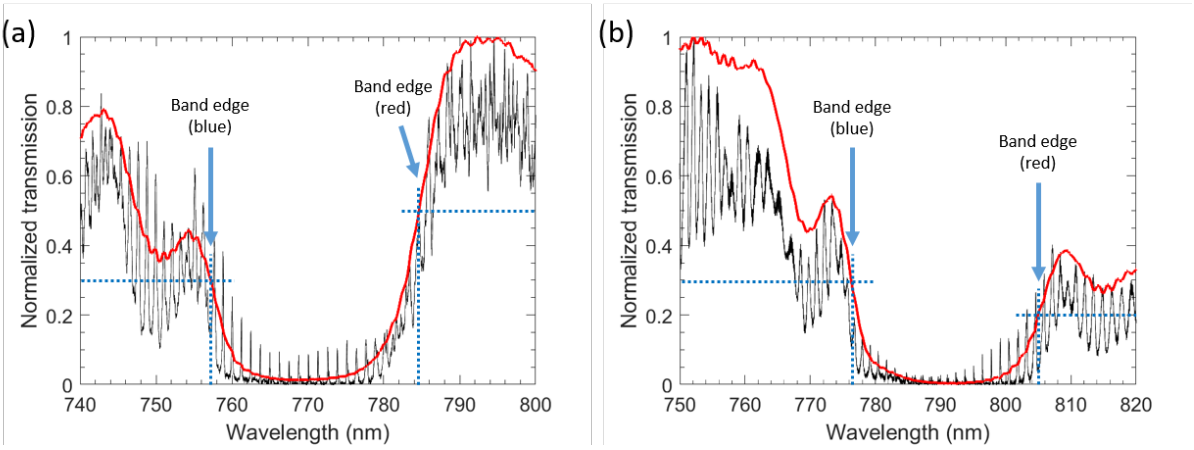

Figure C.2: Stopband edge analysis methods for (a) Cavity-4. Blue and red band edges were estimated from the normalized intensity of 0.3 and 0.5, respectively, as indicated with arrows —(b) Cavity-8. Blue and red band edges were estimated from the normalized intensity of 0.3 and 0.2, respectively, as indicated with arrows. As examples, the spectra at $P_a = 0$ μW are shown. The MATLAB code was written with Dr. Jameesh Keloth.

Appendix D

Supplementary Materials: HOM Fabry-Pérot Fiber Cavity

D.1 Mirror Reflectivity Measurements

The two FBG mirrors consisted of stacked dielectric mirrors coated on the end faces of fiber patchcords (SM1250 (9/80), Fibercore), and a reflectivity of a mirror was measured to be 97% at $\lambda = 776$ nm (Omega Optical). Before performing experiments with an HOM cavity, the reflectivity difference between two ends of mirrors and their dependency on reflectivity to different polarizations were investigated. Figure D.1(a) is an optical setup to measure the reflectivity of a HOM cavity mirror, M_{Cr}. The laser wavelength was set to the experimental working wavelength of $\lambda = 776$ nm, using a diode laser Toptica DL100 pro. The HOM cavity was mounted on a 3D stage, which can move at μm scale and controls the mirror position to maximize the coupling of the incident beam into the fiber cavity, i.e., the fiber core was centered on the reflection measurement. HWP angles were manually rotated by 10° and the intensity was measured at each angle using an oscilloscope. The measured intensity I_{r} can be described in the following form,

$$I_{\mathrm{r}} = I\ HWP\ BS_{\mathrm{t}}\ M_{\mathrm{Cr}}\ BS_{\mathrm{r}}\ M_{\mathrm{r}}, \tag{D.1}$$

where I is the initial intensity at the laser source, HWP is the transmission from a HWP with a specific plate angle, BS_{t} is the transmission from a beam splitter, BS_{r} is the reflection from a beam splitter, and M_{r} is the reflection from a mirror.

However, each optical component can cause errors in accurate measurements. The measured intensity I_{r} includes not only the reflection from a HOM cavity mirror. Beam splitters and mirrors typically have varied transmittance and reflectivity depending on the incident polarization and angles. Therefore, we calibrated the measured reflection intensity I_{r} by the reference intensity I_{ref}, such that

$$I_{\mathrm{ref}} = I\ HWP\ BS_{\mathrm{t}}\ M_{\mathrm{r}}\ BS_{\mathrm{r}}. \tag{D.2}$$

Figure D.1(b) is an optical setup to measure the reference intensity I_{ref}. All optical components were identical as to in Figure D.1(a), and the intensity I_{ref} was recorded with an oscilloscope for manually rotated HWP angles every 10°. Finally, we obtained the reflectivity of a HOM cavity mirror, M_{Cr} from these measured intensity values as

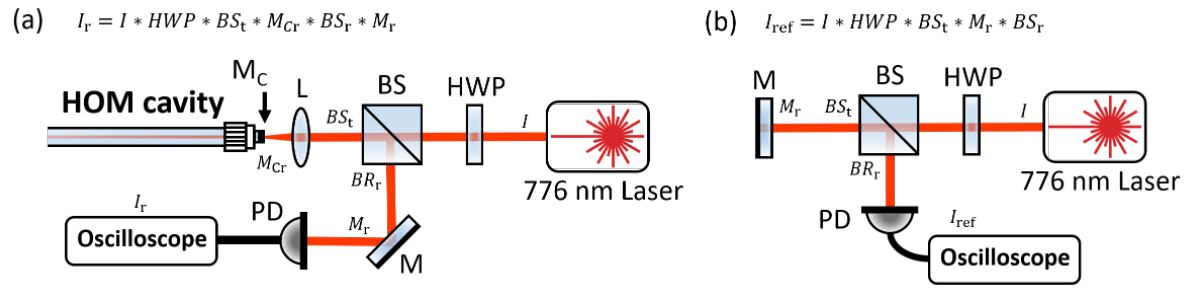

Figure D.1: (a) Schematic of optical setup to measure the HOM fiber cavity mirror reflectivity, I_r. (b) Schematic of optical setup used to measure reference intensity, I_{ref}. HWP: half-wave plate, BS: beam splitter, M: mirror, PD: photodiode, L: lens, M_C: cavity mirror.

$$M_{Cr} = \frac{I_r}{I_{ref}}. \tag{D.3}$$

Figure D.2(a) shows the change of normalized intensity over the different angles of an HWP in the incident beam. Mirror-1 of the HOM cavity (black points) showed larger fluctuations depending on the HWP angles compared to Mirror-2 of the HOM cavity (red points). The mean and standard deviation of the normalized reflectivity of Mirror-1 and Mirror-2 were 99.0±0.5% and 99.4±0.4%, respectively, indicating that the reflectivity in Mirror-1 and Mirror-2 did not have significant deviation. Both Mirror-1 and Mirror-2 had the maximum reflection at the HWP angle of 360°, while Mirror-2 also had the maximum reflection at the angle of 130°, 310°, 320°, 340°, and 350°. However, both Mirror-1 and Mirror-2 did not show maximum reflectivity at the angle of 0°, which is equivalent to 360°. This may be due to an error associated with hand adjustment of the HWP angle. Mirror-1 and Mirror-2 had minimum reflectivity at the HPW angles 230° and 260°, with normalized values of 98.0% and 98.7%, respectively. Even for the same polarization state, horizontal (H), diagonal (D), vertical (V), and antidiagonal (A) states, the measured intensity varied at different angles in both Mirror-1 and Mirror-2. This may be attributed to a very slight beam angle change by rotating the HWP which might have resulted in the change of beam spot at the HOM cavity mirror.

To better understand the input beam polarization dependence of the HOM cavity mirror reflectivity, the normalized intensity values in Figure D.2(a) for each polarization state, H, D, V, and A states, were examined. Figure D.2(b) illustrates the mean and standard deviation of the normalized intensity measured at each polarization state for Mirror-1 (orange), and Mirror-2 (green). The mean normalized reflective intensity of the horizontal beam in Mirror-1 was ∼99.5%, while the vertical beam in this mirror was ∼98.5%. This 1% was the maximum reflectivity change in overall polarization states. For Mirror-2, there was hardly any difference, i.e., $< 1\%$ in normalized reflectivity for all incident beam polarization states. One can also see that the standard deviation errors were relatively large, ranging $\sim \pm 0.2$-0.5%. These errors are likely due to manual adjustment of HWP angles. As mentioned, the change of beam paths due to HWP rotation might have also affected the errors. Moreover, errors might be also induced by the effect of the lens in front of the HOM cavity mirror (see Figure D.1(a)) when calculating the cavity mirror

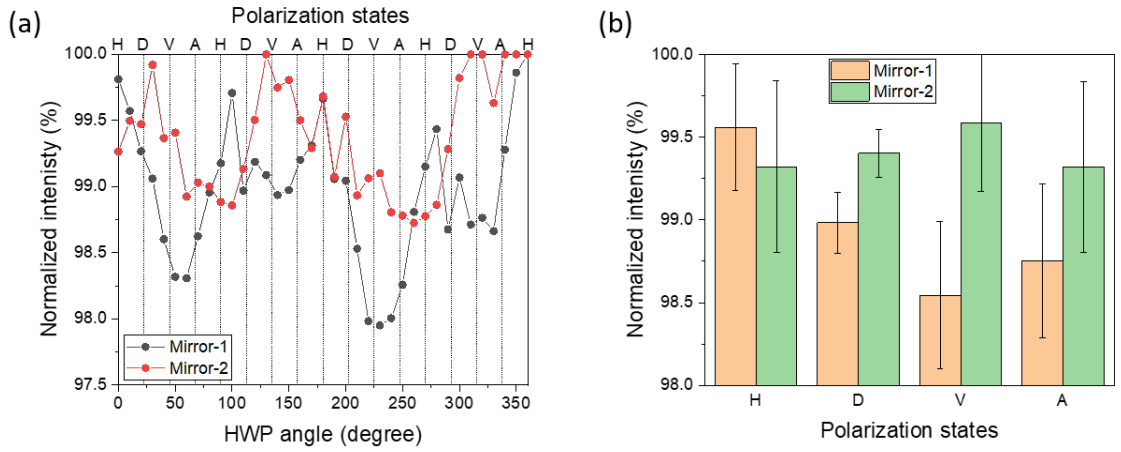

Figure D.2: (a) Change in mirror reflectivity intensity of Mirror-1 (black points) and Mirror-2 (red points) as a function of HWP angle. The reflectivity was normalized to the maximum measured reflectivity. Vertical dotted lines are HWP angles where polarizations are orientated at H: horizontal, D: diagonal, V: vertical, A: antidiagonal. (b) Mirror reflectivity of Mirror-1 (orange) and Mirror-2 (green) with different states of polarization. The reflectivity was normalized to the maximum measured reflectivity. Error bars indicate standard deviation.

reflectivity in Equation D.1. Typically, polarization states do not significantly affect the transmission of optical lenses. However, small errors might have existed. Considering these errors in experiments, the maximum reflectivity change over different polarization states was only 1%. These findings indicate that the HOM cavity mirrors, Mirror-1 and Mirror-2, did not have a significant change in reflectivity for all polarizations.

D.2 Adiabaticity of the HOM-ONF

The trilinear tapering angle was chosen according to previous unit members' experimental studies using SM1250(9/80) fiber (Fibercore) having $n_1 = 1.4586$ and $n_2 = 1.4537$ with $\lambda = 780$ nm [257, 258]. These studies followed a delineation curve of the LP_{11} mode calculated for fibers with $n_1 = 1.4636$ and $n_2 = 1.4559$ at $\lambda = 1064$ nm [257], see Figure D.3.

We noticed that we did not observe the cavity mode intensity profile that looks like LP_{21} or LP_{02} when analyzing images taken from outputs of the cavity with a HOM-OMF, see details in Section 6.7. We plotted delineation curves for all the possible modes in the HOM-OMF, that is, LP_{01}, LP_{11}, LP_{21}, and LP_{02}, see Figure D.4. The local core taper angles to follow the adiabatic criteria for the LP_{21} and LP_{02} modes were lower than the LP_{01} and LP_{11} modes. We marked the local core taper angles at the specific normalized diameter as a sold black line in Figure D.4. One can clearly see that the experimental local core taper angles at the normalized radius of 0.8-0.96 were larger than the critical angles for the LP_{21} and LP_{02} modes. This does not necessarily mean that these modes did not exist at all in the fiber, but these modes were lossy and very likely to be lost as radiation, or as a cavity mode with a wide width, i.e., low F mode. As shown in

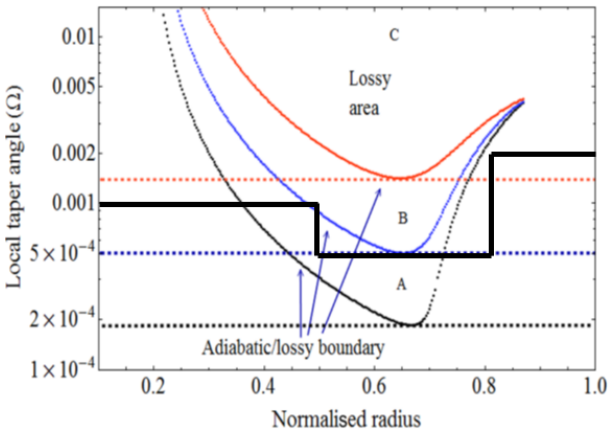

Figure D.3: The delineation curves of LP_{11} modes as a function of normalized core radius, calculated using $n_1 = 1.4636$ and $n_2 = 1.4559$ at $\lambda = 1064$ nm. The different colors of plots indicate three different original fiber cladding diameters, red: 50 μm, blue: 80 μm, and black: 125 μm. The solid bold black line indicates the tapering angle employed in this experiment. Image is taken from [257] with permission from the author.

Figure 6.7(a), the baseline of the cavity transmitted intensity is not zero, implying that some low F modes might have existed. If one chooses local core taper angles lower than critical angles for the LP_{21} and LP_{02} modes, it may be possible to observe the signature of these modes, such as the flour intensity shape we measured in the cavity without tapered fiber (see Figure 6.10).

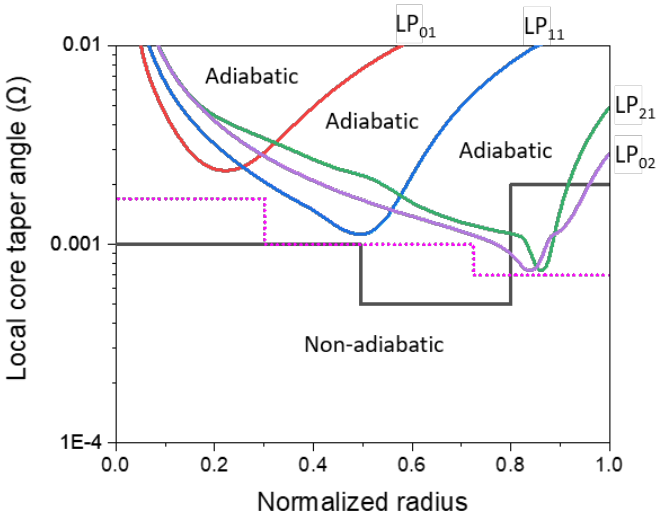

Figure D.4: The delineation curves of LP_{01} (red), LP_{11} (blue), LP_{21} (green), and LP_{02} (purple) as a function of normalized core radius. The local tapering angles employed in this experiment were $\Omega_1 = 2$ mrad (a = 64-80 μm), $\Omega_2 = 0.5$ mrad (a = 40-64 μm) and $\Omega_3 = 1$ mrad ($a = d$/2-40 μm), marked as solid black line. The pink dotted line indicates an ideal local core taper angle for a trilinear shape for adiabatic HOM-OMF to support all of the LP_{01}, LP_{11}, LP_{21}, and LP_{02} modes.

D.3 Effects of the Incident Beam on Cavity Modes

Mode 3 was only resolved in the cavity spectrum taken with the incident coupling MAX, see Figure D.5(a). Same as Mode 2, this mode also had a lobe-shaped intensity pattern, but with the splitting line in the D direction. It had all types of Stokes singularities. The SOPs varied across the beam with some circular and elliptical polarization in both left- and right-handed directions, but the dominant polarization seemed A. This mode had the frequency position very close to the frequency of Mode 2 of the incident beam coupling HIGH, LOW, and MIN, see Figure 6.8(b). Even though the intensity of Mode 2 of the incident beam coupling MAX was very small, the spatial field profile of Mode 3 may have been influenced by some interference from Mode 2 components. There was a very slight peak at the same relative frequency in the spectrum of the incident coupling MIN, but the peak height was too LOW and could not be locked due to the close distance from the adjacent Mode 2, which had higher intensity.

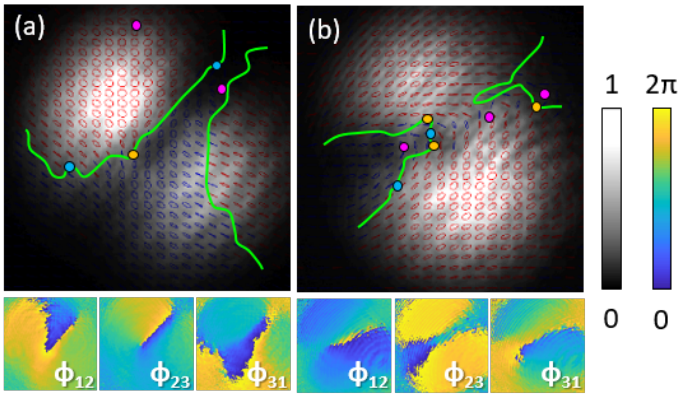

Figure D.5: Mode intensity profiles with the SOPs (top) and Stokes phases (bottom) for (a) Mode 3 generated from the coupling MAX and (b) Mode 4 generated from the coupling LOW. The red and blue SOPs indicate right-handed and left-handed ellipticities, respectively. Scale bars show intensity (from 0 to 1) and Stokes phase (from 0 to 2π). Stokes singularities of σ_{12}, σ_{23}, and σ_{31} are indicated as pink, orange, and blue dots, respectively. L-lines are illustrated as green lines.

Coupling condition LOW had a distinctive mode (Mode 4), while spectra recorded with other incident beam couplings did not have a clear peak at the same frequency (see Figure 6.8(b)). Mode intensity shape and the SOPs and Stokes phases are illustrated in Figure D.5(b). This mode had a lobe-like shape intensity pattern with the split line orientated at the D direction. SOPs at each point of the cavity output cross-section were right-handed ellipses, but not with the uniform ellipse orientation. There are many Stokes singularities in this mode as well. These findings indicate that this cavity mode was created from multiple modes. As Mode 4 also overlapped with Mode 5 for LOW coupling, see Figure 6.8(b), the spatial field structures of Mode 4 may also have some effect from Mode 5.